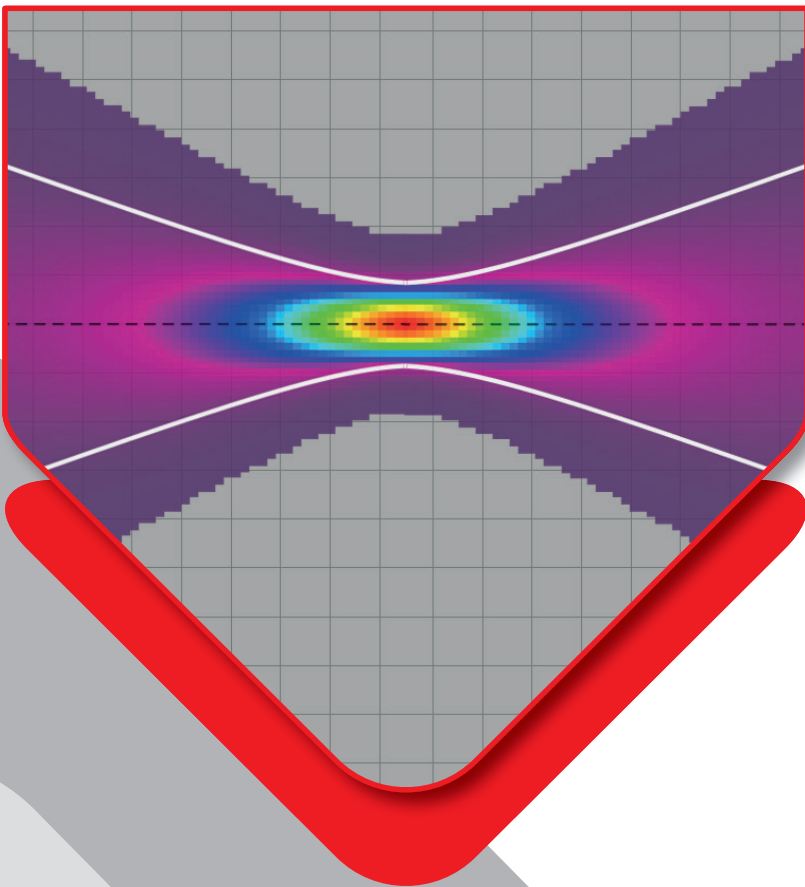


# Multi-Physics Simulation of High-Power Solid-State Laser Systems





Marius Leander Rupp

**Multi-Physics Simulation of High-Power  
Solid-State Laser Systems**

Lasers and Optronics:  
Materials, Technologies and Applications  
**Volume 5.2025**

Editor: Prof. Dr. rer. nat. habil. Marc Eichhorn

Professur für Optronik am  
Karlsruher Institut für Technologie (KIT)

Fraunhofer-Institut für Optronik, Systemtechnik  
und Bildauswertung (IOSB)

# **Multi-Physics Simulation of High-Power Solid-State Laser Systems**

by  
Marius Leander Rupp

Karlsruher Institut für Technologie  
Institut für Regelungs- und Steuerungssysteme

## Multi-Physics Simulation of High-Power Solid-State Laser Systems

Zur Erlangung des akademischen Grades eines Doktors der  
Ingenieurwissenschaften von der KIT-Fakultät für Elektrotechnik  
und Informationstechnik des Karlsruher Instituts für Technologie (KIT)  
genehmigte Dissertation

von Marius Leander Rupp, M.Sc.

Tag der mündlichen Prüfung: 16. Januar 2025  
Hauptreferent: Prof. Dr. rer. nat. habil. Marc Eichhorn  
Korreferent: Prof. Dr.-Ing. Christian Koos

### Impressum



Karlsruhe Institute of Technology (KIT)  
Kaiserstraße 12  
76131 Karlsruhe  
Institute of Control Systems  
[www.irs.kit.edu](http://www.irs.kit.edu)



*This document – excluding parts marked otherwise, the cover, pictures and graphs –  
is licensed under a Creative Commons Attribution 4.0 International License  
(CC BY 4.0): <https://creativecommons.org/licenses/by/4.0/deed.en>*



*The cover page is licensed under a Creative Commons  
Attribution-No Derivatives 4.0 International License (CC BY-ND 4.0):  
<https://creativecommons.org/licenses/by-nd/4.0/deed.en>*

2025

ISSN 2943-2308

DOI 10.5445/IR/1000179649





# **Multi-Physics Simulation of High-Power Solid-State Laser Systems**

Zur Erlangung des akademischen Grades eines  
DOKTORS DER INGENIEURWISSENSCHAFTEN (Dr.-Ing.)

von der KIT-Fakultät für Elektrotechnik und Informationstechnik des  
Karlsruher Instituts für Technologie (KIT)  
angenommene

DISSERTATION

von

**Marius Leander Rupp, M.Sc.**

geboren am 13.03.1994 in Stuttgart

Tag der mündlichen Prüfung: 16.01.2025

Hauptreferent: Prof. Dr. rer. nat. habil. Marc Eichhorn

Korreferent: Prof. Dr.-Ing. Christian Koos



# Kurzfassung

Heutzutage sind Laser unverzichtbar für zahlreiche Anwendungen, darunter Unterhaltungselektronik, Kommunikation, Medizin, industrielle Fertigung sowie Verteidigung und Sicherheit. Abhängig von der Anwendung werden verschiedene Lasertypen verwendet. Der Fokus dieser Arbeit liegt auf Festkörperlasern, die besonders wegen ihrer kompakten Größe, hohen Strahlqualität und hohen Leistungs- und Energieausbeute hervorstechen. Da vollständige Lasersysteme sehr komplex sein können, bieten computergestützte Simulationen eine zeit- und kosteneffiziente Methode für deren Optimierungsprozess. Simulationen ermöglichen die Analyse von ansonsten unzugänglichen Größen und Prozessen, wie z.B. lokaler Inversion und Temperaturdynamik, was zu einem tieferen Verständnis und neuen Designkonzepten führt.

In dieser Arbeit wird ein multiphysikalischer Modellierungsansatz für die Simulation von Hochleistungs-Festkörperlasern entwickelt. Der Ansatz basiert auf der Kombination von drei Untermodellen bezüglich Laserstrahlpropagation, Laserdynamik und thermischen Effekten. Im Verlauf des Manuskripts wird die Steigerung der Simulationsgenauigkeit durch die Erweiterung mit den verschiedenen Teilmodellen und Simulationsansätzen erläutert. Für das erste Untermodell wird die FFT Strahlpropagationmethode verwendet, um den Laserstrahl schrittweise entlang der Propagationsachse zu modellieren. Der Lasergewinn wird mit dem zweiten Untermodell berücksichtigt, bei dem Ratenmodellgleichungen die intrinsischen Populationsdynamiken des Lasermediums berechnen. Die modulare Simulation kann sowohl auf Laserresonatoren als auch auf Verstärker angewendet werden, mit besonderem Augenmerk auf Hochleistungslaser, bei denen die Wärmeentwicklung die Leistung erheblich beeinflussen kann. Aus diesem Grund wird ein drittes Untermodell integriert, welches thermische Effekte und Verteilungen mittels Finite-Differenzen-Methoden simuliert. Nach der iterativen Simulation können die Ausgangseigenschaften des Lasersystems, einschließlich des Laserausgangs und der Verteilungen innerhalb optischer Elemente, bewertet werden. Um die Leistungsfähigkeit

des entwickelten Modells zu demonstrieren, wird es für das Design und die Optimierung experimenteller  $\text{Ho}^{3+}$ :YAG-Festkörperlaser eingesetzt. Zwei Systeme werden entworfen: ein gütegeschalteter linearer Resonator und eine Leistungsverstärkerstufe. Durch den Einsatz des Simulationsmodells konnten bei beiden Lasern Betriebspunkte erreicht werden, die von üblichen  $\text{Ho}^{3+}$ :YAG-Systemen abweichen.

Zusammenfassend präsentiert diese Arbeit ein modulares multiphysikalisches Modell für die präzise Modellierung von Festkörperlasern, das deren Design, Optimierung und Analyse ermöglicht. Das entwickelte Modell wird durch das Design experimenteller  $\text{Ho}^{3+}$ :YAG-Lasersysteme validiert und zeigt seine Effektivität als Entwicklungswerkzeug für Hochleistungslaseranwendungen.

# Abstract

Advancements in laser technology have enabled their widespread use in consumer electronics, communication, medical fields, industrial manufacturing, and defense. Depending on the application, different types of lasers are used. The focus of this work is on solid-state lasers, which offer compact size, high beam quality, and high power and energy efficiency. As these laser systems must be designed and optimized for specific applications, computer-aided simulations provide a time- and cost-efficient method for this process. Simulations allow for the analysis of otherwise inaccessible quantities and processes, such as local inversion and temperature dynamics, leading to a deeper understanding and new design concepts.

In this work, a multi-physics modeling approach is developed for the simulation of high-power bulk lasers. The model consists of three main submodels addressing laser beam propagation, laser gain, and thermal effects. Throughout this manuscript, the simulation accuracy is increased with the implementation of these submodels and various simulation approaches. For the first submodel, the FFT beam propagation method is employed to model the laser beam sequentially along the propagation axis. The laser gain is included with the second submodel, where rate equations are used to calculate the intrinsic population dynamics of the gain medium. The modular simulation structure is capable of modeling both laser resonators and amplifiers, with a specific focus on high-power lasers where heat generation significantly impacts performance. Consequently, a third submodel is incorporated to model thermal effects and distributions based on finite difference methods. At the end of the iterative simulation, the output characteristics of the laser system, including laser output and internal element distributions, can be evaluated. To demonstrate the capabilities of the developed simulation tool, it is employed for the design and optimization of experimental  $\text{Ho}^{3+}$ :YAG bulk lasers. Two systems are designed: a Q-switched linear resonator and a power amplifier stage. By utilizing the developed

simulation model, both designs achieved operation points that deviate from usual  $\text{Ho}^{3+}$ :YAG systems.

In summary, this work presents a modular multi-physics model for the precise modeling of bulk solid-state lasers, enabling their design, optimization, and analysis. The developed model is validated through the design of experimental  $\text{Ho}^{3+}$ :YAG laser systems, showcasing its effectiveness as a design tool for high-power laser applications.

# Contents

<b>Kurzfassung</b> . . . . .	<b>i</b>
<b>Abstract</b> . . . . .	<b>iii</b>
<b>1 Introduction</b> . . . . .	<b>1</b>
<b>2 Fundamental Optical Simulation Model</b> . . . . .	<b>7</b>
2.1 Background on Physical Optics . . . . .	7
2.2 Beam Propagation in Isotropic Media . . . . .	13
2.2.1 Split-Step BPM Approach . . . . .	13
2.2.2 Submodel Validation . . . . .	18
2.3 Beam Propagation in Anisotropic Media . . . . .	20
2.3.1 BPM Adaption for Vectorial Fields . . . . .	20
2.3.2 Submodel Validation . . . . .	24
2.4 Modeling of Bulk Laser Systems . . . . .	26
2.4.1 State-of-the-Art Overview . . . . .	26
2.4.2 Simulation Framework and Modular Structure . . . . .	29
2.4.3 Element Operators . . . . .	32
<b>3 Solid-State Laser Model</b> . . . . .	<b>37</b>
3.1 Background on Laser Physics . . . . .	37
3.2 Solid-State Laser Principles . . . . .	45
3.2.1 Solid-State Geometries and Concepts . . . . .	45
3.2.2 Modes of Laser Light . . . . .	49
3.2.3 Resonator Stability . . . . .	52
3.3 Generalized Simulation of Laser Gain Media . . . . .	55

3.3.1	Basic Rate Equation Model . . . . .	55
3.3.2	Submodel Validation . . . . .	59
3.4	Extended Simulation of $\text{Ho}^{3+}$ -Doped Gain Media . . . . .	63
3.4.1	Specific Rate Equation Model for the $\text{Ho}^{3+}$ Ion . . . . .	63
3.4.2	Submodel Validation . . . . .	67
3.5	Advanced Laser Media Dynamics . . . . .	71
3.5.1	Extension to a Spectrally Resolved Model . . . . .	71
3.5.2	Implementation of Pulsed Operation by Q-switching . . . . .	78
3.6	Simulation of an Exemplary Laser Resonator . . . . .	84
<b>4</b>	<b>Thermal Model for Bulk Elements . . . . .</b>	<b>91</b>
4.1	Background on Thermodynamics in Solids . . . . .	91
4.2	Simulation of the Three-Dimensional Temperature Distribution . . . . .	99
4.2.1	Numerical ADI-FDM Solution . . . . .	99
4.2.2	Example and Submodel Validation . . . . .	105
4.3	Simulation of Three-Dimensional Displacement and Stress Distributions . . . . .	109
4.3.1	Numerical FDM Solution . . . . .	109
4.3.2	Example and Submodel Validation . . . . .	116
4.4	Resulting Thermal Effects Impacting Laser Performance . . . . .	119
4.4.1	Temperature-Dependent Material Parameters . . . . .	119
4.4.2	Stress-Induced Birefringence and Depolarization . . . . .	124
4.4.3	Thermal Lensing . . . . .	131
<b>5</b>	<b>Optimization of <math>\text{Ho}^{3+}</math>:YAG Laser Systems . . . . .</b>	<b>137</b>
5.1	Experimental Methods and Measurement Devices . . . . .	137
5.2	State-of-the-Art $\text{Ho}^{3+}$ :YAG Laser Systems . . . . .	140
5.2.1	High-Power Linear Resonators . . . . .	141
5.2.2	High-Power Amplifiers . . . . .	143
5.3	$\text{Ho}^{3+}$ :YAG Resonator at 2122 nm in Q-switched Operation . . . . .	146
5.3.1	Description and Simulative Optimization . . . . .	146
5.3.2	Experimental Results . . . . .	153
5.3.3	Discussion . . . . .	158
5.4	$\text{Ho}^{3+}$ :YAG Amplifier for a Seed Fiber MOPA at 2048 nm . . . . .	159
5.4.1	Description and Simulative Optimization . . . . .	159
5.4.2	Experimental Results . . . . .	168

5.4.3 Discussion . . . . . 172

**6 Conclusion and Outlook . . . . . 175**

**References . . . . . 181**

**Publications and Conference Contributions . . . . . 199**

**List of Acronyms . . . . . 201**

**Acknowledgements . . . . . 203**



# 1 Introduction

Since the construction of the first laser by Theodore Maiman in 1960, significant advancements have led to the tight integration of lasers across various fields in modern society [1]. The light produced by lasers exhibits high brightness, coherence, and directionality, distinguishing them from incoherent light sources and making them useful for various applications. Innovations such as the development of new spectral ranges through diverse active media, the achievement of higher power classes via novel designs, and the miniaturization and integration of lasers into chips have enabled their widespread use in consumer electronics, communication, medical fields, industrial manufacturing, and defense and security [2]. To meet the specific optical and mechanical requirements depending on the application area, a variety of different laser types have been developed in different designs and levels of integration. One prevalent type, when classified by the active laser medium, are rare-earth-doped solid-state lasers. In comparison to other common laser types, bulk solid-state lasers can achieve a compact size, high beam quality, and high power and energy extraction [3].

The output characteristics of a bulk laser system must be designed and optimized to meet the requirements of the specific application. Here, computer-aided simulations serve as a time- and cost-efficient method for optimizing and analyzing laser systems, thereby reducing the need for extensive experiments. Therefore, within the scope of this work, a novel comprehensive fully-numerical modeling approach is developed and investigated. In comparison to the state-of-the-art, the emphasis of the complete model is on achieving high simulation accuracy and fidelity, while enabling high adaptability through the incorporation of additional physical effects. This can result in increased model complexity and slower computation speed compared to more simplified approaches, but is necessary to realize the capabilities of the model presented in this work. The comprehensive model manages to overcome several limitations of current state-of-the-art laser simulation tools including commercially available ones.

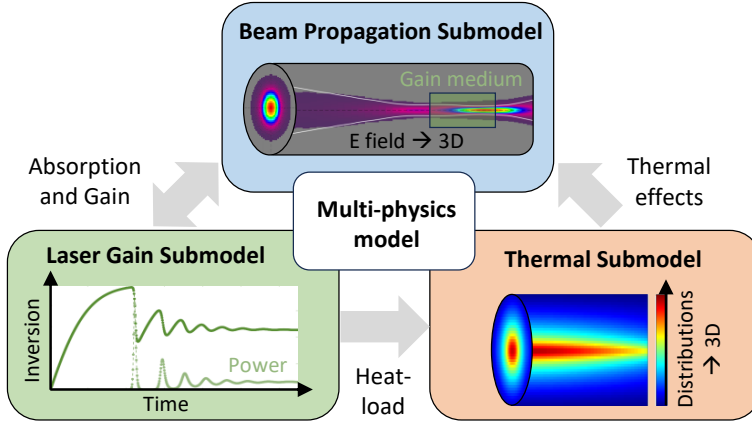


Figure 1.1: Schematic description of the three main submodels of the multi-physics approach concerning beam propagation, laser gain, and thermal effects. The goal of the combined model is to achieve high accuracy, model fidelity, and model adaptability.

A crucial aspect of simulations is to make many quantities and processes within the laser accessible, which cannot be directly measured. This includes local inversion and temperature within the laser medium and their dynamics. By modeling these aspects, a deeper understanding of the internal mechanisms is achieved, which can then be utilized in new design concepts. For instance, simulations can comprehensively model the propagation of laser beams, their interactions with matter, and thermal processes within the laser. However, given that a complete laser system comprises a vast number of degrees of freedom, model approaches of varying complexity are required for an efficient design process. To model bulk solid-state lasers with high precision and account for all relevant physical properties, a complex numerical model is necessary.

The model developed within the scope of this work is based on a multi-physics approach, with a focus on the comprehensive simulation of high-power bulk laser systems and their output characteristics. The model consists of three main submodels addressing laser beam propagation, laser gain, and thermal effects – as illustrated schematically in Fig. 1.1. Regarding the first submodel (Fig. 1.1, blue), the FFT beam propagation method is employed to model the laser beam along with other coherent light sources in a two-dimensional ( $x$ - $y$ ) electromagnetic field representation. This field is propagated sequentially along the propagation axis ( $z$ ), yielding a three-dimensional field distribution. Between the propagation steps, different optical elements

can be defined, leading to a modular simulation structure capable of modeling a wide range of system geometries and arrangements. The specific element operators change the electromagnetic field in accordance with their functionality and include lens, mirror, polarizer, and waveplate operators. The laser gain submodel is included with the gain medium element (Fig. 1.1, green), where rate equations are employed to calculate the intrinsic population dynamics and the influence on the laser field. The time-dependent solution to the rate equations enables the model to consider the temporal dynamics of both continuous-wave and pulsed bulk laser systems. As a consequence of the modular simulation structure, both laser resonators and laser amplifiers can be modeled. While amplifiers represent simpler geometries, where a seed signal laser is amplified by a single- or multi-pass through the gain medium, laser resonators require multiple round-trips to generate a beam from the stimulated emission of vacuum noise.

The focus of this work lies on high-power lasers, where light absorption can lead to heat generation within optical elements such as the laser gain medium. Given the significant impact of heat on laser performance, the multi-physics approach requires the inclusion of a thermal submodel (Fig. 1.1, orange). This is achieved through a numerical three-dimensional simulation of temperature and stress distributions using finite difference methods. These distributions enable the implementation of thermal effects that influence the laser field, encompassing temperature-dependent material parameters, thermal lensing, and stress-induced birefringence. In summary, the modular multi-physics model takes into account the following relevant mechanisms and effects:

Beam Propagation Submodel	Laser Gain Submodel	Thermal Submodel
<ul style="list-style-type: none"> <li>• Diffraction, refraction, and reflection</li> <li>• Polarization states</li> <li>• Isotropic and anisotropic media propagation</li> </ul>	<ul style="list-style-type: none"> <li>• Rate equation modeling</li> <li>• Multi-level population dynamics</li> <li>• Spectral and temporal resolution</li> </ul>	<ul style="list-style-type: none"> <li>• Temperature, displacement, and stress distributions</li> <li>• Temperature-dependence</li> <li>• Thermal lensing and birefringence</li> </ul>

The integration of these submodels enables the comprehensive simulation of bulk solid-state laser systems. The fundamental approach is based on the iterative computation of numerical values, which are updated continuously until a defined end condition is achieved. After simulation, the output characteristics of the laser system can be evaluated, providing insight into performance and inherent properties. For the laser field, this includes laser output power, polarization states, and the temporal and spectral evolution of the field. Furthermore, the distribution of the laser and pump fields at any point within the laser system can be examined. For optical elements experiencing heat development, the temperature, displacement, and stress distributions are computed and can be analyzed. This approach results in the precise modeling of bulk solid-state lasers, and is utilized for the design, optimization, and analysis of such systems.

To demonstrate the capabilities of the developed simulation tool, it is employed for the design and optimization of experimental  $\text{Ho}^{3+}$ :YAG bulk laser systems. For high-power applications, the gain medium  $\text{Ho}^{3+}$ :YAG is typically in-band pumped at the  $^5I_7 \rightarrow ^5I_8$  laser transition to generate radiation in the shortwave infrared region around  $2\text{ }\mu\text{m}$  [4]. This wavelength region is relevant for medical applications and material processing, and owing to the presence of an atmospheric transmission window in the SWIR, it is also of interest for LIDAR applications and security and defense. Furthermore, pulsed lasers in this spectral region can serve as pump sources for nonlinear conversion into the midwave infrared [5]. Two systems are designed within this work, a resonator and an amplifier, both displaying unique spectral output characteristics. The state-of-the-art analysis for high-power  $\text{Ho}^{3+}$ :YAG laser systems reveals that most systems operate around the main emission peak of this gain material at 2090 nm [6–9]. However, the developed simulation model enables the intricate design of highly efficient lasers at various wavelength regions. The first system is a Q-switched linear resonator, optimized for high-power pulsed operation at an operation wavelength of 2122 nm. This shift to a longer emission wavelength provides benefits for specific applications, such as the nonlinear conversion in ZGP which exhibits lower background absorption at wavelengths beyond 2090 nm [10]. The second system is a  $\text{Ho}^{3+}$ :YAG power amplifier stage, seeded by a fiber MOPA with a wavelength of 2048 nm. Given the low emission cross section of  $\text{Ho}^{3+}$ :YAG in this spectral region, the simulation model was utilized to optimize the amplifier stage for high gain by leveraging a thermal lens guiding approach over a long crystal length. The excellent experimental results, consistent with state-of-the-art amplifiers at the main emission peak, underline the potential for highly efficient  $\text{Ho}^{3+}$ :YAG performance across a broad wavelength range.

## Structure of the Work

The manuscript begins with the discussion of the fundamental framework in chapter 2, on which the final simulation model is built. Given that the simulation is based on the concept of laser beam propagation, the basic theory of physical optics leading to the description of the laser beam is provided. The split-step beam propagation method is selected as the most appropriate laser beam model for this work, where Maxwell's equations of electromagnetic wave propagation can be resolved for isotropic or anisotropic propagation media. Moreover, the modular nature of the comprehensive simulation approach is explained, where various system geometries can be modeled by employing sequential element operators. The fundamental model enables the simulation of complex optical arrangements made of multiple optical elements. Throughout this manuscript, this fundamental model is expanded upon with various submodels and simulation approaches, each one enhancing the accuracy of the simulation of high-power laser systems.

In chapter 3, the laser gain submodel is integrated into the multi-physics approach to model the entire laser system. Following an overview of the fundamental laser physics describing the laser gain process, the main principles and system concepts specific to solid-state laser systems are provided. Subsequently, a basic rate equation model for simulating laser gain and absorption is described. In addition to the generalized approach, a more specific model for  $\text{Ho}^{3+}$ -doped gain media is presented, and advanced laser media dynamics, such as the extension to a spectrally resolved model and the inclusion of pulsed laser operation, are implemented. The simulation of an exemplary laser resonator is investigated to demonstrate the capabilities of the model at this stage.

The simulation of the high-power exemplary resonator reveals some deviations with the experimental results, which are attributed to thermal effects. As high-power laser systems induce heat development within optical elements, these effects have to be incorporated into the multi-physics modeling approach. The implementation of a comprehensive thermal submodel is detailed in chapter 4. After the background knowledge of thermodynamic behavior in solids is provided, the numerical solutions for temperature, displacement, and stress distributions in three dimensions are described. Subsequently, the influence of these distributions on the electromagnetic field is discussed, encompassing the thermal dependency of material parameters and thermo-optic effects such as thermal lensing and stress-induced birefringence. After the implementation of the thermal submodel, the simulation of the exemplary resonator exhibits

excellent agreement with the experimental results, validating the accuracy of the complete model.

The preceding chapters describe the development and validation of a multi-physics model for simulating bulk solid-state lasers, demonstrating its effectiveness as a design tool. In chapter 5, the developed model is utilized to investigate the spectral behavior of  $\text{Ho}^{3+}$ :YAG laser systems, resulting in the development of two experimental systems with unique characteristics compared to state-of-the-art systems. The first experimental system is a high-power Q-switched linear resonator with spectral single-line output at 2122 nm, while the second laser system is a  $\text{Ho}^{3+}$ :YAG power amplifier stage for a narrow-linewidth fiber seed MOPA at 2048 nm. By utilizing the developed simulation model, both systems could be designed to exhibit spectral operation points that deviate from the typical  $\text{Ho}^{3+}$ :YAG emission wavelengths, while operating with exceptional performance.

Finally, a summary of the work is provided in chapter 6, and further improvements to the simulation model as well as the  $\text{Ho}^{3+}$ :YAG experiments are discussed.

## 2 Fundamental Optical Simulation Model

The main contribution of this thesis is a generalized multi-physics approach to describe and analyze free-space and resonant geometries for laser generation and amplification. This chapter outlines the framework upon which the final simulation model is built. Since the simulation approach is based on the concept of laser beam propagation, the fundamental theory of physical optics leading to the description of the laser beam is detailed in section 2.1. To simulate the propagation of laser beams, a numerical approach to solving Maxwell's equations for electromagnetic wave propagation is investigated. The split-step beam propagation method (BPM) is chosen the most suitable model for this work, and the specific approach is described for isotropic media in section 2.2. The model is further adapted to include the propagation in anisotropic media and corresponding polarization effects, as described in section 2.3. In the final section 2.4 of this chapter, the modular nature of the complete simulation approach is explained, where different system geometries can be modeled by utilizing sequential element operators.

### 2.1 Background on Physical Optics

To give an overview on the fundamental properties of laser light and diffraction phenomena, an introduction to physical optics is provided in this section. Light can be described by radiation that manifests as electromagnetic waves that oscillate within the electric and magnetic fields. The frequency of these oscillations is used to categorize the electromagnetic spectrum into radio waves, microwaves, infrared, visible, ultraviolet, X-rays, and gamma rays, as depicted in Fig. 2.1. Despite the diverse generation mechanisms and applications of different types of

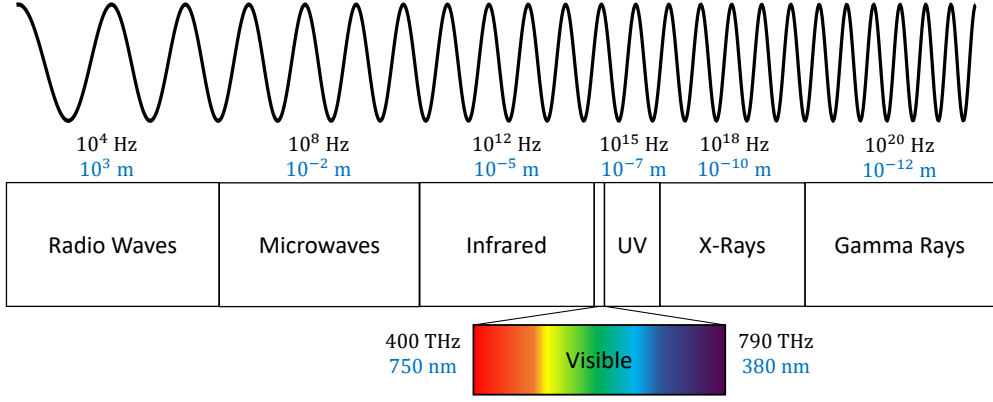


Figure 2.1: Schematic representation of the entire electromagnetic spectrum, ranging from radio waves to gamma rays, with annotations for the radiation type, wavelength, and frequency. Graph adapted from [11].

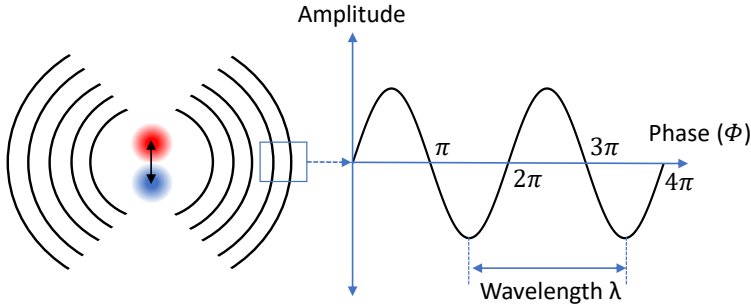


Figure 2.2: Single electromagnetic wave derived from a schematic dipole emitter, illustrating the relationship between amplitude, phase, and wavelength.

electromagnetic radiation, the fundamental physics of wave propagation remain consistent. Consequently, the basic propagation model described in this work should be adaptable to a broad range of the electromagnetic spectrum.

Figure 2.2 shows a single electromagnetic wave as a schematic cutout from a dipole emitter. This representation reveals additional properties of electromagnetic waves: the phase  $\phi$  of the wave denotes the angular position of the oscillation in time and space, while the amplitude  $A$  of the wave is proportionally related to the intensity by  $I \propto A^2$  [12].

While light propagates as an electromagnetic wave, the interaction with matter can act like a particle. This is described as the wave-particle duality, where light can be interpreted as a particle called photon [13]. One of the distinguishing features of the electromagnetic spectrum, the oscillation frequency  $f$ , is connected to the photon energy  $E_{\text{ph}}$  with

$$E_{\text{ph}} = hf = \frac{hc}{\lambda} . \quad (2.1)$$

With the relation to the Planck constant  $h$ , a photon can therefore be described as the smallest possible energy quantification of detectable electromagnetic radiation. Equation (2.1) also shows that the frequency is equal to the speed of light  $c$  divided by the wavelength  $\lambda$ . Given that the speed of light in vacuum is defined with a fixed value of 299792458 m/s, the wavelength can also serve to characterize the electromagnetic spectrum.

In the 19th century, James Clerk Maxwell was one of the first to propose a description of light as an electromagnetic phenomenon. The four equations he formulated remain valid today and are presented in the microscopic partial differential form with equations (2.2) - (2.5), where  $\vec{E}$  represents the electric vector field,  $\vec{B}$  the magnetic vector field,  $\rho$  the electric charge density,  $\vec{J}$  the electric current density,  $\epsilon_0$  the vacuum permittivity,  $\mu_0$  the vacuum permeability, and  $\nabla$  the three-dimensional gradient operator [12, 13].

$$\nabla \cdot \vec{E} = \frac{\rho}{\epsilon_0} \quad (\text{Gauss's law for electricity}) , \quad (2.2)$$

$$\nabla \cdot \vec{B} = 0 \quad (\text{Gauss's law for magnetism}) , \quad (2.3)$$

$$\nabla \times \vec{E} = -\frac{\partial \vec{B}}{\partial t} \quad (\text{Faraday's law}) , \quad (2.4)$$

$$\nabla \times \vec{B} = \mu_0 \vec{J} + \mu_0 \epsilon_0 \frac{\partial \vec{E}}{\partial t} \quad (\text{Ampere-Maxwell law}) . \quad (2.5)$$

These equations are applicable at any point in space and time, illustrating how electric and magnetic fields are interconnected with electric charges, electric currents, and each other. To describe wave propagation in a vacuum, it can be assumed that the electric and magnetic fields are solely functions of space and time, and that no charges or currents exist in the region of interest. This implies that  $\rho$  and  $\vec{J}$  can be set to zero in Eqs. (2.2) and (2.5).

By utilizing the vector identity  $\nabla \times (\nabla \times \vec{E}) = \nabla(\nabla \cdot \vec{E}) - \nabla^2 \vec{E}$ , Faraday's law (2.4) can be simplified to illustrate the wave equation for the magnetic field in vacuum as follows [13]:

$$\mu_0 \epsilon_0 \frac{\partial^2 \vec{B}}{\partial t^2} - \nabla^2 \vec{B} = 0. \quad (2.6)$$

In a similar way, the wave equation for the electric field is derived from the Ampere-Maxwell law (2.5):

$$\mu_0 \epsilon_0 \frac{\partial^2 \vec{E}}{\partial t^2} - \nabla^2 \vec{E} = 0. \quad (2.7)$$

As both differential Eqs. (2.6) and (2.7) have the structure of a wave equation, they confirm that the electric and magnetic fields can propagate as waves. In dielectric media with permittivity  $\epsilon \neq \epsilon_0$  and permeability  $\mu \neq \mu_0$ , the propagation speed of the wave  $v \neq c$  is determined by

$$v = \frac{1}{\sqrt{\mu\epsilon}}. \quad (2.8)$$

This suggests that the wave propagation speed can decrease in different media, a concept related to the phenomenon of refraction, which is discussed later in this section.

Figure 2.3 illustrates a plane linearly polarized wave propagating in the direction of the wave vector  $\vec{k}$  (in this case parallel to the  $z$ -axis). The oscillations of the electric and magnetic fields are perpendicular to each other in three-dimensional (3D) space, as derived from Maxwell's equations. The mentioned polarization is an important property of electromagnetic waves and describes the orientation of the electric field as the wave propagates through space. There are various types of polarization; in linear polarization, the electric field oscillates in a single direction perpendicular to the wave direction. This property of radiation can be exploited to manipulate the electromagnetic field, for instance, only certain linearly polarized components of a light wave may be reflected, transmitted, or absorbed at a polarization filter [12].

Owing to the dipole nature of atoms, electromagnetic waves can be influenced by, and exert influence on, matter. These physical phenomena are described as light-matter interactions and include diffraction, refraction, and reflection. Diffraction refers to the bending of waves around corners or through the apertures of objects. According to the Huygens-Fresnel principle, each

point on an electromagnetic wavefront can be considered a source of spherical waves [14]. The case of an aperture is depicted in Fig. 2.4a. When a light wave encounters the interface of two media with different permittivity and permeability characteristics, the Fresnel equations dictate that the wave may be transmitted or reflected, depending on the material properties and the incident angle relative to the surface, denoted by  $\theta_i$ . In the case of reflection, the optical medium remains unchanged, therefore, each point of contact that the wave makes can be described as

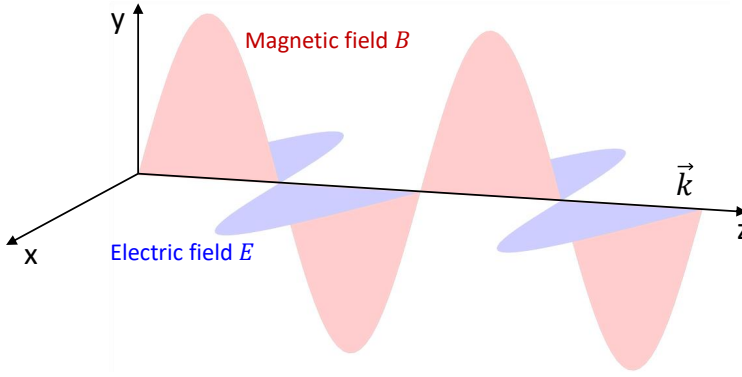
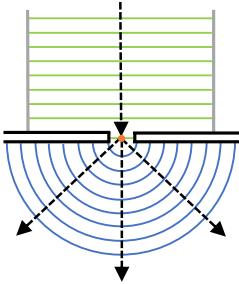
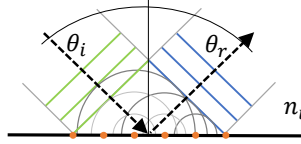


Figure 2.3: 3D diagram depicting a plane linearly polarized wave propagating along wave vector  $\vec{k}$ . As derived from Maxwell's equations, the electric and magnetic field amplitudes are perpendicular to each other.

a. - Diffraction



b. - Reflection



c. - Refraction

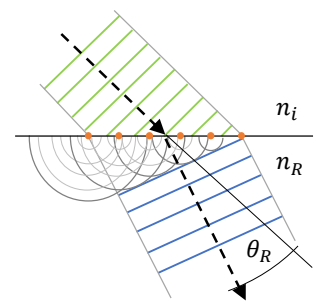


Figure 2.4: Schematic depiction of three types of light-matter interaction. The bending of waves described as diffraction (a), the reflection of waves at an interface (b), and the refraction at this interface after transmission (c).

a source of spherical waves. The angle of reflection  $\theta_r$  is then mirrored at the normal to the surface, as depicted in Fig. 2.4b.

In the case of transmission, as illustrated in Fig. 2.4c, the optical medium changes at the interface, causing the light wave to refract at an angle  $\theta_R$ . As previously noted, the speed of wave propagation within an optical medium is reduced because of the interaction of the field with the charge distributions of the atoms of the medium [15]. This change in speed  $v$  is represented by the absolute refractive index  $n$ , relative to the speed of light in vacuum  $c$  [12]:

$$n = \frac{c}{v} = \sqrt{\frac{\mu\epsilon}{\mu_0\epsilon_0}} . \quad (2.9)$$

As a consequence of the difference in refractive indices  $n_i$  and  $n_R$  at the material interface, the angle of refraction deviates from the incident angle of the wave according to Snell's law by  $n_i \sin(\theta_i) = n_R \sin(\theta_R)$  [14].

Another light-matter interaction is the absorption of light as it traverses an optical medium other than vacuum, which is caused by energy lost to the dipole interaction. This effect can be incorporated into the refractive index as the imaginary part of a complex representation [16]:

$$\underline{n} = n + i\alpha . \quad (2.10)$$

In this case, the real part corresponds to the change in phase velocity of the wave, and the imaginary part describes the optical extinction through the absorption coefficient  $\alpha$ . To relate the index of refraction to the electromagnetic wave propagation of Eq. (2.7), a one-dimensional plane-wave solution in the  $z$ -direction is assumed. For the sinusoidal waveforms of a single frequency (monochromatic), this can be written as [12]

$$\vec{E}(z) = \vec{E}_0(z) \exp(-ink_0z) , \quad (2.11)$$

where the wave number  $k_0 = 2\pi/\lambda$  denotes the spatial frequency of the light wave and  $\vec{E}_0$  is the electric field vector. By incorporating the complex refractive index into Eq. (2.11), the absorption results in an exponential decay in electric field strength.

This corresponds to an attenuation in intensity depending on the propagation distance  $z$ , described with the Beer-Lambert law [16, 17]:

$$I(z) = I_0(z) \exp\left(\frac{-4\pi\alpha z}{\lambda}\right). \quad (2.12)$$

This formulation will be utilized in chapter 3 to describe the absorption, gain, and subsequent effects in the laser model proposed in this work. The numerical solution to the electromagnetic wave equation, which leads to the laser beam propagation inside optical systems, is described in the following section.

## 2.2 Beam Propagation in Isotropic Media

This section discusses the numerical solutions to Maxwell's equations for wave propagation. The split-step beam propagation method is chosen as most suitable for this work, and the model for propagation through isotropic media and vacuum is described in subsection 2.2.1. The simulation of refraction and diffraction of laser beams with this approach is tested and validated in subsection 2.2.2.

### 2.2.1 Split-Step BPM Approach

The solution to the electromagnetic wave equation (2.7) can be described with the complex exponential function for the carrier wave of a given signal  $\vec{E}(\vec{d}, t)$ :

$$\vec{E}(\vec{d}, t) = \vec{\mathbb{E}}(\vec{d}, t) \exp\left[i(\vec{k} \cdot \vec{d} - w_0 t)\right], \quad (2.13)$$

represented with the wave vector  $\vec{k}$  and the angular frequency  $w_0 = 2\pi f$ , while  $\vec{d} = (x, y, z)$  is the position vector. However, as the electric field is still dependent on three-dimensional space, time, and spectral components, a direct numerical solution would be too complex to implement for this work. Therefore, two approximations can be made to simplify the wave equation further, thereby making the resulting equations easier to solve for the types of systems to be simulated. In laser systems, excluding micro- and nano-lasers, the system dimensions often significantly exceed the wavelength of light. Here, a forward-traveling wave with envelope function  $\vec{\mathbb{E}}(\vec{d}, t)$  can be assumed to vary slowly in time  $t$  and space  $\vec{d}$  compared to the wavelength, resulting

in the slowly varying envelope approximation (SVEA) [13]. If  $|\vec{k}| = k_0$  and  $w_0$  of the carrier wave are chosen to satisfy the dispersion relation

$$k_0^2 = \frac{w_0^2}{c^2}, \quad (2.14)$$

meaning that the phase velocity and the group velocity are assumed to be equal, the order of partial derivative in time and propagation direction is reduced, resulting in the SVEA form of the wave equation [13]:

$$2i \frac{w_0}{c^2} \frac{\partial \vec{\mathbb{E}}}{\partial t} = -2i \vec{k} \cdot \nabla \vec{\mathbb{E}}, \quad (2.15)$$

which describes a coherent forward-propagating wave envelope in directions near the  $\vec{k}$  wave vector, where the highest-order derivatives can be neglected if the following assumptions are fulfilled:

$$\frac{\partial^2 \vec{\mathbb{E}}}{\partial t^2} \ll w_0 \frac{\partial \vec{\mathbb{E}}}{\partial t}, \quad (2.16)$$

$$\nabla^2 \vec{\mathbb{E}} \ll \vec{k} \cdot \nabla \vec{\mathbb{E}}. \quad (2.17)$$

The second approximation assumes that wave propagation is dominantly in the  $z$ -direction, and is termed the parabolic approximation. This results in considering  $\vec{k}$  only in the  $z$ -direction and the Laplace operator  $\nabla_{\perp}^2 = \partial^2/\partial x^2 + \partial^2/\partial y^2$  is added in the  $x$ - $y$ -plane exclusively. The resulting partial differential equation for a scalar field  $\mathbb{E}$  can be expressed as [13]

$$k_z \frac{\partial \mathbb{E}}{\partial z} + \frac{w_0}{c^2} \frac{\partial \mathbb{E}}{\partial t} = \frac{1}{2} i \nabla_{\perp}^2 \mathbb{E}. \quad (2.18)$$

which gives an accurate description of the beam, as long as

$$\frac{\partial^2 \mathbb{E}}{\partial z^2} \ll k_z \frac{\partial \mathbb{E}}{\partial z}, \quad (2.19)$$

implying again that  $\mathbb{E}$  does not vary much with  $z$  over a wavelength distance.

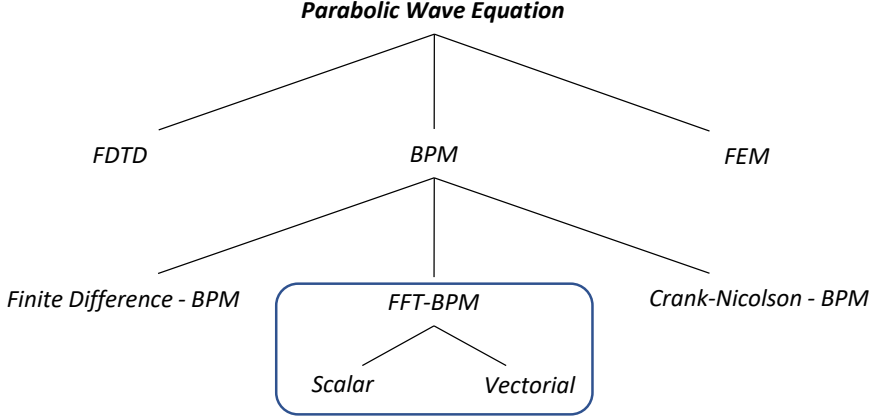


Figure 2.5: Schematic showing different numerical methods for solving the parabolic wave equation. The FFT-BPM has been chosen as the field propagation method for this work.

If the time constant  $t$  is always taken in reference to the time of arrival of the spatial field  $\mathbb{E}(x, y)$  at position  $z$ , the time-independent form of the parabolic approximation is written as [18]

$$\frac{\partial \mathbb{E}}{\partial z} = \frac{i}{2k_z n} \nabla_{\perp}^2 \mathbb{E} - \frac{ik_z}{2} n \mathbb{E}, \quad (2.20)$$

now also considering refraction through the propagation medium by adjusting the wave number with  $k_z \rightarrow k_z n$  and adding a corresponding phase delay term.

Different numerical methods have been developed to solve the electromagnetic wave equation in its parabolic form, each with its own applications and computational complexity [19]. The numerical techniques of interest for this work are the finite difference time domain (FDTD) method, finite element method (FEM), and the BPM. An overview of the most important methods is depicted in Fig. 2.5. The BPM is preferred in this work over the FDTD and FEM methods, as it better suits the size dimensions of the resonators and optical systems to be simulated [20]. There have been a variety of different spatial domain and frequency domain techniques developed for the BPM itself, including finite-difference [21, 22], Crank-Nicolson [23, 24], and fast Fourier transform (FFT) approaches [18, 25]. Spectral domain methods like the FFT-BPM offer the advantage of higher stability in cases of refractive index nonlinearities and also leverage the powerful FFT algorithm for high computational speed [26].

Owing to these advantages, the FFT-BPM is selected as the main propagation algorithm for this work. However, there are some limitations of this method to consider. Firstly, the SVEA simplification has limitations when it comes to modeling discretely or rapidly varying structures; this can lead to numerical inaccuracies in the simulation of specific systems [27]. Regarding the parabolic approximation, light propagating over a wide range of divergence angles can become problematic as well, and to avoid errors, a variable angle limitation must be set for the final implementation [20]. As the FFT-BPM is a monochromatic solution to the wave equation, it is not well-suited for propagating broadband light sources. Nevertheless, the parallel propagation approach for modeling spectral laser dynamics, proposed later in this work (refer to section 3.5.1), attempts to circumvent this issue, although at the cost of increased computational effort.

The chosen FFT-BPM model is largely based on an algorithm developed by Fleck and Feit for the propagation of laser beams through the atmosphere [28]. This method, suitable for isotropic media, has been adapted in this work for the simulation of complex resonator and free-space optical systems. If  $\mathbb{E}^n$  is considered as a complete solution to (2.20) at the propagation step  $n \rightarrow N_z$ , the following exponential expression can be used:

$$\mathbb{E}^{n+1} = \exp \left[ \frac{i}{4k_z n} \Delta z \nabla_{\perp}^2 \right] \exp \left[ -\frac{ik_z}{2} n \Delta z \right] \exp \left[ \frac{i}{4k_z n} \Delta z \nabla_{\perp}^2 \right] \mathbb{E}^n. \quad (2.21)$$

The equation is given in the Euler's formula representation, similarly to Eq. (2.13). The solution involves a symmetric split operator in the first and third terms for diffractive wave propagation over the distance  $\Delta z$ . The second term describes the phase change the wave experiences while traveling through a refractive medium over this distance. Owing to this division, the method is termed the split-step FFT-BPM. The numerical solution to Eq. (2.21) is based on solving each term-operator sequentially from  $n \rightarrow n + 1/3$ , from  $n + 1/3 \rightarrow n + 2/3$ , and finally from  $n + 2/3 \rightarrow n + 1$ . The first diffraction propagation step of the field  $\mathbb{E}(x, y)$  can be represented as a finite two-dimensional Fourier series by resolving the transversal Laplace operator  $\nabla_{\perp}^2$  [28, 29]:

$$\mathbb{E}(x, y)^{n+\frac{1}{3}} = \sum_{j=-\frac{N_x}{2}}^{\frac{N_x}{2}} \sum_{l=-\frac{N_y}{2}}^{\frac{N_y}{2}} \mathbb{E}(x, y)^n \exp \left[ \frac{i\Delta z}{2k_z n} \frac{\pi^2}{N_x^2} (jx)^2 \right] \exp \left[ \frac{i\Delta z}{2k_z n} \frac{\pi^2}{N_y^2} (ly)^2 \right]. \quad (2.22)$$

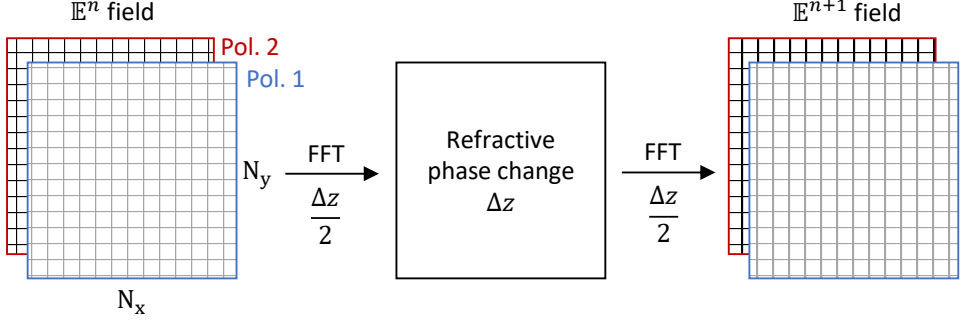


Figure 2.6: Schematic example of a propagation step over  $\Delta z$  with the vectorial split-step FFT-BPM.

This field is depicted on a square grid with side length  $L = N_x \Delta x = N_y \Delta y$  in the  $x$ - $y$  plane. After the application of the two-dimensional discrete FFT, the representation of the electromagnetic field in the spectral domain  $\mathbb{E}'$  is used to apply the change in field intensity and phase of the diffractive propagation along the distance  $\Delta z/2$  [26]. For a single pixel, this yields the precise expression

$$\mathbb{E}'_{jl}(\Delta z) = \mathbb{E}'_{jl}(0) \exp \left[ \frac{i\Delta z}{2k_z n} \frac{\pi^2}{(L/2)^2} j^2 \right] \exp \left[ \frac{i\Delta z}{2k_z n} \frac{\pi^2}{(L/2)^2} l^2 \right]. \quad (2.23)$$

After taking the inverse FFT of the field, the phase change that the wave experiences while traveling through a refractive medium is computed for the spatial domain of the field. This phase change is applied in between the diffraction propagation steps with the numerical expression

$$\mathbb{E}(x, y)^{n+\frac{2}{3}} = \exp \left[ -\frac{ik_z}{2} n \Delta z \right] \mathbb{E}(x, y)^{n+\frac{1}{3}}. \quad (2.24)$$

The second diffraction propagation step is then computed analogous to the first one, which yields the electromagnetic field after all operators  $\mathbb{E}(x, y)^{n+1}$ . The expressions (2.22), (2.23) and (2.24) can therefore be evaluated sequentially to propagate a beam over the distance  $\Delta z$ . Figure 2.6 illustrates a schematic of the split-step process from Eq. (2.21) for the transition from step  $n$  to  $n + 1$ . The two FFT diffraction propagation steps and the refractive phase change are shown for a discretized field in two polarization directions according to the Jones formalism [30]; this vectorization is discussed further in section 2.3.

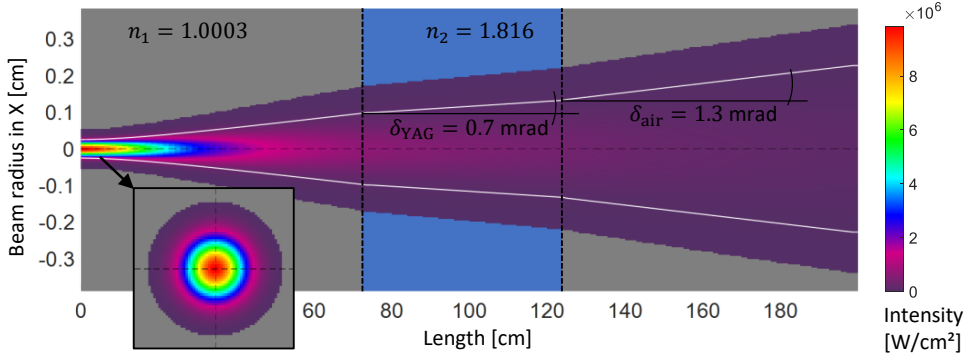


Figure 2.7: Model validation for refraction at an interface of air and YAG, plotted in the  $x$ - $z$ -plane. The Gaussian beam waist is propagated over a distance of 200 cm, with 50 cm of YAG in between.

## 2.2.2 Submodel Validation

The numerical solution is implemented in a FORTRAN environment, which handles the propagation of two-dimensional field distributions over any distance  $\Delta z$ , and should take into account both refraction and diffraction. FORTRAN is chosen as the coding environment for the majority of the demanding computations in this work because of the highly efficient numerical libraries available and the potential for parallelization using OpenMP [31, 32]. To validate the basic model regarding refraction, Fig. 2.7 shows the simulated propagation of a Gaussian laser beam through media with different refractive indices. The simulated intensity distribution is transferred to a Matlab environment for more convenient graphical output [33].

For this validation, the propagation length of  $L_z = 200$  cm is discretized into  $N_z = 200$  steps, while the square field with side dimensions  $L_x = L_y = 1.2$  cm is discretized into  $N_x = N_y = 256$  pixels. The laser beam has a diameter of 0.05 cm at the beam waist and a wavelength of 1000 nm. To test the behavior of the model when passing through different media interfaces, the beam is propagated through a standard atmosphere of air ( $n_{\text{air}} = 1.0003$  at 1000 nm [34]), with a 50 cm thick isotropic yttrium aluminium garnet (YAG) crystal ( $n_{\text{YAG}} = 1.816$  at 1000 nm [35]) in between. The propagation characteristics of Gaussian laser beams are explained in more detail in section 3.2.2. According to Eq. (3.22), the beam waist diameter is limited by diffraction and a divergence half angle  $\delta_{\text{air}} = 1.3$  mrad is expected in the far field for the propagation through air. At the interface to YAG, the divergence angle is expected to change as a consequence

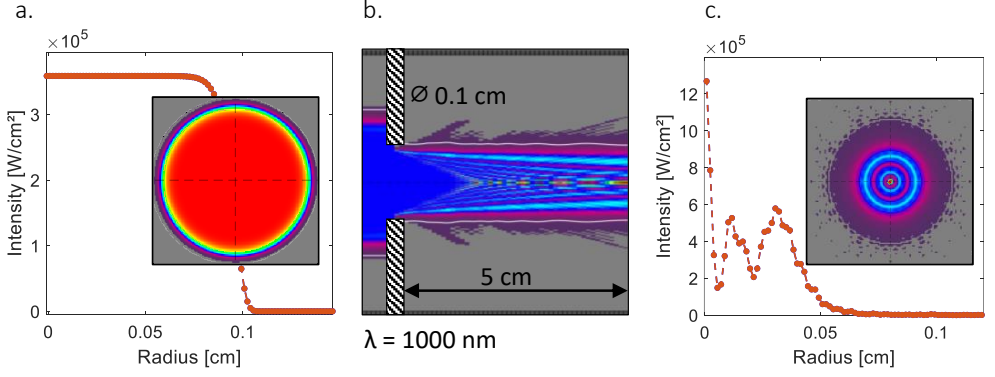


Figure 2.8: Model validation for diffraction of a top-hat beam passing through an aperture. The initial top-hat beam distribution is shown on the left (a), while the free-space simulation in the  $x$ - $z$ -plane is plotted in the middle graph (b). The resulting field distribution on the right (c) shows the diffraction pattern expected for a Fresnel number of 5.

of refraction. According to the change in wave velocity from Eq. (2.9) and Snell's law, the divergence half angle is refracted at an angle  $\delta_{\text{YAG}} = 0.7$  mrad. The white lines in the figure represent the course of the  $D4\sigma$  diameter over the propagation length. Both the far field divergence and the change at the refractive medium are well predicted with the numerical BPM.

To test the propagation model for diffraction, a top-hat beam (near-uniform intensity) of diameter 0.2 cm passing through an aperture of diameter  $D_a = 0.1$  cm is simulated. The field distributions of the input beam and the resulting diffraction pattern are displayed in Fig. 2.8. The number of diffraction rings for a coherent light beam projected through an aperture can be approximated with the Fresnel number

$$F = \frac{(D_a/2)^2}{L_a \lambda}, \quad (2.25)$$

where  $L_a$  is the distance of the observing screen from the aperture [12]. The resulting number corresponds to the half period of zones in the wavefront amplitude at the screen, which changes over distance. For the model validation, a screen distance of 5 cm is chosen, resulting in a diffraction pattern with a Fresnel number of 5. The modeled diffraction pattern is in good agreement with the expected pattern.

In conclusion, the chosen propagation model performs well in predicting refraction and diffraction at the relevant size scales for this work and can be further adapted.

## 2.3 Beam Propagation in Anisotropic Media

The split-step BPM approach from the preceding section is extended to incorporate the propagation of laser beams in anisotropic media. The vectorial field representation and adaptations to the model are detailed in subsection 2.3.1, while the resulting effects such as phase delay and beam walk-off are discussed and validated in subsection 2.3.2.

### 2.3.1 BPM Adaption for Vectorial Fields

Certain crystals or materials under stress exhibit an atomic structure that leads to a non-isotropic crystal matrix along the three spatial dimensions. Consequently, various material parameters exhibit anisotropic values across these directions. This anisotropy includes thermal attributes such as thermal expansion and heat conduction (refer to chapter 4), as well as optical characteristics including gain cross sections (refer to chapter 3). Most relevant to the propagation algorithm is the variation in refractive index depending on the polarization state of the incident light, a phenomenon known as birefringence [13, 36]. This variation can be described by an optical indicatrix, an ellipsoidal geometric depiction of the refractive index as a function of the polarization states of the light in the  $x$ -,  $y$ -, and  $z$ -orientations. The ellipsoid is characterized by the following equation [37]:

$$B_1x^2 + B_2y^2 + B_3z^2 = 1, \quad (2.26)$$

with the indicatrix coefficients given by the relative dielectric impermeability

$$B_{1,2,3} = \frac{1}{n_{1,2,3}^2}, \quad (2.27)$$

Figure 2.9 illustrates the indicatrices for isotropic as well as two anisotropic crystal structures. In isotropic media, the refractive index remains constant across all three spatial dimensions. Conversely, in uniaxial anisotropic crystals, one axis exhibits a refractive index distinct from the other two, indicated by  $n_2 \neq n_1$ . Biaxial anisotropic crystals are characterized by unique

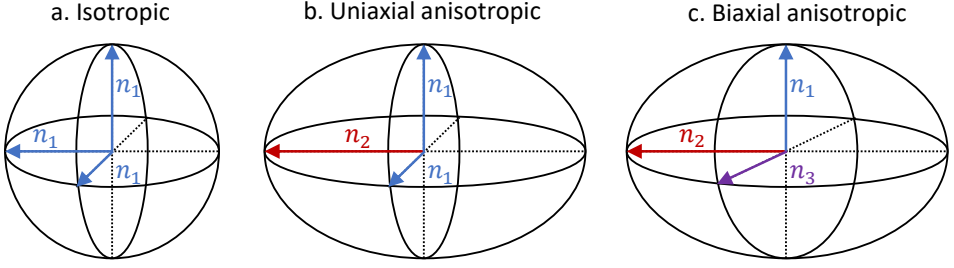


Figure 2.9: Refractive index ellipsoids for isotropic (a), uniaxial anisotropic (b), and biaxial anisotropic (c) crystal structures.

refractive indices along each of the three spatial axes ( $n_3 \neq n_2 \neq n_1$ ) [14]. The paths along which light travels without experiencing birefringence are termed the optical axes of the material [38]. As implied by the terminology, a uniaxial crystal possesses a single optical axis, whereas a biaxial crystal has two. In this work, only uniaxial crystals are considered because of the complexity of the biaxial case. Nonetheless, the biaxial structure can be reduced to a uniaxial approximation for specific crystal orientations parallel to one of the principal axes within the context of the parabolic wave equation. Similarly, uniaxial crystals may exhibit isotropic behavior if the incident direction of the light aligns with the optical axis, resulting in an effective incident angle of  $\theta_i = 0$ .

Birefringence impacts polarized light in various ways; for instance, when light propagates orthogonal to the optical axis ( $\theta_i = \pi/2$ ), the different polarization components experience only a phase shift. For incident angles  $\theta_i \neq \{0, \pi, \pi/2\}$ , the material induces double refraction, where unpolarized light entering the crystal is divided by polarization into two distinct rays, as illustrated in Fig. 2.10 [38]. Light polarized perpendicularly to the optical axis in uniaxial crystals is governed by the ‘ordinary’ refractive index, whereas light polarized parallel is subject to the ‘extraordinary’ refractive index. When unpolarized light divides into the polarization-dependent ordinary and extraordinary rays, the latter experiences more pronounced refraction and its path is altered by the so-called walk-off angle  $\rho$  [38].

The FFT-BPM algorithm of the isotropic case can be modified to incorporate the birefringence effects in uniaxial anisotropic media across various angular matrix orientations [39–41].

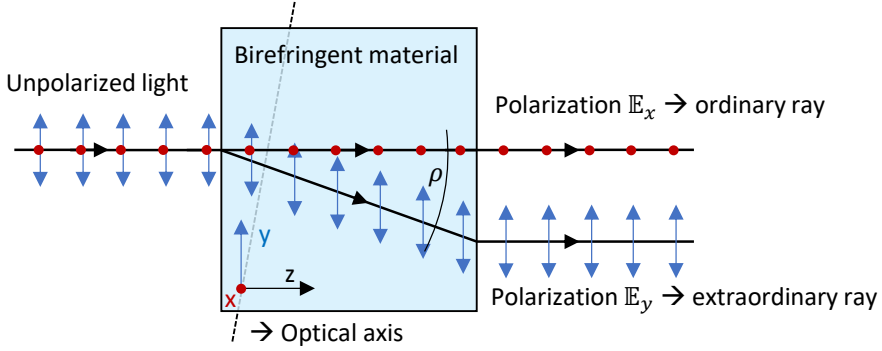


Figure 2.10: Birefringent behavior in a uniaxial anisotropic crystal. Unpolarized light with a specific incident angle relative to the optical axis is split into an ordinary and extraordinary polarization component and propagates along different paths with walk-off angle  $\rho$ .

In the exponential representation of the field according to Eq. 2.13, the transversal wave can be extended to a vector description according to the Jones calculus convention. The Jones vector is thus described by [12]

$$\begin{pmatrix} E_x(\vec{d}, t) \\ E_y(\vec{d}, t) \end{pmatrix} = \begin{pmatrix} \mathbb{E}_x(\vec{d}, t) \exp \left[ i(\vec{k} \cdot \vec{d} - \omega_x t) \right] \\ \mathbb{E}_y(\vec{d}, t) \exp \left[ i(\vec{k} \cdot \vec{d} - \omega_y t) \right] \end{pmatrix}. \quad (2.28)$$

This vector describes the electromagnetic field as polarization components of amplitude and phase in the  $x$ - and  $y$ -directions. In scenarios where the  $y$ -axis aligns with the optical axis, the parabolic wave equation for ordinary polarization  $\mathbb{E}_x$ , within the SVEA framework, mirrors the isotropic case as described in Eq. (2.20) by

$$\frac{\partial \mathbb{E}_x}{\partial z} = \frac{1}{2k_z n_o} i \left( \frac{\partial^2 \mathbb{E}_x}{\partial x^2} + \frac{\partial^2 \mathbb{E}_x}{\partial y^2} \right) - \frac{ik_z}{2} n_o \mathbb{E}_x. \quad (2.29)$$

Here,  $n_o$  denotes the refractive index corresponding to the ordinary direction. To describe the propagation of extraordinary polarization  $\mathbb{E}_y$ , the contribution of the extraordinary refractive index  $n_e$  can be incorporated with the effective wave number  $k_{\text{eff}}$ , given by [39]

$$k_{\text{eff}} = n_e k_z \sqrt{\sin^2(\theta_i) + \gamma^2 \cos^2(\theta_i)}. \quad (2.30)$$

The effective wave number depends on the angle of incidence of the Poynting vector relative to the optical axis  $\theta_i$ , as well as the refractive index ratio  $\gamma^2 = n_e^2/n_o^2$ . Consequently, the parabolic wave equation governing the extraordinary polarization is as follows [39, 42]:

$$\begin{aligned} \frac{\partial \mathbb{E}_y}{\partial z} = & \frac{1}{2k_{\text{eff}}} i \left( \frac{\partial^2 \mathbb{E}_y}{\partial x^2} + [\cos^2(\theta_i) + \gamma^2 \sin^2(\theta_i)] \frac{\partial^2 \mathbb{E}_y}{\partial y^2} \right) - \tan(\theta_i) \frac{\partial \mathbb{E}_y}{\partial y} \\ & - \frac{ik_{\text{eff}}}{2} \mathbb{E}_y, \end{aligned} \quad (2.31)$$

The solutions for both the ordinary and extraordinary adaptations of the parabolic wave equation are resolved utilizing the FFT algorithm. The same sequential split-step approach as with the isotropic case (refer to section 2.2.1) is applied. For the ordinary diffraction propagation step, the phase multiplication term of the spectral domain field  $\mathbb{E}'$  is given similarly to Eq. (2.23) with

$$\mathbb{E}'_{x,jl}(\Delta z) = \mathbb{E}'_{x,jl}(0) \exp \left[ \frac{i\Delta z}{4k_z n_o} \frac{\pi^2}{(L/2)^2} j^2 \right] \exp \left[ \frac{i\Delta z}{4k_z n_o} \frac{\pi^2}{(L/2)^2} l^2 \right]. \quad (2.32)$$

For the extraordinary polarization, the phase multiplication in the spectral domain has to be adapted according to Eq. (2.31), resulting in

$$\begin{aligned} \mathbb{E}'_{y,jl}(\Delta z) = & \mathbb{E}'_{y,jl}(0) \exp \left[ \frac{i\Delta z}{4k_{\text{eff}}} \frac{\pi^2}{(L/2)^2} j^2 \right] \\ & \exp \left[ \frac{i\Delta z}{4k_{\text{eff}}} \frac{\pi^2}{(L/2)^2} c' l^2 \right] \exp \left[ i\Delta z \frac{\pi}{(L/2)} c'' l \right], \end{aligned} \quad (2.33)$$

with the factors  $c' = \sqrt{\gamma^2 \sin^2(\theta_i) + \cos^2(\theta_i)}$ , and  $c'' = \sin(\theta_i) \cos(\theta_i) (\gamma^2 - 1) / (c')^2$  for simplification purposes.

The phase change step through a refractive medium is computed similarly to Eq. (2.24) in the spatial domain. For the ordinary polarization, it is expressed as

$$\mathbb{E}_x(x, y, z + \Delta z) = \exp \left[ -\frac{ik_z}{2} n_o \Delta z \right] \mathbb{E}_x(x, y, z). \quad (2.34)$$

For the extraordinary polarization, the refractive phase change is adapted with the effective wave number  $k_{\text{eff}}$ , resulting in

$$\mathbb{E}_y(x, y, z + \Delta z) = \exp \left[ -\frac{ik_{\text{eff}}}{2} \Delta z \right] \mathbb{E}_y(x, y, z) . \quad (2.35)$$

With these adaptations, the same sequential step-wise algorithm presented for the isotropic case in section 2.2.1 can be utilized to propagate the vectorial field from  $\mathbb{E}_{x,y}^n$  to  $\mathbb{E}_{x,y}^{n+1}$ , along the distance  $\Delta z$  in uniaxial anisotropic media.

### 2.3.2 Submodel Validation

To validate the uniaxial anisotropic model implementation of the FFT-BPM, a propagation simulation through a quartz crystal is conducted. Quartz exhibits birefringent characteristics within its crystal lattice (although weak compared to e.g. calcite), characterized by an ordinary refractive index  $n_o = 1.5350$  and an extraordinary refractive index  $n_e = 1.5438$ , both taken at a wavelength of 1000 nm [43]. In the initial simulation, the phase delay between polarization components  $\mathbb{E}_x(x, y)$  and  $\mathbb{E}_y(x, y)$  is evaluated for a quartz material thickness of  $L_{\text{quartz}} = 0.0057$  cm and an incident angle  $\theta_i = \pi/2$ . This arrangement results in a half-waveplate, where no walk-off is expected, but a phase delay  $\Delta\omega = \pi$  according to [44]

$$\Delta\omega = \frac{2\pi\Delta nL}{\lambda} . \quad (2.36)$$

The element operator of waveplates is described in more detail later on, in section 2.4.3. The simulation outcome, depicted in Fig. 2.11a, shows the intensity modulation for both polarizations for a waveplate rotation of  $22.5^\circ$ . The power initially in  $\mathbb{E}_x(x, y)$  is equally redistributed to  $\mathbb{E}_x(x, y)$  and  $\mathbb{E}_y(x, y)$ , indicative of a  $45^\circ$  polarization rotation, which can be confirmed with the analytical calculations regarding waveplates in section 2.4.3, Eq. (2.41). Figure 2.11b shows the phase distribution plot along the radial axis of the beam in  $x$ -direction, where the absolute phase position of each individual polarization component is plotted in the range of minus  $\pi$  to plus  $\pi$  radians. While the phase curvature is attributed to Gaussian propagation, the phase retardation of the polarization components relative to each other is delayed by  $\Delta\omega = \pi$ , confirming the effectiveness of the model in simulating phase alterations in uniaxial media.

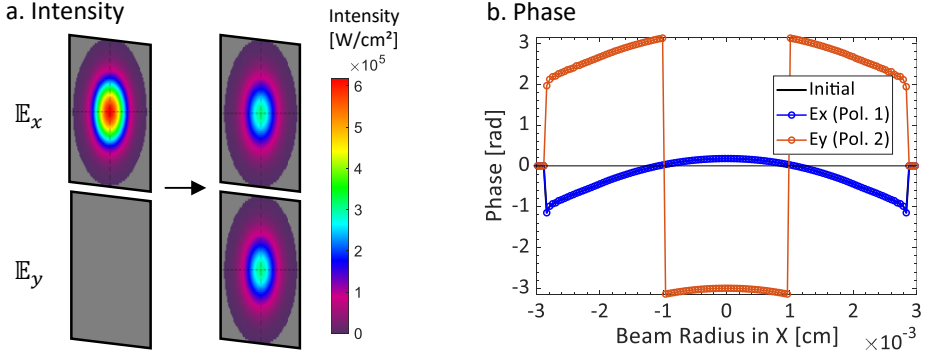


Figure 2.11: Model validation for phase delay when propagating through a uniaxial anisotropic medium. In this example, a quartz crystal of length 0.0057 cm is passed at an incident angle  $\theta_i = \pi/2$ . The resulting change in intensity (a) and phase (b) is shown for both polarization components.

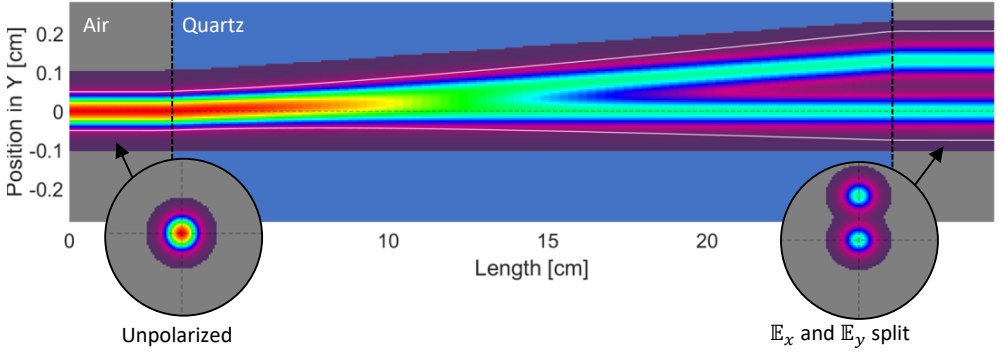


Figure 2.12: Model validation for birefringent walk-off in a uniaxial anisotropic quartz crystal. While passing through the crystal of length 23 cm, the beam is split into two polarization components which show different refractive behavior resulting in the walk-off angle observed.

To validate the simulation regarding walk-off behavior, the quartz thickness is increased to  $L_{\text{quartz}} = 23$  cm, and the incident angle is set to  $\theta_i = \pi/4$ , where maximal walk-off is anticipated. In the simulation results presented in Fig. 2.12, the initially unpolarized light is split into two distinct beams, each corresponding to one of the polarization components  $E_x(x, y)$  and  $E_y(x, y)$ , where the extraordinary beam  $E_y(x, y)$  experiences stronger refraction. This phenomenon aligns with the birefringent predictions illustrated in Fig. 2.10. Although waveplates and most other intrinsically birefringent materials are not commonly cut in orientations that express walk-

off, for certain applications, such as phase-matching for nonlinear frequency conversion, this characteristic has to be taken into account [38, 45].

The numerical model demonstrates validity in predicting light propagation through both isotropic and anisotropic media, which will be necessary for the precise modeling of the laser geometries discussed later in this work.

## **2.4 Modeling of Bulk Laser Systems**

In this section, a concept regarding the fundamental multi-physics model for free-space and resonant solid-state laser systems is discussed. The most important state-of-the-art simulation approaches concerning this work are compared in subsection 2.4.1, bringing the developed model into context. The modular approach of this model is delineated in subsection 2.4.2, while a brief overview of some of the element operators included in the model are given in subsection 2.4.3.

### **2.4.1 State-of-the-Art Overview**

The main contribution of this work is a comprehensive multi-physics simulation model for rare-earth-doped solid-state laser systems. For the purpose of this work, relevant laser systems encompass free-space geometries like amplifiers as well as resonator geometries. A laser resonator is made of multiple optical components, and typically consists of a resonant cavity realized by mirrors and a gain medium, which is pumped with energy. Conversely, laser amplifiers represent simpler geometries, where a seed signal laser is amplified by a single- or multi-pass through the gain medium, and no resonant cavity is needed. Both types of systems will be discussed in more detail in section 3.2.1, this section will focus on providing an overview of corresponding state-of-the-art multi-physics simulation approaches.

Since the construction of the first operational laser and even before then, numerous mathematical models have been proposed to describe the many physical processes involved, each with varying degrees of complexity. To accurately simulate a complete solid-state laser system, a multi-physics approach is necessary, which takes into account at least a solution to Maxwell's equations for wave propagation and a laser physics model concerning the stimulated emission of light. Commonly employed methods often rely on analytical solutions, resolving the propagation

of laser beams with Gaussian propagation algorithms [46] and one-dimensional rate equation models [47]. Although numerical approaches generally offer a higher degree of simulation accuracy and can account for asymmetries, they are computationally intensive, leading to longer simulation times. Nevertheless, the evolution of semiconductor technologies and the subsequent increase in computing power have made complex numerical models more relevant. For resolving wave equations in the context of laser systems, important numerical models include the FDTD method [48], the FEM [49], and the BPM [28]. A comparison of relevant solutions to the parabolic wave equation has been presented in section 2.2.1. When simulating high-power laser systems, as is the objective of this work, thermo-optic effects can significantly influence the laser performance and drastically alter the expected output. Therefore, to achieve high simulation accuracy, a thermal model should be part of a complete multi-physics approach. These thermal challenges can again be resolved either analytically or numerically, however, this increases the complexity of a comprehensive model even further [3].

In Tab. 2.1, state-of-the-art simulation approaches that attempt to solve complete or partial solid-state laser systems and their respective multi-physics models are listed. More approaches can be found in literature, however, this table is limited to the most comparable ones regarding this work. The submodels for laser beam propagation range from Gaussian propagation to more complex 3D FEM and BPM wave solutions. The same applies to the thermal submodels, where both analytical solutions and numerical approaches with FDM and FEM solutions are utilized. The complexity of the laser model also varies, with general models considering simple two-level laser transitions as well as more complex models for specific active ions. Additionally, continuous wave (CW) laser models consider the steady state solution only, while transient and pulsed models take temporal dynamics into account as well. Despite most models sharing the common goal of simulating laser systems, the combination of these different approaches can result in a wide range of model complexity, simulation time, and use cases. Some of these published approaches are employed in commercial simulation software such as LASCAD [50], ASLD [51], LightTrans [52], and COMSOL [53]. While these programs can allow for highly optimized algorithms, they are developed for broad use cases which may limit the complexity of certain aspects of the models in a scientific context. To gain insights into physical mechanisms that may affect the laser performance, a fully transparent and modular simulation model is necessary.

Table 2.1: This table provides an overview of multi-physics solid-state laser simulation approaches relevant to this work. The approaches are compared based on their submodels used for laser beam propagation, thermal effects, and laser physics complexity. The model developed in this work is included at the end of the table to provide context with the state-of-the-art.

Approach	Beam model	Thermal model	Laser model
LASCAD [50, 54]	Gaussian propagation / BPM	Numerical model (FEM)	CW / pulsed models (various ions)
ASLD [54–56]	Dynamic mode analysis (DMA) / finite element	Numerical model (FEM)	CW / transient / pulsed models (various ions)
LightTrans / D. Asoubar et al. [57, 58]	Vectorial field tracing	None / external	CW model (general approach)
COMSOL Multiphysics [53, 59, 60]	Raytracing / beam envelope method	Comprehensive numerical model (FEM)	None / external
M. Eichhorn [61, 62]	Radiation transport model	Analytical model	CW / transient models ( $\text{Er}^{3+}$ )
Y. Shen et al. [63, 64]	Gaussian propagation	Numerical model (FEM)	CW model ( $\text{Nd}^{3+}$ , $\text{Ho}^{3+}$ )
H. Shu et al. [65]	Vectorial Crank–Nicholson BPM	Analytical model	CW model (general approach)
This work	Vectorial split-step FFT-BPM	Numerical model (FDM)	CW / transient / pulsed models (general approach + $\text{Ho}^{3+}$ )

The aim of this work is to provide a multi-physics approach for specialized system and specific laser ions, although it should be adaptable to provide simplified solutions for more generalized systems. This is achieved by combining multiple simulation methods, adapted for the specific requirements of bulk solid-state laser modeling. The result is a comprehensive simulation model uniquely suitable for highly accurate simulation of such laser systems. While it is important to keep computation times as minimal as possible, the emphasis on resolving complex and possibly asymmetric systems requires the use of numerical solutions for laser beam propagation and thermal distributions. The FFT-BPM has been selected to solve the Maxwell equations for wave propagation, as detailed in the preceding sections 2.2 and 2.3. While a basic rate equation model for CW or pulsed laser ion interactions is used, a more specific model is developed for holmium(III) oxide ( $\text{Ho}^{3+}$ )-doped gain media at the spectral range of interest around  $2\text{ }\mu\text{m}$  (refer to chapter 3). A three-dimensional finite difference method (FDM) approach is adopted to model temperature and stress distributions for the thermal model (refer to chapter 4).

The combination of the submodels chosen in this work should allow the resulting multi-physics simulation approach to provide unique insights into complex laser systems. By considering various physical processes and relations even at high power levels, further in-depth research of solid-state lasers is possible.

## 2.4.2 Simulation Framework and Modular Structure

To model a variety of experimental laser arrangements, the fundamental simulation framework requires a modular structure of individual elements. The core approach is depicted in Fig. 2.13 and is based on element operator modules for each potential optical element in the beam path. The beam path is divided into increments of  $\Delta z$ , propagated sequentially in either forward or backward direction depending on the orientation of the beam. Between these steps, various element operators can be positioned to transform or modulate the propagated electromagnetic field  $\mathbb{E}(x, y)$ . A description of specific operators is provided in the subsequent section 2.4.3. As illustrated in the graph, the comprehensive simulation takes numerous input parameters that describe the different subsystems: the overarching system, the electromagnetic field, and the optical elements themselves (with emphasis on the laser crystal). The algorithm for propagating the fields between the elements has been elaborated upon in section 2.2.

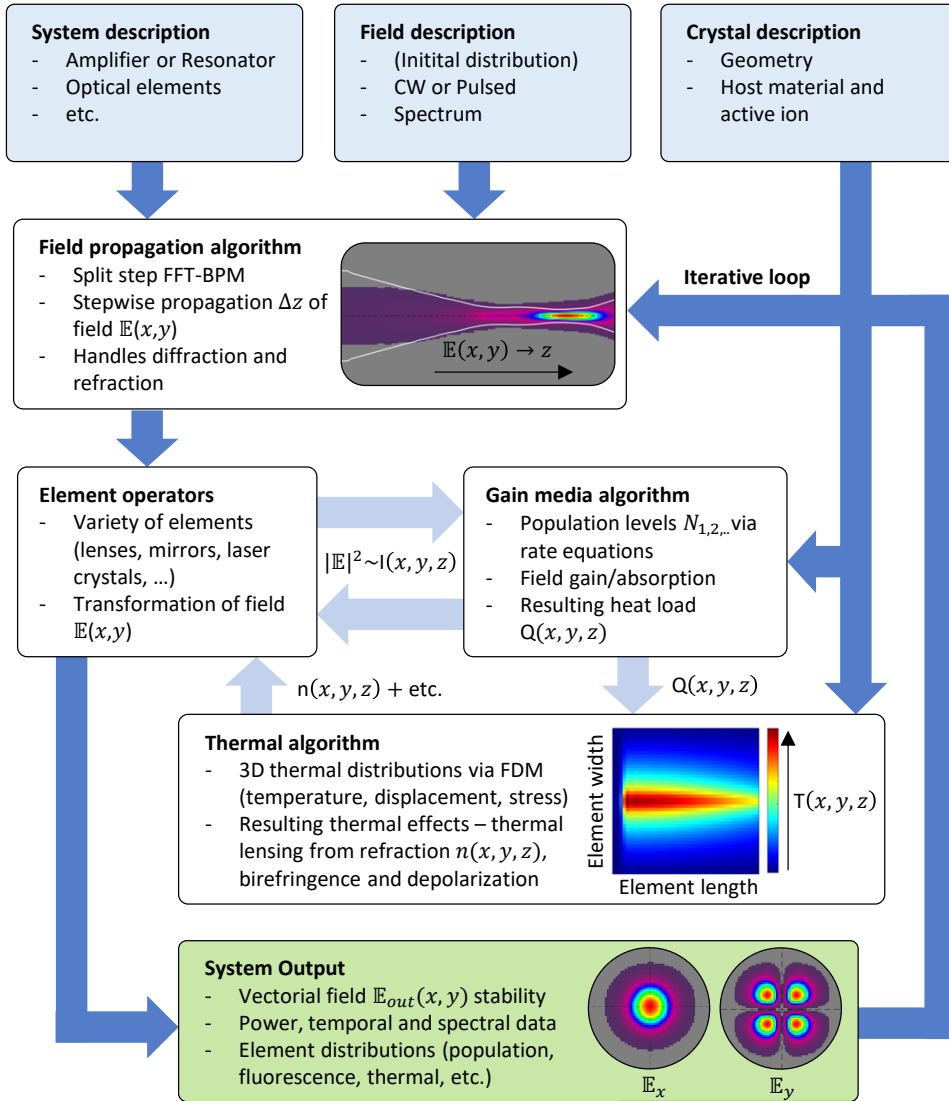


Figure 2.13: This figure provides an overview of the comprehensive simulation structure. A variety of input parameters can be defined and passed to the corresponding submodels, which include the field propagation model, the gain media model, and the thermal model. The resulting system output characteristics are updated iteratively.

The element operator module of the laser crystal encompasses the submodels of the gain medium and the thermal algorithms. The field intensity information from the element is passed to the gain medium algorithm, which computes the population levels using a rate equation model. From these, the laser gain/absorption and heat load  $Q(x, y, z)$  within the element can be computed. The laser physics module and related processes are discussed in greater detail in chapter 3. With the heat load derived from the rate equation model and background absorption, the thermal submodel of the element operator can be computed. This submodel relies on FDM-based numerical models to calculate the temperature  $T(x, y, z)$ , displacement  $D_d(x, y, z)$  and stress  $\sigma_{d,d}(x, y, z)$  distributions in 3D space ( $\vec{d} = x, y, z$ ), as detailed in chapter 4. By utilizing these distributions, the thermal effects that influence the electromagnetic field are calculated (refer to section 4.4). Here, the most significant impact comes from thermal lensing resulting from a change in the refractive index  $n(x, y, z)$ , as well as birefringence and depolarization losses from thermally induced stress. The entire system is simulated iteratively until an end condition is met. This could be a predetermined iteration limit or, more dynamically, a convergence condition of lasing behavior (output power, mode fluctuation, etc.). For laser resonators, one iteration can be described as a resonator round-trip of light. The system output parameters are updated accordingly, encompassing the laser field power, mode distribution, stability, and temporal/spectral data, as well as element-specific data such as absorbed power, thermal distributions, and laser-specific information in the case of the laser crystal.

The schematic representation of the electromagnetic field transformation from a single element operator is shown in Fig. 2.14. To simulate experimental laser arrangements as accurately as possible, a misalignment transformation is incorporated into the model. This accounts for shift in  $x$  or  $y$ , tilt around  $x$  or  $y$ , and rotation around the  $z$ -axis of the optical element and modifies the corresponding element algorithm [29, 66]. To reduce complexity, these transformations are implemented by adjusting the electromagnetic field according to the misalignment, rather than the element itself. This is accomplished by transforming the field prior to the element, and reversing the process after. Element operators can represent either thin or bulk elements. Thin elements usually only encompass a field transformation that aligns with the element function, whereas bulk elements are more complex as they incorporate internal field propagation and potentially the thermal model as illustrated. For bulk elements, the element length  $L_{EO}$  is divided into a certain number of slices  $N_{z,EO}$  with length  $\Delta z_{EO}$ . The propagation and element algorithms can subsequently be iterated over the total number of element slices.

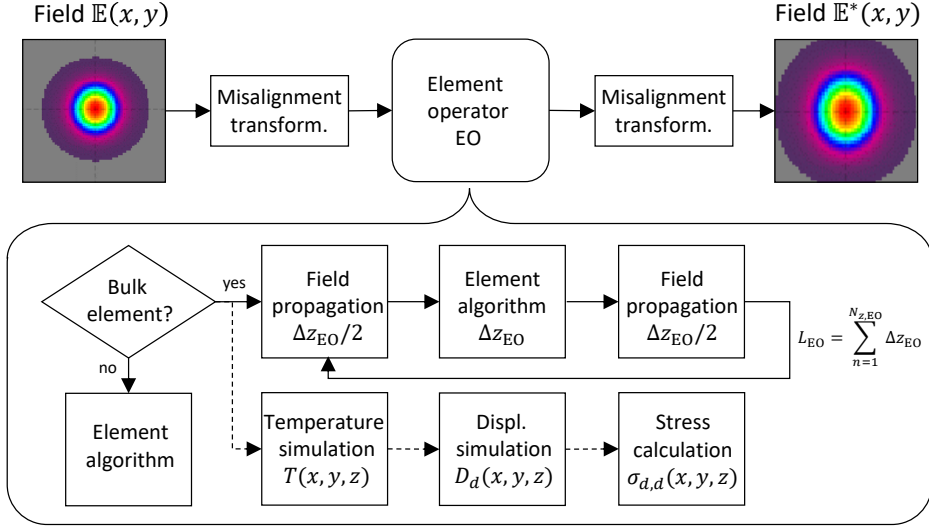


Figure 2.14: This figure illustrates the field transformation at a single element operator, showcasing the modular structure of the simulation approach. The specific algorithms of the operator are shown as a flowchart below the sequential approach.

The most important element operators for modeling laser resonator and amplifier systems relevant to this work are described briefly in the following section.

### 2.4.3 Element Operators

This section details the element-specific transformation functions for some important optical elements within a laser system in the context of this work. These functions do not encompass the entire element operator, but rather describe the transformation of the electromagnetic field  $\mathbb{E}(x, y)$ , termed the 'Element algorithm' in Fig. 2.14. This transformation is described by multiplying the field with the element transfer function  $T_{EO}$ :

$$\mathbb{E}^*(x, y) = \mathbb{E}(x, y)T_{EO} . \quad (2.37)$$

For elements allowing for internal wave propagation, termed 'bulk elements', the propagation algorithm depends on the FFT-BPM detailed in section 2.2.

### Lenses

Convex and concave lenses, which focus or defocus light beams within an optical system, are important components of a comprehensive model to simulate a complete system. The model of special types of lenses, such as achromatic and aspheric types, might also be required for highest accuracy. However, this section focuses on the case of spherical lenses only. To model a thin spherical lens in the paraxial approximation, the phase transformation of the field is described by multiplying the field with the lens phase transfer function  $T_{\text{lens}}$ , as given by [67]

$$T_{\text{lens}}(x, y) = \exp \left[ -i \frac{k_0}{2f_{\text{lens}}} (x^2 + y^2) \right]. \quad (2.38)$$

The function depends on the wave number  $k_0$ , the focal length  $f_{\text{lens}}$  of the lens element, and the transversal field coordinates in  $x$  and  $y$ . This formula represents how the phase of the electromagnetic field is altered because of the varying thickness of the lens across its surface. This results in a spherical phase shift depending on the transversal field position, which leads to the focusing or defocusing of the beam. In addition to the thin element model, the electromagnetic field modulation through a lens can be considered by a bulk element operator as well. However, when applying the direct refraction induced by a curved lens surface through wave propagation alone, the resolution of the field limits the accuracy. For higher accuracy, the thin element approach is therefore preferred, although the bulk element approach may still be useful when considering chromatic aberration.

### Mirrors

With the sequential approach of the overarching model, the mirror element may be viewed as a unique form of thin lens. Given the absence of beam directionality in the model (outside the paraxial direction), the reflection angle of the mirror can be disregarded if it has no influence on the field. In addition to plane mirrors, convex and concave mirrors are treated similarly to the lens. The resulting transfer function  $T_{\text{mirr}}$  is given as a variant of Eq. (2.38) as follows [67, 68]:

$$T_{\text{mirr}}(x, y, \lambda) = \sqrt{1 - R_{\text{mirr}}(\lambda)} \exp \left[ -i \frac{k_0}{2r_{\text{mirr}}} (x^2 + y^2) \right]. \quad (2.39)$$

Here,  $r_{\text{mirr}}$  denotes the radius of curvature of the mirror, and  $R_{\text{mirr}}(\lambda)$  represents the corresponding surface reflectivity, which can be wavelength-dependent. In resonators, the mirror element is crucial for replicating the field, which is incorporated into the model with a light round-trip

according to the Fox and Li algorithm [69]. Equation (2.39) considers only a basic type of mirror, however, there exist variations such as graded reflectivity mirrors, where the reflectivity is a function of the surface position on the mirror [70]. However, this has to be implemented separately and is not considered further for this work. Additionally, in three-dimensional resonator geometries, the beam directionality can affect the polarization state of the beam and should not be ignored. In these systems, the mirror element introduces an image rotation transformation, which has an influence on polarization states and laser performance [66].

### Polarizers

To manipulate the polarization state of light, many optical systems employ polarizer elements, which have to be incorporated into the model. Here, the field has to be considered with the Jones calculus convention with polarization component  $\mathbb{E}_x(x, y)$  and  $\mathbb{E}_y(x, y)$ , as described before in Eq. 2.28. The phase delay  $\Delta w$  is given for the phase retardation of the polarization components angular frequencies  $w_x$  and  $w_y$  relative to each other. For a phase delay near  $\Delta w = 0$  or  $\Delta w = \pi/2$ , the field is described as linearly polarized, while a phase delay  $\Delta w = \pi/4$  corresponds to circular polarization. A linear polarizer can be represented as a thin element that transmits and reflects light polarization components based on its transmission angle  $\theta_t$  relative to the horizontal. The resulting transfer function  $T_{\text{pol}}$  is applied to the Jones vector of the field and is expressed as [12]

$$T_{\text{pol}} = \begin{pmatrix} \cos^2(\theta_t) & \cos(\theta_t) \sin(\theta_t) \\ \cos(\theta_t) \sin(\theta_t) & \sin^2(\theta_t) \end{pmatrix}. \quad (2.40)$$

For increased simulation accuracy, the thin element operator of the polarizer can be used in combination with a bulk element operator for propagation through the material.

### Waveplates

A waveplate is an optical element that induces a phase retardation  $\Delta w$  between the two polarization components. The specific behavior of the element is determined by the induced phase delay, with the most important plate types being the half waveplate (phase delay  $\Delta w = \pi$ ) and the quarter waveplate (phase delay  $\Delta w = \pi/2$ ) [44]. For linearly polarized light, the phase shift of a half waveplate rotates the polarization vector by twice the waveplate rotation angle  $\theta_r$ .

In a thin element approximation, the transfer function  $T_{\text{hw}}$  is again based on the Jones representation, similar to the polarizer element [12]:

$$T_{\text{hw}} = \begin{pmatrix} \cos(2\theta_r) & \sin(2\theta_r) \\ \sin(2\theta_r) & -\cos(2\theta_r) \end{pmatrix}. \quad (2.41)$$

In contrast to the half waveplate, the quarter waveplate retards the polarization components by  $\Delta w = \pi/2$ , causing a linearly polarized wave to transition to elliptical or circular polarization after passing the element, depending on the waveplate rotation angle. Circular polarization can therefore be simplified as the sum of the two orthogonal polarization components with a phase difference of  $\pi/2$ . The corresponding thin element transfer function  $T_{\text{qw}}$  can be written as [12]

$$T_{\text{qw}} = \exp\left(i\frac{\pi}{4}\right) \begin{pmatrix} \cos^2(\theta_r) + i\sin^2(\theta_r) & (1-i)\sin(\theta_r)\cos(\theta_r) \\ (1-i)\sin(\theta_r)\cos(\theta_r) & \sin^2(\theta_r) + i\cos^2(\theta_r) \end{pmatrix}. \quad (2.42)$$

In reality, the behavior of a waveplate is a consequence of the properties of the material from which it is fabricated. Waveplates are typically made from birefringent crystals, where the index of refraction varies for the polarization components of light. To simulate waveplates with high precision, the element can be treated as a bulk element where the phase delay is introduced through the propagation algorithm itself. This concept has been explained for an example waveplate in section 2.3.2, with a focus on the anisotropic propagation algorithm.

### **Etalons**

An etalon is an optical element for wavelength filtering, operating on the principle of a Fabry-Pérot interferometer. Typically made of a glass plate, the two reflective surfaces of the plate form an optical cavity that induces transmission loss based on resonance and destructive interference. This characteristic enables etalons to tune the wavelength within a laser resonator or eliminate undesired laser lines. Consequently, the etalon transfer function  $T_{\text{eta}}(\lambda)$  is wavelength-dependent and defined as [71]

$$T_{\text{eta}}(\lambda) = \frac{1}{1 + R_{\text{eta}}^2(\lambda) - 2 \cdot R_{\text{eta}}(\lambda) \cdot \cos(\delta(\lambda))}. \quad (2.43)$$

$$\text{with } \delta(\lambda) = 4 \cdot \pi \cdot d_{\text{eta}} \cdot \cos(\theta_i) \cdot \frac{n_{\text{eta}}(\lambda)}{\lambda} . \quad (2.44)$$

Here,  $R_{\text{eta}}(\lambda)$  represents the wavelength-dependent reflectivity and  $\delta(\lambda)$  denotes the optical path difference.  $d_{\text{eta}}$ ,  $\theta_i$ , and  $n_{\text{eta}}(\lambda)$  are the etalon thickness, angle of incidence, and refractive index, respectively. Depending on the material of the etalon, its thickness, and coating, a sinusoidal spectral transmission profile can be utilized to generate loss within the cavity, resulting in the suppression of undesired spectral content.

### Others

Apart from the aforementioned optical elements, the complete model employs a range of additional element operators to simulate complex laser systems. This includes aperture elements, which obstruct the transversal field based on the aperture shape, for instance, spherical or rectangular. Detector elements are utilized to acquire the field information at a specific location within the optical system, and source elements are used to generate new electromagnetic fields  $\mathbb{E}_{i \rightarrow i_\lambda}(x, y)$ , where  $i_\lambda$  is the total number of fields to be propagated. The fields produced by the source element do not differ in functionality from the field initially propagated and are used, for instance, to model the pump light in end-pumped laser crystal configurations. Additional element operators include the laser crystal itself (refer to section 3.3) and modulator elements (refer to section 3.5.2), the more complex mechanics of which are explained in the respective sections.

The described element operator approach enables the simulation of various optical systems. Additionally, the modular nature of the approach allows for further expansion by integrating more elements, if necessary.

## 3 Solid-state Laser Model

The fundamental model developed in the preceding chapter enables the simulation of optical arrangements comprising multiple optical elements. The respective BPM-FFT algorithm allows for laser beam propagation through these systems with high precision and comprehensive analysis of the electromagnetic field. However, for the modeling of laser processes, the laser gain medium must be incorporated into the multi-physics approach as well. Section 3.1 provides an overview of the underlying laser physics to describe the laser gain process. An overview of solid-state laser system geometries and concepts is provided in section 3.2. The fundamental model for simulating laser gain and absorption is based on the rate equation model and is discussed in section 3.3 as a generalized approach. An extended model for  $\text{Ho}^{3+}$ -doped gain media is presented in section 3.4, taking into account additional energy levels and transition mechanisms for higher accuracy. Advanced laser media dynamics, such as the extension to a spectrally resolved model and the implementation of pulsed laser operation, are detailed in the subsequent section 3.5. The final section 3.6 of the chapter presents the comprehensive simulation of an exemplary laser resonator, compared with the corresponding experimental results.

### 3.1 Background on Laser Physics

The acronym LASER, standing for 'Light Amplification by Stimulated Emission of Radiation,' provides insight into the physics behind the generation of this type of radiation. This section will focus on the underlying principles regarding this generation process. Many of the physical process descriptions in this section are adapted from the works of Marc Eichhorn on laser physics, referenced in [17].

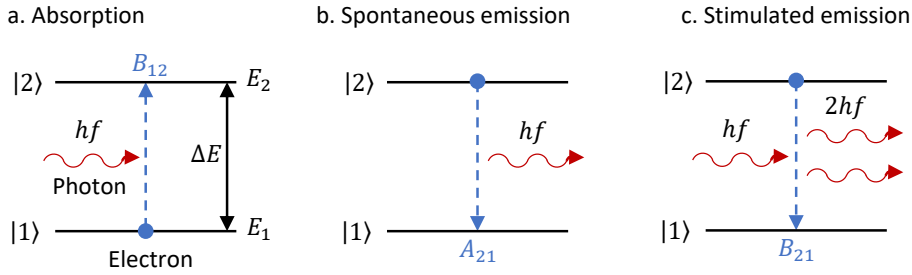


Figure 3.1: Schematic representation of the three fundamental two-level system interactions with a photon: absorption (a), spontaneous emission (b), and stimulated emission (c).

Some of the first studies regarding the fundamental interactions of absorption and emission of photons in a black-body radiation system were proposed by Albert Einstein. He identified three basic processes to describe the system, as illustrated in Fig. 3.1:

**Absorption:** In a simple two-level system, a photon with energy  $E_{\text{ph}} = hf$  (refer to section 2.1, Eq. (2.1)) can be absorbed by an electron, causing a transition from level  $|1\rangle$  to level  $|2\rangle$ .

**Spontaneous emission:** If an electron is already in the higher energy state  $|2\rangle$ , it can spontaneously emit a photon of energy  $hf$  and decay back to the lower energy state  $|1\rangle$ . The phase, polarization, and direction with wave vector  $\vec{k}$  of this emission are random. The radiation produced by this process, called fluorescence, is therefore incoherent.

**Stimulated emission:** Before an electron in the higher energy state  $|2\rangle$  decays spontaneously, an incoming photon may stimulate it in a resonant process to emit a second photon with the same energy  $hf$ . The electron decays to the lower energy state  $|1\rangle$ . The two resulting photons are identical in all their properties and have the same wave vector  $\vec{k}$ . This effect enables the amplification of coherent light and forms the basis of all laser processes.

Given that  $N_m$  denotes the number density of occupied states in energy level  $m$  within a bulk material, the change in this number density can be characterized by the Einstein coefficients  $B_{12}$ ,  $B_{21}$ , and  $A_{21}$ , each of which is defined for a specific process.

The rate of absorption leads to the transition from energy state  $|1\rangle$  to state  $|2\rangle$ , correlating to the change in the number density of the states  $N_2$  and  $N_1$  with [17, 72]

$$\left(\frac{dN_2}{dt}\right)_{\text{abs}} = -\left(\frac{dN_1}{dt}\right)_{\text{abs}} = B_{12}u(f)N_1. \quad (3.1)$$

This absorption rate is directly proportional to the spectral energy density  $u(f)$  according to Planck's law and the number of absorption-enabling electrons at the lower energy state  $N_1$  with the proportionality constant  $B_{12}$ . The same process that changes the population of state  $|2\rangle$  equally diminishes the population of state  $|1\rangle$ . Similarly, the stimulated emission of radiation results in a transition from level  $|2\rangle$  to level  $|1\rangle$  at the rate

$$\left(\frac{dN_2}{dt}\right)_{\text{stim}} = -\left(\frac{dN_1}{dt}\right)_{\text{stim}} = -B_{21}u(f)N_2, \quad (3.2)$$

which is also directly proportional to the spectral energy density  $u(f)$ , the population at the higher energy state  $N_2$ , and the proportionality constant  $B_{21}$ . The spontaneous emission process is described by the Einstein coefficient  $A_{21}$ , which represents the probability of an electron at the higher energy state spontaneously decaying per unit time. The rate of change of the number density is defined by

$$\left(\frac{dN_2}{dt}\right)_{\text{spn}} = -\left(\frac{dN_1}{dt}\right)_{\text{spn}} = -A_{21}N_2. \quad (3.3)$$

From Eq. (3.3), it can be observed that the population at the higher energy state  $N_2$  decays exponentially in the absence of other processes. The decay time constant, defined as  $\tau_{21} = A_{21}^{-1}$ , is referred to as the fluorescence lifetime. Fig. 3.2a shows a schematic illustration of the incoherent fluorescence generated from a crystal pumped with energy. Pumping is the term describing the process of energy transfer into the upper laser level through absorption as per Eq. (3.1). The exponential decay of the fluorescence intensity  $I(t)$  is given by [17, 73]

$$I(t) = I(0) \exp\left(-\frac{t}{\tau_{21}}\right). \quad (3.4)$$

At the time  $t = \tau_{21}$ , the fluorescence intensity  $I(t)$  has decayed to approximately 36.8% of its initial value  $I(0)$ , as depicted in Fig. 3.2b. A prolonged lifetime allows for lower laser light intensities to generate population inversion, a topic that is discussed later in this section.

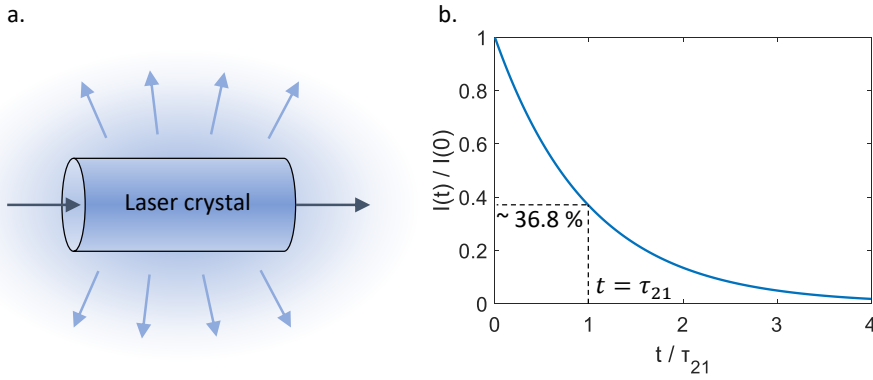


Figure 3.2: The left-hand side (a) presents a schematic illustration of the incoherent fluorescence by spontaneous emission for a laser crystal, while the right-hand side (b) shows a graph relating to the exponential decay of fluorescence intensity over time.

Consequently, the fluorescence lifetime is one of the most important properties enabling an efficient laser process, in addition to the transition cross sections of the material which will be discussed in the following.

The attenuation of electric field strength, as per the Beer-Lambert law, was previously described in section 2.1, Eq. (2.12). It was determined that the intensity decays exponentially over the distance  $z$ , depending on the absorption coefficient  $\alpha$ . In instances where the absorption is triggered by a photon transition from the lower energy state  $|1\rangle$  to the higher state  $|2\rangle$ , the absorption coefficient is proportional to the atom population at the lower state  $N_1$  and can be expressed as [47]

$$\alpha(\lambda) = \sigma_a(\lambda)N_1. \quad (3.5)$$

The constant  $\sigma_a(\lambda)$  is referred to as the absorption cross section of the material. It can be interpreted as an effective cross sectional area associated with an atom, which results in the absorption of photons, as depicted in Fig. 3.3a. However, it is not an actual geometric size of the atom and can differ for various transitions of the same atom. Similarly to the absorption process, the stimulated emission of light can be described as the amplification of the electromagnetic field strength. In analogy to Eq. (2.12), this leads to a change in intensity depending on the propagation distance  $z$  [47]:

$$I(z, \lambda) = I(0, \lambda) \exp [\sigma_e(\lambda)N_2z], \quad (3.6)$$

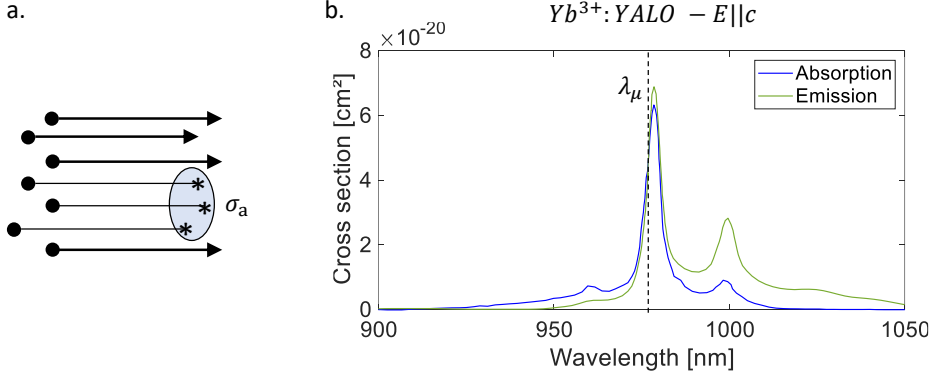


Figure 3.3: The geometrical interpretation of the absorption process is shown on the left (a), while the emission and absorption cross sections of  $Yb^{3+}:YALO$  are plotted on the right (b). Graphs adapted from [17, 75].

which is dependent on the proportionality constant  $\sigma_e(\lambda)$ , termed the emission cross section, as well as the number density of the upper state  $N_2$ . Combining both processes provides a description of the spectral intensity evolution through a laser active medium with

$$I(z, \lambda) = I(0, \lambda) \exp [(\sigma_e(\lambda)N_2 - \sigma_a(\lambda)N_1)z] . \quad (3.7)$$

This equation is crucial for simulating solid-state laser systems, as it can model the absorption and gain processes the laser field experiences in the laser crystal element.

Figure 3.3b provides an example for typical cross section data, illustrating the emission and absorption cross section of a laser medium across the wavelength region of interest [74, 75]. The laser crystal is yttrium orthoaluminate (YALO), a biaxial anisotropic host crystal with ytterbium(III) oxide ( $Yb^{3+}$ ) ions as the active dopant. The cross sections are plotted for the polarization components parallel to the c-axis of the crystal at the  $^2F_{7/2} \rightarrow ^2F_{5/2}$  energy-level transition of  $Yb^{3+}$ . The relationship between emission and absorption cross sections of solid-state lasers is determined by the McCumber relation, where the ratio of emission to absorption increases with the wavelength [76]. The spectroscopic intersection of emission and absorption ( $\sigma_a(\lambda) = \sigma_e(\lambda)$ ) is known as the chemical potential wavelength  $\lambda_\mu$  [17].

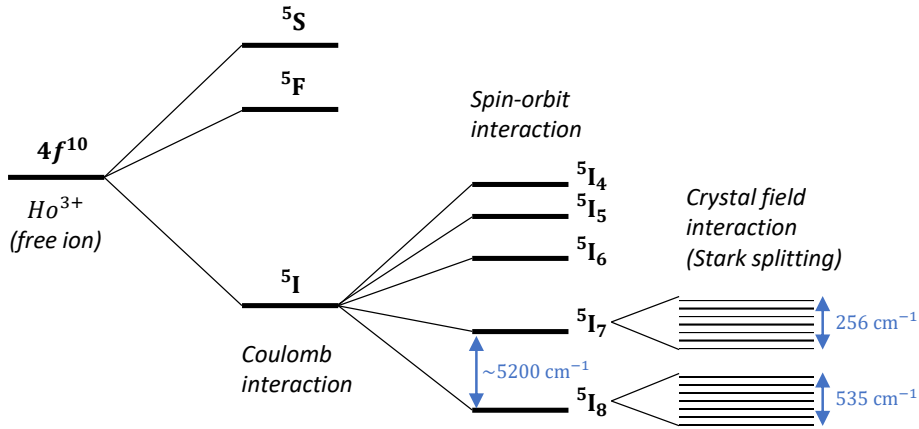


Figure 3.4: Energy level splitting in solid-state hosts caused by different interactions for the example of the  $\text{Ho}^{3+}$  ion. Graph adapted from [17].

For efficient laser operation, the laser wavelength of stimulated emission is typically chosen above this wavelength, while the pump wavelength of optically pumped lasers is typically below.

To explain the energy levels needed for the stimulated emission process, the energy level splitting mechanisms are illustrated in Fig. 3.4 for the example of the  $\text{Ho}^{3+}$  ion. In rare-earth ions, the optically active electron is located in the inner shell and is therefore shielded from the strong influence of the crystal field. This shielding from host phonons enables the long upper state lifetimes necessary for efficient lasing. The electric field of the free ion is divided into different energy levels resulting from the Coulomb interaction and spin-orbit coupling [17, 77]. The diminished influence of the crystal field then leads to a split into separate groups known as manifolds. The possible energy transitions in solid-state gain media are divided by the host crystal field, resulting in a broadening of the laser gain bandwidth. This is caused by the Stark effect, and for the example of  $\text{Ho}^{3+}$ , the manifolds relevant to the  $^5I_7 \rightarrow ^5I_8$  laser transition are separated by an energy difference of about  $5000 \text{ cm}^{-1}$ . For in-band pumped lasers, this results in pump and laser wavelengths in the  $2 \mu\text{m}$  range as both upper and lower laser levels fall into these manifolds [4].

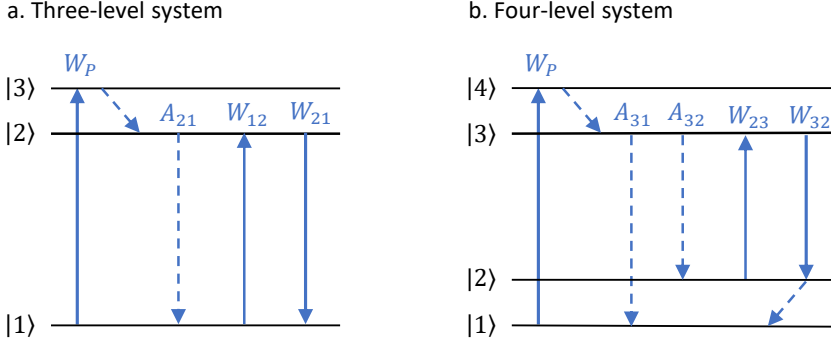


Figure 3.5: Three- (a) and four-level (b) laser schemes and their corresponding energy level transitions.

Stimulated amplification of light in between these manifolds forms the foundation of any laser process, however, as per Eq. (3.7), it is also necessary to consider the reabsorption of this light in a laser-active medium. The light amplification process can be used to trigger laser operation by establishing feedback within an oscillator. The effective gain of light, when traversing an amplification medium along  $z$ , is defined by the corresponding change of intensity with [3]

$$G(z, \lambda) = \frac{I(z, \lambda)}{I(0, \lambda)} = \exp [(\sigma_e(\lambda)N_2 - \sigma_a(\lambda)N_1)z] . \quad (3.8)$$

To amplify the incoming light, the gain must be  $G > 1$ , leading to an effective population inversion. This inversion implies that the effective number of ions in the upper state aiding the stimulated laser process has to be greater than the number of ions in the lower state absorbing the light. The effective population inversion is thus defined as

$$\sigma_e(\lambda)N_2 > \sigma_a(\lambda)N_1 . \quad (3.9)$$

In a two-level system, this inversion cannot be achieved. Because of the symmetry of the absorption and emission processes in Eqs. (3.1) and (3.2), only an equilibrium of the two populations  $N_2$  and  $N_1$  is possible. To disrupt this symmetry, at least a third level is required, leading to a system involving two main energy differences and, consequently, two separate wavelengths in an optically pumped system. Figure 3.5 illustrates the basic energy state transitions of three- and four-level schemes.

In contrast to the two-level scheme, the three-level scheme introduces the pump radiation with energy density  $u_P(v_P)$ , which increases the number of ions in energy level  $|3\rangle$  as per [17]

$$\left(\frac{dN_3}{dt}\right)_{\text{pump}} = W_P N_1, \quad (3.10)$$

where  $W_P = B_{13}u_P(v_P)N_1$  is the pump transition rate from state  $|1\rangle$  to  $|3\rangle$ . Assuming that the relaxation, potentially induced by host crystal phonons, from states  $|3\rangle \rightarrow |2\rangle$  is considerably faster than the pumping of level  $|3\rangle$ , the population of  $|3\rangle$  remains low ( $N_3 \approx 0$ ). This relation leads to a description of the remaining two laser levels by

$$\frac{dN_2}{dt} = W_P N_1 + W_{12}N_1 - W_{21}N_2 - A_{21}N_2, \quad (3.11)$$

$$N_1 \approx N - N_2, \quad (3.12)$$

where  $N$  is the constant total ion population of the system. Consequently, if the pump rate  $W_P$  can offset all upper-level decay, population inversion is achievable in a three-level system. In this simple case, only the spontaneous emission rate  $A_{21} = \tau_2^{-1}$ , depending on the upper state lifetime  $\tau_2$ , has to be compensated. Nonetheless, a pump rate of  $W_P = A_{21}N_2$  is necessary to reach the laser threshold.

In a four-level scheme, this threshold can be considerably lowered by also diminishing the lower level population. As depicted in Fig. 3.5b, the lower laser level  $|2\rangle$  is no longer the ground-state of the system, and a rapid relaxation from  $|2\rangle$  to the ground state  $|1\rangle$  is assumed ( $N_2 \approx 0$ ), analogous to the fast relaxation from  $|4\rangle \rightarrow |3\rangle$  ( $N_4 \approx 0$ ). The energy level transitions of the four-level scheme are subsequently described by

$$\frac{dN_3}{dt} = W_P N_1 + W_{23}N_2 - W_{32}N_3 - (A_{32} + A_{31})N_3, \quad (3.13)$$

$$N_1 \approx N - N_3. \quad (3.14)$$

The laser transition from  $|3\rangle \rightarrow |2\rangle$  does not suffer from any reabsorption at the laser wavelength, enabling population inversion at a low laser threshold. In reality, the assumptions of rapid relaxation is not always met, as particularly a population of the lower laser level  $|2\rangle$  must be considered for many laser materials [4]. This leads to reabsorption, or stimulated emission of the pump light, and the resulting laser scheme can be viewed as a mixture of the three- and

four-level schemes. It is therefore termed the quasi-three-level laser scheme, and most active ions of interest to this work ( $\text{Ho}^{3+}$ ,  $\text{Tm}^{3+}$ ,  $\text{Yb}^{3+}$ ) exhibit this nature.

In the context of this work, the model implementation of the laser theory discussed in this section is limited to bulk solid-state media. Therefore, different solid-state laser concepts and geometries will be explored in the subsequent section.

## 3.2 Solid-State Laser Principles

This section aims to provide an overview of solid-state laser principles and concepts. Subsection 3.2.1 explores specific solid-state laser geometries and typical arrangements, with a focus on laser amplifiers and laser resonators. The spatial and temporal coherence characteristics of laser light, related to longitudinal and transverse modes, are discussed in subsection 3.2.2. Finally, the stability condition for laser resonators is described in subsection 3.2.3.

### 3.2.1 Solid-State Geometries and Concepts

The fundamental physics outlined in the previous section, describing the generation of laser light, apply to a broad range of laser materials and configurations. The most relevant systems fall into categories such as semiconductor (diode) lasers pumped by applying electric currents, gas lasers energized by electric discharge, chemically pumped dye lasers, and most relevant to this work, optically pumped solid-state lasers [47]. Solid-state lasers are further subdivided into different gain media and fundamental principles. Potential gain media include transparent glasses, ceramics, and crystals, each displaying vastly different thermal and spectroscopic material parameters. This work focuses on bulk-type lasers, made of a solid piece of gain medium, in contrast to alternative solid-state designs developed to bypass the thermal challenges that high-power bulk lasers commonly encounter [3]. These alternative systems include disc-type lasers and fiber lasers, and although the fundamental approaches of the developed model for bulk lasers could be adapted for these systems [3, 78], they are not further discussed in this work.

Figure 3.6 illustrates the fundamental bulk laser geometries relevant to this work. The most basic case is the bulk laser amplifier, depicted in Fig. 3.6a, where a seed laser beam is amplified in power and energy as it passes through the laser gain medium. However, to generate laser light

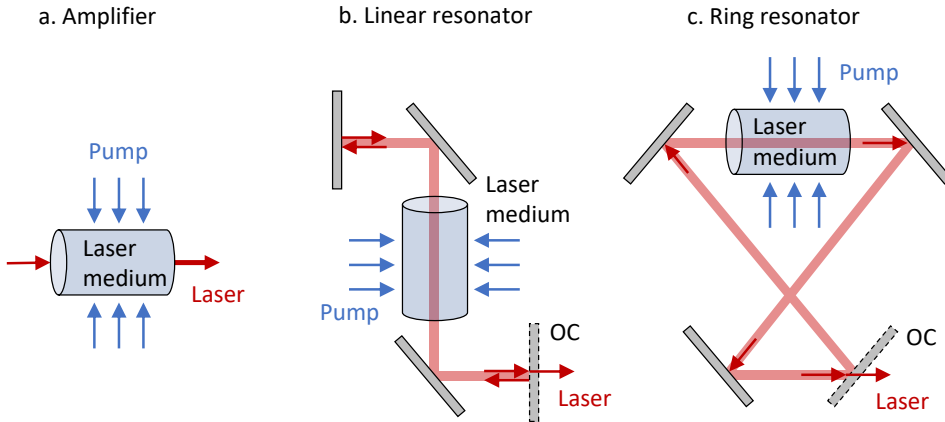


Figure 3.6: The bulk laser configurations relevant to this work include laser amplifiers (a) and resonant cavities for laser generation. Depending on the mirror placement, the resonators can be designed as linear (b) or ring (c) type.

from quantum noise, a resonator is required. Here, the basic types are divided into linear, also known as standing-wave resonators and ring resonators. Linear resonators (figure 3.6b) form a cavity with two end mirrors, where the light propagates from one mirror to the other, creating a standing wave pattern in the electromagnetic field. Conversely, ring resonators (figure 3.6c) circulate the light in the two different directions and lack end mirrors. Ring resonators can thus exhibit two output beams at the outcoupling mirror, unless one of the directions is suppressed. Another difference is that in linear resonators, optical elements within the cavity are passed twice by the light, while elements in ring resonators are only passed once. This consideration is important for the modeling of these types of resonant laser systems. In Fig. 3.6, the schematic pumping mechanism of the gain media implies a side pumping configuration. Optically pumped bulk solid-state laser systems are typically end pumped or side pumped by incoherent or coherent light sources, where the name relates to the pump direction relative to the signal laser beam.

The amplification of laser light from quantum noise to a perceptible output beam requires optical feedback from a resonator. A schematic illustration of the feedback condition for a linear resonator is presented in Fig. 3.7. In a linear resonator, two mirrors are incorporated to form the laser cavity: one with a high reflectivity of the laser wavelength (HR mirror) and one with partial reflectivity. The partially reflective mirror, termed the output coupler (OC

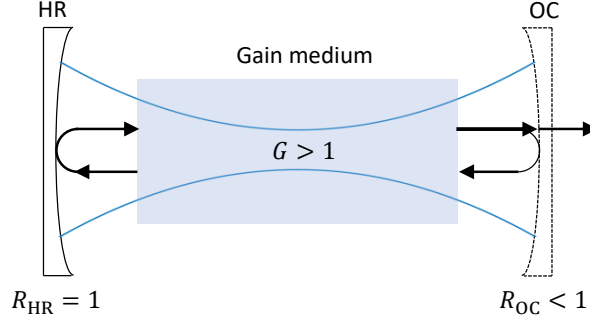


Figure 3.7: Feedback condition of the electromagnetic field depicted in a schematic representation for a linear laser resonator. Graph adapted from [17].

mirror), is used to couple out the laser light at one end. An effective gain  $G > 1$  is required to achieve population inversion, as defined in Eq. (3.8). While this is enough to amplify light in a single pass through the gain medium (e.g. in a laser amplifier), a resonant cavity introduces loss at the OC element with reflectivity  $R_{OC} < 1$ , as well as additional losses  $\Lambda$  in the system. In stable laser operation, the electromagnetic field strength must replicate itself after one round-trip, thus requiring the following single pass gain  $G$  to compensate for the introduced losses [17]:

$$G > \frac{1}{\sqrt{R_{HR}(1 - \Lambda)R_{OC}}} . \quad (3.15)$$

To achieve the required gain for high power output, the light has to complete numerous round-trips, passing through the gain medium each time.

The temporal evolution of laser light generation must be taken into account as well. A laser system is typically operated in two different states: CW and pulsed operation. CW refers to an uninterrupted, constant laser output. In contrast, pulsed lasers generate optical flashes of output light. There are many mechanisms and techniques for generating pulsed laser light, with Q-switching being most relevant to this work and discussed in section 3.5.2. Figure 3.8 illustrates the temporal evolution of output power for two operation modes in an exemplary laser system. In both examples, an average output power of 12 W is achieved. For the laser in CW operation, the onset of laser operation is defined by relaxation oscillations, also known as spiking. This phenomenon results from a delay in the amplification of quantum noise relative to the population inversion. A temporary buildup of an upper state population  $\Delta N_2 > N_{th}$  above

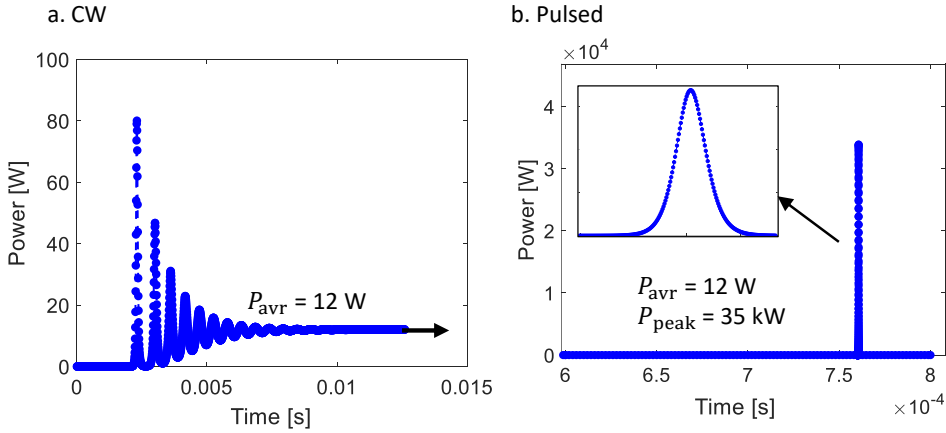


Figure 3.8: Comparison of the temporal evolution of laser power for CW lasers (a) and pulsed laser systems (b).

threshold can occur shortly after the initiation of pumping. The laser output oscillates until a steady state is achieved after a certain time interval [17]. Contrarily, in pulsed operation, this does not occur depending on the pulse generation method. In the case of Q-switching, as shown in Fig. 3.8b, feedback within the cavity is inhibited by introducing high loss. This results in a deliberate buildup of upper state population, which is extracted as a pulse of optical power when the additional loss is removed. In steady operation, the energy contained in each pulse is defined as

$$E_P = \frac{P_{avr}}{f_{rep}}, \quad (3.16)$$

where  $f_{rep}$  represents the repetition rate of the pulse generation. The peak power of a single pulse can significantly exceed the average power  $P_{avr}$ , as shown in the plotted example, and is approximated from the pulse full width at half maximum (FWHM)  $\tau_P$  and the energy by

$$P_{peak} = k \frac{E_P}{\tau_P}. \quad (3.17)$$

Here,  $k$  is a dimensionless approximation factor that depends on the pulse shape, for example it is  $k \approx 1$  for rectangular pulses and  $k \approx 0.94$  for Gaussian-like pulse shapes [79]. While these equations provide a reasonable approximation regarding the pulsed performance of a system, and additional analytical solutions can be employed to describe gain media under Q-switching,

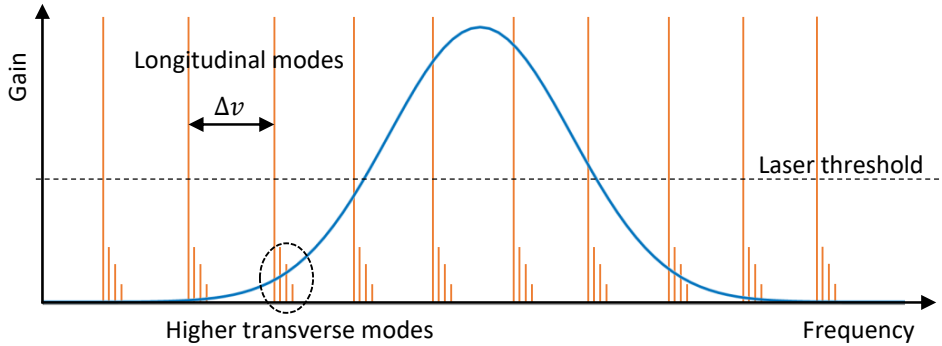


Figure 3.9: Exemplary gain bandwidth over the output frequency (blue line). The longitudinal and transverse mode peaks of a linear resonator, separated by the mode spacing  $\Delta\nu$ , are shown in orange. Graph adapted from [80].

a numerical model is essential for comprehensively describing the temporal processes in a laser.

### 3.2.2 Modes of Laser Light

This section aims to provide insight into the optical properties of laser radiation and corresponding modes of light. The stimulated emission process, detailed in section 3.1, leads to light generation characterized by its spatial and spectral coherence. Spatial coherence relates to beam divergence, which is typically very small compared to an incoherent light source. Regarding spectral coherence, the wavelength of a laser can exhibit a very narrow linewidth (near monochromatic) with uniform polarization [3]. However, not all lasers display a narrow linewidth, particularly pulsed lasers can have a very broad spectrum. The smallest possible linewidth is determined by the characteristics of the laser resonator and gain medium. One limiting factor is the spectral width of the laser gain medium. An exemplary gain distribution is plotted in Fig. 3.9 in blue. This gain bandwidth, termed  $\Delta G$ , typically depends on the emission and absorption cross sections, and can vary in broadness above the laser threshold for different systems.

For stable lasing to occur, the electromagnetic field must replicate itself within a resonator, as detailed in the preceding section 3.2.1. Owing to this requirement, in linear resonators, only specific standing wave patterns can form where the field does not interfere destructively. The optical

path length  $L_R$ , separating the end mirrors of the resonator, dictates these patterns. The permitted longitudinal modes of the cavity, depicted in Fig. 3.9 in orange, are those where the mirror distance equals an exact multiple of half the laser wavelength  $\lambda_L$  [80]:

$$q = \frac{2L_R}{\lambda_L} . \quad (3.18)$$

In this equation,  $q$  represents the mode order, which is typically very large since the resonator length significantly surpasses the light wavelength. The resonator length consequently also determines the separation of the longitudinal modes with mode spacing  $\Delta v$  [80]:

$$\Delta v = \frac{c}{2L_R} . \quad (3.19)$$

Only those modes where the gain of the laser medium surpasses the laser threshold are amplified and emitted as the laser output. Therefore, the supported number of emitted modes  $M$  can be estimated from the mode spacing and the spectral gain bandwidth by

$$M \approx \frac{\Delta G}{\Delta v} . \quad (3.20)$$

Consequently, the resulting spectrum of a linear resonator may consist of a single longitudinal mode or a combination of multiple modes.

While the longitudinal mode behavior relates to the temporal coherence of laser light, the spatial coherence is discussed next. In addition to the longitudinal modes, Fig. 3.9 also depicts transverse electromagnetic (TEM) modes at a small spectral offset. Given that typical resonator geometries are not one-dimensional but extend in transverse directions as well, it is possible for higher-order transverse modes to be excited. Because of the transversal offset, they typically experience a shifted effective resonator length and therefore also a shift in frequency [3, 80]. Depending on the particular symmetry of the laser resonator, the intensity profiles of higher-order transverse modes in typical resonators can be represented by a superposition of plane waves in two forms: Hermite-Gaussian ( $\text{TEM}_{mn}$ ) and Laguerre-Gaussian ( $\text{TEM}_{pl}$ ) [81]. Hermite-Gaussian modes are typically used for systems with rectangular symmetry, characterized by two indices  $m$  and  $n$  which denote the number of nodes in the horizontal and vertical directions, respectively. Conversely, Laguerre-Gaussian modes are more suitable for systems with spherical symmetry and are described by the two indices  $p$  and  $l$ , where  $p$  denotes the radial node number and  $l$  the azimuthal index, indicating the number of times the phase completes  $2\pi$  radians on a closed loop around the beam axis. The intensity distributions for lower order Laguerre-Gaussian

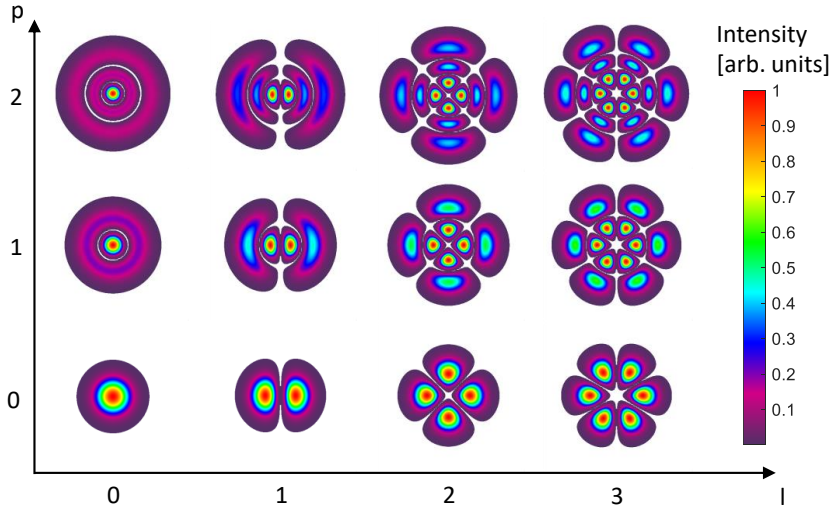


Figure 3.10: Intensity distribution of the Laguerre-Gaussian TEM modes up to indices  $p = 2$  and  $l = 3$ .

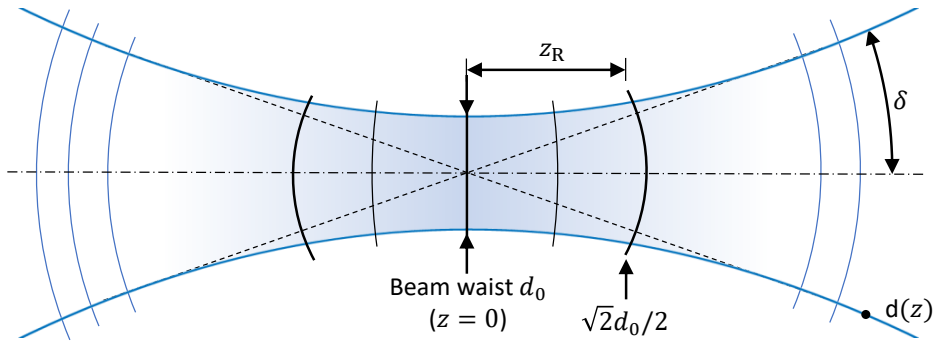


Figure 3.11: Propagation characteristics of TEM beams in the paraxial approximation showing the behavior around the beam waist. Graph adapted from [82].

modes are depicted in Fig. 3.10 [81]. In waveguide structures, there may be variations to the typical modes encountered in free-space.

The lowest transverse mode, denoted  $\text{TEM}_{00}$ , exhibits a pure Gaussian intensity distribution and is therefore also referred to as a Gaussian beam. The characteristics of the TEM beam around the beam waist are plotted in Fig. 3.11 in the direction of the wave vector [82]. The

beam diameter of the Gaussian  $d(z)$  is defined as the  $D4\sigma$  width where the intensity in the horizontal or vertical direction is four times the standard deviation. The length where the beam diameter stays below  $\sqrt{2}d_0/2$  (the beam area below twice that of the waist area) is termed the Rayleigh-length  $z_R$ . Here, the beam is described in the near field by a hyperbole. Beyond the Rayleigh-length, the beam is described in the far field by the divergence half-angle  $\delta$  of the asymptotes:

$$\delta = \arctan \left( \frac{d_0}{2z_R} \right) . \quad (3.21)$$

For a perfectly Gaussian beam, the minimum waist diameter a beam can be focused to is limited by diffraction and depends on the divergence angle and the wavelength by [82]

$$d_{0,\text{TEM00}} = \frac{2\lambda}{\delta n \pi} . \quad (3.22)$$

The presence of the refractive index  $n$  implies that the waist diameter also depends on the medium the beam propagates through. For beams with higher order mode content, the beam propagation ratio  $M^2$  is defined to relate the divergence to the minimal focus size that can be achieved in a Gaussian beam. If the waist diameter  $d_0$  and divergence angle  $\delta$  of a certain beam are known, the  $M^2$  value is defined as [82]

$$M^2 = \frac{\pi}{\lambda} \delta \frac{d_0}{2} . \quad (3.23)$$

This value is widely used to characterize laser systems by their 'beam quality' and the method of measurement for a real beam is regulated by the ISO standard 11146 [83]. The goal of the measurement is to capture enough diameter points in the near field to characterize the beam waist and enough points in the far field to characterize the divergence [84].

### 3.2.3 Resonator Stability

The stability of a laser resonator is defined by its ability to confine light within its structure over several round-trips. In stable resonators, intracavity geometric rays remain within the system, provided the initial transversal offset is not too large. Given that the mirrors confining the field do not extend indefinitely in the transversal direction, the rays must be refocused within the cavity, which can be realized by curved mirror surfaces, as shown with Fig. 3.12a. The

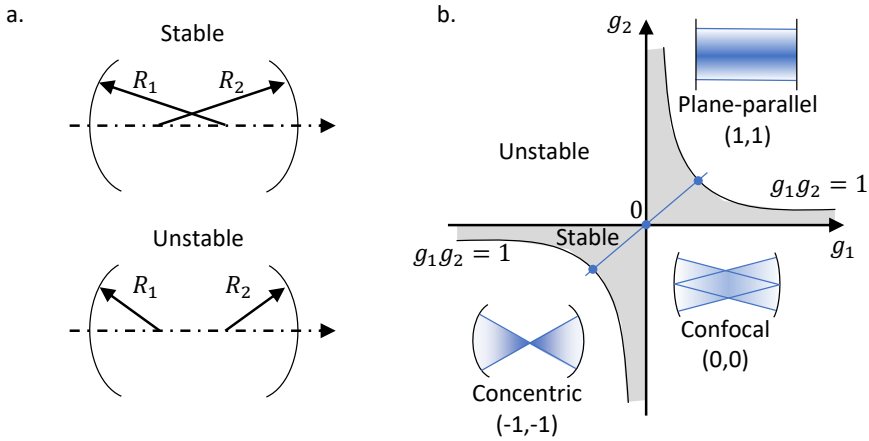


Figure 3.12: Stable and unstable resonators (a) and the corresponding stability diagram (b) of a linear resonator. Graphs adapted from [17].

electromagnetic field that forms within the resonator is then described by the TEM modes that have been described in the preceding section 3.2.2. The geometrical stability of a simple linear resonator is characterized using the resonator parameters  $g_1$  and  $g_2$  [17]:

$$g_1 = 1 - \frac{L}{R_1} , \quad (3.24)$$

$$g_2 = 1 - \frac{L}{R_2} . \quad (3.25)$$

These parameters are dependent on the radius of curvature of the cavity end mirrors  $R_1$  and  $R_2$ , as well as the cavity length  $L$ . The stability criteria for linear resonators is then expressed as

$$0 \leq g_1 g_2 \leq 1 \quad \rightarrow \quad \text{stable} , \quad (3.26)$$

$$g_1 g_2 < 0 \quad \text{or} \quad g_1 g_2 > 1 \quad \rightarrow \quad \text{unstable} . \quad (3.27)$$

A graphical representation of the stability of a linear resonator is the stability diagram in Fig. 3.12b, which illustrates the zone of stability based on the resonator parameters  $g_1$  and  $g_2$ .

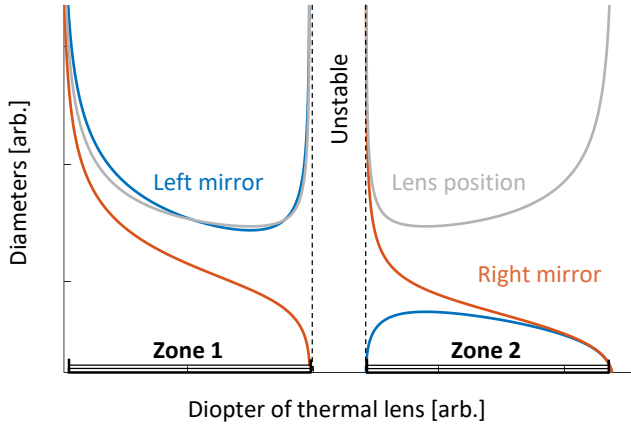


Figure 3.13: Stability zones of a linear resonator including a thermal lens.

The stability zone and criteria for ring resonators are described by a different formulation, and also differ based on the two possible propagation directions. A more detailed explanation of the specific resonator stability conditions for ring resonators is provided by M. Eichhorn in reference [17]. Regarding unstable resonators, laser operation is still possible. Despite a ray injected into an unstable resonator being ejected eventually, for certain applications they are preferred over stable resonators. In these systems, the diffraction losses resulting from instability are used to generate the outcoupling from the resonator. This can be achieved, for instance, through the use of variable reflectivity mirrors, where the reflection diminishes as the distance from the beam axis increases. The complexity of unstable resonators often requires a numerical model for analyzing these systems.

Although the stability criteria defined in Eq. (3.27) provide a comprehensive overview of basic resonators, the impact of a thermal lens inside the cavity is not accounted for. As the energy loss within the gain medium results in the material heating up, this subsequently changes the refractive index. The resulting refractive index profile acts as a variable lens within the cavity, changing in accordance with the pump power of the laser. The underlying mechanisms of thermal lensing are explained in section 4.4.3. The resonator exhibits one (for ring resonators) or two (for linear resonators) stability zones, depending on the dioptric power of the thermal lens. V. Magni offers a detailed formulation of the thermal lens effects on stability, where the stability zones for linear resonators are investigated [85, 86]. Figure 3.13 illustrates the stability

zones for an arbitrary linear resonator, where the beam diameters at the cavity end mirrors and the lens position are calculated using Gaussian matrix propagation. According to V. Magni, the laser system exhibits greater sensitivity to misalignment in zone 2. The laser becomes unstable in between the stability zones, however, careful design of the laser system can bridge the two stability zones, thereby enhancing the full stability of the laser. When the pump power of a laser is increased, leading to a rise in the dioptric power of the thermal lens, the end of a stability zone may be reached. This can result in a phenomenon known as thermal roll-over, where the resonator becomes unstable and the laser output power stagnates with increasing pump power. Compared to linear resonators, ring resonators only have one stability zone since the laser beam only passes the thermal lens once per round-trip. An analysis for the stability of ring resonators including a variable lens, is presented akin to the formulation of V. Magni in reference [87].

In the subsequent section, the laser principles discussed in this chapter so far are utilized to model the transformation of the propagated electromagnetic field through the laser gain medium.

## 3.3 Generalized Simulation of Laser Gain Media

This section goes further into the multi-physics model approach, detailing the modeling of the laser gain medium element. Subsection 3.3.1 describes the fundamental concept of the rate equation model for a general solution, while the simulation accuracy of this approach is compared to an experimental resonator in subsection 3.3.2.

### 3.3.1 Basic Rate Equation Model

Similarly to the element operator representation from chapter 2, Fig. 2.14, the gain media algorithm for a single slice of the element operator is depicted in Fig. 3.14. The aim is to accurately model the variation in electromagnetic field strength and intensity of a beam traversing the medium with high precision and transversal resolution. Given that the model approach is iterative with  $m_i \rightarrow M_{\max}$  iterations, the initial iteration of the laser system to be simulated  $m_i = 0$  (the first round-trip in the case of a resonator) propagates through the medium without interaction. This is necessary to calculate the intensity distribution of all beams

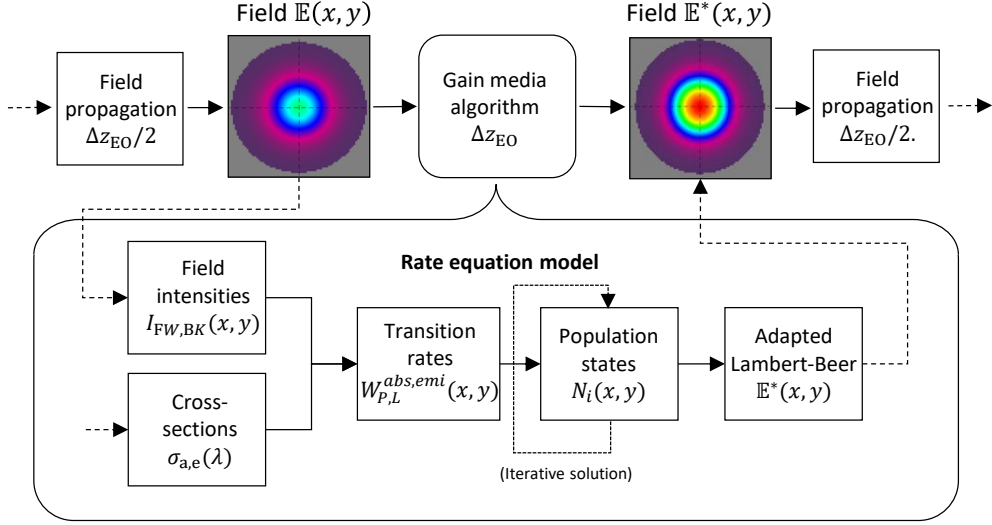


Figure 3.14: Schematic representation of the laser gain media algorithm as a special case of element operator.

$I_{FW,BK}(x, y)$  for the forward and backward pass of light, which is then used in the rate equation model of the subsequent iteration  $m_i = 1$ . Using the cross section data  $\sigma_{a,e}(\lambda)$  of the laser gain medium to be simulated, the energy transition rates of pump ( $W_P$ ) and laser ( $W_L$ ) light are calculated at each slice [17, 88]:

$$W_P^{abs}(x, y) = [I_{P,FW}(x, y) + I_{P,BK}(x, y)] \frac{\lambda_P}{hc} \sigma_a(\lambda_P), \quad (3.28)$$

$$W_P^{emi}(x, y) = [I_{P,FW}(x, y) + I_{P,BK}(x, y)] \frac{\lambda_P}{hc} \sigma_e(\lambda_P), \quad (3.29)$$

$$W_L^{abs}(x, y) = [I_{L,FW}(x, y) + I_{L,BK}(x, y)] \frac{\lambda_L}{hc} \sigma_a(\lambda_L), \quad (3.30)$$

$$W_L^{emi}(x, y) = [I_{L,FW}(x, y) + I_{L,BK}(x, y)] \frac{\lambda_L}{hc} \sigma_e(\lambda_L). \quad (3.31)$$

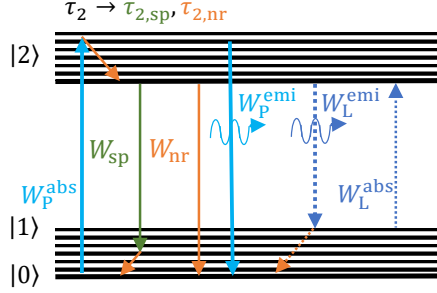


Figure 3.15: Energy transfer mechanisms of interest in the basic rate equation approach.

The cross sections, as well as the photon energy  $E_{ph} = \lambda/(hc)$ , are dependent on the wavelength of the pump and laser light. For four-level laser materials, the rate of pump emission  $W_p^{emi}$  and rate of laser absorption  $W_L^{abs}$  are typically negligible, as predicted. However, these rates become significant for three-level and quasi-three-level materials, where laser reabsorption and stimulated emission of the pump can diminish the efficiency.

The energy transfer diagram is presented for the basic rate equation model in Fig. 3.15, similarly to the four-level scheme depicted in Fig. 3.5. In addition to the rates of pump and laser light absorption and emission, the upper laser level  $|2\rangle$  is depopulated by spontaneous emission with a rate  $W_{sp} = 1/\tau_{sp}$  and non-radiative decay with a rate of  $W_{nr} = 1/\tau_{nr}$ . The resulting upper state lifetime  $\tau_2$  is thus dependent on both the lifetime of spontaneous emission  $\tau_{sp}$ , leading to a decay with mean wavelength  $\bar{\lambda}_{sp}$ , and the lifetime of non-radiative decay  $\tau_{nr}$  [89, 90]:

$$\frac{1}{\tau_2} = \frac{1}{\tau_{sp}} + \frac{1}{\tau_{nr}}. \quad (3.32)$$

The mechanism of non-radiative decay is typically induced by lattice vibrations of the host matrix, leading to ion decay into the ground state, where the energy difference is dissipated as heat (refer to section 3.1). According to quantum mechanics, these lattice vibrations are quantised as phonons, where optical phonons are associated with higher frequency vibrations, resulting in the described absorption mechanism [47]. Besides phonons directly interacting with the upper laser level, non-radiative decay may also be caused by nearest neighbor ion interactions, where ions can be excited to higher energy states and decay from there. These effects are dependent

on the population of the different manifolds and are not considered in the generalized model, but will be addressed in section 3.4 for the case of  $\text{Ho}^{3+}$ .

With all relevant energy transfer rates of the generalized approach defined, the rate equations resulting in the population distribution of the laser material are adapted from Eqs. (3.13) and (3.14) as follows [4, 17]:

$$\begin{aligned} \frac{dN_2(x, y)}{dt} = & [W_P^{\text{abs}}(x, y) + W_L^{\text{abs}}(x, y)] N_1(x, y) \\ & - [W_P^{\text{emi}}(x, y) + W_L^{\text{emi}}(x, y) + W_{\text{sp}} + W_{\text{nr}}] N_2(x, y) , \end{aligned} \quad (3.33)$$

$$\begin{aligned} \frac{dN_1(x, y)}{dt} = & [W_P^{\text{emi}}(x, y) + W_L^{\text{emi}}(x, y) + W_{\text{sp}} + W_{\text{nr}}] N_2(x, y) \\ & - [W_P^{\text{abs}}(x, y) + W_L^{\text{abs}}(x, y)] N_1(x, y) . \end{aligned} \quad (3.34)$$

The simulation of the laser gain medium requires solving the rate equations for each slice in the  $z$ -direction with a transversal distribution in  $x$  and  $y$ . The solution to the differential equations is provided with a numerical time step  $\Delta t$ , which can be selected to be significantly larger than the light propagation time from one slice to another, without compromising accuracy. Consequently, at each iteration  $m_i$  of the simulation, the three-dimensional population distribution of the laser gain medium is updated until equilibrium is achieved. The gain and absorption of the laser fields  $\mathbb{E}_L(x, y)$  and  $\mathbb{E}_P(x, y)$  along the propagation axis  $n \rightarrow N_z$  are then computed with an adaptation of Eq. (3.8) for each slice:

$$\mathbb{E}_L^{n+1}(x, y) = \mathbb{E}_L^n(x, y) \exp [0.5(\sigma_e(\lambda_L)N_2(x, y) - \sigma_a(\lambda_L)N_1(x, y))\Delta z] , \quad (3.35)$$

$$\mathbb{E}_P^{n+1}(x, y) = \mathbb{E}_P^n(x, y) \exp [0.5(\sigma_e(\lambda_P)N_2(x, y) - \sigma_a(\lambda_P)N_1(x, y))\Delta z] . \quad (3.36)$$

If the material exhibits anisotropy, the equations are computed for each polarization component in  $x$  and  $y$ , as the spectroscopic material parameters may vary in these directions. Additionally, as the laser gain medium is modeled in a three-dimensional mesh along  $(x, y, z)$ , advanced doping profiles can be easily integrated into the model. For instance, doping segmentation or undoped end-caps exhibit a different doping concentration at each gain media slice. This results in a total ion population density  $N_{\text{total}}(z)$  variable in the  $z$ -direction, which can be utilized to design laser gain media for specific applications [91].

Table 3.1: Spectroscopic material parameters used for the basic rate equation approach for  $\text{Ho}^{3+}:\text{YAG}$  and  $\text{Yb}^{3+}:\text{YALO}$  (parallel to the optical c-axis).

Parameters	$\text{Ho}^{3+}:\text{YAG}$	$\text{Yb}^{3+}:\text{YALO}(\text{llc})$	Units
$\lambda_L$	2090.3	1040	nm
$\lambda_P$	1908	978	nm
$N_{\text{total}} (\text{@}1\text{at.}\%)$	$1.38E20$	$1.92E20$	$\text{cm}^{-3}$
$n_x$	1.81	1.96	-
$n_y$	1.81	1.94	-
$\sigma_e(\lambda_L)$	$1.2E-20$	$0.5E-20$	$\text{cm}^2$
$\sigma_e(\lambda_P)$	$7.7E-21$	$6.1E-21$	$\text{cm}^2$
$\sigma_a(\lambda_L)$	$2.1E-21$	$0.68E-21$	$\text{cm}^2$
$\sigma_a(\lambda_P)$	$1.2E-20$	$6.6E-21$	$\text{cm}^2$
$\tau_{\text{sp}}$	$7.9E-3$	$0.5E-3$	s
$\tau_{\text{nr}}$	0.0478	-	s
$\bar{\lambda}_{\text{sp}}$	1988.0	996.0	nm

### 3.3.2 Submodel Validation

The spectroscopic material parameters utilized with this generalized approach are listed in Tab. 3.1 for two laser gain media. The data provided on the left column is for  $\text{Ho}^{3+}:\text{YAG}$  at the  $^5I_7 \rightarrow ^5I_8$  laser transition, with a pump wavelength of  $\lambda_P = 1908$  nm and a laser wavelength of  $\lambda_L = 2090.3$  nm. The spectral data encompasses the refractive index in  $x$ - and  $y$ -direction  $n_{x,y}$  [92], which are identical for YAG as it is an isotropic material, as well as the cross sections  $\sigma_{e,a}$  at the pump and laser wavelengths [93, 94] and the upper state lifetimes  $\tau_{\text{sp}}$  and  $\tau_{\text{nr}}$  [95]. The  $\text{Yb}^{3+}:\text{YALO}$  data is displayed in the right column for the  $^2F_{7/2} \rightarrow ^2F_{5/2}$  laser transition with a pump wavelength of  $\lambda_P = 978$  nm and a laser wavelength of  $\lambda_L = 1040$  nm [75, 96, 97]. As the host is biaxial anisotropic, the data is presented for light propagating parallel to the optical c-axis of the material, resulting in different refractive indices for the  $x$ - and  $y$ -axis [98].

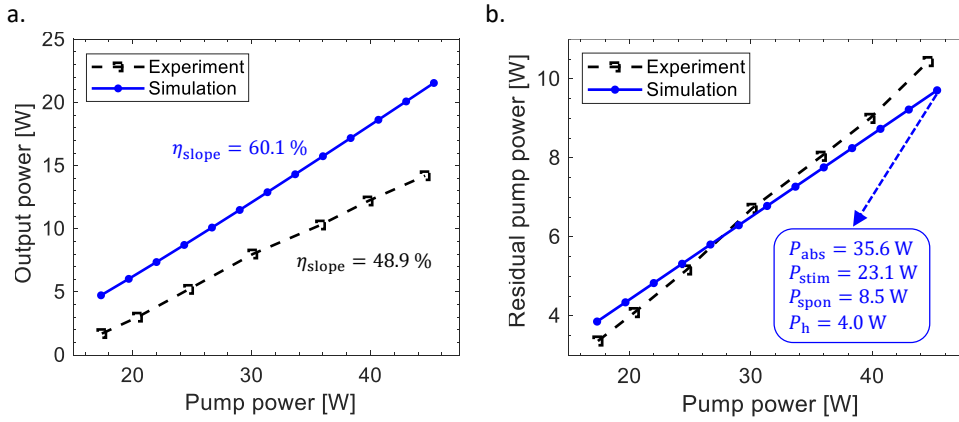


Figure 3.16: Comparison of simulation and experiment for an exemplary linear resonator of a Ho<sup>3+</sup>:YAG laser. The results of output power over pump power are shown on the left (a), while the residual pump power is shown on the right (b).

To validate the basic rate equation model, a simulation of an exemplary linear resonator is conducted. The arrangement mirrors the resonator detailed later in section 3.6, where the optical components and input parameters are explained in more detail. The laser gain medium is a Ho<sup>3+</sup>:YAG crystal, with a doping concentration of 1.1 at.% and a crystal length of 1.8 cm. Utilizing the spectroscopic material parameters listed in Tab. 3.1, the resonator is simulated over a pump power range of 17.5 to 45 W. The output power and residual pump power versus incident pump power are depicted in Fig. 3.16, comparing the simulated results (in blue) with experimentally measured results (in black). The simulated resonator was modeled in the same configuration as the experimental arrangement. The slope efficiency of the simulated output can be determined with linear regression, and exhibits a value of  $\eta = 60.1\%$ , while the experimental laser demonstrates a slope of  $\eta = 48.9\%$ . While the simulated results do not perfectly match with the experimental ones, the model at this stage does work as intended and the model accuracy will be increased with the extension of further submodels and model approaches in later sections.

For the simulation results at a pump power of 45 W, 35.6 W is absorbed by the laser gain medium, resulting in a residual pump power of 9.4 W. The absorbed power is further split into the stimulated emission at  $P_{\text{stim}} = 23.1 \text{ W}$ , the spontaneous emission at  $P_{\text{spont}} = 8.5 \text{ W}$ , and the power dissipated as heat within the crystal at  $P_{\text{h}} = 4.0 \text{ W}$ . Notably, at this operating point, the stimulated emission does not equal the output power, which is a consequence of additional

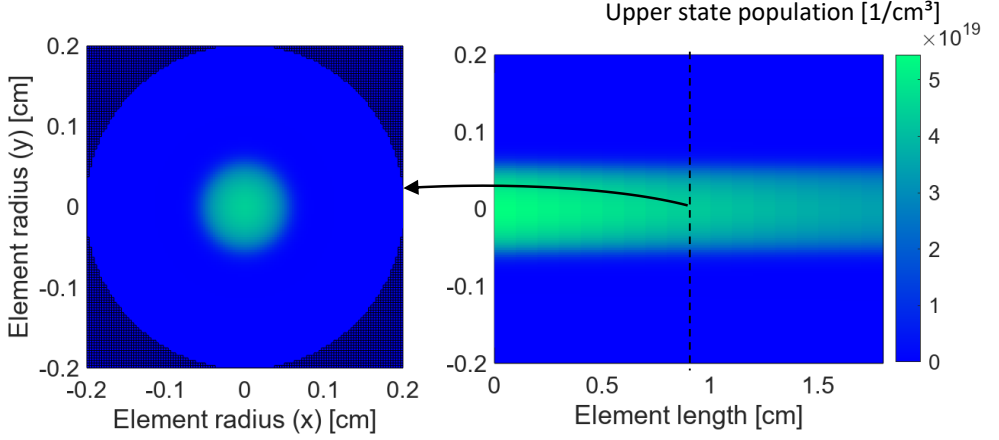


Figure 3.17: Simulated upper state population as three-dimensional distribution of the exemplary laser gain medium.

losses within the cavity approximated in the model. The power of stimulated emission  $P_{\text{stim}}$  can be calculated from the variation of laser field intensity in the  $z$ -direction, taking into account both forward and backward directions with

$$P_{\text{stim}} = \sum_{x,y}^{N_{x,y}} \left[ \left( \frac{\partial I_{L,\text{FW}}(x,y)}{\partial z} + \frac{\partial I_{L,\text{BK}}(x,y)}{\partial z} \right) \Delta x \Delta y \right]. \quad (3.37)$$

The power in spontaneous emission  $P_{\text{sp}}$  is calculated from the sum of the three-dimensional population distribution  $N_2(x, y, z)$  and the time of spontaneous decay  $\tau_{\text{sp}}$ :

$$P_{\text{sp}} = \sum_{x,y,z}^{N_{x,y,z}} N_2(x, y, z) \frac{\Delta z \Delta x \Delta y}{\tau_{\text{sp}}} \frac{hc}{\bar{\lambda}_{\text{sp}}}. \quad (3.38)$$

The power dissipated in heat  $P_h$  is then calculated as the difference from the total absorbed power with the power lost to stimulated and spontaneous emission.

Even though the accuracy of the simulation model for  $\text{Ho}^{3+}$ -doped gain media still has to be improved, the generalized model can already be useful for analyzing processes within the laser gain medium and potential optimization approaches. Figure 3.17 illustrates the simulated upper state population at a pump power of 45 W for a steady state solution. As the numerical model

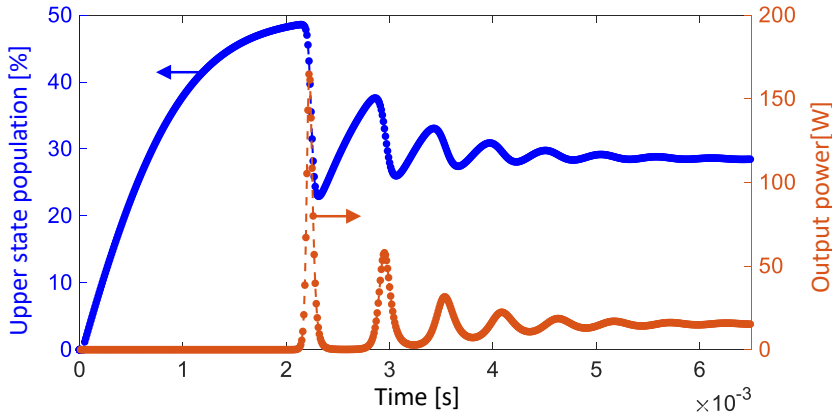


Figure 3.18: Simulated power spiking and the temporal evolution of the upper state population (in the crystal center) inside the laser gain medium at the start of CW laser operation.

propagates the electromagnetic field through the crystal, this three-dimensional distribution is computed and updated at each iteration. In contrast to analytical models, this allows for the simulation of asymmetric configurations, complex beam shapes and mode structures, and the resulting populations within the gain medium.

As discussed in section 3.2.1, a laser resonator in CW operation undergoes power spiking at the start of laser operation and these temporal processes can be investigated with this model approach. Figure 3.18 depicts the temporal evolution of output power and upper state population (averaged through the center of the crystal) for a pump power of 45 W. The build-up of inversion and resulting spiking can be seen in the simulation results, leading to an equilibrium and continuous power output of 22.3 W. When equilibrium is reached, and no further changes in output power and population are detected in the simulation, the end condition is achieved and the simulation concludes.

Considering the discrepancies between the simulation and experimental results observed in Fig. 3.16, the potential cause could be a lack of accuracy of the spectroscopic material data from Tab. 3.1, taken from literature. The geometric input data might also not be consistent with the experimental arrangement. Nevertheless, neither of these factors would likely result in such a significant difference in performance. The primary source of discrepancy comes from the energy level splitting of the  $\text{Ho}^{3+}$  ion, as previously illustrated in Fig. 3.4. The specific energy differences that separate the manifolds lead to the higher energy states  $^5I_5$  and  $^5I_6$ , which also

impact the  $^5I_7 \rightarrow ^5I_8$  laser transition. This can introduce additional losses in the laser gain medium as these levels are not considered in the basic rate equation model, thereby explaining the observed performance difference. One potential approach involves changing the rate of non-radiative decay  $W_{nr}$ , but this would only approximate the solution and fail to consider the actual mechanisms behind these losses. Consequently, the extension of the basic rate equation model to a more intricate model that accounts for all the relevant energy transitions of the active ion is required. It is worth noting that such an extension is not always necessary. For instance, the Yb<sup>3+</sup>:YALO laser gain medium previously discussed is solely influenced by the manifolds of the  $^2F_{7/2} \rightarrow ^2F_{5/2}$  transition. Thus, no other manifolds need to be considered and the generalized approach is sufficient as an accurate model. However, this is not a typical characteristic of laser ions, which makes Yb<sup>3+</sup> a popular choice for numerous applications. For example, the thin-disc laser systems mentioned earlier consist of a very thin active gain medium that requires a very high doping concentration for efficient performance, and Yb<sup>3+</sup> is particularly suitable for this purpose [99].

To improve the simulation accuracy of the Ho<sup>3+</sup>:YAG laser systems considered in this work, the extension to a specific rate equation model for Ho<sup>3+</sup>-doped gain media is discussed in the subsequent section.

## 3.4 Extended Simulation of Ho<sup>3+</sup>-Doped Gain Media

This section extends the generalized laser gain model of the preceding section for the specific case of Ho<sup>3+</sup>-doped gain media. By incorporating all relevant energy levels and transfer processes, as detailed in subsection 3.4.1, the simulation accuracy can be greatly improved. The comparison of this extended model with the generalized approach is discussed in subsection 3.4.2.

### 3.4.1 Specific Rate Equation Model for the Ho<sup>3+</sup> Ion

The preceding section demonstrated that the generalized approach might not provide sufficient accuracy when modeling laser gain media, particularly if more than two manifolds influence the laser process. This applies to Ho<sup>3+</sup>-doped gain media at the laser transition from the  $^5I_7 \rightarrow ^5I_8$

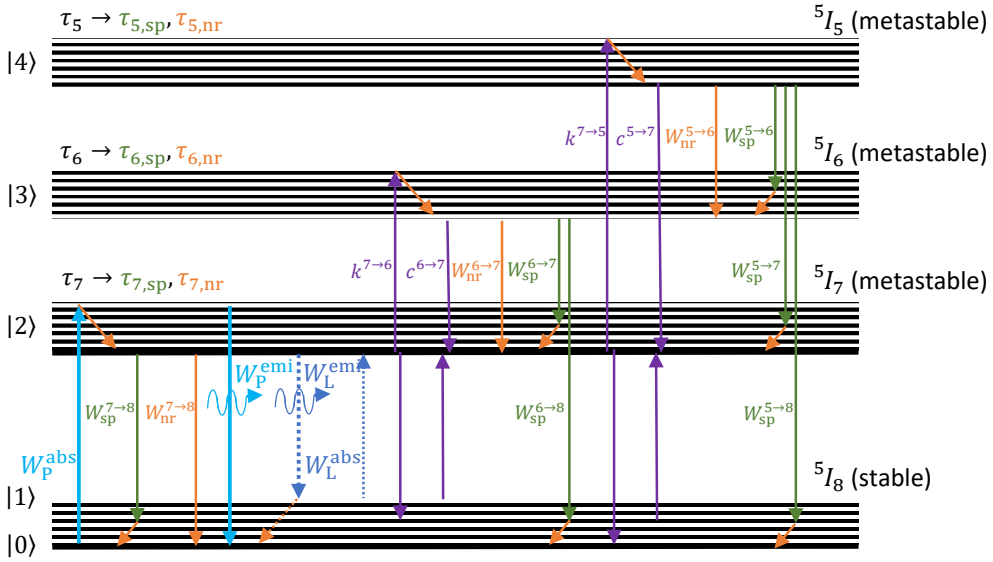


Figure 3.19: Energy transfer mechanisms of the specific rate equation approach for  $\text{Ho}^{3+}$ , including all energy levels relevant to the  $^5I_7 \rightarrow ^5I_8$  laser transition.

manifolds. In addition to the transition rates outlined in the generalized approach, nearest neighbor interactions such as energy transfer upconversion (ETU) and cross-relaxation can affect the population at the upper laser level  $^5I_7$  ( $|2\rangle$ ). Figure 3.19 presents the extended energy level diagram for the  $\text{Ho}^{3+}$  ion at the  $^5I_7 \rightarrow ^5I_8$  laser transition. The nearest neighbor processes, illustrated in purple, include the ETU from the  $^5I_7$  to  $^5I_6$  energy levels with the rate  $k_{7 \rightarrow 6}$  and the ETU from  $^5I_7$  to  $^5I_5$  with the rate  $k_{7 \rightarrow 5}$ . When two ions at the higher energy state  $^5I_7$  are in proximity, the energy of one ion may transfer to the other. Consequently, the donor ion relaxes to the ground state  $^5I_8$ , while the receiving ion ascends to a higher energy state (either  $^5I_6$  or  $^5I_5$ ) based on the initial energy of both ions in the  $^5I_7$  manifold [100]. The likelihood of this occurrence depends on the population of the  $^5I_7$  level  $N_{I_7}$ , with a higher population leading to increased ETU losses. The second relevant nearest neighbor interaction, cross relaxation, also depends on the population states. This interaction can be described as the inverse of the ETU process, where an ion pair at different energy levels allows the higher energy ion to transfer energy to the lower energy ion, resulting in both ions residing at the intermediate energy level. For  $\text{Ho}^{3+}$ , this can occur with the levels  $^5I_5$  or  $^5I_6$  and ground state  $^5I_8$ . Consequently, the ion pair settles in energy level  $^5I_7$ , with corresponding cross

relaxation rates of  $c_{5 \rightarrow 7}$  and  $c_{6 \rightarrow 7}$  [101]. The cross relaxation transition can be beneficial in the context of achieving inversion, for instance, the two-for-one process in thulium(III) oxide (Tm<sup>3+</sup>) significantly enhances laser efficiency when extracting 2  $\mu\text{m}$  output at pump wavelengths around 700 – 800 nm [102, 103].

Both, the rates of ETU and rates of cross relaxation are dependent on the doping concentration of the active laser ions, with higher ion concentrations leading to higher transition rates [104]. The relation of the rate of cross relaxation with the concentration of active ions is defined as [105]

$$c_{i \rightarrow j} = \frac{1}{\tau_i} \left( \frac{C_{\text{ion}}}{C_{i \rightarrow j, \text{cr}}} \right)^2 \frac{1}{N_{\text{total}}} , \quad (3.39)$$

where  $C_{\text{ion}}$  is the doping concentration of the material and  $C_{i \rightarrow j, \text{cr}}$  is a material dependent doping concentration for which the cross relaxation rate for energy level  $i$  equals the decay rate according to the upper state lifetime  $\tau_i$ . The ETU transition rate dependency on the doping concentration can be described by the following equation [106]:

$$k_{i \rightarrow j} = U_{i \rightarrow j} \frac{C_{\text{ion}}^2}{C_{\text{ion}}^2 + C_{i \rightarrow j, \text{etu}}^2} . \quad (3.40)$$

Here,  $C_{i \rightarrow j, \text{etu}}$  is a characteristic doping concentration for the ETU process from state  $i$  to state  $j$ , and  $U_{i \rightarrow j}$  is a corresponding rate of upconversion.

Resulting from the additional energy transfer processes at the higher energy levels  $^5I_5$  and  $^5I_6$ , the rate equations for Ho<sup>3+</sup>-doped gain media at the  $^5I_7 \rightarrow ^5I_8$  laser transition can be formulated as follows:

$$\frac{dN_{15}(x, y)}{dt} = N_{17}^2(x, y)k_{7 \rightarrow 5} - N_{15}(x, y) \left[ c_{5 \rightarrow 7}N_{18}(x, y) + \frac{1}{\tau_{15, \text{nr}}} + \frac{1}{\tau_{15, \text{sp}}} \right] , \quad (3.41)$$

$$\begin{aligned} \frac{dN_{16}(x, y)}{dt} = & N_{17}^2(x, y)k_{7 \rightarrow 6} - N_{16}(x, y) \left[ c_{6 \rightarrow 7}N_{18}(x, y) + \frac{1}{\tau_{16, \text{nr}}} + \frac{1}{\tau_{16, \text{sp}}} \right] \\ & + N_{15}(x, y) \left[ \frac{1}{\tau_{15, \text{nr}}} + \frac{1}{\tau_{15, \text{sp}}} \beta_{5 \rightarrow 6} \right] , \end{aligned} \quad (3.42)$$

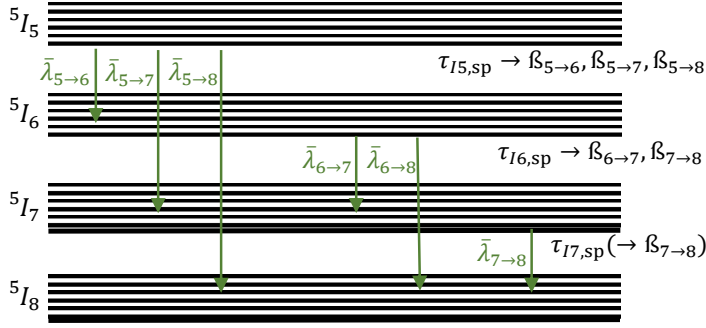


Figure 3.20: Branching ratios for the spontaneous decay of the  $\text{Ho}^{3+}$  ion at the energy levels of interest.

$$\begin{aligned}
 \frac{dN_{I7}(x, y)}{dt} = & -2N_{I7}^2(x, y)(k_{7 \rightarrow 6} + k_{7 \rightarrow 5}) - N_{I7}(x, y) \left[ \frac{1}{\tau_{I7, \text{nr}}} + \frac{1}{\tau_{7, \text{sp}}} \right] \\
 & + N_{I6}(x, y) \left[ 2c_{6 \rightarrow 7}N_{I8}(x, y) + \frac{1}{\tau_{I6, \text{nr}}} + \frac{1}{\tau_{I6, \text{sp}}} \beta_{6 \rightarrow 7} \right] \\
 & + N_{I5}(x, y) \left[ 2c_{5 \rightarrow 7}N_{I8}(x, y) + \frac{1}{\tau_{I5, \text{sp}}} \beta_{5 \rightarrow 7} \right] \\
 & + N_{I8}(x, y) [W_{\text{P}}^{\text{abs}}(x, y) + W_{\text{L}}^{\text{abs}}(x, y)] \\
 & - N_{I7}(x, y) [W_{\text{P}}^{\text{emi}}(x, y) + W_{\text{L}}^{\text{emi}}(x, y)] , \tag{3.43}
 \end{aligned}$$

$$\begin{aligned}
 \frac{dN_{I8}(x, y)}{dt} = & N_{I7}^2(x, y)(k_{7 \rightarrow 6} + k_{7 \rightarrow 5}) - N_{I8}(x, y) [c_{5 \rightarrow 7}N_{I5}(x, y) + c_{6 \rightarrow 7}N_{I6}(x, y)] \\
 & + N_{I7}(x, y) \left[ \frac{1}{\tau_{I7, \text{nr}}} + \frac{1}{\tau_{I7, \text{sp}}} \right] + N_{I6}(x, y) \frac{1}{\tau_{I6, \text{sp}}} \beta_{6 \rightarrow 8} \\
 & + N_{I5}(x, y) \frac{1}{\tau_{I5, \text{sp}}} \beta_{5 \rightarrow 8} - N_{I8}(x, y) [W_{\text{P}}^{\text{abs}}(x, y) + W_{\text{L}}^{\text{abs}}(x, y)] \\
 & + N_{I7}(x, y) [W_{\text{P}}^{\text{emi}}(x, y) + W_{\text{L}}^{\text{emi}}(x, y)] . \tag{3.44}
 \end{aligned}$$

Here, the energy transfer rates of the full system of equations result in the description of the populations  $N_{I5}$ ,  $N_{I6}$ ,  $N_{I7}$ , and  $N_{I8}$ . To solve the population differentials, a numerical time step  $\Delta t$  can be utilized. To accelerate reaching the steady state solution, an iterative solver such as the Newton or Runge-Kutta methods could be implemented as well [107, 108]. In addition to the previously discussed rates, the rate of spontaneous decay from higher energy states  $i$  is now represented by the branching ratio  $\beta_{i \rightarrow j}$  of this state. If the higher energy state permits decay

Table 3.2: Additional spectroscopic material parameters for Ho<sup>3+</sup>:YAG, used for the specific rate equation approach.

Parameters	Values	Units
$\tau_{15,\text{sp}}$	$4.4E-3$	s
$\tau_{16,\text{sp}}$	$3.5E-3$	s
$\tau_{17,\text{sp}}$	$7.9E-3$	s
$\tau_{15,\text{nr}}$	$1.3E-6$	s
$\tau_{16,\text{nr}}$	$4.5E-5$	s
$\tau_{17,\text{nr}}$	0.0478	s
$k_{7 \rightarrow 5}$ (@1at.%)	$3.8E-18$	cm <sup>3</sup> /s
$k_{7 \rightarrow 6}$ (@1at.%)	$0.4E-18$	cm <sup>3</sup> /s
$c_{5 \rightarrow 7}$ (@1at.%)	$1.1E-17$	cm <sup>3</sup> /s
$c_{6 \rightarrow 7}$ (@1at.%)	$2.6E-18$	cm <sup>3</sup> /s

to multiple lower energy states, the probability of decay is divided among the options [90]. Figure 3.20 illustrates this behavior for the Ho<sup>3+</sup> ion at the relevant energy states, along with the corresponding mean wavelengths of spontaneous decay  $\bar{\lambda}_{i \rightarrow j}$ .

### 3.4.2 Submodel Validation

The validation of the extended laser model for Ho<sup>3+</sup>-doped gain media is conducted for the same Ho<sup>3+</sup>:YAG laser resonator used for the generalized model in section 3.3.2. The comprehensive spectroscopic data for the Ho<sup>3+</sup>:YAG gain medium at the  $^5I_7 \rightarrow ^5I_8$  laser transition is listed in Tab. 3.2. Taking into account the spectroscopic data for Ho<sup>3+</sup>:YAG of the generalized model from Tab. 3.1, the extended laser gain medium can be modeled, encompassing all relevant laser processes. The table comprises the lifetimes of spontaneous decay  $\tau_{i,\text{sp}}$  and non-radiative decay  $\tau_{i,\text{nr}}$  at the manifolds of higher energy [90, 109]. Furthermore, the rates of ETU  $k_{i \rightarrow j}$  [100, 110, 111] and cross relaxation  $c_{i \rightarrow j}$  are included [93, 101].

Table 3.3: Branching ratios and mean wavelengths of spontaneous decay for  $\text{Ho}^{3+}:\text{YAG}$ , used for the specific rate equation approach.

Transition	Branching ratio $\beta_{i \rightarrow j}$	Mean wavelength $\bar{\lambda}_{i \rightarrow j}$ in nm
$^5I_5 \rightarrow ^5I_6$	0.064	3917.0
$^5I_5 \rightarrow ^5I_7$	0.542	1655.0
$^5I_5 \rightarrow ^5I_8$	0.394	903.0
$^5I_6 \rightarrow ^5I_7$	0.142	2866.0
$^5I_6 \rightarrow ^5I_8$	0.858	1174.0
$^5I_7 \rightarrow ^5I_8$	1.	1988.0

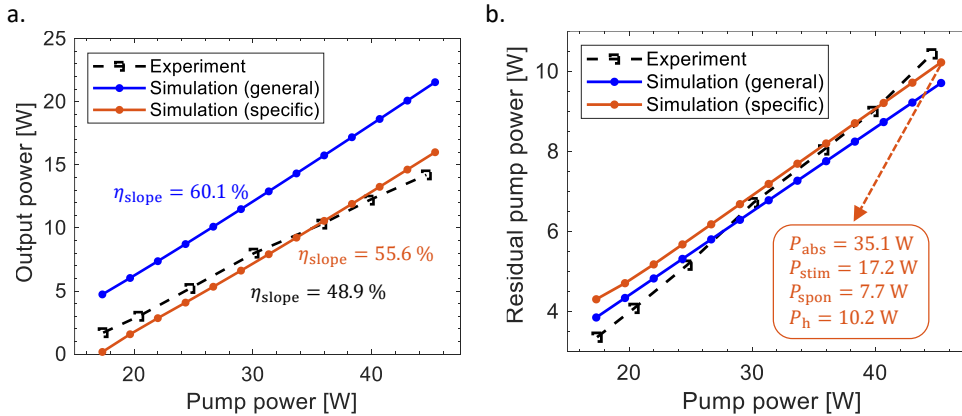


Figure 3.21: Comparison of simulated and experimental power curves (a) and residual pump powers (b) for the exemplary linear resonator, including the simulated results for the generalized approach (blue) and the specific rate equation model (orange).

The branching ratios and corresponding mean wavelengths for this laser transition in  $\text{Ho}^{3+}:\text{YAG}$  are listed in Tab. 3.3 [90, 112]. All parameters are taken from the referenced literature.

With the material parameters for extended model, the exemplary linear resonator detailed in section 3.6 can be simulated again for comparison with the generalized model. The output power (a) and residual pump power (b) versus incident pump power are illustrated in Fig. 3.21. The resonator simulation spans a pump power range of 17.5 to 45 W, including the results from

the general model (in blue), the results from the specific model (in orange), and the experimental results (in black). In comparison to the general model, the output power evolution over pump power aligns more closely with the experimental data, displaying a reduced slope efficiency of  $\eta = 55.6\%$ . At a pump power of 45 W, 35.1 W is absorbed by the laser gain medium, resulting in a residual pump power of 9.9 W. The absorbed power is distributed as  $P_{\text{stim}} = 17.2$  W for stimulated emission,  $P_{\text{spon}} = 7.7$  W for spontaneous emission, and  $P_h = 10.2$  W dissipated as heat within the crystal. Compared to the general model, the stimulated emission has notably decreased from  $P_{\text{stim}} = 23.1$  W to  $P_{\text{stim}} = 17.2$  W, while the power dissipated as heat has increased from  $P_h = 4.0$  W to  $P_h = 10.2$  W. The residual pump power and spontaneous emission experienced only minor changes, with the power from spontaneous decay now divided into three levels at  $P_{17,\text{spon}} = 7.5$  W,  $P_{16,\text{spon}} = 0.18$  W, and  $P_{15,\text{spon}} = 0.02$  W. The total power of spontaneous decay for each manifold is calculated as follows:

$$P_{15,\text{spon}} = \sum_{x,y,z}^{N_{x,y,z}} N_{15}(x,y,z) \frac{\Delta z \Delta x \Delta y}{\tau_{15,\text{sp}}} \left( \frac{hc}{\bar{\lambda}_{5 \rightarrow 6} \beta_{5 \rightarrow 6}} + \frac{hc}{\bar{\lambda}_{5 \rightarrow 7} \beta_{5 \rightarrow 7}} + \frac{hc}{\bar{\lambda}_{5 \rightarrow 8} \beta_{5 \rightarrow 8}} \right), \quad (3.45)$$

$$P_{16,\text{spon}} = \sum_{x,y,z}^{N_{x,y,z}} N_{16}(x,y,z) \frac{\Delta z \Delta x \Delta y}{\tau_{16,\text{sp}}} \left( \frac{hc}{\bar{\lambda}_{6 \rightarrow 7} \beta_{6 \rightarrow 7}} + \frac{hc}{\bar{\lambda}_{6 \rightarrow 8} \beta_{6 \rightarrow 8}} \right), \quad (3.46)$$

$$P_{17,\text{spon}} = \sum_{x,y,z}^{N_{x,y,z}} N_{17}(x,y,z) \frac{\Delta z \Delta x \Delta y}{\tau_{17,\text{sp}}} \frac{hc}{\bar{\lambda}_{7 \rightarrow 8} \beta_{7 \rightarrow 8}}. \quad (3.47)$$

The change in power distribution compared to the general model suggests that the nearest neighbor processes implemented in the specific model introduce additional non-radiative decay rates from the higher energy states. This is attributed to the ETU process combined with the considerably shorter non-radiative lifetimes of the  $^5I_5$  and  $^5I_6$  levels, compared to the respective spontaneous decay lifetimes.

Considering the discrepancy in simulated output power between the general and specific models, the simulated powers express a large offset over the whole pump power range. This suggests that the implementation of ETU leads to a relatively constant decrease in output power over the power curve. This can be explained by considering the change in average upper state population along the center of the crystal, as illustrated in Fig. 3.22. Above the laser threshold, the rate

of stimulated emission becomes dominant. The laser reaches a steady-state condition where the rate of photon emission balances the rate of photon absorption and other losses. Given that the ETU process is dependent on the population of the upper laser level, the constant inversion results in a constant population drain to the higher energy levels  ${}^5I_5$  and  ${}^5I_6$  – which leads to a constant reduction in stimulated emission. It is noteworthy that a decline in upper state population with rising pump power can be observed in Fig. 3.22 for both model implementations, even though it was mentioned that this should be constant above threshold. However, this is only true for a one-dimensional model, with this three-dimensional approach, the decline can be attributed to beam diameter changes across the pumping range, introduced by a gain guiding effect [113]. This behavior is explained in more detail in section 3.6, where the laser intensity within the resonant cavity is discussed.

The implementation of the specific rate equation model for  $\text{Ho}^{3+}$ -doped gain media has significantly improved the performance for these laser systems, as evidenced with the example of  $\text{Ho}^{3+}:\text{YAG}$  [114]. Nonetheless, there are still some discrepancies with the experimental results, which will be addressed in the subsequent chapter 4 by taking into account thermal effects as well. Furthermore, the model presented in this section is specifically designed for the  $\text{Ho}^{3+}$  ion at the  ${}^5I_7 \rightarrow {}^5I_8$  laser transition. Any additional active ion or laser transitions may express unique behavior and must be implemented accordingly.

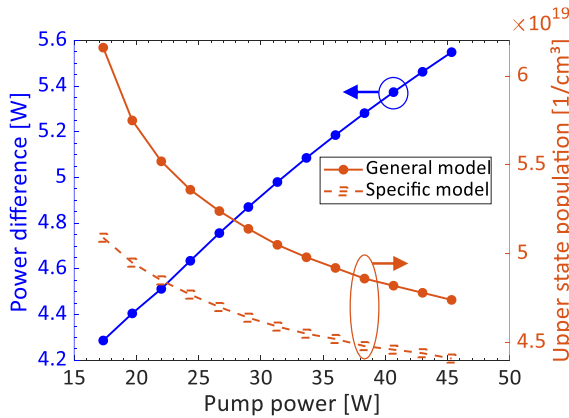


Figure 3.22: Output power difference of the generalized model compared with the specific model for  $\text{Ho}^{3+}:\text{YAG}$  (blue curve). The corresponding upper state population is plotted with the orange curves.

## 3.5 Advanced Laser Media Dynamics

This section discusses the implementation of advanced laser gain modeling concepts. This includes the extension to a spectrally resolved model, as described in subsection 3.5.1, as well as the implementation of a concept regarding the modeling of pulsed laser systems in subsection 3.5.2.

### 3.5.1 Extension to a Spectrally Resolved Model

In the previous sections, the combination of the laser model and beam propagation method was restricted to the propagation of a single vectorial electromagnetic field  $\mathbb{E}_{x,y}(x, y)$ . This field represents a single monochromatic wavelength, while in a real laser system, the pump and laser wavelengths are rarely near monochromatic. To further improve the presented simulation model, a numerical extension of the spectrum is implemented. Although the FFT-BPM itself is restricted to the propagation of monochromatic fields, the simultaneous propagation of a spectral field array  $\mathbb{E}_{x,y}(x, y, s)$  with a number of spectral fields  $s \rightarrow s_\lambda$  can approximate spectral laser behavior, provided the spectral resolution  $\Delta\lambda$  is sufficiently small.

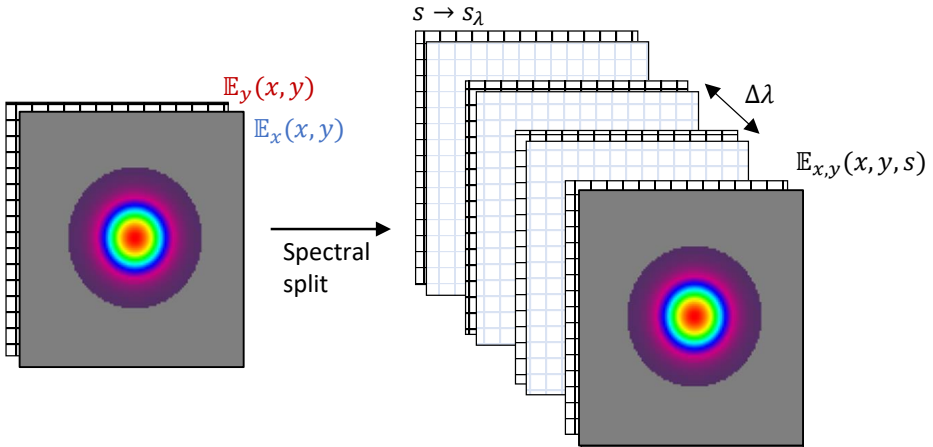


Figure 3.23: Schematic illustration regarding the spectral splitting of the electromagnetic field.

The total laser power is then composed of the sum of the spectral components such that

$$P_{\text{total}} = \sum_s^{s_\lambda} \sum_{x,y}^{N_{x,y}} I_{x,y}(x, y, s) \Delta x \Delta y. \quad (3.48)$$

The spectral splitting of the electromagnetic field is depicted schematically in Fig. 3.23. To estimate the resulting spectrum from a given laser system, the main contributing factors leading to a specific output spectrum need to be analyzed. While the propagation of the spectral field components is one aspect that may influence the spectral behavior, given that destructive interference of the standing wave pattern inside a linear resonator leads to longitudinal mode formation as discussed in section 3.2.2, other influences must be considered. The influence of optical elements which specifically interact with the laser spectrum, like etalons or spectral coating dependencies, is incorporated into the respective element operators (see section 2.4.3). For bulk elements with dispersive media, the relationship between the refractive index and wavelength can be described by the Sellmeier equation as follows [115]:

$$n^2(\lambda) = 1 + \sum_j \frac{B_j \lambda^2}{\lambda^2 - C_j}, \quad (3.49)$$

where  $B_j$  and  $C_j$  are experimentally determined Sellmeier coefficients, specific to each transparent material.

This section will focus on the influence of the laser gain medium on the spectral output of the laser, where the primary influence comes from the spectrally resolved cross sections. This discretization of an overarching wavelength group is shown as a schematic example for  $\lambda_i = 1908 \text{ nm}$  in Fig. 3.24. In this case, the spectrum is divided into five spectral steps ( $s_\lambda = 5$ ) with a spectral resolution  $\Delta\lambda = 0.25 \text{ nm}$ , leading to the interaction of the fields with the spectrally resolved cross sections  $\sigma_{a,e}(\lambda)$  of  $\text{Ho}^{3+}:\text{YAG}$  as the laser gain medium. In contrast to the monochromatic model, where energy transition rates were limited to pump and laser wavelengths as per Eqs. (3.28) - (3.31), the rate equation models are extended to encompass arbitrary absorption and emission rates as follows:

$$W_{\text{abs}}(x, y) = \sum_i^{i_\lambda} \sum_s^{s_\lambda} [I_{\text{FW}}(x, y, i, s) + I_{\text{BK}}(x, y, i, s)] \frac{\lambda_{i,s}}{hc} \sigma_a(\lambda_{i,s}), \quad (3.50)$$

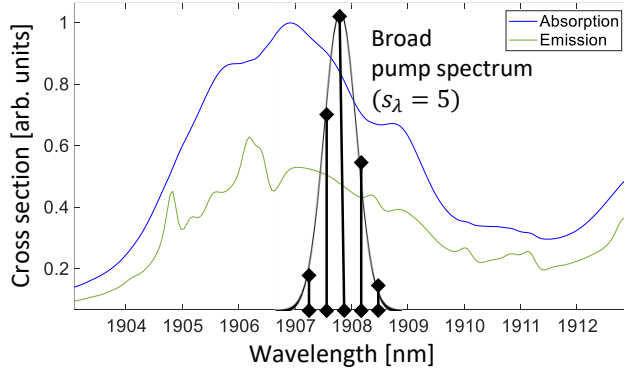


Figure 3.24: Discretization of an exemplary spectrum into the spectral components with the corresponding absorption and emission cross sections of  $\text{Ho}^{3+}:\text{YAG}$ .

$$W_{\text{emi}}(x, y) = \sum_i^{i_\lambda} \sum_s^{s_\lambda} [I_{\text{FW}}(x, y, i, s) + I_{\text{BK}}(x, y, i, s)] \frac{\lambda_{i,s}}{hc} \sigma_e(\lambda_{i,s}), \quad (3.51)$$

where  $i \rightarrow i_\lambda$  signifies the sum of all overarching light fields in the system, including the pump and laser fields. These generalized rates of laser energy transition,  $W_{\text{abs}}$  and  $W_{\text{emi}}$ , can therefore replace the specific rates for pump and laser transition,  $W_{\text{L},P}^{\text{abs}}$  and  $W_{\text{L},P}^{\text{emi}}$ , in the rate equations (3.41) - (3.44). The  $\text{Ho}^{3+}:\text{YAG}$  cross section data for the  ${}^5I_7 \rightarrow {}^5I_8$  laser transition is shown in Fig. 3.25 from 1800 nm to 2200 nm. The data is derived from literature references [94, 116] and displayed as normalized values relative to the emission peak. For this example laser resonator system, the pump wavelength is known to be 1908 nm and the corresponding cross section data can be discretized according to the spectral linewidth of the pump. In the case of a laser amplifier, the signal wavelength can be discretized in the same way.

For the laser wavelength of resonators, a special approach has to be taken, because the spectrum will emerge from the gain process and is unknown at the start of the simulation. In the context of  $\text{Ho}^{3+}:\text{YAG}$ , the output spectrum could potentially be located anywhere where the emission cross section significantly surpasses the absorption cross section, as illustrated in Fig. 3.25. To obtain a definitive result, the whole spectral range of interest from 2000 nm to 2150 nm has to be included in the simulation. The corresponding spectral resolution  $\Delta\lambda$  must be selected to be sufficiently small, to resolve all relevant emission peaks.

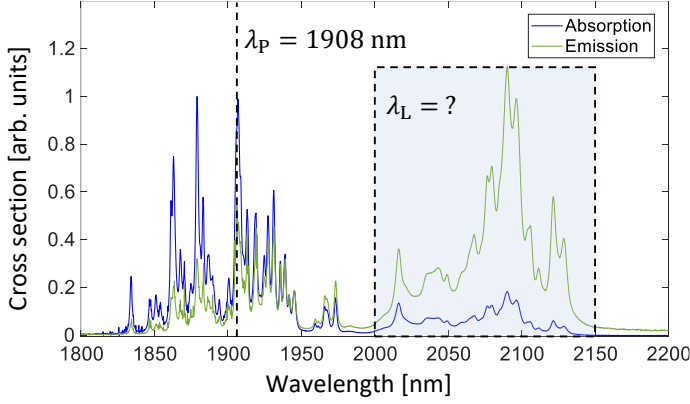


Figure 3.25: Emission and absorption cross sections of  $\text{Ho}^{3+}:\text{YAG}$  for the  ${}^5I_7 \rightarrow {}^5I_8$  laser transition near room temperature (300 K).

At the start of laser operation, the pumping of the gain medium results in spontaneous emission, initiated by quantum noise. A fraction of the generated spontaneous emission will couple into the resonator modes and undergo amplification through the feedback condition of the resonator. The correlation of spontaneous emission to the manifold lifetimes is described by the Judd-Ofelt theory [117, 118], which connects the intensity and relation of electron transitions within the 4f shell of rare-earth ions [119]. For the purposes of this model, a simplified method to laser initiation has been adopted. The spectrally dependent fluorescence power from manifold  $m$  is defined for a single voxel of the laser gain medium with volume  $V_p = \Delta x \Delta y \Delta z$  as follows:

$$P_{\text{sp},m}(x, y, z, \lambda) = \frac{N_m(x, y, z)}{\tau_{m,\text{sp}}} \frac{hc}{\lambda} \frac{\Delta\lambda \sigma_e(\lambda)}{\int \sigma_e(\lambda) d\lambda}. \quad (3.52)$$

In this case, the integral over the emission cross section represents the spectral portion of fluorescence power, dependent on the spectral resolution  $\Delta\lambda$ . While this equation describes the total fluorescence power emitted from a voxel, only a fraction along the optical axis will be coupled into the feedback of the resonator.

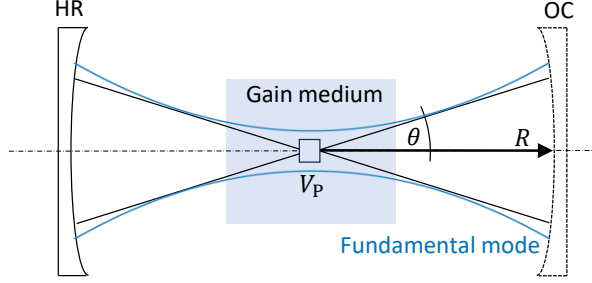


Figure 3.26: Schematic illustration of the geometric coupling of incoherent fluorescence to the laser mode at the initiation of laser operation from quantum noise.

This is heavily dependent on the resonator geometry and is approximated by an angular coupling factor  $\delta$ , resulting in the coupled fluorescence power from all contributing manifolds  $m \rightarrow M$ :

$$P_{\text{sp}}(x, y, z, \lambda) = \sum_m^M P_{\text{sp},m}(x, y, z, \lambda) \exp(-\delta), \quad (3.53)$$

with

$$\delta = \frac{2\pi R^2(1 - \cos(\theta))}{4\pi R^2}. \quad (3.54)$$

The angular coupling factor depends on the spherical cap, assumed to couple into the mode with angle  $\theta$ , relative to the full sphere that spans the resonator with radius  $R = L/2$  (assuming a central crystal position). A schematic illustration of this geometric coupling factor is depicted in Fig. 3.26. The fraction of power  $P_{\text{sp}}(x, y, z, \lambda)$  is incorporated into the corresponding spectral fields propagating through the gain medium at each slice  $\Delta z$  from  $z \rightarrow N_z$ , leading to an approximate coupling from spontaneous emission into the laser modes. In addition to the laser initiation from quantum noise, the fluorescence of the laser crystal can also affect the laser performance once feedback has been established. For instance, the reabsorption of fluorescence results in an effective broadening of the pumped zone in the transversal direction of the gain medium [120, 121]. However, the implementation of this effect into the model would require a three-dimensional simulation of the incoherent fluorescence, which would require an extensive

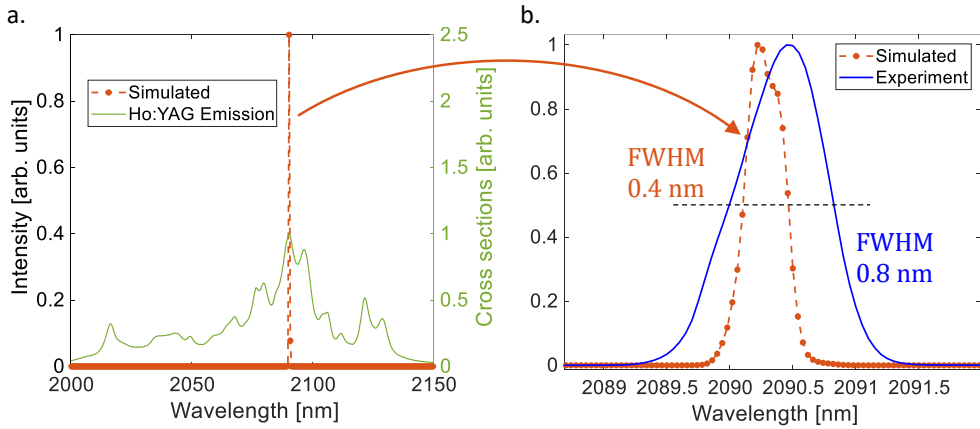


Figure 3.27: Simulated output spectrum of an exemplary linear resonator. On the left (a), simulated for a broad spectral range, and on the right (b), simulated with higher resolution and compared with the spectrum measured in experiment.

computational effort. Since the impact on laser performance from this effect is assumed to be small, this is not further investigated.

The simulated steady-state solution to the spectral output of the exemplary resonator discussed in section 3.6 is presented in Fig. 3.27. On the left (a), the spectrum is simulated over the complete spectral range of interest from 2000 nm to 2150 nm. The spectrum shows single-line emission at the highest peak of emission cross section at approximately 2090 nm. The right graph (b) presents the spectral peak simulated with higher resolution (orange), as well as the spectrum measured in experiment (blue) for this specific operation point. While the spectral FWHM is not exactly replicated, the emission at the same spectral line is already a useful result. The difference in FWHM can be explained by a convergence issue with the numerical approach. Figure 3.28 illustrates the convergence of a single spectrally resolved simulation, where the output power convergence is plotted in black, while the maximum change in spectral distribution is depicted in blue. The convergence condition of stable output power is achieved well before the output spectrum reaches equilibrium. The narrowing of the spectral output is shown as an inset in the graph. This behavior leads to an issue with the model, where with enough iterations, a single longitudinal mode will emerge; which does not match the behavior observed in experiment.

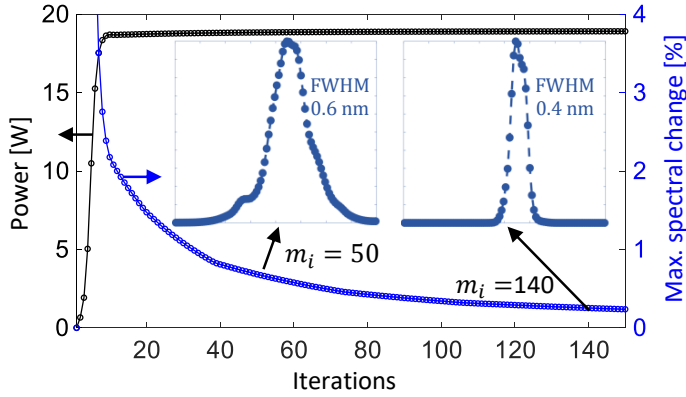


Figure 3.28: Comparison of the iterative convergence for output power and the maximum change in spectral distribution.

The longitudinal mode structure of linear resonators has been discussed in section 3.2.2; for the case of this exemplary resonator a longitudinal mode number of  $M = 55$  is calculated at a gain bandwidth of  $\Delta G = 27.5$  GHz, which corresponds to the spectrum measured in experiment. When the resolution of the model is chosen high enough and a mode extinction approach is implemented for the standing wave interference, the longitudinal mode structure could be implemented with an FFT-BPM model approach [122]. However, the modeling of longitudinal modes with the FFT-BPM is not deemed helpful for the spectral convergence issue. In the actual resonator, mode competition effects, which are challenging to model, will broaden the resulting spectrum and may lead to temporally dynamic behavior [123, 124]. For instance, in a linear resonator, a distinct standing wave pattern is formed inside the cavity for each longitudinal mode. This leads to spatial hole burning, where the dominant mode will strongly saturate its gain at the peaks of the standing wave; while another mode sees reduced gain saturation as its standing wave pattern is formed at different locations. Since the FFT-BPM model used in this simulation approach operates on a macroscopic level far above the wavelength, these effects can not be considered. An approximate mode competition loss factor could be applied to approximate these effects, however, this would have to be done for each laser system specifically. Owing to these limitations, the spectral model of resonators is primarily suitable to determine the position of spectral peaks rather than estimating the spectral width.

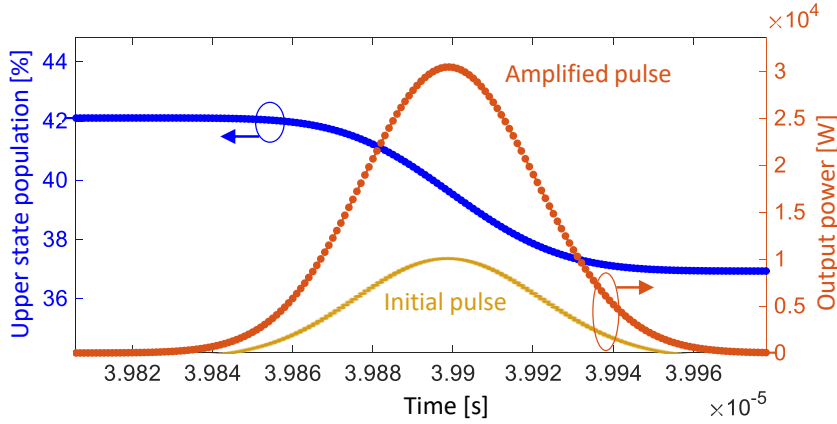


Figure 3.29: Simulated temporal behavior in an exemplary amplifier with pulsed signal.

### 3.5.2 Implementation of Pulsed Operation by Q-switching

While up until now, laser systems could already be modeled temporally, the specific case of pulse generation and amplification has not yet been discussed. First, the amplification of pulsed seed signals in laser amplifiers is considered, as this presents the simplest case of pulsed behavior regarding this work. The model for pulsed amplifiers is based on discretizing the seed pulse to be amplified. This can be achieved without modifying the existing model, by mapping the incoming pulse power  $P_{\text{ini}}(t)$  to the corresponding time step according to

$$E_{\text{ini}} = \sum_t^{\tau_{\text{FW}}} P_{\text{ini}}(t) \Delta t, \quad (3.55)$$

where the initial pulse energy  $E_{\text{ini}}$  is equivalent to the sum of the pulse power at each time step  $\Delta t$  over the full temporal width of the pulse  $\tau_{\text{FW}}$ . The time resolution used in the rate equation models must be sufficiently small to resolve the pulse passing through the amplifier and account for the time-dependent gain properties of the medium. Moreover, several pulses may need to be simulated until equilibrium is achieved and the convergence condition is met. Figure 3.29 illustrates the simulated temporal behavior in an exemplary amplifier with a pulsed signal. Here, an initial pulse (light orange curve) with peak power  $P_{\text{peak}} = 10$  kW is amplified to approximately  $P_{\text{peak}} = 30$  kW (orange curve), with the average upper state population in the crystal center shown in blue. In the absence of a pulse passing through the crystal, the constant

pump absorption creates inversion, which is quickly depopulated by stimulated emission from the subsequent pulses. A pulsed  $\text{Ho}^{3+}$ :YAG amplifier system, modeled with this approach, is described in section 5.4. If ultrashort pulses are to be simulated, the BPM needs to be adjusted for rapid propagation variations owing to the short temporal width [125, 126], although this will not be relevant for the model approach of this work.

In contrast to pulse amplification, pulse generation in a laser resonator requires further adaptation of the presented model. There exist several methods to generate pulsed output in laser resonators [3]:

- *Gain switching*, through rapid modulation of the laser gain via a change in pump power (for example, using flash lamps).
- *Mode-locking*, where ultrashort pulses can be achieved by constructive interference of multiple longitudinal modes in a broadband resonator.
- *Q-switching*, where modulation of resonator round-trip losses, defined by the Q-factor, is used to deplete the stored energy of the gain medium in a short time span.

While there are even more techniques to achieve laser pulse generation, this work will focus on the generation process by active Q-switching only. This method is utilized for the generation of pulses in the nanosecond regime in bulk solid-state lasers, which will be employed with the optimized  $\text{Ho}^{3+}$ :YAG system described in section 5.3. The Q-factor, after which the technique is named, relates the energy stored in the cavity  $E_{\text{st}}$  to the energy loss per round-trip  $E_{\Lambda}$  [17, 127]:

$$Q = 2\pi \frac{E_{\text{st}}}{E_{\Lambda}} \approx 2\pi \frac{c}{\lambda_L} \frac{T_{\text{RT}}}{\Lambda_M}. \quad (3.56)$$

The fundamental concept involves the insertion of a modulating element into the resonant cavity to introduce temporally varying losses. In the low Q regime, the laser threshold should not be reached, allowing energy to accumulate in the laser gain medium through constant pumping. At a certain point, the modulator losses are switched off and laser feedback is reestablished, transitioning to the high Q zone. For weakly damped oscillations, the Q-factor can also be expressed by the round-trip time  $T_{\text{RT}}$  and the power losses introduced by the modulator element at each round-trip  $\Lambda_M$ . However, at the regime of the resonators discussed in this work, the value of the Q-factor itself has little information value regarding the Q-switching process and corresponding output optimization [127].

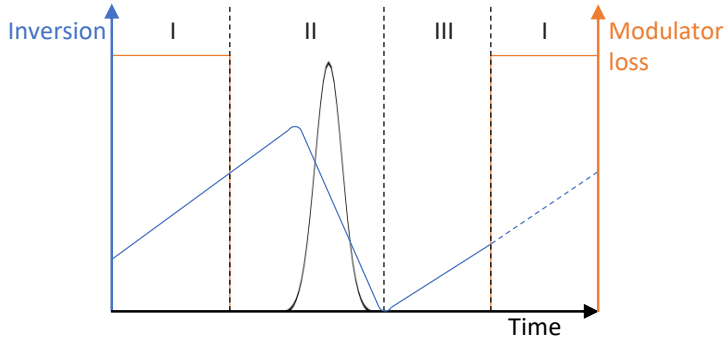


Figure 3.30: Schematic description of the temporal phases of pulse generation utilized with the model.

To incorporate the temporal resonator loss into the model approach, an operator for the modulator element is added. When the resonator is simulated with temporal resolution  $\Delta t$ , the pulse generation process can be divided into three phases [128, 129]. Phase I corresponds to the low Q-factor zone, while phases II and III represent the high Q-factor zone, where energy is extracted to form a pulse. Figure 3.30 schematically illustrates the behavior of inversion and intracavity power across the three phases. The resonator gain per round-trip, as described in Eq. (3.15), is now modified to account for modulator losses as follows:

$$G(t) = \frac{1}{\sqrt{R_{HR}(1 - \Lambda)(1 - \Lambda_M(t))R_{OC}}} . \quad (3.57)$$

The losses are either active or not, depending on the phase.

$$\Lambda_M(t) \begin{cases} > 0, & \text{for phase I} \\ = 0, & \text{for phase II and III} \end{cases} \quad (3.58)$$

Furthermore, the time step  $\Delta t$  can be adjusted for the different phases. Although all phases could be calculated with the smallest time step necessary, a larger time step can be selected for phases I and III to achieve a reasonable simulation time. Depending on the specific system parameters, a relatively long time span between each subsequent pulse has to be covered. Here, a larger time step should be used without compromising accuracy. If the time step is chosen too large, the rate equation model may result in numeric errors, so a balance has to be found.

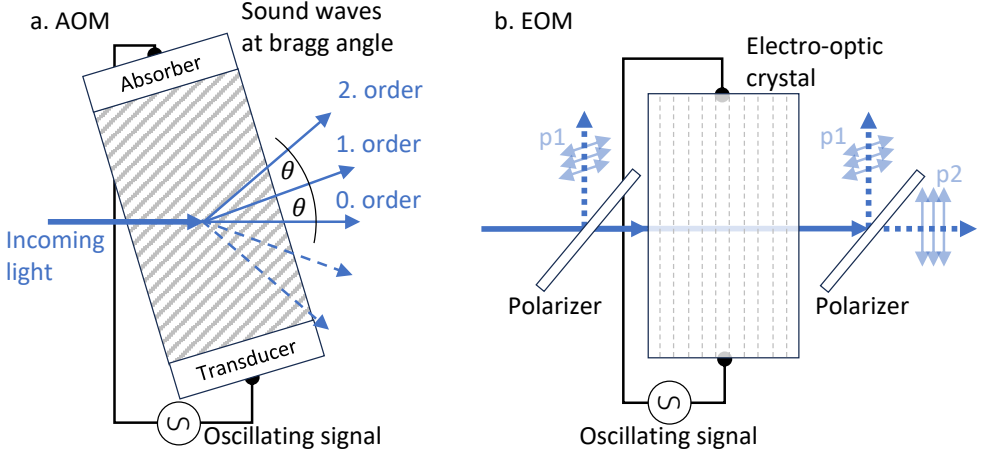


Figure 3.31: Schematic description of the modulator types relevant to this work. The diffraction of a light beam passing an AOM is shown on the left (a), while the polarization dependent behavior of an EOM is shown on the right (b).

In phase II, the time step is chosen equal to the round-trip time  $T_{RT} = L_{RT}/c$  for the highest possible resolution of pulse formation. To summarize:

$$\Delta t \begin{cases} > T_{RT}, & \text{for phase I} \\ = T_{RT}, & \text{for phase II} \\ > T_{RT}, & \text{for phase III} \end{cases} \quad (3.59)$$

The specific implementation of the modulator element varies depending on the type of modulator used. This work focuses on active Q-switching with acousto-optic modulators (AOMs) and electro-optic modulators (EOMs), which utilize different methods to achieve loss modulation. Figure 3.31 provides a schematic depiction of the two modulator types. The AOM operates on the principle of Bragg diffraction, where a sound wave with wavelength  $\lambda_{AO}$  is generated within an acousto-optic material (e.g., glass). This sound wave, typically in the radio frequency (RF) regime, compresses the material, leading to an oscillating refractive index distribution that scatters the incoming light. The sound wave is produced by a transducer at one end of the material and absorbed at the other end. Essentially, no signal is applied in the high Q-factor zone, allowing for an undisturbed passage of light. In the low Q-factor zone, an oscillating signal is applied, resulting in the diffraction of a beam at Bragg angle with a diffraction order of

$2\lambda_{AO}\theta = m\lambda_L$ . The higher order content of light exits the resonant cavity, creating the desired loss and preventing the laser oscillation within the cavity [44]. When modeling this device, the frequency of Q-modulation  $f_Q = 1/T_Q$ , single pass loss  $\Lambda_M$ , and loss time interval  $I_Q$  are used as defining parameters. The loss time interval  $I_Q$  relates the time in the low Q zone  $T_{lowQ}$  to the time of a full modulation cycle  $T_Q$  by

$$I_Q = \frac{T_{lowQ}}{T_Q} . \quad (3.60)$$

Simulating the actual diffracting behavior offers little benefit, as the light diffracted at higher orders does not follow the paraxial beam approximation and cannot be propagated with the same FFT-BPM approach.

The EOM functions based on the principle of polarization modulation. An oscillating signal is applied to an electro-optic crystal to alter the anisotropic behavior of the crystal. Essentially, the anisotropy of the refractive index is modulated to achieve a time-dependent waveplate functionality. Depending on the length of the crystal and the strength of the applied signal, polarization rotation analogous to a half-wave or quarter-waveplate can be realized. If additional linear polarizers are positioned before and after the crystal, the incoming beam may be reflected depending on the Q-modulation zone [44]. The element can be implemented in a manner similar to the waveplate transfer function described in section 2.4.3, with temporal modulation added. Compared to an AOM, higher single pass losses  $\Lambda_M$  can be achieved and the device can typically be operated at a lower modulation frequency. For both types of modulators, the desired loss time interval  $I_Q$  and signal pattern in the actual device is controlled by a function generator.

When the modulator element is incorporated in the full simulation approach, actively Q-switched laser resonators and their temporal behavior can be modeled with high precision. The comparison of simulated pulse output parameters with results measured experimentally is shown in Fig. 3.32. The evolution of pulse peak power over pump power is plotted in blue, while the evolution of pulse FWHM is plotted in orange. The pulsed results demonstrate good agreement across the entire pumping range, indicating that the pulsed model is effective in predicting Q-switched resonators. The laser system used for this example is a linear  $\text{Ho}^{3+}$ :YAG resonator designed for power scaling, including an AOM for Q-factor modulation. This system is the same as the one detailed in section 5.3 (tuned to 2090 nm), where the optimization process of said laser is discussed.

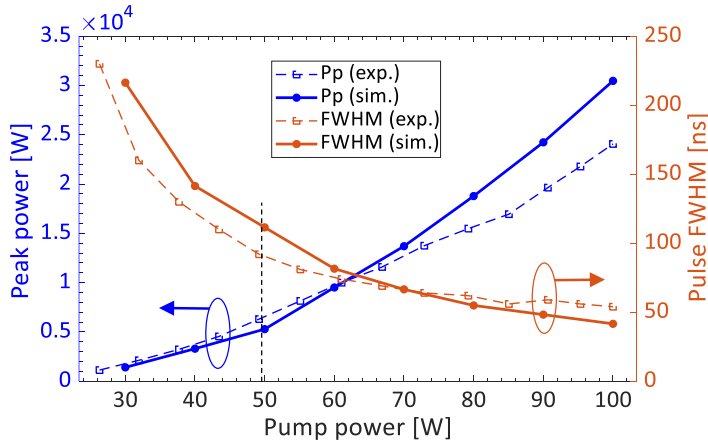


Figure 3.32: Comparison of simulated results with experimental data regarding the pulse characteristics with rising pump power. The change in peak power is plotted in blue, while the change in pulse FWHM is plotted in orange.

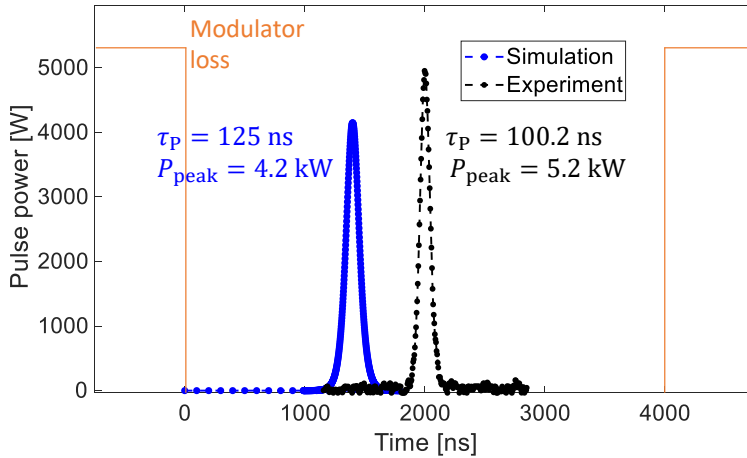


Figure 3.33: Temporal behavior of a single pulse generated with AOM Q-switching. Comparison of the simulated behavior (in blue) with a pulse measured in experiment (in black).

The specific temporal behavior for a single pulse is depicted in Fig. 3.33. The pulses shown are generated using the same laser resonator as the preceding graph at a pump power of 50 W (Fig. 3.32, black dotted line). The time axis is represented in relation to the initiation of the modulator loss ( $t = 0$ , plotted in orange), which in the context of the experiment, corresponds to

the signal of the function generator. The time interval of the high Q-factor zone  $T_{\text{highQ}} \approx 4000$  ns, as seen in the graph, can be determined from the pulse repetition rate  $f_{\text{rep}} = 50$  kHz and a loss time interval  $I_Q = 0.8$ , as per Eq. (3.60). The pulse form is well replicated by the model, with the simulated pulse exhibiting a peak power  $P_{\text{peak}} = 4.2$  kW at a FWHM  $\tau_P = 125$  ns. The peak power of the pulse measured experimentally is calculated using Eqs. (3.16) and (3.17) from the average power and intensity measured in arbitrary units. The measured pulse displays a peak power  $P_{\text{peak}} = 5.2$  kW at a FWHM  $\tau_P = 100.2$  ns.

It is noteworthy that the build-up times  $T_{bu}$  of the pulses do not align very well, with the simulated pulse showing a build-up time of  $\sim 1000$  ns while the measured pulse arrives at  $\sim 1800$  ns. The experimental pulse has a shorter pulse-width and higher peak power which indicates higher single-pass gain, therefore, it would be expected to arrive before the longer simulated pulse. Although one contributing factor to this discrepancy could be the travel time of the electric signal in the experiment, this will not have such a large impact. The main contribution is presumed to come from the start-up time of the sound wave within the AOM. Assuming a speed of sound in the glass medium of  $V \approx 4500$  m/s at a material length of about  $L = 1.0$  cm, the sound wave will take  $T = L/(2V) \approx 1000$  ns to traverse the half-length of the acousto-optic material [130]. It is important to note that this provides only a rough estimation of the delay time observed in the pulse measured experimentally, and issues with the simulation accuracy could also contribute.

Some deviations of simulated results compared with experiments are always to be expected, nevertheless, the experimental validation of a laser resonator with the model developed so far is discussed in the subsequent section.

## 3.6 Simulation of an Exemplary Laser Resonator

The model developed so far shows potential for laser system simulations with high accuracy, utilizing the field propagation algorithm in combination with the modeling of population states in the laser gain medium. To validate the functionality of this model approach, an experimental laser resonator is set up and the measured results are compared with the model predictions. The described resonator is identical to the one used for comparing experimental values in the preceding sections of this chapter (except section 3.5.2, where a pulsed laser was used).

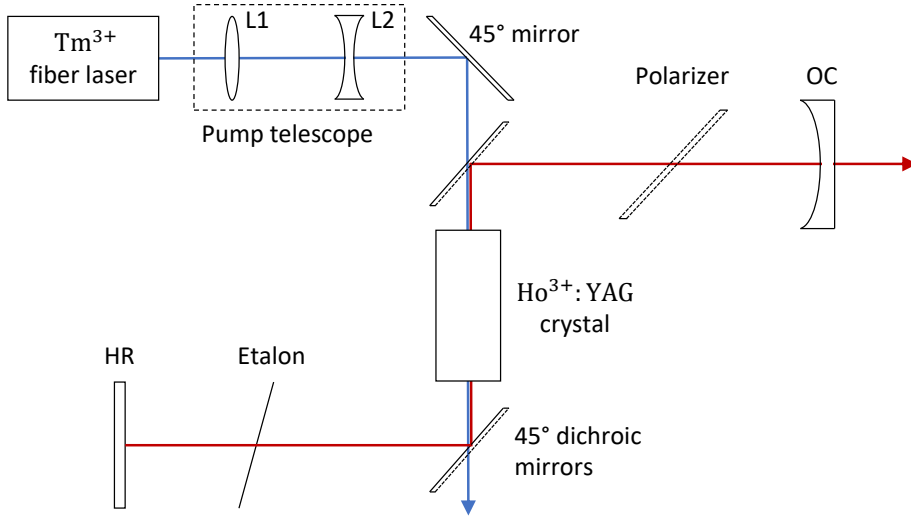


Figure 3.34: Schematic diagram of the linear Ho<sup>3+</sup>:YAG laser resonator operated in the CW regime, used to validate the developed model.

Figure 3.34 illustrates a schematic depiction of the arrangement. The system is made of a linear laser resonator in a Z-shaped configuration, where the pump light passes two dichroic mirrors at a 45° angle to enter and exit the cavity. The pump is generated from a CW Tm<sup>3+</sup> fiber laser at a wavelength of 1908 nm, which is collimated to 0.6 cm. A two-lens telescope, composed of a convex (L1) and concave (L2) lens, is employed to focus the beam into the laser crystal. The telescope is designed for a beam waist diameter of 0.1 cm inside the crystal. The cavity itself consists of a plane HR mirror at one end, with a reflectivity  $R_{HR} > 99.9\%$  at the expected laser wavelength around 2000 – 2200 nm. At the opposite end of the cavity, the OC mirror enables outcoupling with a reflectivity of  $R_{OC} = 50\%$ . To improve resonator stability, the mirror has a concave curvature with a radius of  $r_{HR} = 100$  cm, while the total cavity length is 30 cm. The two plane dichroic mirrors are specifically coated to transmit light at 1908 nm and reflect light at 2000 – 2200 nm, enabling the desired single pass of pump light through the laser crystal. The laser crystal itself is a Ho<sup>3+</sup>:YAG crystal with a length of 1.8 cm and diameter of 0.4 cm. The crystal has a doping concentration of active Ho<sup>3+</sup> ions of  $C_{Ho} = 1.1\%$ . To dissipate the absorbed power lost to heat, the crystal is mounted in a copper heat sink which is water cooled to a temperature of 293 K. Additionally, the cavity incorporates a linear polarizer, to ensure a linearly polarized output beam, as well as an etalon tuned for highest transmission at the

spectral  $\text{Ho}^{3+}$ :YAG peak at 2090 nm. Since there is no modulator element inside the cavity, the resonator is expected to generate laser light in CW operation.

Similar  $\text{Ho}^{3+}$ :YAG resonators operated in CW have been demonstrated in literature, where average output powers of up to 150 W have been reported [131, 132]. However, power scaling is not the objective with this laser system, rather it is the validation of the simulation model. Therefore, a resonator operating suboptimally and exhibiting higher order modes or unstable behavior is very suitable for this purpose, as all these effects should be taken into account with a comprehensive multi-physics model [114]. To model the experimental laser resonator, the optical elements used for the simulation are listed in Tab. 3.4. The general input parameters of the field to be propagated are specified in the first row of the table. The arrangement consists of eight element operators, ranging from the HR to OC mirror. The second column gives the positions of these elements, starting with the HR mirror at position 0 cm and ending with the OC mirror at position 30 cm. The third column details the defining input parameters for each element. Additionally, the laser crystal element includes the specific  $\text{Ho}^{3+}$ :YAG spectral data previously discussed in tables 3.1, 3.3, and 3.2. After all input parameters are defined, the simulation of the laser resonator can be conducted.

The field intensity distribution inside the cavity, simulated for a pump power of  $P_p = 45$  W, is illustrated in Fig. 3.35. The graph represents the iterative nature of the simulation, depicting successive forward and backward passes through the cavity for each round-trip. The results are shown for a steady-state solution where the iterative process has reached equilibrium. The intensity profiles are presented as a cut through the three-dimensional electromagnetic field distribution in the  $y$ - $z$ -plane. With this pump power, the simulation exhibits a Gaussian beam throughout the entire cavity, suggesting optimal mode matching between the simulated pump beam and the fundamental mode of the cavity. Notably, at the location of the laser crystal, a lensing behavior in propagation direction can be observed. This is not a thermally induced lens but rather the gain guiding effect that was mentioned briefly in section 3.4.2. It can be explained by a decrease in beam size based on the transversal distribution of laser gain. As the overlapping pump and laser beams both exhibit a Gaussian distribution, the exponential factor of the modified Beer-Lambert law (equation (3.7)) contributes to enhanced gain in the beam center, leading to a reduction in beam diameter [113, 133].

The comparison of laser spectra for this resonator was previously discussed in section 3.5.1 for a pump power of 45 W, where the predicted emission at the 2090 nm line aligned well with the experimental measurement. The resonator behavior regarding output power (a) and

Table 3.4: Sequential element operators used for modeling the laser resonator, along with their corresponding positions and input parameters. The first row provides the general input parameters that define the propagated laser field.

Elements	Position	Element Data
General	-	<ul style="list-style-type: none"> <li>- Field size (<math>W_{x,y}</math>) <math>\rightarrow 0.4 \times 0.4</math> cm</li> <li>- Field resolution (<math>N_{x,y}</math>) <math>\rightarrow 128 \times 128</math> pixels</li> <li>- Propagation resolution (<math>\Delta z</math>) <math>\rightarrow 0.1</math> cm</li> <li>- Time resolution (<math>\Delta t</math>) <math>\rightarrow 1E-5</math> s</li> </ul>
(1) HR mirror	0 cm	<ul style="list-style-type: none"> <li>- Reflectivity at 2000-2200 nm (<math>R_{HR}</math>) <math>\rightarrow 99.9</math> %</li> <li>- Curvature (<math>r_{HR}</math>) <math>\rightarrow</math> plane</li> </ul>
(2) Etalon	5 cm	<ul style="list-style-type: none"> <li>- Thickness (<math>d_{eta}</math>) <math>\rightarrow 0.01</math> cm</li> <li>- Refractive index (<math>n_{eta}</math>) <math>\rightarrow 1.5</math></li> <li>- Reflectivity (<math>R_{eta}</math>) <math>\rightarrow 4</math> %</li> </ul>
(3) 45° dichroic mirror	10 cm	<ul style="list-style-type: none"> <li>- Reflectivity at 1908 nm <math>\rightarrow 0.2</math> %</li> <li>- Reflectivity at 2000-2200 nm <math>\rightarrow 99.9</math> %</li> <li>- Curvature <math>\rightarrow</math> plane</li> </ul>
(4) Ho <sup>3+</sup> :YAG crystal	13.5 cm	<ul style="list-style-type: none"> <li>- Crystal length (<math>L_{LM}</math>) <math>\rightarrow 1.8</math> cm</li> <li>- Crystal diameter (<math>D_{LM}</math>) <math>\rightarrow 0.4</math> cm</li> <li>- Ho<sup>3+</sup> concentration (<math>C_{Ho}</math>) <math>\rightarrow 1.1</math> at. %</li> <li>- Spectral data from tables 3.1, 3.3, and 3.2</li> </ul>
(5) Tm <sup>3+</sup> pump source	10 cm	<ul style="list-style-type: none"> <li>- Wavelength (<math>\lambda_P</math>) <math>\rightarrow 1908</math> nm</li> <li>- Maximum power (<math>P_{P,max}</math>) <math>\rightarrow 100</math> W</li> <li>- Beam quality (<math>M_{x,y}^2</math>) <math>\rightarrow &lt; 1.1</math></li> <li>- Beam waist diameter (<math>d_{P,0}</math>) <math>\rightarrow 0.1</math> cm</li> <li>- Propagation direction <math>\rightarrow</math> backward</li> </ul>
(6) 45° dichroic mirror	20 cm	<ul style="list-style-type: none"> <li>- Reflectivity at 1908 nm <math>\rightarrow 0.2</math> %</li> <li>- Reflectivity at 2000-2200 nm <math>\rightarrow 99.9</math> %</li> <li>- Curvature <math>\rightarrow</math> plane</li> </ul>
(7) Polarizer	25 cm	<ul style="list-style-type: none"> <li>- Transmission angle (<math>\theta_t</math>) <math>\rightarrow 0</math> rad</li> </ul>
(8) OC mirror	30 cm	<ul style="list-style-type: none"> <li>- Reflectivity at 2000-2200 nm (<math>R_{OC}</math>) <math>\rightarrow 50</math> %</li> <li>- Curvature (<math>r_{OC}</math>) <math>\rightarrow 100</math> cm (concave)</li> </ul>

residual pump power (b) with increasing pump power is displayed in Fig. 3.36. The model accurately predicts the output of the laser resonator up to a pump power of 45 W (as compared in section 3.4.2), but beyond this point, the accuracy of the model diminishes rapidly, where it

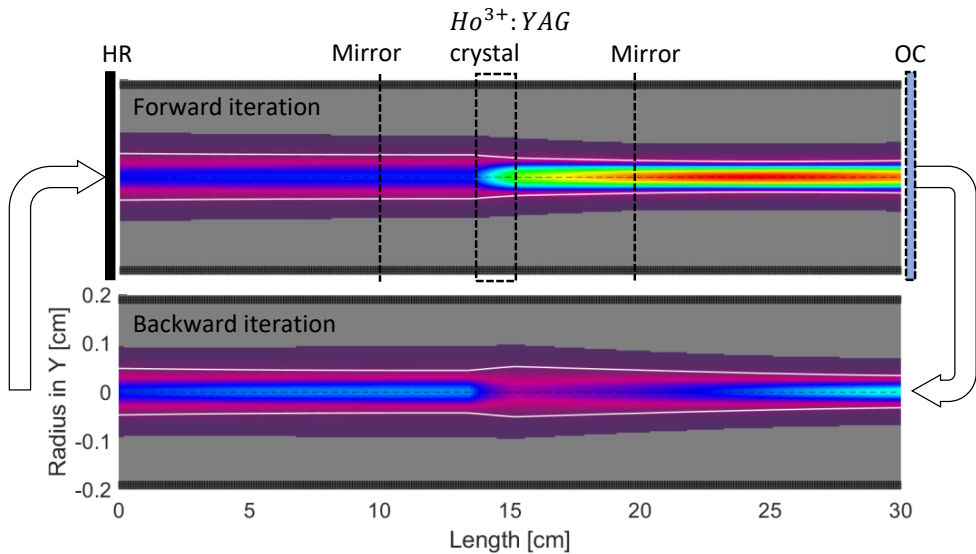


Figure 3.35: Simulation of laser intensity within the resonant cavity, depicted for a single iterative round-trip in both forward and backward directions. The intensity is represented as a cut in the  $y$ - $z$ -plane.

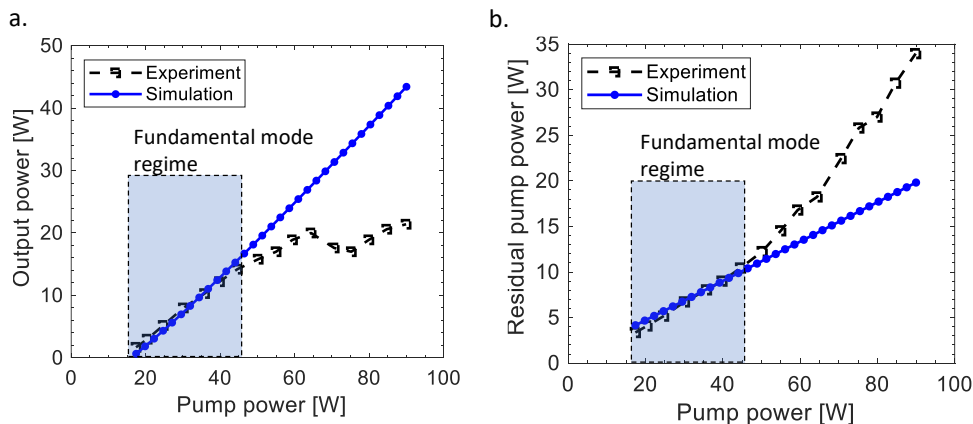


Figure 3.36: Comparison of the output power over incident pump power (a) and residual pump power over incident pump power (b) for the simulated and experimental results.

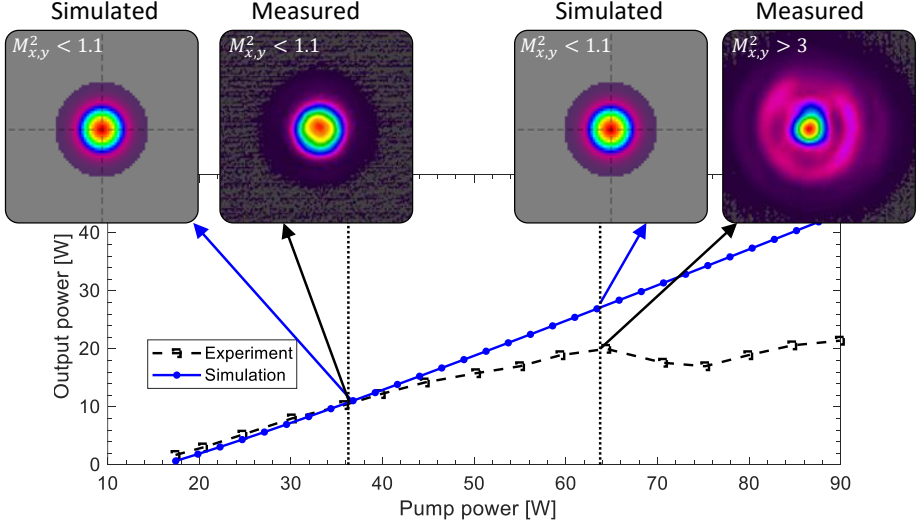


Figure 3.37: Comparison of the output beam profiles of the laser resonator in simulation and experiment. The beam profiles and  $M^2$  values are compared at pump powers of 35 and 65 W.

predicts a much higher output power. The low pump power region, where the model performs well, can be characterized as the fundamental mode regime. The assumption is that beyond this point, the experimental laser arrangement no longer exhibits a fully fundamental laser mode, which could account for this deviation. This assumption is confirmed with Fig. 3.37, where the output beam of the laser resonator at two distinct pump power operation points is compared. At a pump power of 35 W, both the simulated and experimental beams exhibit a Gaussian beam profile with an  $M^2 < 1.1$ , indicating that the beam shows close to diffraction-limited behavior. However, at a pump power of 65 W, where the deviation is already large, the simulation maintains a Gaussian beam profile, whereas the experimental laser shows higher order mode content and a measured  $M^2 > 3$ .

Although the FFT-BPM can model diffraction and higher order modes just fine, this behavior is assumed to originate from the fundamental mode becoming unstable, caused by an increase in thermal lensing with higher pump powers. The thermal lensing effect has not been addressed so far and is not yet implemented into the model. Figure 3.38 shows the calculated stability zones (refer to section 3.2.3) for the Z-shaped resonator incorporating a thermal lens with a central position in the cavity. The fundamental mode diameters remain relatively constant over a dioptric power from 0 to  $0.04 \text{ cm}^{-1}$ , beyond which the unstable zone starts while the second

stability zone is far from the first. The maximum dioptric power of the thermal lens for which the fundamental mode is stable corresponds to a focal length of 25 cm. It can be assumed that this effective thermal lens is surpassed at a pump power of approximately 50 W in the experimental resonator, where the experimental results start to diverge from the simulation. The thermal roll-over of the output power is superimposed onto the stability diagram (Fig. 3.38) as a black dotted line at the assumed position. As the first stability zone ends, the fundamental mode diameter at the crystal position increases rapidly, as depicted with the stability curves. Given that the pump diameter within the crystal remains unchanged, the mode matching between pump and laser beam is getting worse, resulting in a decrease in output power and higher order modes becoming more dominant. The previously discussed beam profile shows signs of higher modes at 65 W, confirming this assumption. It is noteworthy that the stability curves derived from V. Magni [85] show the behavior for the fundamental mode only and not the higher order modes of the cavity, the stability of which cannot be easily predicted.

Although the model so far incorporates comprehensive submodels for beam propagation and laser gain, the inclusion of a thermal model is essential to develop a multi-physics approach suitable for simulating power scaling and design issues of bulk solid-state lasers. To address this, a numerical thermal model is introduced in the following chapter.

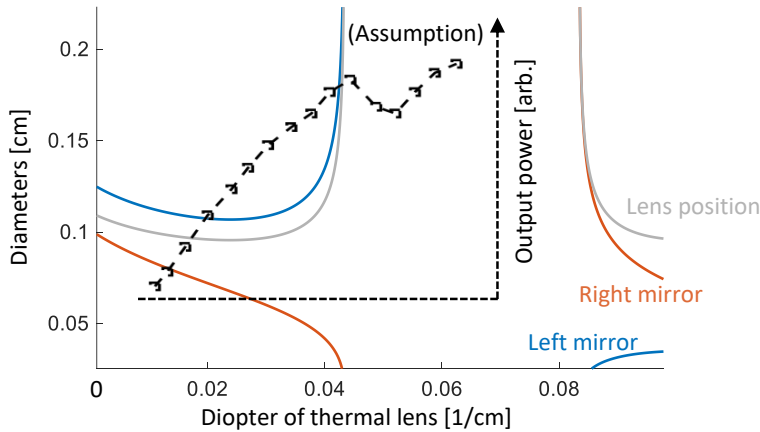


Figure 3.38: Dependency of the Z-shaped  $\text{Ho}^{3+}$ :YAG resonator stability on the dioptric power of the corresponding thermal lens.

## 4 Thermal Model for Bulk Elements

The preceding chapters addressed the development of a numerical model for solid-state laser systems, encompassing resonators and amplifiers. The remaining deviations between the model and experimental results have been attributed to thermal effects within the laser gain medium, which significantly influence laser performance. This chapter presents the implementation of thermal simulation algorithms and the resulting thermal effects into the overarching model, thereby providing a comprehensive solution for the entire multi-physics process. An overview of thermodynamic behavior in solids is discussed in section 4.1. The numerical solution for the three-dimensional temperature distribution is described in section 4.2, while the solutions regarding the displacement and stress distributions are provided in section 4.3. The final section 4.4 of this chapter discusses the impact of these distributions on the electromagnetic field, including the thermal dependency of material parameters and thermo-optic effects.

### 4.1 Background on Thermodynamics in Solids

As previously discussed, the pumping mechanisms described in chapter 3 result in the undesired side effect of non-radiative decay within the active laser medium. Additionally, every bulk optical element in the laser system may undergo background power absorption when a laser beam passes the material. In both cases, heat is generated in the optical elements, which influences the performance of the laser setup. Consequently, this section introduces the basic concepts of thermodynamics that lead to the thermally induced interaction of the material with the electromagnetic field.

When microscopic processes like energy absorption or non-radiative recombination induces vibrations in the material matrix (phonons), the macroscopic energy stored in the material is

described as heat. For a given volume  $V = \Delta x \Delta y \Delta z$  of material absorbing energy, the internal heat can be represented by the source term  $Q(x, y, z)$ , expressed in units of power per unit volume [3]. Heat is not stored in the volume indefinitely; in solids, it can be transferred through three primary mechanisms [134]:

- Conduction*, the most common form of heat transfer in solids. It occurs when thermal energy is transferred through the vibration of atoms and molecules within the material. The rate of heat conduction is governed by Fourier's law.

- Convection*, involves the transfer of heat through the movement of fluid molecules. Therefore, energy transfer by convection can only occur at surfaces where the solid interacts with a fluid or gas (such as air or water).

- Radiation*, all bodies emit thermal radiation if their temperature is above absolute zero. This form of heat transfer occurs through electromagnetic waves and does not require a contact medium. The intensity of the thermal radiation is directly related to the material temperature, as described with the Stefan–Boltzmann law.

To determine the thermal behavior within a bulk material, heat conduction alone is used to calculate the temperature profile  $T(x, y, z)$ , as the other two mechanisms are neglectable for the cases of the solid materials relevant to this work. According to Fourier's law, the heat flux is proportional to the negative gradient of temperature and the thermal conductivity of the material. In the one-dimensional differential form along  $x$  it is written as [134]

$$q_x = -k_{\text{th}} \frac{dT}{dx}, \quad (4.1)$$

where  $q_x$  is the local heat flux,  $k_{\text{th}}$  is the thermal conductivity of the material, and  $T$  is the temperature. By substituting the three-dimensional formulation  $q = -k_{\text{th}} \nabla T$  into the conservation of energy principle  $\rho C_p \partial T / \partial t = -\nabla q$ , the flow of heat in a material volume can be described by

$$\frac{\partial T}{\partial t} = \frac{k_{\text{th}}}{\rho C_p} \nabla^2 T, \quad (4.2)$$

where  $\rho$  is the density,  $C_p$  is the specific heat at constant pressure, and the Laplace operator  $\nabla^2 = \partial^2 / \partial x^2 + \partial^2 / \partial y^2 + \partial^2 / \partial z^2$ . Together with the thermal conductivity, the three thermal parameters describe the thermal diffusivity  $\lambda_{\text{th}} = k_{\text{th}} / (\rho C_p)$ , which determines the rate at which

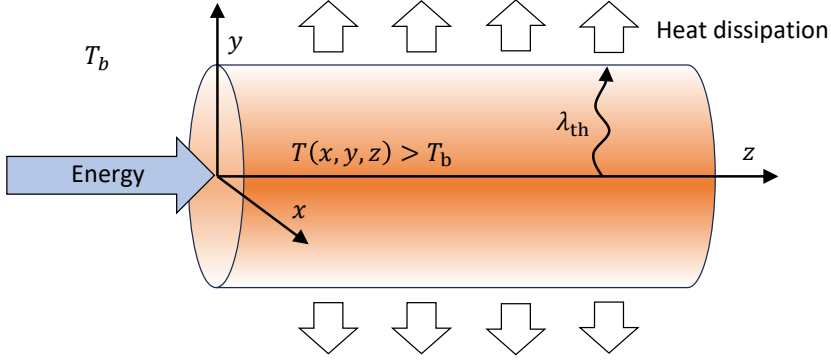


Figure 4.1: Energy balance and temperature distribution in a schematic bulk rod where energy is introduced at one end face and dissipated at the lateral surface.

heat disperses through the material. Most material parameters can themselves be dependent on the temperature of the volume, a behavior which is further discussed in section 4.4.1. For the time being, no temperature dependency is assumed. In isotropic media with internal heat generation  $Q$ , this heat flow can be reformulated to the discretized heat equation in three dimensions, defined as [134]

$$\frac{\partial T(x, y, z)}{\partial t} = \frac{k_{th}}{\rho C_p} \left[ \frac{\partial^2 T(x, y, z)}{\partial x^2} + \frac{\partial^2 T(x, y, z)}{\partial y^2} + \frac{\partial^2 T(x, y, z)}{\partial z^2} \right] + \frac{1}{\rho C_p} Q(x, y, z). \quad (4.3)$$

This partial differential equation is essential for many applications by modeling heat transfer and similar diffusion processes.

Figure 4.1 depicts the energy and power balance of a schematic end-pumped bulk laser rod. In this case, optical energy is introduced at one end face of the rod, resulting in heat development along the  $z$ -axis, leading to a temperature peak in the center of the rod. Thermal conduction causes a spread of the temperature throughout the bulk of the material, where heat is dissipated at the lateral surface. The resulting temperature profile is highly dependent on the boundary condition at the material interface. The most important boundary conditions of interest are of the Dirichlet or Neumann type. The Dirichlet boundary condition defines the value that a solution must take on the boundary of the domain; in this context, a fixed boundary

temperature  $T_b$  is set. For example, the values on the  $x$ - $y$ -plane for  $z = 0$  can be defined with [134]

$$T(x, y, 0) = T_b . \quad (4.4)$$

The Neumann boundary condition defines the value of the derivative of the solution at the boundary. In the context of the heat equation, this could represent a fixed heat flux across the boundary. For the same boundary plane example, the thermal resistance  $R_{th}$  at the boundary (in units of temperature per unit power) can be used to model a conduction or convection boundary [134, 135]:

$$\frac{\partial T}{\partial z}(x, y, 0) = \frac{1}{k_{th} R_{th,b} A_b} [T_b - T(x, y, 0)] , \quad (4.5)$$

where  $A_b$  is the effective area normal to the direction of heat flow. If the Neumann condition is chosen with a flux of zero, this is expressed by an infinite thermal resistance and implies that there is no heat flow. Consequently, an insulating boundary can be modeled, described by

$$\frac{\partial T}{\partial z}(x, y, 0) = 0 . \quad (4.6)$$

Although a spatially resolved boundary condition is relevant for complex numerical solutions, a basic solution to the heating behavior in laser rods can be described by assuming radial symmetry and no heat transfer in the  $z$ -direction. This approximation is not suitable for arbitrary heat loads, but is nonetheless useful for simple temperature estimations and will be used in section 4.3.2 as a validation for the numerical solution. Given a laser rod of length  $L$  and total radius  $R$ , the heat flow is considered as purely radial and the heat equation Eq. (4.3) is reduced to [17, 136]

$$\frac{\partial^2 T(r)}{\partial r^2} = \frac{Q_a}{k_{th}} - \frac{1}{r} \frac{\partial T(r)}{\partial r} , \quad (4.7)$$

with the volumetric heat load

$$Q_a = \frac{P_h}{\pi R^2 L} . \quad (4.8)$$

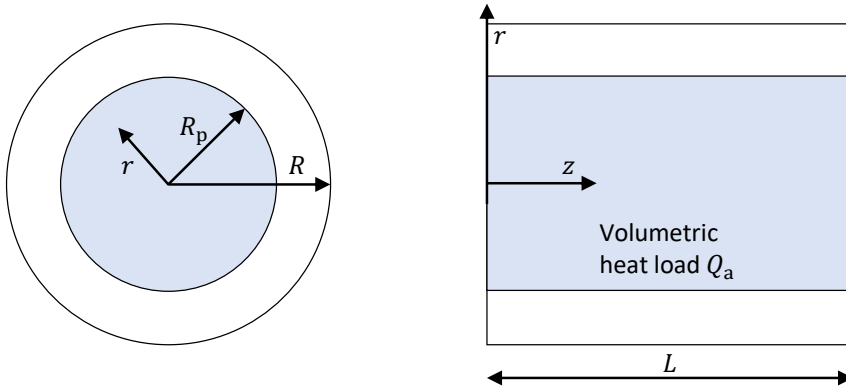


Figure 4.2: Illustration of an end-pumped laser rod for the analytical solution of heat distribution.

Here,  $P_h$  is the total power dissipated as heat over the full length and diameter of the rod. In the case of a homogeneous heat load, the parabolic temperature profile can then be estimated with an analytical solution [17]:

$$T(r) = T_b + \frac{Q_a}{4k_{th}} (R^2 - r^2) . \quad (4.9)$$

An illustration of the basic laser rod for the analytical solution is shown in Fig. 4.2. While an approximate solution can be sufficient for some cases, a numerical solution provides higher accuracy and considers asymmetries and other spatial and temporal influences. For instance, in the analytical solution presented, the radius of pump light  $R_p$  is not taken into account, which provides only a very limited solution.

In addition to the direct impact of temperature on laser performance, the heating of a bulk material results in thermal expansion, where a change in temperature induces a change in the size and density of the material volume. This phenomenon can lead to additional interactions with the electromagnetic field that have to be taken into account, and is characterized by the thermal expansion coefficient  $\alpha_{th}$ . For instance, linear expansion in the  $x$ -direction is expressed with [134]

$$D_x = \alpha_{th} \Delta_x T \Delta x , \quad (4.10)$$

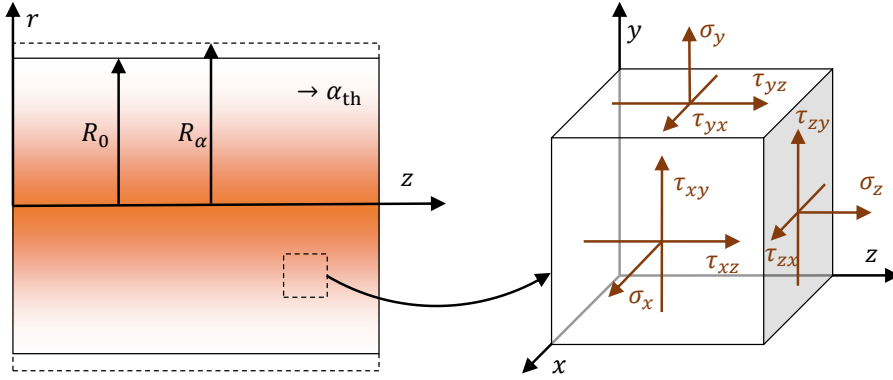


Figure 4.3: Schematic representation of thermal expansion and consequent stress development on a volume element within the thermally loaded material.

where the length change in  $x$ -direction  $D_x$  depends directly on the change in temperature  $\Delta_x T$  and the particular length  $\Delta x$ . For anisotropic materials, the thermal expansion coefficient and other material parameters may also exhibit anisotropy, which must be considered in a model representation.

The displacement of small control lengths can lead to elastic strain  $\varepsilon$  within the bulk material, defined for the case of thermal expansion with  $\varepsilon_{x,\text{th}} = D_x / \Delta x$ . This strain results in internal forces, described by the stress reaction of the material, where stress  $\sigma$  is the force per unit area represented in the tensor form [137]:

$$\sigma_{dd} = \begin{pmatrix} \sigma_{xx} & \tau_{xy} & \tau_{xz} \\ \tau_{yx} & \sigma_{yy} & \tau_{yz} \\ \tau_{zx} & \tau_{zy} & \sigma_{zz} \end{pmatrix}. \quad (4.11)$$

Figure 4.3 illustrates the thermal expansion in a typical rod geometry with a hotter inner part and a cooler outer part. The figure also shows the stress reaction of a volume element within the bulk material, where  $\sigma_{xx}$ ,  $\sigma_{yy}$ ,  $\sigma_{zz}$  are the normal stress components, and  $\tau_{xy}$ ,  $\tau_{xz}$ ,  $\tau_{yx}$ , etc. are the shear stress components.

The deformation of elastic bodies can be described with the generalized Hooke's law of elasticity in the three spatial dimensions [137, 138]:

$$\varepsilon_x = \frac{1}{E} [\sigma_{xx} - \nu(\sigma_{yy} + \sigma_{zz})] + \alpha_{\text{th}}(\Delta_x T), \quad (4.12)$$

$$\varepsilon_y = \frac{1}{E} [\sigma_{yy} - \nu(\sigma_{xx} + \sigma_{zz})] + \alpha_{\text{th}}(\Delta_y T), \quad (4.13)$$

$$\varepsilon_z = \frac{1}{E} [\sigma_{zz} - \nu(\sigma_{xx} + \sigma_{yy})] + \alpha_{\text{th}}(\Delta_z T). \quad (4.14)$$

The deformation behavior is determined by the material parameters of elastic modulus  $E$  and the Poisson's ratio  $\nu$ , which describes the ratio of transverse contraction or expansion in the direction of the stretching force. These equations describe the behavior in small uniform control volumes of the domain, however, the bulk material can undergo non-uniform temperature distributions, material inhomogeneities, and different boundary conditions. Solving the stress response in the complete domain requires a numerical solution for the displacement distribution based on the Navier-Stokes equations for elasticity - expressed in the form of the stress tensor by [137, 139]

$$\sigma_{xx} = \frac{E}{1+\nu} \left[ \frac{\partial u}{\partial x} + \frac{\nu}{1-2\nu} \left( \frac{\partial u}{\partial x} + \frac{\partial v}{\partial y} + \frac{\partial w}{\partial z} \right) \right] - \frac{E\alpha_{\text{th}}\Delta_x T}{1-2\nu}, \quad (4.15)$$

$$\sigma_{yy} = \frac{E}{1+\nu} \left[ \frac{\partial v}{\partial y} + \frac{\nu}{1-2\nu} \left( \frac{\partial u}{\partial x} + \frac{\partial v}{\partial y} + \frac{\partial w}{\partial z} \right) \right] - \frac{E\alpha_{\text{th}}\Delta_y T}{1-2\nu}, \quad (4.16)$$

$$\sigma_{zz} = \frac{E}{1+\nu} \left[ \frac{\partial w}{\partial z} + \frac{\nu}{1-2\nu} \left( \frac{\partial u}{\partial x} + \frac{\partial v}{\partial y} + \frac{\partial w}{\partial z} \right) \right] - \frac{E\alpha_{\text{th}}\Delta_z T}{1-2\nu}, \quad (4.17)$$

$$\tau_{xy} = \frac{E}{2(1+\nu)} \left( \frac{\partial u}{\partial y} + \frac{\partial v}{\partial x} \right), \quad (4.18)$$

$$\tau_{xz} = \frac{E}{2(1+\nu)} \left( \frac{\partial u}{\partial z} + \frac{\partial w}{\partial x} \right), \quad (4.19)$$

$$\tau_{yz} = \frac{E}{2(1+\nu)} \left( \frac{\partial v}{\partial z} + \frac{\partial w}{\partial y} \right). \quad (4.20)$$

In this context, the displacement  $D_d$  in the three spatial directions is given by  $u$ ,  $v$ , and  $w$  in each point for the  $x$ -,  $y$ -, and  $z$ -direction, respectively. The source term of thermal expansion is incorporated by the thermal expansion coefficient and the directional temperature gradient  $\Delta_d T$ .

Similarly to the temperature distribution, an analytical solution is possible for the stress response of the symmetric case with a uniform temperature in a rod geometry. This approximation will be used later on in section 4.3.2 as a comparison to the numerical solution for displacement and stress. In cylindrical coordinates, the three components of normal stress for a free-moving boundary are given by [140]

$$\sigma_r(r) = \frac{1}{4} \Delta T_{\text{rod}} \left( \frac{r^2}{R^2} - 1 \right) \frac{\alpha_{\text{th}} E}{1 - \nu}, \quad (4.21)$$

$$\sigma_t(r) = \frac{1}{4} \Delta T_{\text{rod}} \left( \frac{3r^2}{R^2} - 1 \right) \frac{\alpha_{\text{th}} E}{1 - \nu}, \quad (4.22)$$

$$\sigma_z(r) = \frac{1}{2} \Delta T_{\text{rod}} \left( \frac{2r^2}{R^2} - 1 \right) \frac{\alpha_{\text{th}} E}{1 - \nu}, \quad (4.23)$$

where  $\sigma_r$  is the radial stress component,  $\sigma_t$  is the tangential component, and  $\sigma_z$  is the component in the  $z$ -direction of the rod.  $\Delta T_{\text{rod}}$  is the temperature difference between the rod center and its surface.

For the multi-physics model approach of this work, the goal is to simulate complex and asymmetric distributions in three-dimensional space. Therefore, a numerical solution for temperature, displacement, and stress based on solving the respective differential equations is necessary. Figure 4.4 represents the thermal algorithm for a bulk element operator, including the resulting thermal effects that will influence the electromagnetic field propagating through the element. The execution of this thermal submodel is handled iteratively, with the thermal distributions being updated at each roundtrip or, to minimize computation time, at dynamic intervals correlated with optical convergence of the laser model. Whenever the thermal distributions are refreshed, the resulting thermal effects impact all light beams in the system and subsequently modify the initial heat load distribution. This feedback has to be integrated into the convergence condition of the simulation. A steady-state solution must now consider both the optical and thermal equilibrium. The specific numerical solutions employed to determine the thermal distributions are explained in the subsequent sections.

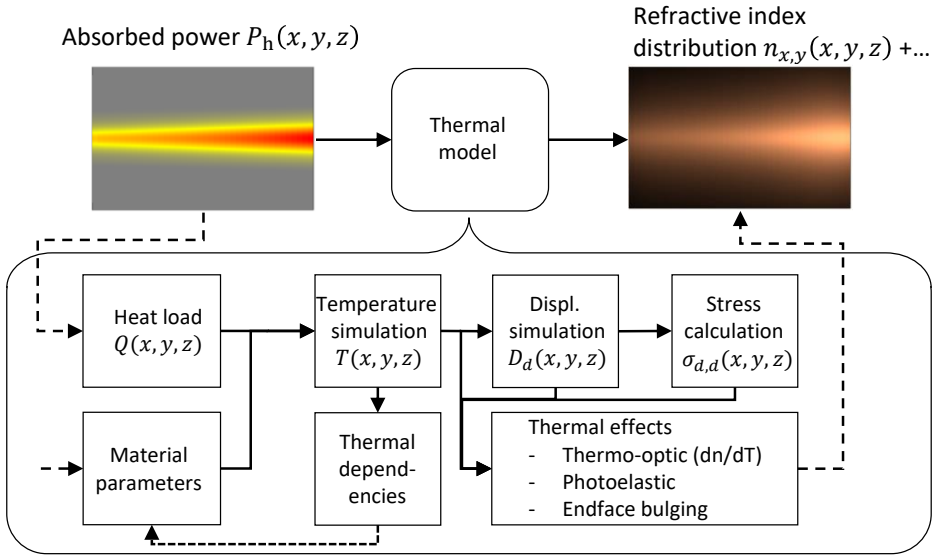


Figure 4.4: Schematic representation of the complete thermal algorithm as a part of the element operator of bulk elements with power absorption.

## 4.2 Simulation of the Three-Dimensional Temperature Distribution

In this section, the numerical solution to describe the temperature distribution in bulk elements is discussed. In subsection 4.2.1, the ADI-FDM approach to solving the heat equation and corresponding boundary conditions is explained. Subsequently, an example simulation and validation of the model are conducted in subsection 4.2.2.

### 4.2.1 Numerical ADI-FDM Solution

As discussed in the previous sections, potentially inhomogeneous and asymmetric heat loads from the absorption of laser light require a numerical solution for the heat equation (4.3). The heat load distribution of the laser gain medium  $Q(x, y, z)$ , expressed in power per unit volume, is derived from the multi-physics model discussed in chapters 2 and 3.

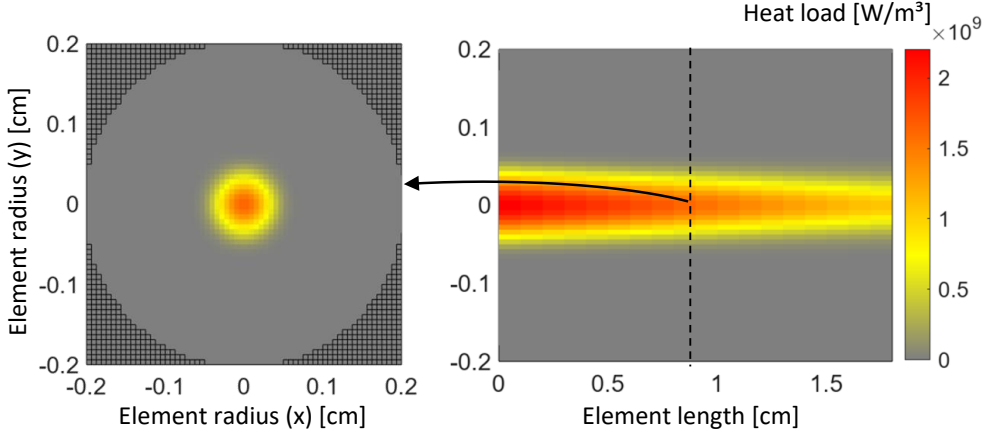


Figure 4.5: Simulated heat load of the exemplary laser gain medium as a three-dimensional distribution, dissipating a power of 10.2 W as heat.

The distribution can be determined by the following equation:

$$Q(x, y, z) = -\frac{1}{C\rho} \sum_i^{i_\lambda} \left[ \frac{\partial I_{\text{FW}}(x, y, z, i)}{\partial z} + \frac{\partial I_{\text{BK}}(x, y, z, i)}{\partial z} \right] - \frac{1}{C\rho} \sum_m^{N_{\text{max}}} \left[ \frac{N_m(x, y, z)}{\tau_m} \sum_j^{m-1} \left( \frac{hc}{\bar{\lambda}_{m \rightarrow j} \beta_{m \rightarrow j}} \right) \right], \quad (4.24)$$

where the first term characterizes the variation of intensity distribution in the  $z$ -direction, accounting for both backward ( $I_{\text{BK}}$ ) and forward ( $I_{\text{FW}}$ ) distributions as a sum of all spectral fields  $i_\lambda$ , including pump and laser light. As absorption will result in a negative contribution, the overall value of  $Q$  should always be positive in the absence of numerical errors. The intensity gain from stimulated emission is then taken into account by a positive variation of the laser field, if applicable. The second term deducts the power lost to spontaneous decay (refer to section 3.3.2, Eq. (3.38)) of all relevant energy levels  $N_m$  from the total absorbed power of the gain medium.

For other bulk elements that undergo background absorption of laser light, determined by the absorption coefficient  $\alpha$ , the heat load is similarly described to Eq. (4.24), however, now only considering the first term for field absorption. Figure 4.5 shows the simulated heat load

distribution of the laser gain medium from the resonator discussed in section 3.6, at a pump power of 45 W. The total power dissipated as heat is 10.2 W, resulting from the absorption of the corresponding Gaussian laser beams. This heat distribution is used as the initial condition for the numerical simulation of the temperature in 3D space.

As described in section 4.1, thermal conduction in solids, related to the Brownian motion of atoms, is described with the differential form of the heat equation (4.3). A range of numerical techniques are available to solve this equation, and given that the problem is described with a parabolic partial differential equation (PDE), two finite discretization methods are of interest [19, 141]:

- *Finite element methods (FEM)*, which divide the problem domain into smaller, simpler parts called finite elements. These elements form a mesh, and the solution is approximated within each element using interpolation functions.

- *Finite difference methods (FDM)*, where the differential equation is approximated directly by replacing derivatives with finite differences. The problem domain is represented by a grid of points.

While both methods are capable of numerically solving the heat equation, there are certain differences to consider [19]. The complex mesh generation capabilities of the FEM give it a greater flexibility in handling complex geometries and boundary conditions, whereas the FDM is more suitable for simpler geometries. While the FEM can typically achieve higher accuracy, the FDM can handle regular, structured grids effectively and is simpler to implement. The optical elements relevant to this work can typically be approximated as cylindrical or cubic geometries with simple boundary conditions. The FDM is therefore selected to model the temperature distribution of bulk elements, as its relative ease of implementation makes it more suitable for integration into the multi-physics model approach.

These general methods further divide into explicit or implicit solutions, where implicit methods compute the system status at a future time  $t + 1$  from the system statuses at present  $t$  and future times  $t + 1$  combined, while explicit methods calculate the solution only from the currently known status  $t$ . Explicit methods are typically simpler to solve, however, they are more susceptible to numerical errors owing to temporal limitations [19]. An example of a straightforward explicit approach is the direct-forward-Euler method, with more complex implicit solutions such as the Crank-Nicolson method or alternating-direction implicit method (ADI) also commonly used [142, 143]. The ADI-FDM method is selected for this work because

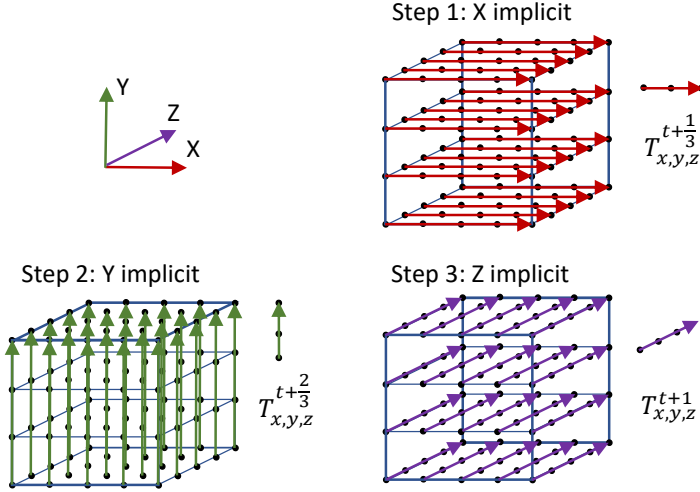


Figure 4.6: Temporal approach of the ADI method, where the distribution is solved iteratively by splitting the time step into the three spatial directions. Graph adapted from [145].

of its high stability, linear runtime, and memory usage [144]. This method does not solve the three-dimensional problem directly, but rather addresses a series of three one-dimensional problems, as depicted in Fig. 4.6. Depending on the selected time step  $\Delta t$ , the steady state solution can be achieved in a few iterations. The method used in this work is adapted from the simulation approach of Wang et al. [145], who outlined the original ADI method of Douglas and Gunn [144] for transient thermal convection problems of chip-level geometries. For this work, the method is adapted for conduction problems in solid bulk media absorbing laser light. The heat conduction formulation from Eq. (4.3) can be rewritten in an implicit form as follows:

$$T^{t+1} = T^t + c_x \frac{\partial_x^2}{2} (T^{t+1} + T^t) + c_y \frac{\partial_y^2}{2} (T^{t+1} + T^t) + c_z \frac{\partial_z^2}{2} (T^{t+1} + T^t) + \frac{\Delta t}{\rho C_p} Q, \quad (4.25)$$

with dimensionless conduction factors  $c_x = \lambda_{th} \Delta t / (\Delta x)^2$ ,  $c_y = \lambda_{th} \Delta t / (\Delta y)^2$ , and  $c_z = \lambda_{th} \Delta t / (\Delta z)^2$ . The operators  $\partial_x^2$ ,  $\partial_y^2$ , and  $\partial_z^2$  imply that the spatial derivative of the temperature still has to be discretized.

Given the ADI approach, the solution to Eq. (4.25) is divided into three sub-time steps corresponding to the three dimensions with

$$T^{t+1/3} = T^t + c_x \frac{\partial_x^2}{2} (T^{t+1/3} + T^t) + c_y \partial_y^2 T^t + c_z \partial_z^2 T^t + \frac{\Delta t}{\rho C_p} Q \quad \text{Step 1 ,} \quad (4.26)$$

$$\begin{aligned} T^{t+2/3} = T^t + c_x \frac{\partial_x^2}{2} (T^{t+1/3} + T^t) + c_y \frac{\partial_y^2}{2} (T^{t+2/3} + T^t) \\ + c_z \partial_z^2 T^t + \frac{\Delta t}{\rho C_p} Q \end{aligned} \quad \text{Step 2 ,} \quad (4.27)$$

$$\begin{aligned} T^{t+1} = T^t + c_x \frac{\partial_x^2}{2} (T^{t+1/3} + T^t) + c_y \frac{\partial_y^2}{2} (T^{t+2/3} + T^t) \\ + c_z \frac{\partial_z^2}{2} (T^{t+1} + T^t) + \frac{\Delta t}{\rho C_p} Q \end{aligned} \quad \text{Step 3 .} \quad (4.28)$$

In this case, the full step  $t \rightarrow t + 1$  is divided into the three steps from  $t \rightarrow t + 1/3$ , from  $t + 1/3 \rightarrow t + 2/3$ , and finally from  $t + 2/3 \rightarrow t + 1$ . In step 1, the  $x$ -direction is implemented implicitly, while  $y$ - and  $z$ -directions are explicit. Therefore, at this time step, the system of equations has three unknown variables  $T_{i-1,j,k}^t$ ,  $T_{i,j,k}^t$ , and  $T_{i+1,j,k}^t$  at each row of grid points  $(y, z)$ . The first step can then be expressed as a tridiagonal matrix of each  $(y, z)$  row, where the outer two equations are defined by the boundary conditions discussed later in this section.

At the initial point of the simulation ( $t = 0$ ), the temperature  $T(x, y, z, t)$  at grid point  $(i, j, k)$  is denoted as  $T(i\Delta x, j\Delta y, k\Delta z, t\Delta t)$ , abbreviated to  $T_{i,j,k}^t$ . The discretization around node  $T_{i,j,k}^t$  is illustrated in Fig. 4.7. The three steps can now be derived in detail for a single node according to [144, 146]

$$\begin{aligned} -c_x T_{i-1,j,k}^{t+1/3} + 2(1 + c_x) T_{i,j,k}^{t+1/3} - c_x T_{i+1,j,k}^{t+1/3} = [c_x T_{i-1,j,k}^t + 2c_y T_{i,j-1,k}^t \\ + 2c_z T_{i,j,k-1}^t + 2(1 - c_x - 2c_y - 2c_z) T_{i,j,k}^t + c_x T_{i+1,j,k}^t \\ + 2c_y T_{i,j+1,k}^t + 2c_z T_{i,j,k+1}^t] + \frac{2\Delta t}{\rho C_p} Q_{i,j,k} \end{aligned} \quad \text{Step 1 ,} \quad (4.29)$$

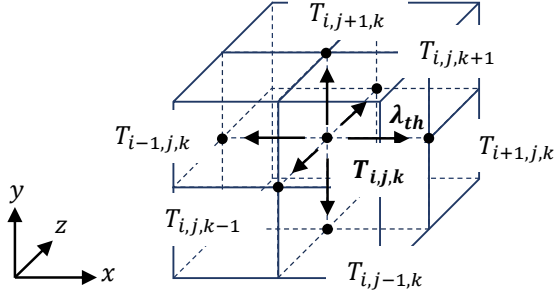


Figure 4.7: Schematic illustration of the three-dimensional grid discretization around node  $T_{i,j,k}^t$ .

$$\begin{aligned}
 -c_y T_{i,j-1,k}^{t+2/3} + 2(1 + c_y) T_{i,j,k}^{t+2/3} - c_y T_{i,j+1,k}^{t+2/3} &= [c_x T_{i-1,j,k}^{t+1/3} - 2c_x T_{i,j,k}^{t+1/3} \\
 &+ c_x T_{i+1,j,k}^{t+1/3}] + [c_x T_{i-1,j,k}^t + c_y T_{i,j-1,k}^t \\
 &+ 2c_z T_{i,j,k-1}^t + 2(1 - c_x - c_y - 2c_z) T_{i,j,k}^t + c_x T_{i+1,j,k}^t \\
 &+ c_y T_{i,j+1,k}^t + 2c_z T_{i,j,k+1}^t] + \frac{2\Delta t}{\rho C_p} Q_{i,j,k}
 \end{aligned}
 \quad \text{Step 2 , (4.30)}$$

$$\begin{aligned}
 -c_z T_{i,j,k-1}^{t+1} + 2(1 + c_z) T_{i,j,k}^{t+1} - c_z T_{i,j,k+1}^{t+1} &= [c_x T_{i-1,j,k}^{t+1/3} - 2c_x T_{i,j,k}^{t+1/3} \\
 &+ c_x T_{i+1,j,k}^{t+1/3}] + [c_y T_{i,j-1,k}^{t+2/3} - 2c_y T_{i,j,k}^{t+2/3} + c_y T_{i,j+1,k}^{t+2/3}] \\
 &+ [c_x T_{i-1,j,k}^t + c_y T_{i,j-1,k}^t + c_z T_{i,j,k-1}^t \\
 &+ 2(1 - c_x - c_y - c_z) T_{i,j,k}^t + c_x T_{i+1,j,k}^t + c_y T_{i,j+1,k}^t \\
 &+ c_z T_{i,j,k+1}^t] + \frac{2\Delta t}{\rho C_p} Q_{i,j,k}
 \end{aligned}
 \quad \text{Step 3 , (4.31)}$$

To solve the first step, there are  $i \rightarrow I$  equations for each  $(y, z)$  value. As previously mentioned, the three unknown variables can be expressed as a tridiagonal system in combination with the values on the right-hand side of Eq. (4.29). The tridiagonal matrix can then be solved by Gaussian elimination [147]. This is repeated for all three steps to reach the three-dimensional solution at time  $t + 1$ , and iterated temporally until the thermal convergence condition is met or a steady state is reached.

The implementation of the Dirichlet and Neumann boundary conditions, as per Eqs. (4.4) and (4.5), involves the use of the central difference approximation to discretize the grid nodes at the

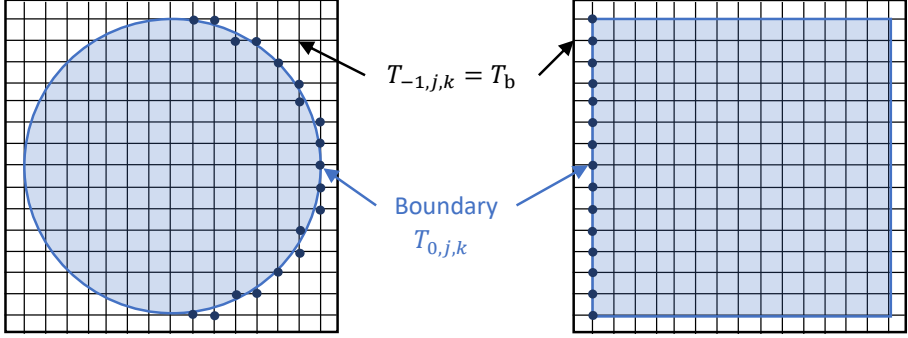


Figure 4.8: Illustration of boundary nodes for two rod geometries, with a cylindrical rod on the left and a cubic rod on the right.

boundary [135]. For instance, this results in the Neumann condition in the  $x$ -direction given by

$$T_{0,j,k}^t = T_{1,j,k}^t + \frac{2\Delta x}{k_{th}R_{th,b}\Delta y\Delta z}(T_{-1,j,k}^t - T_{1,j,k}^t). \quad (4.32)$$

Figure 4.8 provides an illustration of different boundary geometries, with a cylindrical rod geometry on the left and a cubic rod on the right. The cylindrical rod example also demonstrates the discretization of the circular boundary, where a higher resolution leads to a more accurate representation of the cylindrical shape with this FDM approach.

## 4.2.2 Example and Submodel Validation

With the boundary conditions defined, the temperature distribution in three-dimensional bulk elements can be simulated. The material parameters for the host materials YAG and YALO (cut parallel to the optical  $c$ -axis) are provided in Tab. 4.1. The table includes the values of thermal conductivity, density, and specific heat for YAG and YALO, as taken from literature [148–150]. Additionally, the table contains the elastic modulus and Poisson's ratio, which are relevant for the subsequent displacement simulation in section 4.3, as well as the  $dn/dT$  value for modeling the thermal lens in section 4.4.3. It should be noted that while YALO(IIc) is an anisotropic material, not all parameters are defined for the different axis components. Some

Table 4.1: Thermal material parameters for the hosts YAG and YALO(lIc) utilized in the temperature simulation, along with additional parameters for subsequent displacement and stress modeling. The values are given for a temperature of 300 K.

Parameters	YAG	YALO(lIc)	Units
$k_{\text{th}}$	0.14	0.11	W/(cm K)
$\rho$	0.0046	0.0054	kg/cm <sup>3</sup>
$C_p$	590	400	J/(kg K)
$\Theta_D$	520	557	K
$\alpha_{\text{th}}$	$7.6E-6$	x $\rightarrow 9.5E-6$ y $\rightarrow 10.8E-6$	1/K
$E$	311	300	GPa
$\nu$	0.25	0.27	-
$dn/dT$	$8.1E-6$	x $\rightarrow 9.7E-6$ y $\rightarrow 14.5E-6$	1/K

parameters exhibit more anisotropy than others, and a lack of literature values limits the available data.

Figure 4.9 shows the simulated temperature distribution in three dimensions for the specific heat load provided with Fig. 4.5. The temperature is given for the steady state, where the iterative FDM has met its convergence criteria. The boundary conditions at the interface to the copper cooling block (lateral surface) are defined as Dirichlet type with a temperature of 293 K and the end faces are considered with an insulating boundary. Given that copper has a high heat conduction compared to YAG, the Dirichlet boundary is a valid approximation for this simulation.

To further validate the numerical model, a comparison with the analytical solution as discussed in Eq. (4.9) is conducted. For comparison with the analytical solution, a homogeneous heat load of 25 W is dissipated across a YAG crystal rod of length 2 cm and diameter 0.4 cm. This heat load is continuous in time and fills the entire crystal aperture with a radius  $R_p = 0.2$  cm. Figure 4.10 shows the simulated temperatures as a cut through the crystal center along the  $x$ -axis. For the homogeneous heat profile, the temperature simulated numerically with the FDM model (blue dots) aligns well with the analytical calculation (black line), both indicating a peak temperature

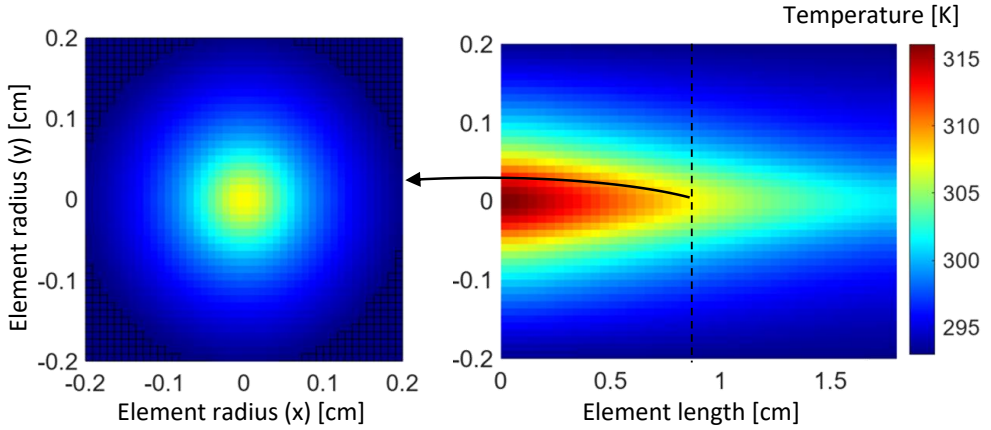


Figure 4.9: Simulated temperature as a three-dimensional distribution of the exemplary laser gain medium at the steady state.

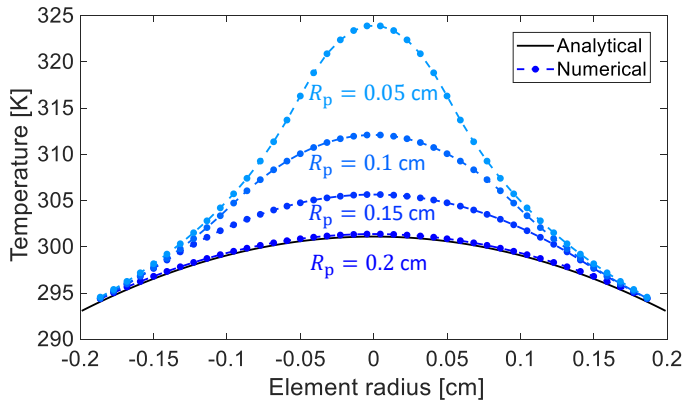


Figure 4.10: Validation of the numerical FDM-ADI model in comparison to the analytical solution for homogeneous heat loads. The numerical solution is depicted for different heat load diameters with a constant power dissipated in heat.

around 302 K. Additional numerical simulations for the same crystal are presented, where the total heat load of 25 W is dissipated over a smaller diameter at the center, with a radius reduced down to  $R_p = 0.05$  cm. Despite the crystal geometry and power dissipated in heat remaining constant, the temperature rises significantly, reaching a peak of 324 K at the smallest radius. This highlights the limitations of the analytical solution, which can only calculate homogeneous heat

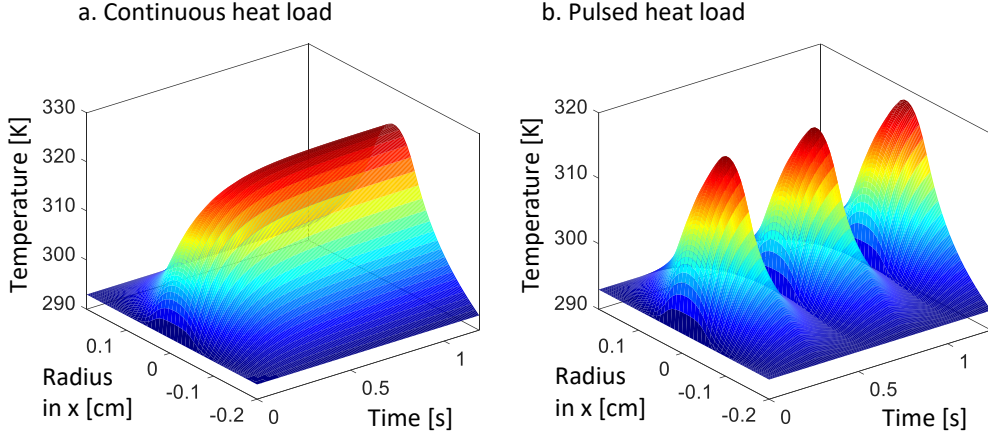


Figure 4.11: Temporal evolution of the temperature profile along the  $x$ -axis. The left graph (a) illustrates the case of a continuous heat load, while the right graph (b) demonstrates the dynamic behavior in the event of a temporally pulsed heat load.

loads. While there exist analytical models that consider the pump beam radius and deviations in the  $z$ -direction [137, 151], asymmetric and inhomogeneous heat loads require a numerical solution for sufficient accuracy within the scope of this work.

The numerical implementation using the FDM algorithm enables the analysis of temporal thermal behavior in the system, depending on the selected time step  $\Delta t$ . To avoid numerical errors, this time step must be small enough to satisfy the stability condition [141]

$$\frac{\lambda_{\text{th}} \Delta t}{(\min(\Delta x, \Delta y, \Delta z))^2} \leq \frac{1}{2}. \quad (4.33)$$

This equation is also referred to as the Courant–Friedrichs–Lewy condition (CFL) for diffusion problems, which must be considered for the solution to remain stable and accurate. Figure 4.11 compares a continuous heat load with a temporally varying load. The bulk material simulated is identical to the one used for the comparison with the analytical model at the smallest heat load radius  $R_p = 0.05$  cm. While the continuous heat load results in a steady-state solution after approximately 0.5 s of time elapsed, the pulsed load is applied repetitively at a frequency of 2 Hz and a duty cycle of 50 %. For this example, the time scale is chosen such that the pulsed heat source leads to a dynamic temperature profile in the crystal. However, for many laser systems relevant to this work, the steady-state solution is sufficient. For example, when

simulating a laser with a repetition rate of 50 kHz, the pulse-to-pulse time varies much faster than the thermal conduction process, resulting in the steady-state solution being an accurate approximation.

With the implementation of the FDM-ADI method, temperature distributions in bulk elements can be modeled numerically with high precision. In the following section, the displacement and stress resulting from thermal expansion will be added to the thermal sub-model.

## 4.3 Simulation of Three-Dimensional Displacement and Stress Distributions

In this section, the numerical solution to describe the displacement and stress distributions is provided. In subsection 4.3.1, the numerical solution to the Navier-Stokes equations for elasticity is discussed, resulting in the three-dimensional displacement distribution and resulting stresses in the material. Subsequently, an example simulation and validation of the model are conducted in subsection 4.3.2.

### 4.3.1 Numerical FDM Solution

In addition to the direct influence of the temperature distribution on the electromagnetic field (refer to sections 4.4.1 and 4.4.3), thermal expansion leads to stress responses in the bulk material, potentially affecting laser performance through additional mechanisms. The specific thermal effects like stress-induced birefringence will be discussed in section 4.4.2, while this section concentrates on the development of a comprehensive numerical displacement and stress model to complement the thermal submodel.

Thermal expansion causes displacements in the three-dimensional domain  $D_d(x, y, z)$ , represented at each point by  $u$  in the  $x$ -direction,  $v$  in the  $y$ -direction, and  $w$  indicating the displacement in the  $z$ -direction. A numerical solution must be obtained for the Navier-Stokes equations for elasticity, outlined in Eqs. (4.15) - (4.20). This task is more complex than solving the single second-order PDE that describes heat conduction, as it requires solving a set of coupled second-order hyperbolic PDEs. The generalized Navier-Stokes equation is typically

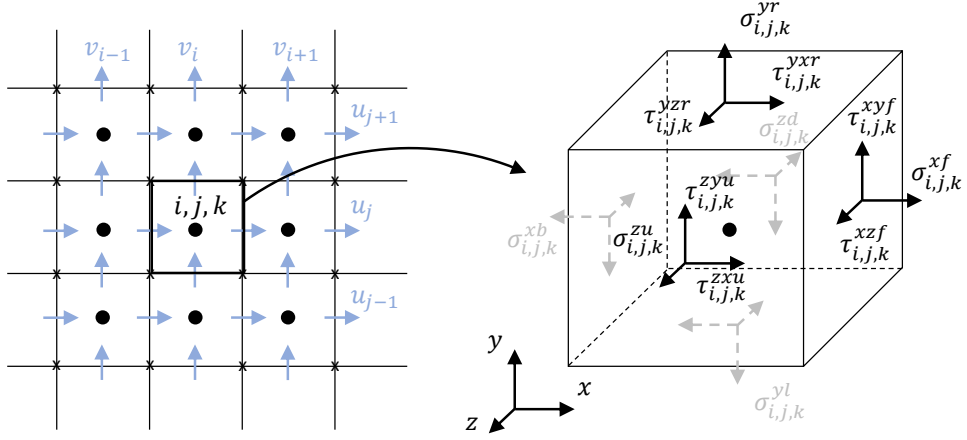


Figure 4.12: Staggered locations of the displacements  $u$  and  $v$  in a two-dimensional schematic illustration, showing the stress control volume at position  $i, j, k$  on the right hand side.

solved using FEM approaches. However, similar to the temperature distribution, FDM methods are viable and provide certain advantages. Although not as well-suited for complex geometries and boundary conditions, the FDM method is similar to the temperature solution and simpler to implement [141, 152]. This makes it particularly suitable for integration into the multi-physics approach of this work. The chosen method is a control volume FDM, based on the work of Hattel and Hansen [153], and operates similarly to the ADI approach discussed in the previous section. This method is adapted in the context of this work for bulk elements absorbing laser light.

Owing to the complexity of the PDE set, a staggered grid approach is utilized, in which each dependent variable uses a different grid [153, 154]. Figure 4.12 illustrates this approach, demonstrating how the  $x$ -direction displacement  $u$  is computed at the faces normal to the  $x$ -direction, and  $v$  is computed at the faces normal to the  $y$ -direction. The same applies to  $w$  in the  $z$ -direction, which is not depicted in the two-dimensional (2D) representation. The numerical solution is formulated for the static equilibrium of the stress components displayed on the right-hand side of Fig. 4.12 for a single control volume. Three types of control volumes are defined, as shown in Fig. 4.13, for the displacement (a), the normal stress components (b), and the shear stress components (c). The following equations describe the algorithm for a

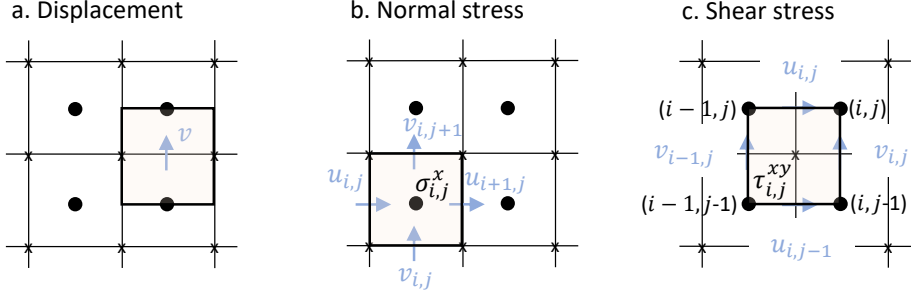


Figure 4.13: Different types of control volumes employed in the model approach: the control volume for the displacement (a), the control volume for normal stresses (b), and the shear stress control volume (c). Graph adapted from [153].

single iterative step in the  $x$ -direction, from which the solution of the  $y$ - and  $z$ -directions can be extrapolated equivalently. The formulation of the normal stress  $\sigma_{xx}$  is given in accordance with Hooke's law (Eqs. (4.12) - (4.14)):

$$\sigma_{xx} = \frac{E}{1+\nu} \left( 1 + \frac{\nu}{1-2\nu} \right) \frac{\partial u}{\partial x} \frac{E}{1+\nu} \frac{\nu}{1-2\nu} \left( \frac{\partial v}{\partial y} + \frac{\partial w}{\partial z} \right) - K \Delta T_x, \quad (4.34)$$

with

$$K = \frac{E \alpha_{th}}{1-2\nu}. \quad (4.35)$$

Subsequently, the M-terms are defined, which represent the resistance against the build-up of stress in the  $x$ -direction:

$$Mx_{i,j,k} = \Delta x / \left[ \frac{E_{i,j,k}}{1+\nu_{i,j,k}} \left( 1 + \frac{\nu_{i,j,k}}{1-2\nu_{i,j,k}} \right) \right], \quad (4.36)$$

$$Mvy_{i,j,k} = \Delta y / \left[ \frac{E_{i,j,k}}{1+\nu_{i,j,k}} \frac{\nu_{i,j,k}}{1-2\nu_{i,j,k}} \right], \quad (4.37)$$

$$Mvz_{i,j,k} = \Delta z / \left[ \frac{E_{i,j,k}}{1+\nu_{i,j,k}} \frac{\nu_{i,j,k}}{1-2\nu_{i,j,k}} \right], \quad (4.38)$$

$$Mxy_{i,j,k} = \Delta y / \left[ \frac{E_{i-1,j,k}}{4(1 + \nu_{i-1,j,k})} + \frac{E_{i,j,k}}{4(1 + \nu_{i,j,k})} \right] , \quad (4.39)$$

$$Mxz_{i,j,k} = \Delta z / \left[ \frac{E_{i-1,j,k}}{4(1 + \nu_{i-1,j,k})} + \frac{E_{i,j,k}}{4(1 + \nu_{i,j,k})} \right] . \quad (4.40)$$

The discretization of material parameters  $E$  and  $\nu$  allows for the treatment of problems with non-uniform material data, such as at material interfaces.

The normal stress component  $\sigma_{xx}$  of Eq. (4.34) can be reformulated in a discretized form using these resistances such that

$$\sigma_{i,j,k}^{xx} = \frac{u_{i+1,j,k} - u_{i,j,k}}{Mx_{i,j,k}} + \frac{v_{i,j+1,k} - v_{i,j,k}}{My_{i,j,k}} + \frac{w_{i,j,k+1} - w_{i,j,k}}{Mz_{i,j,k}} - K\Delta_x T_{i,j,k} . \quad (4.41)$$

For a single volume element as illustrated in Fig. 4.12, the equilibrium equation in the  $x$ -direction is then derived by

$$\frac{\sigma_{xf} - \sigma_{xb}}{\Delta x} + \frac{\tau_{yxr} - \tau_{yxl}}{\Delta y} + \frac{\tau_{z xu} - \tau_{z xd}}{\Delta z} = 0 . \quad (4.42)$$

In this formulation, the stress components labeled with  $f$  and  $b$  correspond to the neighboring volumes in the  $x$ -direction, while  $r$  and  $l$  are the volumes in the  $y$ -direction, and  $u$  and  $d$  are the volumes in the  $z$ -direction, as depicted in Fig. 4.12 on the stress volume. Similar formulations apply to the  $y$ - and  $z$ -directions. The discretized equilibrium equations can then be reformulated in terms of coefficients  $a$ . For the equilibrium in  $x$ , the components  $\sigma_{xf}$ ,  $\sigma_{xb}$ ,  $\sigma_{yr}$ ,  $\sigma_{yl}$ ,  $\sigma_{zu}$ , and  $\sigma_{zd}$ , denote the normal stress components of the neighboring control volumes to the central control volume coefficient  $a_p$ , and the shear stress components are termed accordingly. The general equation to be solved can consequently be written as [153, 155]

$$a_p D_p = \sum_{nb} a_{nb} D_{nb} + b . \quad (4.43)$$

Here,  $D_p$  is the unknown displacement of the central point (depending on the direction),  $a_{nb}$  are the coefficients of the neighboring control volumes,  $D_{nb}$  is the unknown displacement value at the neighboring volumes, and  $b$  is a source term independent of  $D$ . Equation (4.42) can then be reformulated with the corresponding neighboring volumes, resulting in

$$-a_{xb} D_{xb} + a_{xp} D_{xp} - a_{xf} D_{xf} = a_{xr} D_{xr} + a_{xl} D_{xl} + a_{xu} D_{xu} + a_{xd} D_{xd} + b^x . \quad (4.44)$$

This equation describes the split step in the  $x$ -direction, with the formulations for the  $y$ - and  $z$ -directions being similarly defined to calculate steps 2 and 3 of the ADI-like approach. The coefficients are identified by discretizing all stress components in the given equilibrium equation, resulting in

$$a_{i,j,k}^{xp} = \frac{2}{2\Delta x M x_{i,j,k}} + \frac{2}{2\Delta x M x_{i-1,j,k}} + \frac{2}{\Delta y (M x y_{i,j+1,k} + M x y_{i,j,k})} + \frac{2}{\Delta y (M x y_{i,j,k} + M x y_{i,j-1,k})} + \frac{2}{\Delta z (M x z_{i,j,k+1} + M x y_{i,j,k})} + \frac{2}{\Delta z (M x z_{i,j,k} + M x y_{i,j,k-1})}, \quad (4.45)$$

$$a_{i,j,k}^{xf} = \frac{2}{2\Delta x M x_{i+1,j,k}}, \quad (4.46)$$

$$a_{i,j,k}^{xb} = \frac{2}{2\Delta x M x_{i-1,j,k}}, \quad (4.47)$$

$$a_{i,j,k}^{xr} = \frac{2}{\Delta y (M x y_{i,j+1,k} + M x y_{i,j,k})}, \quad (4.48)$$

$$a_{i,j,k}^{xl} = \frac{2}{\Delta y (M x y_{i,j,k} + M x y_{i,j-1,k})}, \quad (4.49)$$

$$a_{i,j,k}^{xu} = \frac{2}{\Delta z (M x z_{i,j+1,k} + M x y_{i,j,k})}, \quad (4.50)$$

$$a_{i,j,k}^{xu} = \frac{2}{\Delta z (M x z_{i,j,k} + M x y_{i,j-1,k})}. \quad (4.51)$$

The source term  $b^x$  encompasses the coupling to the displacements in the  $y$ - and  $z$ -directions  $v$  and  $w$ , as well as to the thermal expansion in the  $x$ -direction from temperature difference  $\Delta_x T$ , and is expressed as

$$b_{i,j,k}^x = f_{i,j,k}^{xv1} v_{i-1,j,k} + f_{i,j,k}^{xv2} v_{i,j,k} + f_{i,j,k}^{xv3} v_{i-1,j+1,k} + f_{i,j,k}^{xv4} v_{i,j+1,k} + f_{i,j,k}^{xw1} w_{i-1,j,k} + f_{i,j,k}^{xw2} w_{i,j,k} + f_{i,j,k}^{xw3} w_{i-1,j,k+1} + f_{i,j,k}^{xw4} w_{i,j,k+1} + g f_{i,j,k} + g b_{i,j,k}, \quad (4.52)$$

with the source term coefficients:

$$f_{i,j,k}^{xv1} = \frac{2}{2\Delta x M v y_{i-1,j,k}} + \frac{2}{\Delta y (M y x_{i,j,k} + M y x_{i-1,j,k})}, \quad (4.53)$$

$$f_{i,j,k}^{xv2} = \frac{2}{2\Delta x M v y_{i,j,k}} - \frac{2}{\Delta y (M y x_{i,j,k} + M y x_{i-1,j,k})}, \quad (4.54)$$

$$f_{i,j,k}^{xv3} = \frac{2}{2\Delta x M v y_{i-1,j,k}} - \frac{2}{\Delta y (M y x_{i,j+1,k} + M y x_{i-1,j+1,k})}, \quad (4.55)$$

$$f_{i,j,k}^{xv4} = \frac{2}{2\Delta x M v y_{i,j,k}} + \frac{2}{\Delta y (M y x_{i,j+1,k} + M y x_{i-1,j+1,k})}, \quad (4.56)$$

$$f_{i,j,k}^{xw1} = \frac{2}{2\Delta x M v z_{i-1,j,k}} + \frac{2}{\Delta z (M z x_{i,j,k} + M z x_{i-1,j,k})}, \quad (4.57)$$

$$f_{i,j,k}^{xw2} = \frac{2}{2\Delta x M v z_{i,j,k}} - \frac{2}{\Delta z (M z x_{i,j,k} + M z x_{i-1,j,k})}, \quad (4.58)$$

$$f_{i,j,k}^{xw3} = \frac{2}{2\Delta x M v z_{i-1,j,k}} - \frac{2}{\Delta z (M z x_{i,j,k+1} + M z x_{i-1,j,k+1})}, \quad (4.59)$$

$$f_{i,j,k}^{xw4} = \frac{2}{2\Delta x M v z_{i,j,k}} + \frac{2}{\Delta z (M z x_{i,j,k+1} + M z x_{i-1,j,k+1})}, \quad (4.60)$$

$$g f_{i,j,k} = \frac{K_{i,j,k}}{\Delta x} \Delta_x T_{i,j,k}, \quad (4.61)$$

$$g b_{i,j,k} = -\frac{K_{i-1,j,k}}{\Delta x} \Delta_x T_{i-1,j,k}. \quad (4.62)$$

With these definitions, the first equilibrium equation is discretized and can be solved as the first step of the ADI approach, with steps 2 and 3 proceeding according to their respective spatial directions. The formulation of Eq. (4.44) results in a tridiagonal matrix with an implicit left side, analogous to the temperature ADI, and can be efficiently solved using Gaussian elimination [147].

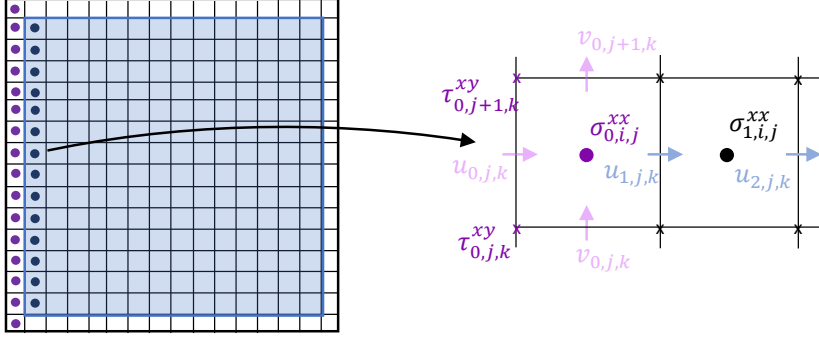


Figure 4.14: Depiction of the boundary for the displacement simulation, where outer displacement and stress nodes (in purple) have to be extrapolated.

However, for a complete solution the behavior at the boundary has to be discussed first. Two types of boundary conditions exist: prescribed stresses and prescribed displacements, with the stresses potentially being either normal or shear. Figure 4.14 illustrates an exemplary boundary in two dimensions, demonstrating the fundamental approach of extrapolating outer nodes for inclusion in the tridiagonal matrices [156]. The case of prescribed displacements is the most straightforward, as the values at the boundary can be interpolated between the prescribed and inner displacements. For instance, for the  $x$ -boundary, this results in

$$u_{1,j,k} = u_{0,j,k} + \frac{u_{2,j,k} - u_{0,j,k}}{2}, \quad (4.63)$$

where  $u_{0,j,k} = \bar{u}_{xf}$  represents the prescribed displacement in the  $xf$ -direction at a constant spacing  $\Delta x$ . The adjusted equilibrium equation in the  $x$ -direction can then be described at the boundary by adjusting the coefficients with superscript '\*'. This leads to adapted coefficients for the equilibrium equation at step 1 as follows:

$$b_{0,j,k}^{x*} = b_{0,j,k}^{x*} + 2a_{0,j,k}^{xf}u_{0,j,k}, \quad (4.64)$$

$$a_{0,j,k}^{xf*} = 0. \quad (4.65)$$

The case of the prescribed stresses is not as straightforward. Here, the boundary nodes for the normal stress  $\sigma_{0,i,j}^{xx}$  and shear stress  $\tau_{0,i,j}^{xy}$  must be approximated by linear extrapolation. More detailed explanations of the extrapolation processes for such boundary conditions are provided

in references [153] and [157]. In short, the coefficients of the equilibrium equations must be adjusted, similarly to the prescribed displacements. For step 1, for example, the equilibrium in  $x$  results in

$$a_{0,j,k}^{xp*} = a_{0,j,k}^{xp} - a_{0,j,k}^{xf} \left( 1 + \frac{1}{3} \frac{Mx_{0,j,k}}{Mx_{1,j,k}} \right), \quad (4.66)$$

$$a_{0,j,k}^{xb*} = a_{0,j,k}^{xb} - a_{0,j,k}^{xf} \left( 1 + \frac{1}{3} \frac{Mx_{0,j,k}}{Mx_{1,j,k}} \right), \quad (4.67)$$

$$b_{0,j,k}^{x*} = b_{0,j,k}^{x*} + a_{0,j,k}^{xf} \frac{2Mx_{0,j,k}}{3} \left[ \frac{2}{3} \left( \frac{v_{0,j+1,k} - v_{0,j,k}}{Mvy_{0,j,k}} + \frac{w_{0,j,k+1} - w_{0,j,k}}{Mvz_{0,j,k}} - K_{0,j,k} \Delta_x T_{0,j,k} \right) - \frac{1}{2} \left( \frac{v_{1,j+1,k} - v_{1,j,k}}{Mvy_{1,j,k}} + \frac{w_{1,j,k+1} - w_{1,j,k}}{Mvz_{1,j,k}} - K_{1,j,k} \Delta_x T_{1,j,k} \right) - \sigma_{0,i,j}^{xx} \right]. \quad (4.68)$$

The displacements and stresses in  $y$ - and  $z$ -direction on the 'xf' boundary are considered similarly, with additional adjustments to the equilibrium coefficients. This is applicable to all boundaries in the three directions, resulting in the formulation of the complete solution.

### 4.3.2 Example and Submodel Validation

With the behavior of the model at the boundary defined, the tridiagonal matrix for each ADI step can be updated iteratively until a steady state solution is achieved, leading to a three-dimensional description of the displacements in the  $x$ -,  $y$ -, and  $z$ -directions. The displacement distribution in the  $x$ -direction for the temperature distribution from Fig. 4.9 is plotted in Fig. 4.15 for the same laser operation point. In this instance, the boundary is set to a prescribed displacement of zero in the  $x$ - and  $y$ -directions and a free boundary in the  $z$ -direction (prescribed stresses equal zero). The values of elastic modulus  $E$  and Poisson's ratio  $\nu$  are taken from Tab. 4.1 (section 4.2.2) for the rod material YAG. To calculate the stress tensor, described in Eq. (4.11), from the simulated displacement distributions, an analytical calculation utilizing Hook's law is conducted. Here, the staggered grid must be taken into account, where the control volumes of stress and strain components must be considered separately. Figure 4.16 depicts the calculated three-dimensional distribution of the normal stress in the  $x$ -direction for the corresponding displacements. Unlike

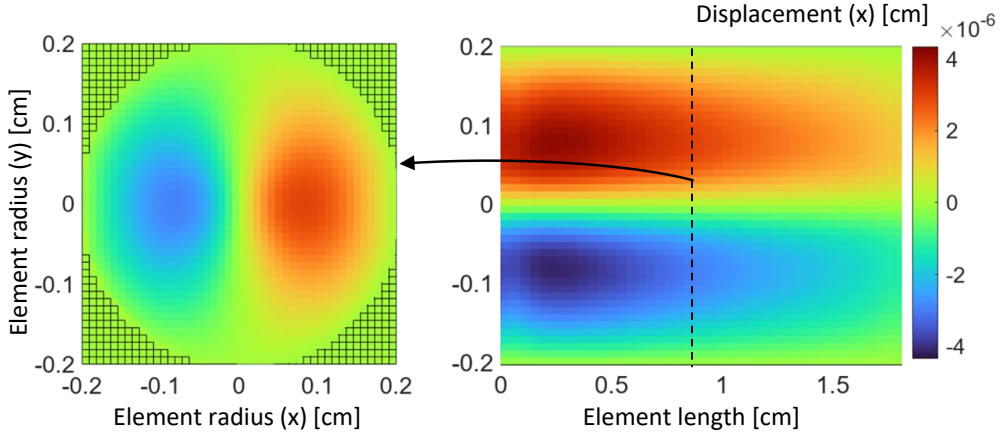


Figure 4.15: Simulated displacement in the  $x$ -direction as a three-dimensional distribution of the exemplary laser gain medium at the steady state.

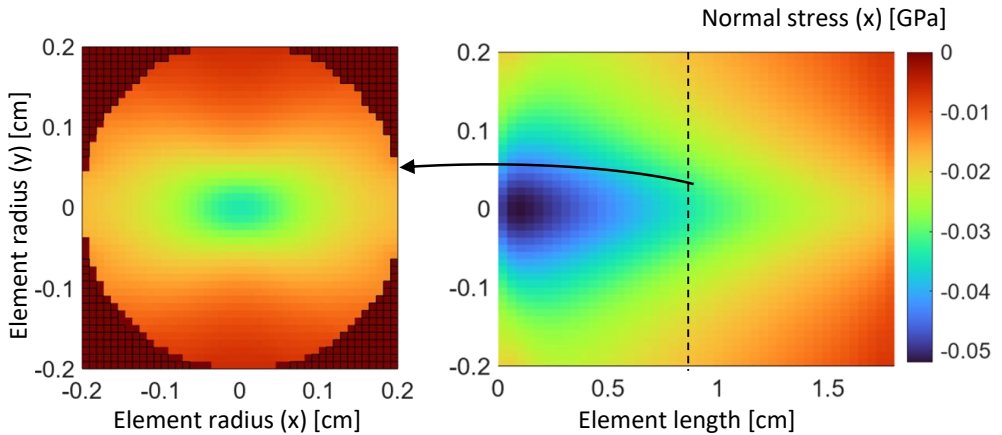


Figure 4.16: Simulated normal stress in the  $x$ -direction as a three-dimensional distribution of the exemplary laser gain medium at the steady state.

the numerical FDM that describes the temperature distribution, the displacement method does not provide a temporal solution itself, but rather takes into account an equilibrium of volume forces only. Consequently, the temporal behavior of displacement and stress is coupled to the temporal evolution of the temperature profile. In essence, when the temporal displacement and

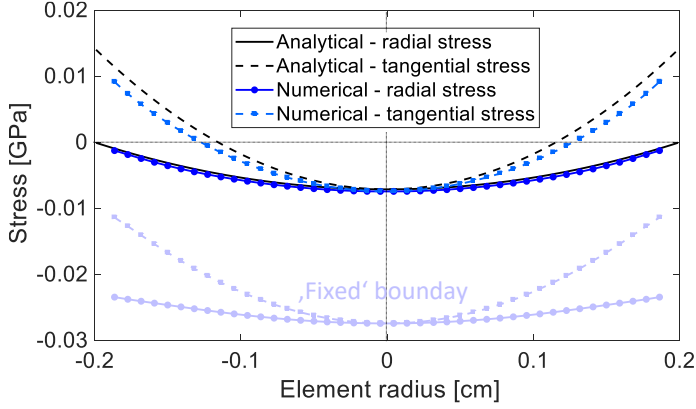


Figure 4.17: Validation of the numerical displacement and stress model in comparison to the analytical solution for homogeneous heat loads and free boundaries. Additionally, the numerical solution is depicted for the case of a fixed boundary.

stress evolution is required, the displacement FDM must be resolved at every iterative time step  $\Delta t$  of the heat equation FDM.

The numerical model can once again be compared with the analytical solutions outlined in Eqs. (4.21) - (4.23), provided a homogeneous heat load and no asymmetries are assumed. The radial and tangential stress components of the numerical solution can be calculated from the stress tensor  $\sigma_{dd}$  by

$$\sigma_r(x, y, z) = \frac{\sigma_{xx}(x, y, z) + \sigma_{yy}(x, y, z)}{2} + \frac{\sigma_{xx}(x, y, z) - \sigma_{yy}(x, y, z)}{2} \sin(2\theta_r) - \tau_{xy}(x, y, z) \sin(2\theta_r), \quad (4.69)$$

$$\sigma_t(x, y, z) = \frac{\sigma_{xx}(x, y, z) + \sigma_{yy}(x, y, z)}{2} - \frac{\sigma_{xx}(x, y, z) - \sigma_{yy}(x, y, z)}{2} \sin(2\theta_r) + \tau_{xy}(x, y, z) \sin(2\theta_r), \quad (4.70)$$

where  $\theta_r$  is the polar angle of the  $x$ - $y$ -plane, relative to the rod center. Figure 4.17 presents the comparison of the radial and tangential stress components with the analytical solutions for a one-dimensional cut through the rod center. The rod has been simulated with a homogeneous heat load filling the entire rod aperture with  $R_p = 0.2$  cm. For a free boundary, the methods

align closely, with small deviations in the tangential stress. The analytical solution again has significant limitations, where asymmetric temperature profiles cannot be easily considered [158]. Further, the case of a 'fixed' boundary in the  $x$ - and  $y$ -directions ( $u_{0,j,k} = 0$ ,  $v_{i,0,k} = 0$ , etc.) is plotted in the same graph in light blue, showing an increase in internal stress, which cannot be replicated by the analytical solution provided.

In conclusion, comprehensive methods for numerically simulating the temperature, displacement, and stress distributions in bulk elements have been introduced. In the subsequent sections, thermal effects derived from these distributions are implemented into the model, further enhancing the capabilities of the multi-physics model.

## 4.4 Resulting Thermal Effects Impacting Laser Performance

This section discusses the implementation of thermal effects relevant to laser systems that arise from the simulated temperature, displacement, and stress distributions. The temperature dependency of material parameters is discussed in subsection 4.4.1. The subsequent subsections consider thermo-optic effects, with stress-induced birefringence discussed in subsection 4.4.2 and thermal lensing in subsection 4.4.3.

### 4.4.1 Temperature-Dependent Material Parameters

As previously noted, the heating of bulk media in the laser beam path impacts both the material itself and the corresponding light-matter interaction. One such impact is the dependency of material parameter values on the temperature of the bulk material. Depending on the levels of power absorption and resulting temperatures, these dependencies can significantly affect laser performance. All material parameters exhibit some degree of temperature dependency, with some changing more than others; however, it is challenging to account for all dependencies in this model approach, given that the behavior is not always known for all parameters and may vary for different types of bulk material. This section details only the most straightforward or most important dependencies. The temperature dependency is provided for two types of parameters: thermal parameters that impact the thermal simulations themselves, and spectral parameters, which affect the electromagnetic field. The model can be expanded to

include more dependencies, for instance, if the temperature behavior for a parameter specific to a material is described in literature, a fit can be used to incorporate this behavior into the model.

The thermal parameters include the heat capacity  $C_p$  and the thermal conductivity  $k_{th}$ . As these parameters are used in the numerical model of the temperature distribution, the values must be updated iteratively with the temperature FDM to account for the actual thermal behavior of the material. This is implemented by a three-dimensional matrix representation of the parameters in  $x$ ,  $y$ , and  $z$ . The dependency of the two mentioned parameters can be estimated by the Debye model for solid materials, which relates the atom lattice phonons to the parameter values [159]. Therefore, this dependency can be calculated universally for all solid materials and does not need to be approximated by a fit from measured values. The discretized specific heat capacity  $C_p$  is given by [61]

$$C_p(x, y, z, T) = C_{\max} f_D(x, y, z, T) , \quad (4.71)$$

where  $C_{\max} = 628.5 \text{ J/(kg K)}$  is the heat capacity of YAG at Debye temperature  $\Theta_D$  and  $f_D$  is the Debye function as follows:

$$f_D(x, y, z, T) = 3 \left[ \frac{T(x, y, z)}{\Theta_D} \right]^3 \int_0^{\Theta_D/T(x, y, z)} \frac{i^4 \exp(i)}{(\exp(i) - 1)^2} di . \quad (4.72)$$

The additional values for the temperature dependency of YAG have been listed in Tab. 4.1 (section 4.2.2). The dependency of the thermal conductivity  $k_{th}$  is described in relation to the temperature-dependent heat capacity by [61]

$$k_{th}(x, y, z, T) = k_{th}(T_0) \frac{C_p(x, y, z, T) g_D(x, y, z, T_0)}{C_p(x, y, z, T_0) g_D(x, y, z, T)} , \quad (4.73)$$

where  $T_0 = 300 \text{ K}$  for the values given in Tab. 4.1 and the specific Debye function  $g_D$  is given by

$$g_D(x, y, z, T) = \left[ \frac{T(x, y, z)}{\Theta_D} \right]^3 \int_0^{\Theta_D/T(x, y, z)} \frac{i^2}{\exp(i) - 1} di . \quad (4.74)$$

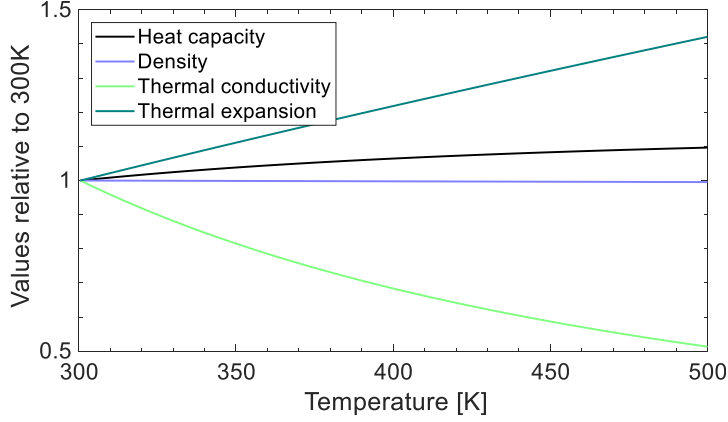


Figure 4.18: Temperature dependency of the material parameters relevant to the thermal submodels, including the heat capacity (black line), density (blue line), thermal conductivity (green line), and thermal expansion (cyan line).

In addition to the discussed parameters, the temperature dependency of the density  $\rho$  can be calculated from the thermal expansion  $\alpha_{th}$  by

$$\rho(x, y, z, T) = \rho(T_0) [1 - 3\alpha_{th}(T(x, y, z) - T_0)] . \quad (4.75)$$

The behavior of these thermal parameters is depicted in Fig. 4.18 for YAG, across a temperature range of 300 to 500 K. The black curve describes the heat capacity behavior, the blue curve represents density, and the green curve describes the thermal conductivity. The thermal conductivity exhibits a significant temperature dependency, with the value nearly halving across the full range, while the density and heat capacity do not show such a strong dependency. The dependency of the thermal expansion  $\alpha_{th}$  is also plotted, represented by the cyan curve. Unlike the other parameters, the behavior of this parameter is not described by an universal model but is fitted from measured values. The temperature dependency for YAG is adopted from reference [160] and fitted by

$$\alpha_{th} = B_{\alpha} C_{\alpha} T(x, y, z)^{C_{\alpha}-1} , \quad (4.76)$$

with dimensionless coefficient  $C_{\alpha} = 1.69$  and coefficient  $B_{\alpha} = 9E-8 \text{ K}^{-C_{\alpha}}$  describing the parameter behavior for YAG according to the reference values.

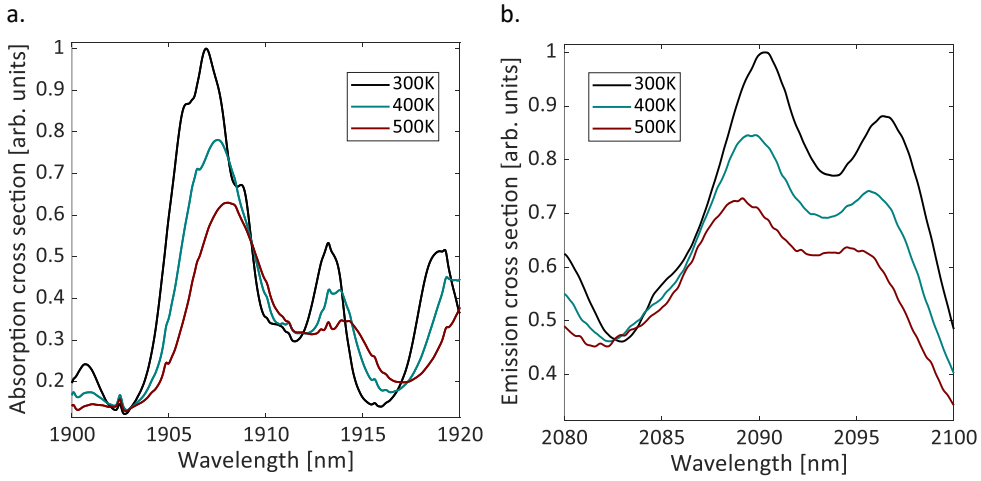


Figure 4.19: Temperature dependency of the absorption (a) and emission (b) cross sections for Ho<sup>3+</sup>:YAG over the respective wavelength ranges for pump and laser wavelengths.

Besides the thermal parameters for bulk elements, certain spectroscopic material parameters, specific to the laser gain medium, also exhibit a strong temperature dependency. The most significant impact on laser performance comes from the dependency of the emission and absorption cross sections. The absorption cross section behavior of Ho<sup>3+</sup>:YAG is plotted in Fig. 4.19a, in the pump wavelength range of 1900 to 1920 nm, displayed in normalized values relative to the peak at 300 K. The emission cross section behavior is plotted in the right graph (b) for a wavelength range of 2080 to 2100 nm. The cross section curves have been measured for a temperature range from 300 to 500 K, and show a strong dependency on temperature with the pump absorption and laser emission values decreasing, which generally leads to a deterioration in laser performance. For straightforward implementation into the model, linear interpolation is employed to calculate the cross section values  $\sigma_{a,e}(\lambda, T)$  for the specific bulk material temperature distribution. In addition to measurement, the temperature dependency could be approximated by the spectral theory developed by M. Eichhorn et al., as cited in reference [161]. This model takes into account the changes in line position and line broadening of the specific laser level transitions contributing to the full cross section range, according to the Boltzmann occupation factors. However, precise line position and transition strength data for the full spectrum of the gain medium are necessary to implement this approach and it is not considered further for this work.

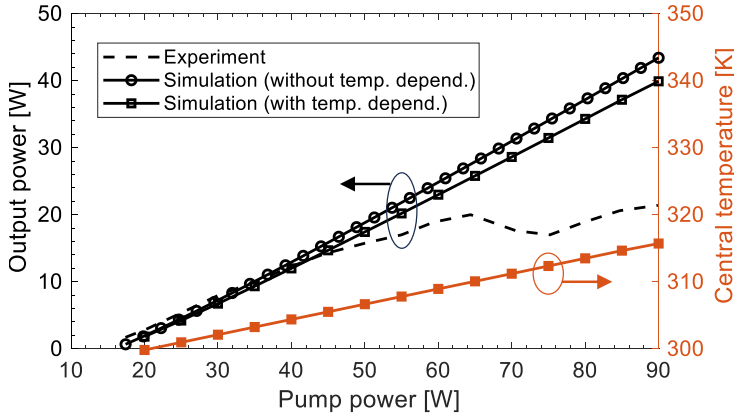


Figure 4.20: Impact of temperature-dependent material parameters on the laser resonator model, shown with the change of output power for the exemplary  $\text{Ho}^{3+}:\text{YAG}$  resonator. The corresponding temperature in the crystal center is plotted with the orange curve.

With the implementation of the discussed temperature dependency into the multi-physics model, a more accurate model representation can be expected [162]. Figure 4.20 compares the change in output power against the launched pump power for the exemplary laser resonator discussed in section 3.6. The power curves are plotted in black, with the dotted line corresponding to the experimentally measured values. The solid line with circular plot markers corresponds to the simulated values before the inclusion of temperature-dependent material parameters (using fixed values at 300 K), while the solid line with square markers represents the model with the temperature dependency included. The graph also depicts the temperature increase at the crystal center, represented by the orange line. As expected, the temperature rises steadily with increased pump power launched on the crystal, reaching a peak central temperature of 316 K at a pump power of 90 W. Since this temperature increase is relatively low for high-power applications, the output behavior does not change drastically. It can be observed that the laser slope efficiency decreases, aligning more closely with the experimental results. However, the simulation does not yet show thermal roll-over, a point further discussed in the subsequent sections.

For the model to achieve highest accuracy, the temperature dependency of other material parameters might be worth considering as well. For instance, the rate of thermal change in refractive index  $dn/dT$ , and rates for upconversion  $ETU$  and cross relaxation of the laser gain medium can influence laser performance. If the temperature dependency of these values is

known from literature, a fit similar to the one outlined for thermal expansion can be implemented. For this work, these additional influences are not taken into account but could be one way to further improve the model accuracy.

#### 4.4.2 Stress-Induced Birefringence and Depolarization

An additional thermal effect that impacts the performance of bulk solid-state laser systems is stress-induced birefringence and subsequent depolarization. The interaction between the electromagnetic field and anisotropic media has been discussed in more detail in section 2.3. In that section, it was determined that the refractive index can exhibit anisotropic behavior, as described by the optical indicatrix of the material. As an example, for YAG, which is naturally an isotropic material, the equation for the undisturbed indicatrix is as follows:

$$B_{00}(x^2 + y^2 + z^2) = 1 . \quad (4.77)$$

Here, the indicatrix coefficient  $B_{00} = B_{11} = B_{22} = B_{33}$  represents a component of the relative dielectric impermeability tensor  $B_{dd}$ . In the isotropic case, the indicatrix corresponds to the equation of a sphere. However, under stress, the indicatrix deforms locally which can be expressed with the model developed by Koechner et al. [37]:

$$B_{11}x^2 + B_{22}y^2 + B_{33}z^2 + 2B_{12}xy + 2B_{13}xz + 2B_{23}yz = 1 . \quad (4.78)$$

The coefficients of the dielectric impermeability tensor are derived from either the local stress tensor  $\sigma_{ij}$  and the piezooptic tensor  $\pi_{mn}$ , or the strain tensor  $\epsilon_{ij}$  and the photo-elastic tensor  $p_{mn}$ . The subsequent implementation will consider only the piezooptic tensor, a material parameter that describes the piezooptic response of a material.

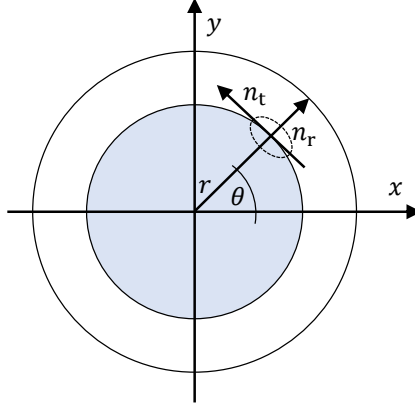


Figure 4.21: Local variation of the indicatrix resulting from thermal stress in an end-pumped laser rod, represented by radial and tangential refractive indices.

When expanded in matrix form, the impermeability is described with

$$\begin{pmatrix} B_{11} \\ B_{22} \\ B_{33} \\ B_{12} \\ B_{13} \\ B_{23} \end{pmatrix} = \begin{pmatrix} B_{0,11} \\ B_{0,22} \\ B_{0,33} \\ 0 \\ 0 \\ 0 \end{pmatrix} + \begin{pmatrix} \pi_{11} & \pi_{12} & \pi_{13} & \pi_{14} & \pi_{15} & 0 \\ \pi_{12} & \pi_{11} & \pi_{13} & -\pi_{14} & -\pi_{15} & 0 \\ \pi_{13} & \pi_{13} & \pi_{33} & 0 & 0 & 0 \\ \pi_{14} & -\pi_{14} & 0 & \pi_{44} & 0 & -\pi_{15} \\ \pi_{15} & -\pi_{15} & 0 & 0 & \pi_{44} & \pi_{14} \\ 0 & 0 & 0 & -\pi_{15} & \pi_{14} & \pi_{66} \end{pmatrix} \begin{pmatrix} \sigma_{xx} \\ \sigma_{yy} \\ \sigma_{zz} \\ \tau_{xy} \\ \tau_{xz} \\ \tau_{yz} \end{pmatrix}. \quad (4.79)$$

While the piezooptic effect, which describes the change of refractive index caused by internal pressure in the material, is present in all solids, it is especially relevant for crystals that exhibit high piezooptic coefficients, such as YAG.

The impermeability matrix of Eq. (4.79) allows for the description of local birefringence variation in an end-pumped laser rod. Figure 4.21 provides a schematic illustration of such a rod, where the local indicatrix is now given for the radial and tangential refractive index components  $n_r$  and  $n_t$ . This representation is specific to rods with lateral cooling applied, as different geometries can lead to a more complex indicatrix change, which must be modeled

Table 4.2: Coefficients of the piezooptic tensor for the bulk crystal YAG. Values taken from [163].

Parameters	YAG values	Units
$\pi_{11}$	$-0.30285E-12$	$\text{m}^2/\text{N}$
$\pi_{12}$	$0.11158E-12$	$\text{m}^2/\text{N}$
$\pi_{13}$	$0.17187E-12$	$\text{m}^2/\text{N}$
$\pi_{33}$	$-0.36313E-12$	$\text{m}^2/\text{N}$
$\pi_{44}$	$-0.14693E-12$	$\text{m}^2/\text{N}$
$\pi_{66}$	$-0.20722E-12$	$\text{m}^2/\text{N}$
$\pi_{14}$	$-0.08525E-12 \cos(3\varphi)$	$\text{m}^2/\text{N}$
$\pi_{15}$	$-0.08525E-12 \sin(3\varphi)$	$\text{m}^2/\text{N}$

accordingly. Given the cylindrical crystal geometry, the refractive index components can be calculated similarly to the radial and tangential stress components of Eqs. (4.69) and (4.70). After discretization, the polar impermeability is described by [163, 164]

$$B_r(x, y, z) = \frac{1}{2}[(B_{11}(x, y, z) + B_{22}(x, y, z)) + \sqrt{(B_{11}(x, y, z) - B_{22}^2(x, y, z)) + 4B_{12}^2(x, y, z)}], \quad (4.80)$$

$$B_t(x, y, z) = \frac{1}{2}[(B_{11}(x, y, z) + B_{22}(x, y, z)) - \sqrt{(B_{11}(x, y, z) - B_{22}^2(x, y, z)) + 4B_{12}^2(x, y, z)}], \quad (4.81)$$

which results in the polar refractive index components

$$n_r(x, y, z) = \frac{1}{\sqrt{B_r(x, y, z)}}, \quad (4.82)$$

$$n_t(x, y, z) = \frac{1}{\sqrt{B_t(x, y, z)}}. \quad (4.83)$$

With the equations outlined so far, the refractive index profile resulting from thermal stresses can be modeled. Table 4.2 lists the coefficient values of the piezooptic tensor for YAG, as

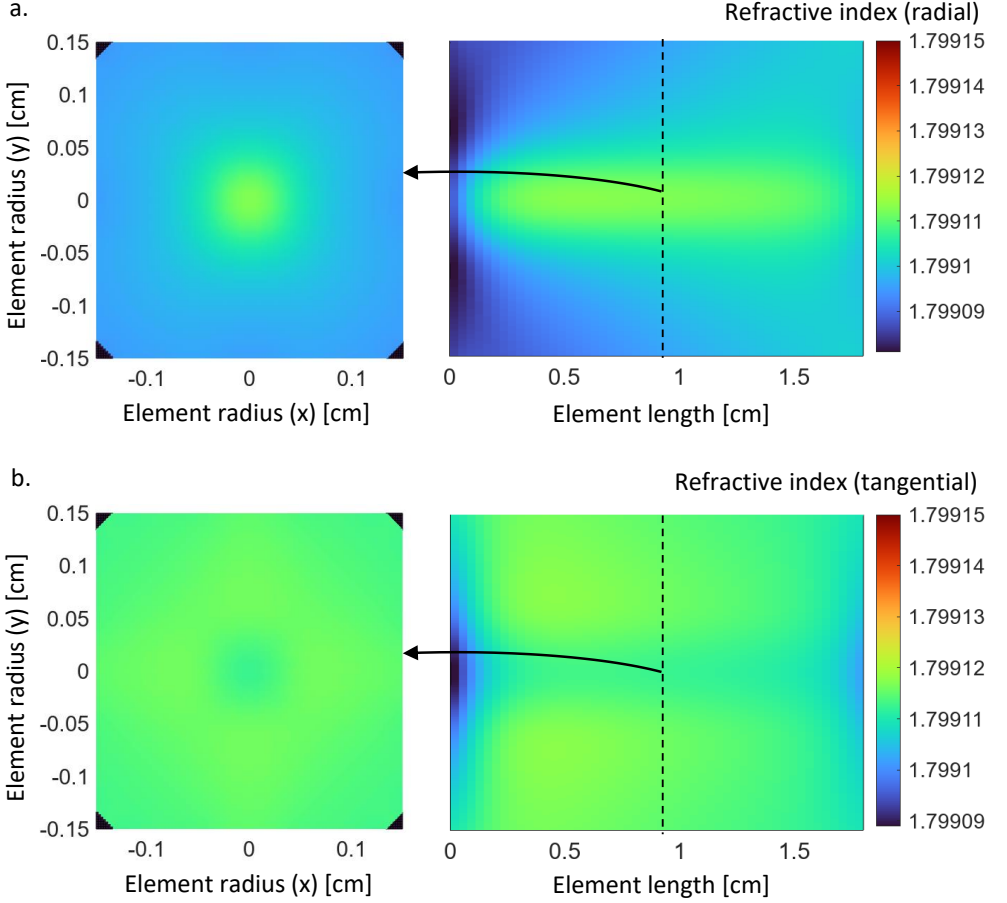


Figure 4.22: Simulated radial (a) and tangential (b) refractive index components as three-dimensional distributions of the exemplary laser gain medium.

described in reference [163]. Here,  $\varphi$  represents the cut angle of the crystal relative to the  $[101]$  lattice direction.

The three-dimensional distributions of the refractive index are depicted in Fig. 4.22 for the exemplary laser resonator previously discussed, at a pump power of 45 W. The upper graph (a) shows the radial component of the refractive index, while the lower graph (b) provides the tangential component. Until now, the interaction of the vectorial electromagnetic field  $\mathbb{E}_{x,y}(x,y)$  with transparent refractive media was considered for the  $x$  and  $y$  components of the refractive

index. However, to include stress-induced birefringence, the polar components must be taken into account following the Jones calculus convention. This is done for each slice  $\Delta z$  of the bulk material, along the propagation axis of the beam.

Initially, the local phase delay  $\Delta w(x, y)$  matrix is calculated from the polar refractive index components  $n_{r,t}$  and the polar angle  $\theta$  as follows [165]:

$$\begin{pmatrix} \Delta w_{xx}(x, y) & \Delta w_{xy}(x, y) \\ \Delta w_{yx}(x, y) & \Delta w_{yy}(x, y) \end{pmatrix} = \begin{pmatrix} -\cos(\theta) & -\sin(\theta) \\ \sin(\theta) & -\cos(\theta) \end{pmatrix} \begin{pmatrix} \exp[-i\Delta z k n_r(x, y)] & 0 \\ 0 & \exp[-i\Delta z k n_t(x, y)] \end{pmatrix} \begin{pmatrix} \cos(\theta) & \sin(\theta) \\ -\sin(\theta) & \cos(\theta) \end{pmatrix}. \quad (4.84)$$

Here, the middle term represents the Jones matrix of the refractive index contribution, while the outer matrices transform the polar coordinates back to the Cartesian coordinates of the electromagnetic field. The polarization components of the field after propagation  $\mathbb{E}_{x,y}^*(x, y)$  are then determined by

$$\begin{pmatrix} \mathbb{E}_x^*(x, y) \\ \mathbb{E}_y^*(x, y) \end{pmatrix} = \begin{pmatrix} \Delta w_{xx}(x, y) & \Delta w_{xy}(x, y) \\ \Delta w_{yx}(x, y) & \Delta w_{yy}(x, y) \end{pmatrix} \begin{pmatrix} \mathbb{E}_x(x, y) \\ \mathbb{E}_y(x, y) \end{pmatrix}. \quad (4.85)$$

This incorporates the stress-induced birefringence into the propagation algorithm, enabling the modeling of polarization dependent effects such as depolarization losses and resulting field distortions like astigmatism.

As a consequence of the refractive index distributions calculated for the laser resonator from Fig. 4.22, the corresponding depolarization can be simulated. The field ejected at the intracavity linear polarizer is displayed in Fig. 4.23 on the right hand side. Above the simulated field, the ejected field measured in the corresponding experiment is presented, validating that the implemented birefringence model functions as expected. At the pump power of 45 W and a polarized laser output power in the  $\mathbb{E}_x$  field of around 15 W, 0.17 W is lost as depolarized power at the polarizer. The ejected  $\mathbb{E}_y$  field exhibits a cloverleaf-like intensity distribution, which is expected for the depolarization losses from thermally induced stress-birefringence with lateral cooling [166]. This specific intensity distribution is associated with the contribution of the shear

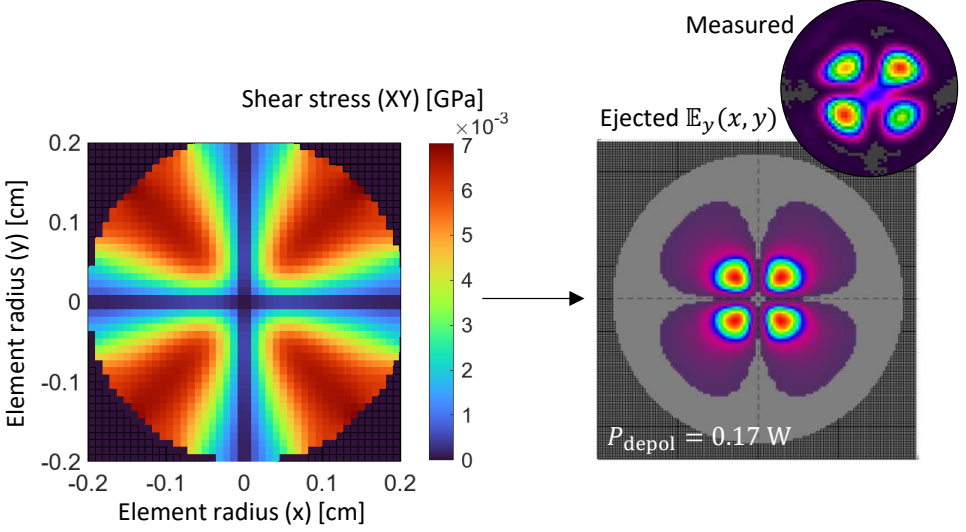


Figure 4.23: Depolarization losses at a linear polarizer inside a resonator, resulting in parts from the shear stress distribution in the laser rod depicted on the left hand side.

stress  $\tau_{xy}$  component to the refractive index. The simulated distribution of this is depicted in the left graph of Fig. 4.23. It is important to note that the distribution is given in relation to the polarization axis. Consequently, a radially tilted polarization would generate a correspondingly tilted cloverleaf pattern.

Besides polarization losses, the dominant  $\mathbb{E}_x$  field undergoes astigmatism, which arises from radial and tangential contributions to the refractive index alteration. Given that the exemplary field is polarized in the  $x$ -direction, the transverse field expanding in the  $x$ -direction mainly interacts with the radial stress component. Conversely, the transverse field expanding in the  $y$ -direction mainly sees the tangential stress component, resulting in a local phase delay difference. This astigmatism contributes to the thermal lens of the laser gain medium, which will be further explained in the subsequent section. In the absence of a polarizing element inside the cavity, the laser output is typically unpolarized, leading to no depolarization loss. Also, astigmatism and birefringence would not occur, as the radial and tangential refractive index contributions are averaged over all polarization states.

Figure 4.24 illustrates the effect of the implementation of stress-induced thermo-optic effects on the laser performance. This is simulated for the exemplary laser resonator detailed in section 3.6.

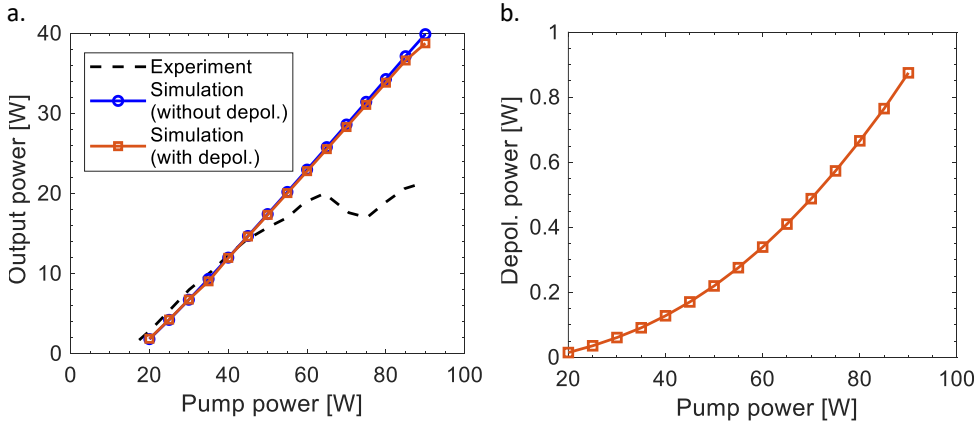


Figure 4.24: Influence of stress-induced birefringence on the laser resonator model. The left graph (a) depicts the variation in output power after implementation, while the right graph (b) illustrates the increase in depolarization losses with pump power.

The left graph (a) presents the laser output power over the launched pump power. The results measured in the experiment are plotted with the black dotted curve, while the orange and blue curves represent the performance with and without the incorporation of stress-induced effects, respectively. The temperature-dependent material parameters discussed in the preceding section are already incorporated in the blue curve. The power ejected at the intracavity polarizer over the pump power is plotted in the right graph (b). For this particular resonator, the depolarization loss is relatively low, reaching a maximum of 0.9 W at a pump power of 90 W, which explains the small performance difference in Fig. 4.24a. However, the implementation of the discussed effects is crucial for an accurate model, as different resonator geometries will be more affected and depolarization losses can be analyzed and compensated [167, 168]. Factors contributing to the impact of stress-induced birefringence and depolarization include the choice of bulk material, the output coupler (OC) reflectivity and resulting intracavity powers, as well as the mode diameter relative to the rod diameter. The latter contribution is further discussed in section 5.4.1, where the simulation model indicates that larger mode diameters lead to higher depolarization losses.

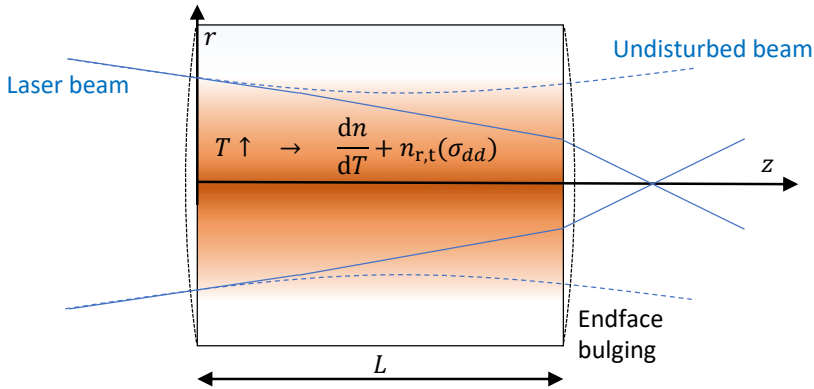


Figure 4.25: Thermal lensing in an end-pumped laser rod, caused by the three main mechanisms: the thermo-optic effect, the photoelastic effect, and endface bulging.

### 4.4.3 Thermal Lensing

In this section, thermal lensing of the gain medium and other intracavity bulk elements, and its implementation into the simulation model, will be investigated. Thermal lensing is defined as the focusing or defocusing of a laser beam passing through a bulk element, caused by the temperature profile. Figure 4.25 provides a schematic representation of the thermal lens effect in an end-pumped laser rod. The main contribution to this lensing effect arises from three mechanisms [140, 169]:

- *Thermo-optic effect*, characterized by the refractive index dependency  $dn/dT$ , which results in a three-dimensional refraction gradient directly from the temperature increase.
- *Photoelastic effect*, where thermal expansion-induced mechanical stresses lead to additional changes in the refractive index. This mechanism has been discussed in the preceding section 4.4.2.
- *Endface bulging*, directly caused by the displacement in the propagation direction from thermal expansion, where the bulging endfaces function as an additional lens.

The contribution of each mechanism to the total effective lens (with focal length  $f_{th}$ ) of the bulk element varies based on the material and system specifications. Typically, the thermo-optic effect has the most significant impact [170].

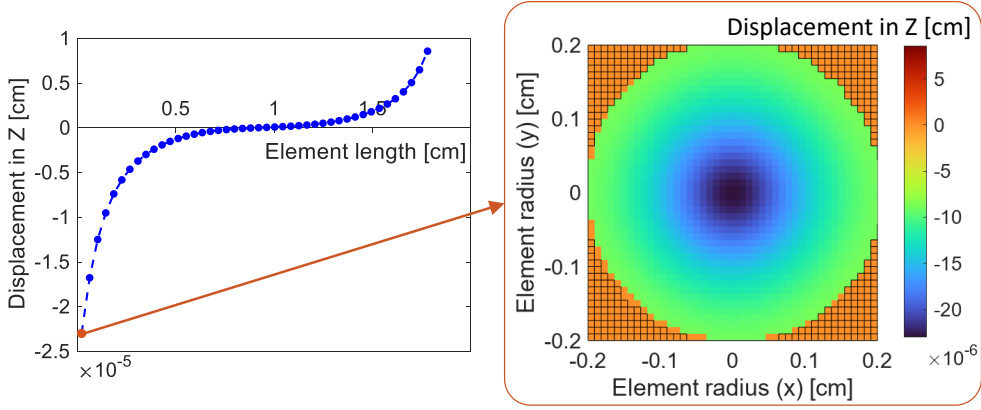


Figure 4.26: Simulated displacement from thermal expansion in the  $z$ -direction for the exemplary  $\text{Ho}^{3+}$ :YAG laser resonator, leading to endface bulging.

The model implementation of the photoelastic effect has been addressed in the previous section 4.4.2. Here, the thermal expansion with coefficient  $\alpha_{\text{th}}$ , resulting from the temperature profile, leads to a stress response of the material characterized by the stress tensor  $\sigma_{dd}$ . In addition to the previously described depolarization, the radial and tangential refractive index change  $n_{r,t}$  creates a transversal profile that induces a lensing effect. This contribution is typically astigmatic, resulting in birefringence and asymmetries in the output beam profile [37].

Implementing endface bulging is straightforward if the three-dimensional displacement distribution is simulated as outlined in section 4.3.1. The bulging effect depends solely on the displacement caused by thermal expansion in the  $z$ -direction [171]. An example distribution is illustrated in Fig. 4.26 for the previously discussed laser resonator at a pump power of 45 W. The graph on the left displays the central displacement along the  $z$ -axis, which is also the propagation axis of the pump and laser beams. Since the endfaces are not confined by a boundary, the surfaces can expand, leading to the observed increase in displacement. The maximum displacement at the left end face corresponds to the two-dimensional displacement in the  $x$ - $y$ -slice depicted on the right side of Fig. 4.26. The distribution exhibits an almost spherical curvature, contributing to the lens-like behavior of the bulk rod.

The lensing effect is implemented by simply adjusting the element thickness discretized in the  $x$ - $y$ -plane, resulting in adjusted slices  $\Delta z^*(x, y)$  at the endfaces of the element with

$$\Delta z_0^*(x, y) = \Delta z + D_z(0, x, y) , \quad (4.86)$$

$$\Delta z_{Nz}^*(x, y) = \Delta z + D_z(N_z, x, y) , \quad (4.87)$$

where  $D_z(0, x, y)$  and  $D_z(N_z, x, y)$  are the transversal displacement distributions at both endface slices of the element operator. The FFT-BPM field propagation algorithm, detailed in section 2.2, then accounts for the transversal change in phase delay from the displacement and refracts the beam according to the effective thermal lens contribution.

The final contribution to be incorporated comes from the thermooptic effect, characterized by the material parameter  $dn/dT$ , with the value specific to YAG provided in Tab. 4.1 (section 4.2.2). Given the discretized three-dimensional refractive index profile, the contribution from a temperature increase can be implemented using the following equation [169]:

$$n_{x,y}(x, y, z, T) = n_{x,y}(x, y, z, T_0) + \frac{dn}{dT} [T(x, y, z) - T_0] , \quad (4.88)$$

where  $n_{x,y}$  represents the refractive index relative to the  $\mathbb{E}_x$  or  $\mathbb{E}_y$  polarization states. The simulated three-dimensional refractive index distribution is depicted in Fig. 4.27 for the  $\mathbb{E}_x$  polarization from the temperature distribution of the  $\text{Ho}^{3+}$ :YAG crystal simulated in section 4.2.2. The refractive index distribution is closely connected to the temperature distribution as expected. In comparison with the radial and tangential refractive index contribution from the photoelastic effect, shown before in Fig. 4.22, the change in refractive index is significantly larger. This suggests that the thermooptic effect has the greatest influence on the thermal lens for this particular laser system and operation point.

With the integration of all thermal effects into the simulation model, the behavior of the exemplary resonator outlined in section 3.6 can be reevaluated. The output power over the incident pump power is plotted in Fig. 4.28a. Here, the black dotted curve corresponds to the experimental values, whereas the orange and blue curves represent the simulation with and without the inclusion of all thermal lensing contributions, respectively. It can be observed that the simulated output power behavior now closely aligns with the experimental values, exhibiting the same decline in output power around the 60 W mark. The residual pump power, depicted on

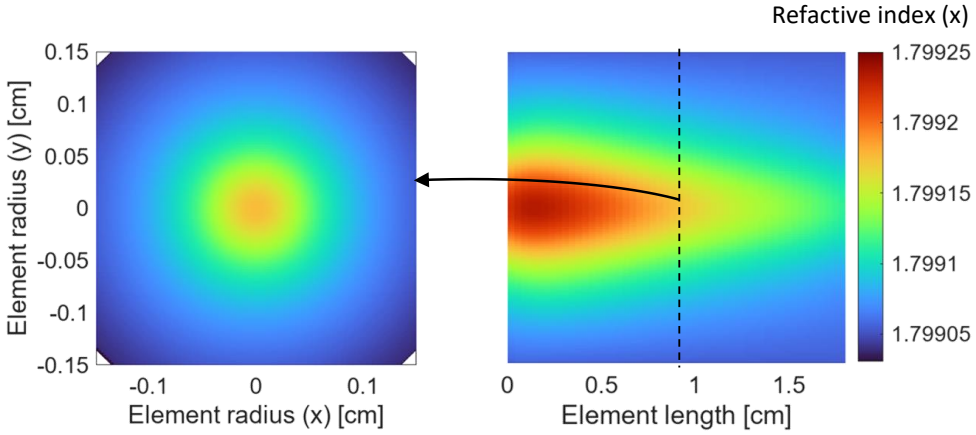


Figure 4.27: Simulated refractive index distribution for the  $E_x$  polarization of the exemplary laser gain medium, modified by the thermo-optic contribution.

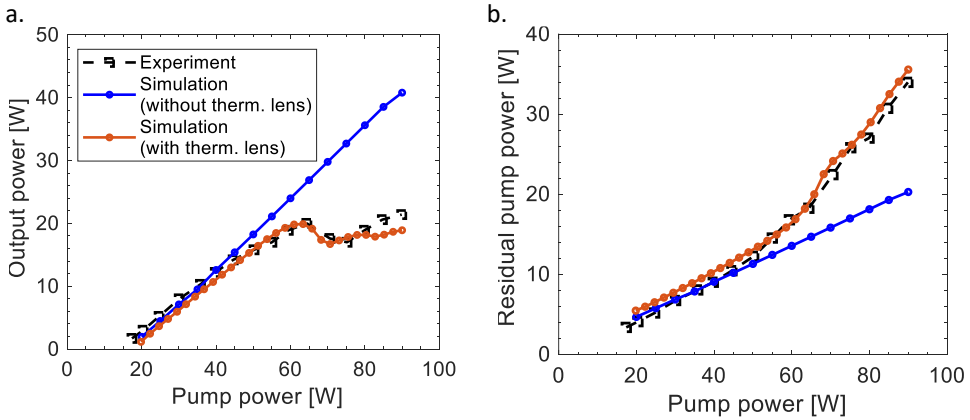


Figure 4.28: Impact of the combined thermal lensing effects on the laser resonator model, shown by the output power over incident pump power (a) and the residual pump power (b).

the right graph (b), validates the precision of the simulation and aligns with the behavior of the experimental values. The initial assumption of the thermal effects inducing thermal roll-over, associated with the stability of resonators including a variable lens (refer to section 3.2.3), appears to be accurate. Furthermore, the main contribution to the thermal roll-over comes from

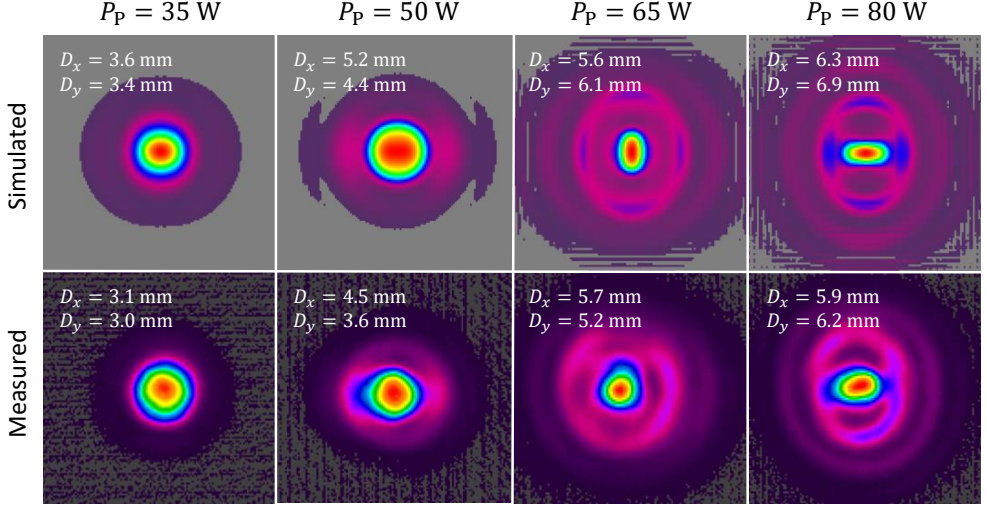


Figure 4.29: Comparison of the field distributions after the OC mirror at different pump powers, where the upper row displays the simulated fields and the lower row shows the fields measured in experiment.

the  $dn/dT$  contribution, although all implemented thermal effects contributed to the reduction in laser performance.

The mechanism leading to the observed behavior can be explained in further detail by considering the field distribution of the laser field after the OC mirror. A comparison of simulated fields (top row) with the measured field distributions (bottom row) is presented in Fig. 4.29. The  $D4\sigma$  beam diameters  $D_{x,y}$  are provided for the center intensities in  $x$ - and  $y$ -direction. At a pump power of 35 W, both fields exhibit a near Gaussian distribution, suggesting that the fundamental mode is stable within the resonator and mode matching between pump and laser mode is achieved. However, with increasing pump powers, starting from 50 W, the field exhibits distortions attributed to the addition of higher order mode content. As explained in section 3.2.2, higher order transverse modes can exist in a resonator, but are suppressed on purpose by the gain profile acting as an aperture for the fundamental mode only. If mode matching weakens or the fundamental mode loses stability, the higher order modes can emerge. In this instance, the field distributions show indications of higher order Laguerre-Gaussian TEM mode content where the radial asymmetries are likely coming from the stress-induced birefringence, as excluding

this effect from the simulation results in symmetric beam profiles. In summary, the increase of power absorption with higher pump powers leads to an increase in rod temperature in the laser gain medium and more pronounced thermal lensing. If this lensing gets stronger to the point where the fundamental mode leaves the established stability zone, higher order modes become more dominant, accompanied by a larger laser mode diameter and deteriorated mode matching with the pump beam. This explains the specific field distributions at higher pump powers, as well as the reduction in output power referred to as thermal roll-over.

While the simulation shows high agreement with the experiment in the case of this resonator chosen for validation, such high precision is not always attainable with the model. For instance, the behavior of thermal roll-over with this resonator is heavily dependent on a variety of influences, spanning from the material parameters to the precise positioning of the laser gain medium and optical elements. Even a small change of pump diameter or resonator length can result in a different stability behavior and onset of thermal roll-over. The goal of simulating this resonator as accurately as possible was to validate the simulation, and this validation was performed with a variety of different resonator geometries to fine-tune the material parameters, specifically of  $\text{Ho}^{3+}:\text{YAG}$ . Most parameters were sourced from literature, however, there are typically multiple sources available, each offering different parameter values. Therefore, fine-tuning the exact values is necessary for achieving high precision of the model. Every additional unique laser gain material implemented into the model must be fine-tuned accordingly, if high simulation accuracy is required. This should highlight that the complexity of the model in certain cases results in a large effort in gathering input parameters, which should not be underestimated.

After the successful validation with  $\text{Ho}^{3+}:\text{YAG}$ , the multi-physics model can be utilized to optimize additional experimental laser systems. This is done in the following chapter, and although the simulation accuracy may not match that of the exemplary validation resonator, the model has evolved into a powerful tool for designing and analyzing bulk solid-state lasers.

## 5 Optimization of $\text{Ho}^{3+}$ :YAG Laser Systems

The preceding chapters presented the development and validation of a multi-physics model for simulating bulk solid-state lasers, indicating its effectiveness as a design tool. This chapter employs the developed model to investigate the spectral behavior of  $\text{Ho}^{3+}$ :YAG laser systems, resulting in the development of two experimental systems with unique characteristics compared to state-of-the-art systems. As the focus of this work so far has been on simulation methods, some background information on experimental methods and measurement devices is provided in section 5.1. An overview of state-of-the-art laser systems relevant to this work is discussed in section 5.2. This context allows for a comparison of the developed laser systems, with an emphasis on the spectral operation points that deviate from the typical  $\text{Ho}^{3+}$ :YAG emission wavelengths. The design process of the first experimental system is detailed in section 5.3, resulting in a high-power Q-switched linear resonator with single-line spectral output at 2122 nm. In section 5.4, the second laser system, a  $\text{Ho}^{3+}$ :YAG power amplifier stage for a narrow-linewidth fiber seed MOPA at 2048 nm, is designed and characterized.

### 5.1 Experimental Methods and Measurement Devices

While the characterization of laser systems designed in simulation is typically straightforward, as all information describing the laser is available as numerical data, the characterization of experimental laser systems requires a more detailed explanation. In this section, methods and devices for measuring laser power, pulse characteristics, spectral output, and beam quality and intensity distribution are delineated. The characterization will be specific to  $\text{Ho}^{3+}$ :YAG laser

systems with pump and laser wavelengths in the short wave infrared (SWIR) region. Compared to lasers in the visible spectral region, these systems require specialized measurement devices, as for example the wavelength sensitivity of silicon-based sensors is limited in the SWIR range.

### **Power Measurement**

To measure the average power of laser beams in the 2  $\mu\text{m}$  region, optical power meters based on dissipated heat are employed. Unlike with laser beams in the visible range, photodiodes, which offer higher sensitivity and faster response times, cannot be used because of the aforementioned limitation. Although these issues can be circumvented by using, e.g. germanium-based sensors instead of silicon, thermal sensors are typically preferred for their robustness [172]. The power meters in use are based on thermopiles, which are essentially a series of thermocouples connected together. Thermocouples operate on the thermoelectric effect, which involves the generation of a voltage when there is a temperature difference across different materials. The thermopile sums the voltage of all thermocouples, resulting in a higher overall voltage which is proportional to the temperature difference across the device. If the full beam is captured in the aperture of the sensor head and reflections are taken into account by calibration, the optical power can be related to the power dissipated in heat. Depending on the beam size and expected power, different types of power meters offer a different specified power range and accuracy, and should be chosen accordingly.

### **Pulse Characterization**

Pulse characterization involves the temporal measurement of power or intensity counts related to the pulsed output of laser light. Contrary to the average power measurement previously described, the temporal resolution plays a significant role in this case. Thermal sensors, due to the slow speed of thermal convection, are not suitable for resolving the characteristics of the nanosecond pulses investigated later in this work. An alternative could be photodiodes, which utilize the photoelectric effect to convert high-energy photons directly into an electric current proportional to the incident intensity [173]. However, light in the SWIR range might not have sufficient energy to result in good signal-to-noise ratios. A viable option is the use of photoelectromagnetic (PEM) detectors. Here, the internal photoelectric effect at the light-absorbing interface generates free electrons, leading to a charge carrier gradient along the semiconductor material. When a perpendicular magnetic field is applied, the charges move to the opposite side of the detector, creating an electric field. The corresponding voltage can be

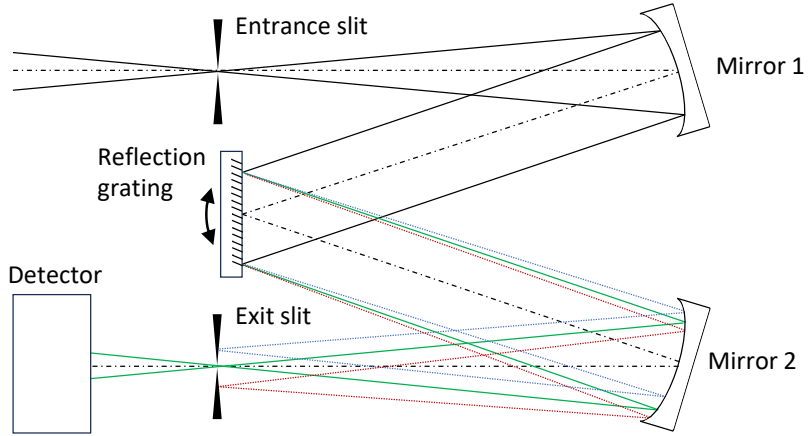


Figure 5.1: Schematic description of the light path in a monochromator based on the Czerny–Turner design. Graph adapted from [175].

related to the incident light intensity and the employed PEM detector can be connected to an oscilloscope with sufficient bandwidth to resolve the pulses to be measured [174]. The pulse energy, repetition rate, and pulse width can then be determined from the temporal pulse intensity measurement.

### Spectral Characterization

To determine the spectral content of the emitted laser light, a monochromator is utilized. This optical device transmits a defined narrowband portion of the incident electromagnetic spectrum, while filtering out all other spectral content. Typically, this is achieved through either dispersion at a prism or diffraction at a diffraction grating [44]. The device used for spectral characterization in this work is an imaging spectrometer, based on the scanning Czerny–Turner design [175]. A schematic description on the monochromator mechanism is depicted in Fig. 5.1. The incoming light is directed at an entrance slit placed at the effective focus of a subsequent curved mirror. This mirror collimates the light and reflects it onto a reflection grating, blazed for a specific wavelength range. The beam is then separated into its spectral components and reflected at different diffraction angles onto a second curved mirror. This mirror focuses all spectral components onto the exit plane, where an exit slit can be adjusted to select only a specified spectral resolution of the split focal points to pass onto a detecting element. The grating is subsequently rotated to scan over the full spectral range to be analyzed,

with the resulting resolution dependent on the exit slit size, the turning speed, and the detector sensitivity. For the experiments detailed later in this chapter, a grating with 300 lines/mm is used, blazed for a central wavelength of 2000 nm. The detector is made of indium gallium arsenide (InGaAs) cooled to liquid-nitrogen temperatures, chosen for the high signal-to-noise ratio it can achieve.

### **Laser Beam Characterization**

The characterization of laser beam properties encompasses two aspects. Firstly, the beam quality, which is related to the beam propagation ratio  $M^2$  as discussed in section 3.2.2, should be measured. Secondly, the field distribution has to be measured to identify higher order mode content and other asymmetric effects not captured by a single  $M^2$  value. A camera-based beam profiler enables the measurement of both aspects using a single device. To image laser beams in the SWIR range, the sensor pixel array is typically made from pyroelectric materials, which can produce temporary voltages depending on the material temperature. Contrary to more common photoelectric arrays, the pixel distance has to be larger to avoid temperature transition between neighboring pixels, resulting in a limited camera resolution. If this device can resolve the beam with sufficient resolution, the diameters in the  $x$ - and  $y$ -directions can be determined. By measuring these values in the near field of a beam focus as well as the far field, the beam waist diameter and divergence angle can be calculated, and the  $M^2$  value can be fitted in accordance with ISO standard 11146 [83].

Regarding the characterization of the laser systems discussed in subsequent sections, the methods and device types specified in this section were used to acquire the presented experimental data.

## **5.2 State-of-the-Art Ho<sup>3+</sup>:YAG Laser Systems**

This section aims to provide an overview of the applications and state-of-the-art of high-power Ho<sup>3+</sup>:YAG laser systems relevant to this work, aiming to put the developed lasers of the later sections into context. Subsection 5.2.1 compares high-power linear resonators with a focus on Q-switched systems, while high-power amplifier systems are compared in subsection 5.2.2.

### 5.2.1 High-Power Linear Resonators

The Ho<sup>3+</sup>:YAG systems relevant to this work are categorized into two types: high-power resonators, as discussed in this section, and power amplifiers, discussed in the following section 5.2.2. Both system types aim to offer laser solutions for applications requiring high-power laser light in the 2  $\mu$ m range, which encompasses medical applications, material processing, and defense applications [176, 177]. For resonators, the focus is on Q-switched systems that generate high-energy pulses in the ns-pulse region, as the generation of CW light is more commonly addressed by fiber lasers. In particular, pulsed lasers in the 2  $\mu$ m region serve as efficient pump sources for generating mid-infrared radiation through difference-frequency generation in zinc germanium phosphide (ZGP) optical parametric oscillators (OPOs) [5], which is the objective of many laser arrangements presented in the following literature references. It should be noted that the provided state-of-the-art overview compares laser systems by the metrics defined as relevant for the scope of this work, and does not consider all intricacies of these systems. While one laser system may appear inferior to another on the provided graphs, the objectives of the works may vary. The laser systems developed for this work, outlined in subsequent sections, are aimed to operate at atypical spectral regions, not commonly addressed by Ho<sup>3+</sup>:YAG. As the multi-physics model allows for the design and optimization of spectrally resolved lasers, this feature was taken advantage of to build unique systems at their specific wavelengths. While the developed laser systems have useful applications on their own, another goal was to demonstrate that Ho<sup>3+</sup>:YAG can operate efficiently at wavelengths far from the emission peak, where it is typically used. Therefore, the operation wavelength is a critical metric that will be compared with state-of-the-art systems.

Figure 5.2 provides a comparison of state-of-the-art Q-switched Ho<sup>3+</sup>:YAG laser resonators. Here, the average output power is plotted over the wavelength range of interest, 2000 to 2150 nm, which corresponds to the broad emission spectrum of Ho<sup>3+</sup>:YAG where the cross section values are noticeably above zero. Each plot marker represents a referenced state-of-the-art laser system, where the plot marker color corresponds to the  $M_{x,y}^2$  values of the laser resonator at that operation power. The average output power and  $M^2$  value are chosen as the most suitable metrics to contextualize the resonator developed in this work, as both are limiting factors for the provided applications. Only high-power systems will be compared, which, in the case of resonators, limits the systems average output power to above 10 W. In addition to Q-switched laser resonators, denoted by filled circles, some significant CW resonators are presented, corresponding to the square plot markers. The resonator developed for this work is

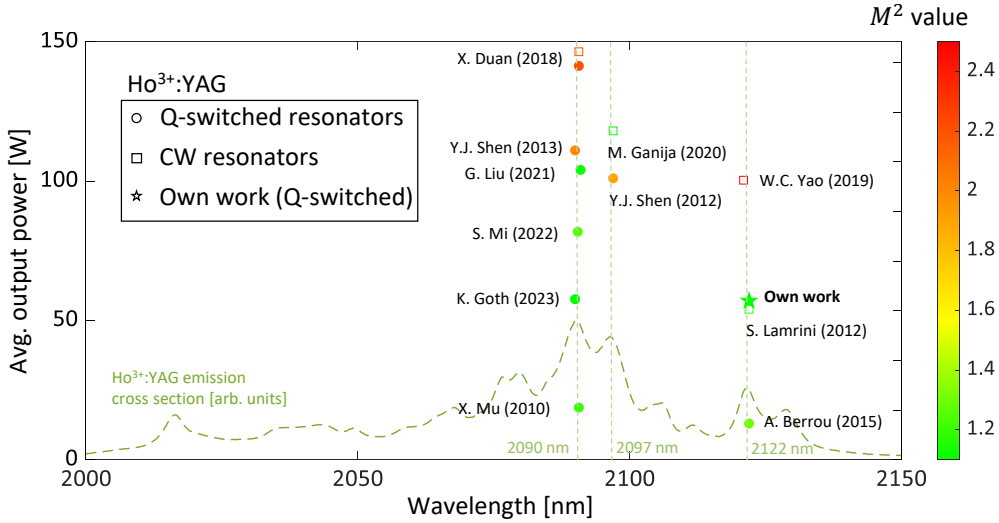


Figure 5.2: Comparison of state-of-the-art high-power Q-switched Ho<sup>3+</sup>:YAG laser resonators, providing context for the resonator developed in section 5.3. The graph compares the average output power and  $M^2$  values over the wavelength region of interest.

represented with a star-shaped marker and is termed 'own work' in the graph. Additionally, the emission cross section of Ho<sup>3+</sup>:YAG is plotted as a green dotted line over the full spectrum to highlight the relevant emission peaks. Only laser systems with single-line emission are compared, as some free-running lasers may exhibit multi-line spectral emission, which is typically not beneficial for the provided applications.

The graph reveals that most Q-switched high-power laser resonators operate at approximately 2090 or 2097 nm, representing the two highest emission peaks of bulk Ho<sup>3+</sup>:YAG. The highest output power in Q-switched operation at 2090 nm was reported by X. Duan et al., with an average output power of 141.3 W with  $M_{x,y}^2 < 2.2$  [9]. Other systems have consistently achieved over 50 W [6–8, 91]. In the same publication, Duan and his group also demonstrated the highest average output power from any Ho<sup>3+</sup>:YAG single-resonator, with 146.4 W in CW operation. A highly efficient resonator constructed by G. Liu et al. achieved a power of 104 W while maintaining a high beam quality with  $M_{x,y}^2 < 1.1$  [7]. The work of X. Mu et al. is also notable in this regard; despite achieving only 18.7 W, they demonstrated the Ho<sup>3+</sup>:YAG resonator with the highest slope efficiency of  $\eta = 81.2\%$  relative to the launched pump power,

by incorporating a multi-pass of pump light inside the resonator. While the wavelength of 2097 nm does not exhibit the highest emission peak for Ho<sup>3+</sup>:YAG, the effective spectral gain could be more efficient at this wavelength taking into account the reabsorption of laser light at the main peak at 2090 nm. The highest average output power at this spectral line was reported by Y.J. Shen et al. in Q-switched operation, demonstrating a power of 101 W with  $M_{x,y}^2 < 1.9$  [178]. The highest output power in CW operation was reported by M. Ganija and his group, with a power of 118 W at a close to diffraction-limited beam quality beam quality of  $M_{x,y}^2 < 1.1$  [132].

Taking this shift from the main spectral peak even further, the red-shifting of the effective spectral gain can even cause the 2122 nm spectral line to start lasing. However, this typically only occurs in lasers that exhibit multi-line spectral output as the gain at this wavelength remains low compared to the main spectral peaks. The objective of the laser resonator designed in section 5.3 was to demonstrate the possibility of high-power Q-switched operation at this spectral line, with performance metrics comparable to other emission lines. Reaching higher emission wavelengths enables benefits for specific applications, for example the nonlinear conversion in ZGP has lower background absorption at longer wavelengths [10]. Prior to the publication of these results in [179], other laser systems with single-line emission at this wavelength were operated either in CW [131, 180], with W.C. Yao reporting the highest average power of 100.3 W, or Q-switched at low powers. A. Berrou et al. demonstrated pulsed single-line emission with an average output power of 13 W and a corresponding  $M_{x,y}^2 < 1.3$  [181]. Although achieving high average powers in Q-switched operation at this emission line is not as straightforward compared to the main emission peaks, the resonator developed in this work achieved an output power of 57 W with  $M_{x,y}^2 < 1.2$ , showcasing highly efficient operation. The design process of this resonator is detailed in section 5.3 and has been enabled by the simulation model developed in this work.

## 5.2.2 High-Power Amplifiers

The state-of-the-art discussion of the previous section indicates that the output power of Ho<sup>3+</sup>:YAG bulk resonator systems, without compromising beam quality, is limited to around 100 - 150 W. This limit is assumed to come from high power absorption leading to thermal roll-over, related to the thermal lensing effect described in section 4.4.3, and appears to be limiting for both CW and Q-switched systems. A solution can be found in the use of master

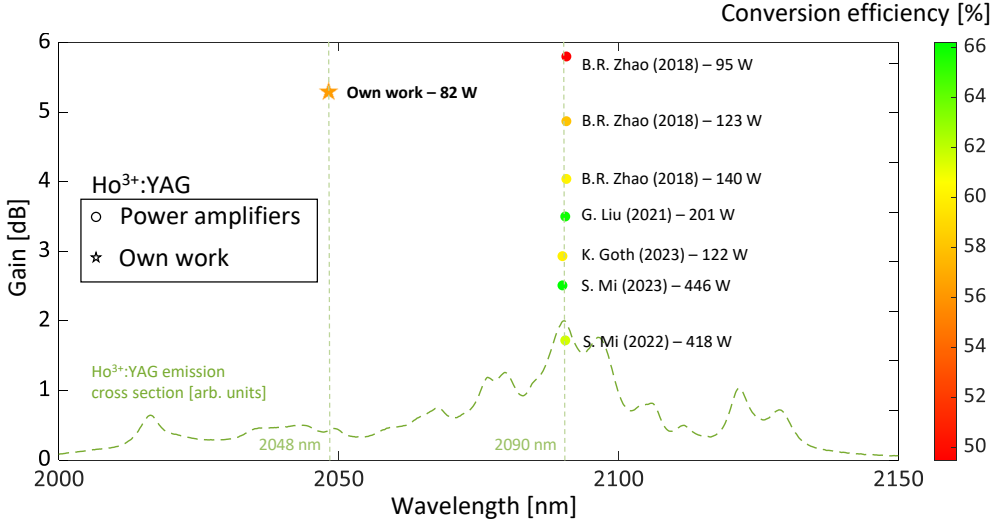


Figure 5.3: Comparison of state-of-the-art Ho<sup>3+</sup>:YAG power amplifier stages with linearly polarized output, providing context for the amplifier developed in section 5.4. The graph compares the gain and optical conversion efficiency over the wavelength region of interest.

oscillator power amplifier (MOPA) systems, which can amplify a seed laser to significantly higher power levels while maintaining a high beam quality at the cost of system size and complexity. A comparison of linearly polarized Ho<sup>3+</sup>:YAG power amplifier stages is provided in Fig. 5.3, compared over the same wavelength range as the previous resonators. The main metric for comparison is the total gain of the amplifier stage at maximum power operation, defined by

$$G = 10 \log_{10} \left( \frac{P_{\text{out}}}{P_{\text{in}}} \right), \quad (5.1)$$

measuring the amplified output power  $P_{\text{out}}$  relative to the initial seed power  $P_{\text{in}}$ , expressed in decibels (dB). In contrast to the previous graph, the color scheme of the plot markers indicates the corresponding optical conversion efficiency from incident pump power to amplification power, putting the amplifier stage efficiency in context. Compared to resonator systems, the average output power and  $M^2$  value may not accurately characterize the amplifier performance, as they are strongly dependent on the initial seed source. The amplifiers displayed are classified

as high-power, defined with an output power  $P_{\text{out}} > 50$  W. In the graph, the seed power after amplification is written next to the reference markers.

In comparison to the resonators in Fig. 5.2, state-of-the-art high-power MOPA systems have an even more restricted spectral range, as all referenced systems emit at the 2090 nm peak. This is likely because of the direct impact of the emission cross section on the total achievable gain, with a higher cross section correlating to more gain in the same length of bulk crystal. The highest gain values have been demonstrated by B.R. Zhao et al. [182], with the three stages of their MOPA system reaching a maximum output power of 231 W. The gain of the three stages, ordered by seed power from highest to lowest, is  $G = 4.0$ ,  $G = 4.9$ , and  $G = 5.8$  dB, respectively. Although the gain achieved is quite high, the optical conversion efficiency is only within the range of 50 to 60 %. S. Mi and his group achieved the highest average output power of any Ho<sup>3+</sup>:YAG MOPA with 446 W [183], increased from their initial publication with 418 W [8] by optimizing the depolarization losses of the amplifier stage. However, the gain values of the individual amplifier stages at these high power levels were limited between  $G = 1.7$  and  $G = 3$  dB. Other publications [7, 184] have shown similar gain performance, with G. Liu et al. achieving the highest conversion efficiency of 66 % [7]. It appears that power amplifier stages with high gain typically suffer from lower optical conversion efficiency, which can be attributed to the need for higher pump power to saturate the full length of the gain medium.

While all of the presented laser systems use Ho<sup>3+</sup>:YAG MOPAs to amplify seed lasers from Ho<sup>3+</sup>:YAG resonators at 2090 nm, the amplifier developed for this work aims to demonstrate that efficient operation with high-gain is achievable over a wide spectrum, not just limited to the spectral peak. The amplifier was seeded by a fiber laser MOPA operating at a wavelength of 2048 nm, far from any spectral peak of Ho<sup>3+</sup>:YAG. Despite the low emission cross section at this spectral point, the amplifier stage was able to amplify a pulsed signal with an incident power of 24 W to an output power of 81.6 W, resulting in a total gain of  $G = 5.3$  dB. Only the optical conversion efficiency, at 56.4 %, slightly suffered from the lower gain cross sections at this spectral operation point. To reach these unique results, an intricate design process was required as outlined in section 5.4. In addition to the output metrics at this spectral operation point, the results indicate that efficient performance of Ho<sup>3+</sup>:YAG amplifiers is possible over a broad spectral range.

The design process of the laser systems developed in this work, guided by the multi-physics model developed in the preceding chapters, will be discussed in the following sections.

## 5.3 Ho<sup>3+</sup>:YAG Resonator at 2122 nm in Q-switched Operation

The state-of-the-art overview in section 5.2.1 revealed that Ho<sup>3+</sup>:YAG resonators typically operate at the main emission peaks at 2090 and 2097 nm. However, this section introduces a novel approach for designing a linear resonator in Q-switched operation at the 2122 nm line. The experimental arrangement and design process are outlined in subsection 5.3.1. Given the challenges at this operation point, such as the red-shifting of the output spectrum to a longer wavelength without risking optical damage in Q-switched operation, the developed simulation model is an essential tool to guide the design processes. The experimental results are presented in subsection 5.3.2, followed by a brief discussion in subsection 5.3.3.

### 5.3.1 Description and Simulative Optimization

The laser resonator presented in this section is designed with the objective to achieve efficient performance at the 2122 nm spectral line at high power levels, close to diffraction-limited beam quality, and Q-switched operation. This section details the corresponding design process, guided by the simulation model, in a step-by-step manner. The schematic arrangement of the laser resonator is displayed in Fig. 5.4. Although the specific element details and positions have not been determined yet, some boundary conditions can already be defined. The chosen pump source is a commercially available Tm<sup>3+</sup>-doped fiber laser with a maximum output power limited to around 102 W and a beam quality of  $M^2 < 1.1$ . This pump power limitation will restrict the maximum output power achievable by the final resonator. The resonator itself has a linear geometry, where the pump light is coupled into the resonator by an dichroic incoupling mirror (IC), which is highly reflective ( $R > 99.5\%$ ) for the pump at 1908 nm as well as the p-polarization from 2000 to 2200 nm and highly transmissive ( $R < 0.05\%$ ) for the s-polarization at 2000 to 2200 nm. Utilizing this property, the IC also serves as the polarizing element inside the cavity ensuring linearly polarized output. The resonator itself is made of an high reflectance (HR) mirror, which is highly reflective ( $R > 99.9\%$ ) for the signal light and

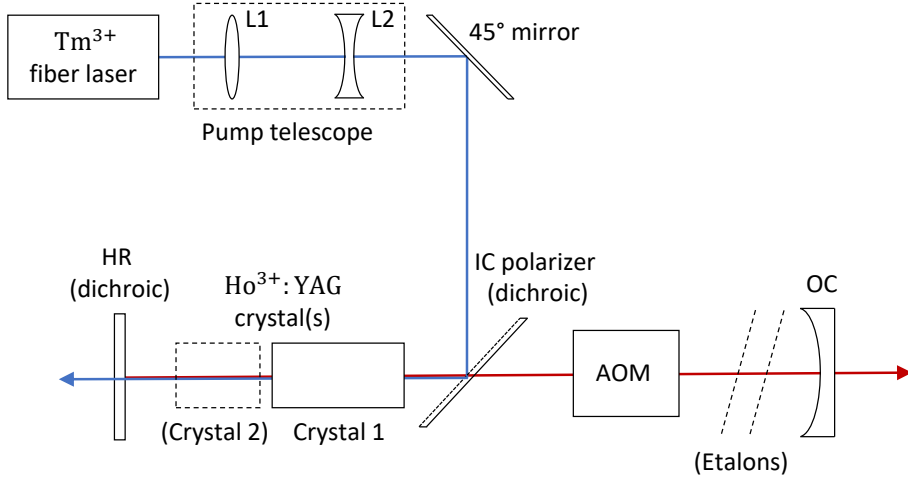


Figure 5.4: Basic schematic of the developed linear Ho<sup>3+</sup>:YAG laser resonator, including the optical elements and their general position.

highly transmissive ( $R < 0.05\%$ ) for the pump light, resulting in a single pass of the pump. The specifications of the OC mirror, located at the other end of the cavity, will be discussed later in this section. Between the IC and HR mirrors, there is sufficient space to place one or multiple Ho<sup>3+</sup>:YAG crystals as the laser gain media. Moreover, the cavity contains an AOM to enable Q-switched operation. Inside the resonator, there is further space for multiple etalons, which can be utilized to shift the output spectrum to the desired 2122 nm line as will be explained later in this section.

To limit the number of variable parameters, some assumptions about efficient laser performance can be used to specify the resonator geometry. As discussed in section 4.4.3, the thermal lens typically limits the resonator stability at high pump power. Therefore, to maintain resonator stability over a wide pump power range, the resonator length should be as short as possible while including all necessary optical elements inside the cavity. This also results in a smaller fundamental mode diameter, which increases the potential for intracavity damage due to high power and energy densities. Therefore, a moderate cavity length of 16 cm is chosen for this resonator. Additionally, a plane HR mirror and a plano-concave OC mirror with a radius of curvature of 0.5 m are selected to constrict the mode. These parameters are chosen to guarantee stable lasing conditions under Q-switched operation, given that a plane-plane cavity could

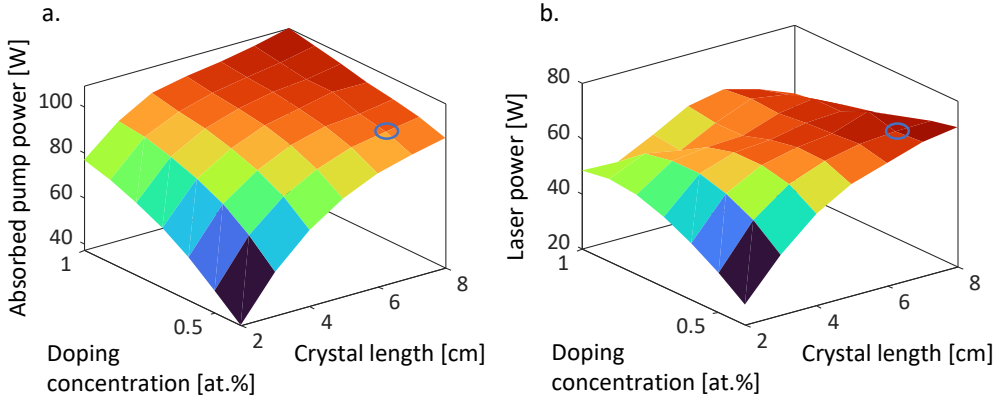


Figure 5.5: Simulative optimization of a single  $\text{Ho}^{3+}$ :YAG crystal as the laser gain medium. The left graph (a) depicts the pump power absorption over the crystal length and doping concentration, while the right graph (b) displays the corresponding laser output power.

result in unstable pulsing behavior as the fundamental mode is less restricted in the transverse directions.

After defining the basic resonator, the multi-physics simulation model can be employed to identify the optimal laser crystal configuration for this resonator. The experimental crystal will be placed in a copper heat sink for lateral cooling, consequently, the temperature simulation is performed with a Dirichlet boundary of 293 K, corresponding to the cooling temperature of the heat sink. For this initial simulation, an OC reflectivity of 50 % is chosen, while the impact of this variable will be discussed later in this section. Figure 5.5 presents the outcomes of a two-dimensional parameter sweep conducted with the simulation model at a pump power of 100 W. The crystal length, ranging from 2 to 8 cm, is chosen as the first variable parameter, where the maximum length corresponds to the space between the HR and IC mirror within the cavity. Additionally, the crystal doping concentration is varied from 0.4 to 1.0 at.-% as the second variable parameter. Figure 5.5a illustrates the absorbed pump power as the dependent variable of the parameter sweep. As expected, at short crystal lengths with low doping concentrations, only about 40 W of the pump is absorbed, while at the maximum length of 8 cm and a doping concentration of 1.0 at.-%, nearly the entire 100 W are absorbed. Nevertheless, the second dependent variable, the laser output power depicted in Fig. 5.5b, indicates that the crystal specification with maximum pump absorption does not optimize laser performance. The peak output power of 71 W is achieved at a crystal length of 7 cm and a

doping concentration of 0.5 at.%. Although the maximum absorbed pump power is found at high doping concentrations, this also results in higher rates of upconversion in the gain medium, subsequently reducing the efficiency and increasing thermal effects in the crystal. As the comprehensive simulation model accounts for all relevant effects, the optimal operation point can be easily determined.

After the identification of an optimal single-crystal with the preceding parameter study, the optimization of a multi-crystal design with shorter crystals is conducted. A dual-crystal configuration with available elements is optimized, which corresponds to the same pump absorption and output power values as for the optimized single-crystal. The Ho<sup>3+</sup>:YAG crystal that interacts with the pump light first has a doping concentration of 0.47 at.% at a dimension of 4 mm in diameter and 34 mm in length, while the second crystal has a doping concentration of 0.75 at.% at a dimension of 4 mm in diameter and 26 mm in length. Corresponding to the simulated fundamental mode diameter, the pump beam is focused into the center of the first crystal with a beam waist diameter of 0.6 mm. The use of two laser crystals with different doping concentrations enables a design similar to a segmented crystal [91], where the pump absorption and resulting thermal effects can be more effectively distributed over the full length of the gain medium [185].

The dual-crystal approach leads to a shorter total length compared to the equivalent single-crystal, providing more flexibility for the crystal placement inside the cavity. A simulated single-variable parameter sweep is performed to determine the optimal positioning of the laser crystals, with the results shown in Fig. 5.6. The crystal position is defined as the distance of the second crystal from the HR mirror, and is swept over a distance of 0 to 3.5 cm. The simulated results suggest that the best resonator performance is achieved at the highest distance from the HR mirror, in terms of both output power and beam quality. This outcome is expected, as the higher distances correspond to a more central effective position of the total thermal lens. As detailed in section 3.2.3, concerning the stability of linear resonators that include a variable lens, the highest stability is typically reached when the effective thermal lens position is in the center of the cavity along the propagation axis (taking mirror curvatures into account). With these results in mind, the crystals are placed with a distance of 3.5 cm from the HR mirror, increasing the power scalability of the system.

While the optimization process discussed so far can result in a functional and efficient laser resonator, the main objective of spectral output at the 2122 nm line must be addressed next. One method to achieve the red-shifting of the spectral content of a laser resonator involves the use

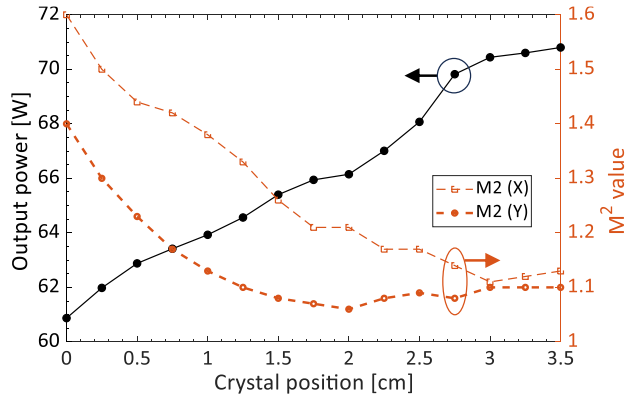


Figure 5.6: Simulated parameter sweep regarding the optimal crystal position inside the linear resonator. The laser output power (black curve) and  $M^2$  values (orange curve) in  $x$  and  $y$  are plotted over the crystal position relative to the HR mirror.

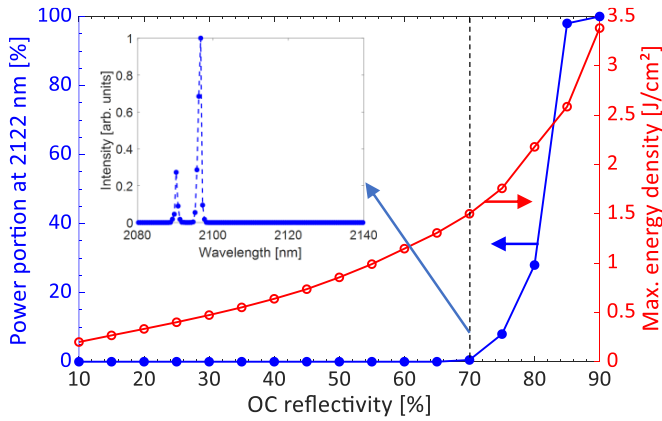


Figure 5.7: Simulated parameter sweep regarding the OC reflectivity of the linear resonator, and its influence on the spectral content at the 2122 nm line (blue curve). Additionally, the maximum intracavity energy density is plotted as the red curve.

of high OC reflectivities [186]. With this method, low round-trip losses result in longer cavity photon lifetimes and high intracavity signal intensity, which leads to strong signal reabsorption (for quasi-three-level laser materials) that favors long-wavelength spectral peaks. However, this approach is less suitable for achieving high pulse energies in Q-switched operation, as the high intracavity energy densities may increase the risk of damage to optical elements. To assess this

behavior, a parameter sweep is performed regarding the reflectivity of the OC mirror, ranging from 10 to 90 %, as depicted in Fig. 5.7. The curve in blue relates to the spectral content of the 2122 nm line, relative to the total output power across the full spectrum. The free-running resonator starts lasing at the 2122 nm line when the reflectivity surpasses 70 %. However, single-line emission is only achieved at reflectivities higher than 90 %, prior to which multi-line lasing with the 2090 and 2097 nm lines is simulated. The inset illustrates the simulated spectrum at a reflectivity of 70 %, where the spectral content at the 2122 nm line is just starting with a portion of 0.1 %, while the main part of the power remains in the spectral peaks at 2090 nm and 2097 nm.

The resonator is simulated in Q-switched operation, as detailed in section 3.5.2, with an AOM repetition frequency of 50 kHz. As the pulsed operation could result in high intracavity energy densities and this can lead to damage at the optical surfaces. The red curve in Fig. 5.7 shows the peak energy density in the resonator, which rises drastically at higher OC reflectivities. To prevent optical damage in the experimental resonator, a reflectivity of 70 % is selected for the final arrangement, as this specification shows signs of 2122 nm content and the maximum energy density remains smaller 1.5 J/cm<sup>2</sup>. The energy density  $\rho_E$  is often defined by optical element manufacturers for the laser-induced damage threshold (LIDT) and is expressed as

$$\rho_E = \frac{P_{\text{avg}}}{f_{\text{rep}} A}, \quad (5.2)$$

where  $P_{\text{avg}}$  is the average laser power,  $f_{\text{rep}}$  is the repetition frequency, and  $A$  is the area of the beam incident on the optical surface.

The damage potential is investigated via the simulation model for the resonator with an OC reflectivity of 70 % at the peak pump power of 102 W. Figure 5.8 illustrates the corresponding intracavity energy densities (red curves), average powers (dotted blue curves), and mode diameters (dotted black curves) across the entire resonator length in simulated forward (a) and backward (b) direction. The values are normalized to the total maximum values of each metric, while the maximum values of the individual directions are written at the respective position. The drop in intracavity power and energy density around a resonator length of 11 cm in the forward direction can be attributed to depolarization losses at the polarizer. The highest energy density of 1.5 J/cm<sup>2</sup> is reached near the HR mirror in the backward simulation direction. Although the intracavity power is not at its maximum, it is relatively high, while the mode

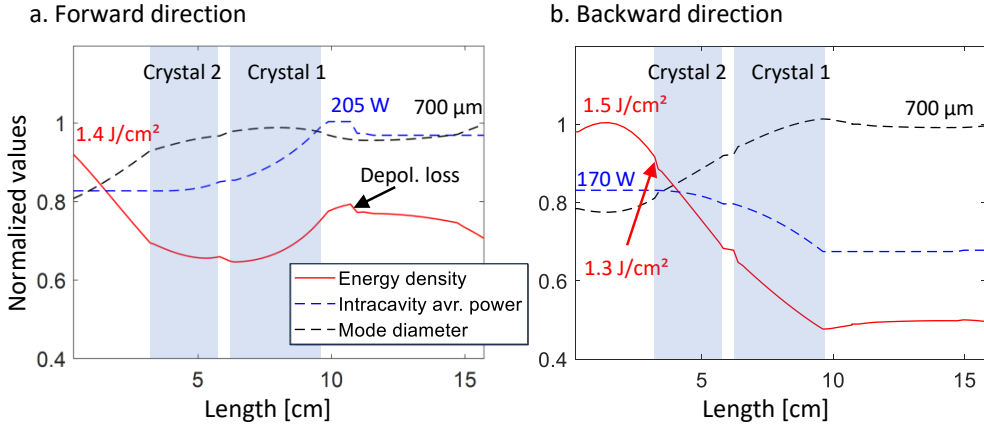


Figure 5.8: Normalized intracavity energy densities (red curves), average powers (dotted blue curves), and mode diameters (dotted black curves) of the linear resonator with an OC reflectivity of 70 %, plotted over the full length of the resonator. The left graph (a) shows the simulated forward direction, while the right graph (b) shows the backward direction.

diameter is the smallest across the full cavity length. However, this peak energy density is reached in a free space portion of the resonator where no damage should occur, the most critical elements to consider are the crystal endfaces (depicted in transparent blue). Here, the highest energy density is in the backward pass at the left endface of the second crystal, corresponding to a value of 1.3 J/cm<sup>2</sup>. This energy density is below the threshold specified by the coating manufacturer, and the OC with reflectivity of 70 % should result in no issues in the experiment.

However, at this OC reflectivity, it was shown in Fig. 5.7, that the 2122 nm emission line barely starts to lase. Therefore, at this operation point, a method to suppress the dominant 2090 and 2097 nm lines must be found. Since no other options for spectral filtering were available, the most straightforward method is the use of etalons to suppress the undesired spectral content. The functionality and model implementation of the etalon element is detailed in section 2.4.3. Essentially, an etalon introduces spectrally dependent transmission  $T_{\text{eta}}(\lambda)$  inside the cavity, where the residual beam is reflected at the etalon angle of incidence  $\theta_i$ . Figure 5.9 displays the transmission function of two etalons selected to suppress the dominant 2090 and 2097 nm spectral lines, tuned for the maximum transmission at 2122 nm such that no loss is introduced at this line. Additionally, the emission cross section of Ho<sup>3+</sup>:YAG is plotted (green line) to

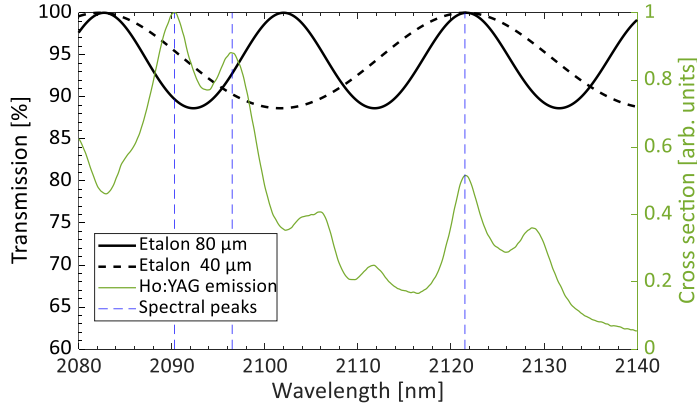


Figure 5.9: Transmission functions for two etalons with a thickness of 80  $\mu\text{m}$  and 40  $\mu\text{m}$  for the 2080-2140 nm wavelength region. The green line shows the relative emission cross section of Ho<sup>3+</sup>:YAG with the relevant peaks in the region of interest.

relate the relevant spectral peaks. Both etalons can be placed inside the cavity simultaneously for the highest suppression. The available etalons are uncoated and made of silica glass, which determines the surface reflectivity at around 4 %. The thickness directly influences the frequency of the sinusoidal transmission function and is chosen at 80  $\mu\text{m}$  and 40  $\mu\text{m}$  so that all the relevant spectral peaks are addressed. The angle of incidence can then be used to shift the transmission function for the maximum transmission at the laser wavelength of 2122 nm. By adopting the approach of using two etalons inside the cavity, the OC reflectivity required for single-line operation at 2122 nm can be efficiently reduced to 70%, minimizing the risk of damage to the intracavity elements.

In the following section, the experimental results that were achieved with this novel laser resonator design are discussed.

### 5.3.2 Experimental Results

The preceding investigation, guided by the developed simulation model, gives a clear path for the buildup of the experimental arrangement. Initially, the resonator is configured in CW operation without any intracavity etalons. Measurements with OC reflectivities of 50, 70, and 90 % were conducted to validate the spectral behavior simulated with the parameter sweep of

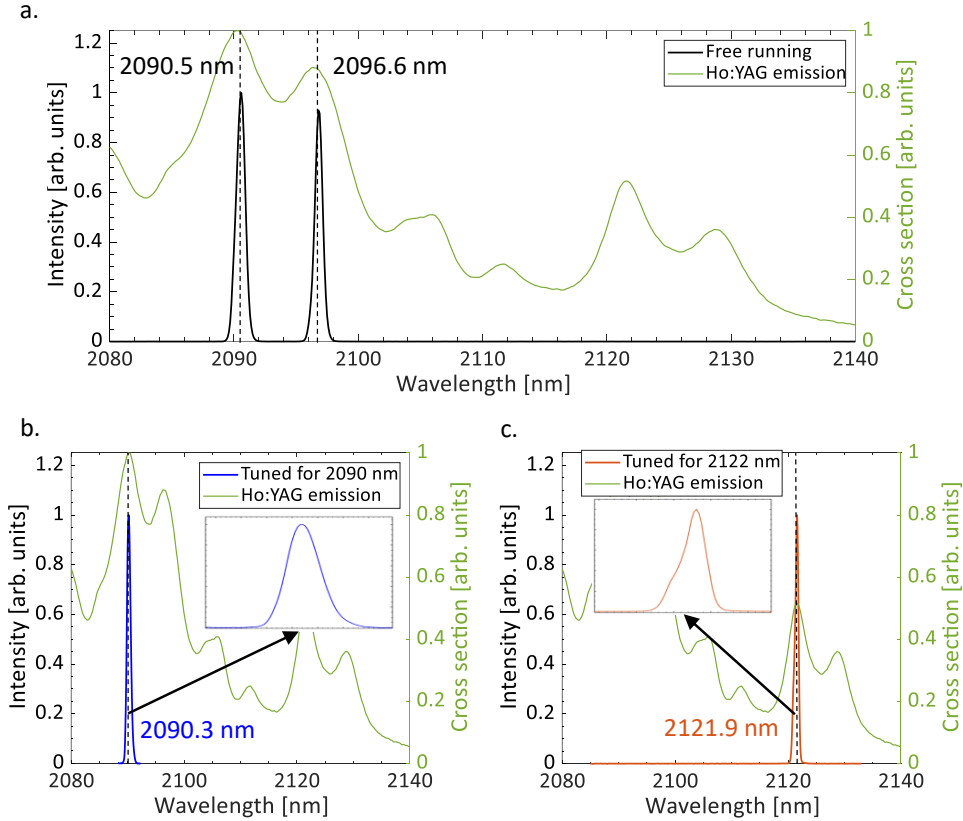


Figure 5.10: Output spectra of the Ho<sup>3+</sup>:YAG laser under Q-switched operation. Measured without any etalons in free running operation (a), with one etalon tuned to 2090 nm (b), and with two etalons tuned to 2122 nm (c). The green lines depict the emission cross section of Ho<sup>3+</sup>:YAG in the region of interest.

Fig. 5.7. The spectra measured at low reflectivities exhibited no indication of 2122 nm content, whereas with an OC reflectivity of 90 %, single-line lasing at this spectral peak was achieved; confirming the simulated results.

In the following, an OC reflectivity of 70 % was used for pulsed operation, as designed with the simulation. An AOM was placed inside the cavity and operated with a repetition frequency of  $f_Q = 50$  kHz and a loss time interval  $I_Q = 0.8$ . The spectra measured with the Q-switched linear resonator, operated at the maximum pump power of 100.7 W, are displayed in Fig. 5.10. All

measurements were performed in accordance with section 5.1 using a Horiba iHR 320 imaging spectrometer, while the spectrum was scanned with 0.1 nm resolution using a 300 lines/mm grating blazed for 2  $\mu\text{m}$ . Initially, the resonator was operated without any intracavity etalons in free running operation, the corresponding measured spectrum is presented in Fig. 5.10a. Here, the laser emits two distinct emission lines centered at 2090.5 nm and 2096.6 nm. These results diverge slightly from the simulated free-running spectrum in the design stage, depicted in the inset of Fig. 5.7. Although the multi-line lasing behavior at the two spectral lines was accurately predicted, in the simulation most of the power is located at the peak at 2097 nm, whereas in the experiment the power distribution is relatively balanced. Nonetheless, the spectral tuning utilizing intracavity etalons works as expected. A 40  $\mu\text{m}$  etalon was inserted inside the cavity and tuned to 2090 nm, resulting in Fig. 5.10b with a central peak of 2090.3 nm. Lastly, two etalons (80  $\mu\text{m}$  and 40  $\mu\text{m}$ ) were inserted inside the cavity and precisely tuned for the 2122 nm emission line, as illustrated in Fig. 5.9. With the resulting suppression of the naturally occurring 2090 nm and 2096 nm lines, single-line emission with a central peak of 2121.9 nm could be achieved. The corresponding spectrum is displayed in Fig. 5.10c. The insertion of two etalons was necessary as one etalon did not exhibit sufficient suppression for both dominant peaks at 2090.5 nm and 2096.6 nm. The graphs show an insertion with magnified views of the spectral peaks. All spectra were measured at the respective maximum output powers for the different arrangement configurations.

Figure 5.11 depicts the measured output power and residual pump power against the incident pump power in Q-switched operation for two spectral operation points. The laser output beam was linearly polarized, owing to the intracavity IC mirror acting as a linear polarizer for the laser wavelength. The first operation point, with single-line emission at 2090 nm (blue dots), achieved a maximum output power of 67.1 W and a corresponding slope efficiency of 70.3 % relative to the incident pump power. This result was obtained utilizing only one etalon within the resonator, demonstrating the efficiency of the basic resonator design. The second operation point, where two etalons were used to shift the output spectrum to the less dominant 2122 nm spectral line, is represented by the orange dots. At this point, a maximum output power of 56 W and a corresponding slope efficiency of 64.4 % were achieved. To the author's knowledge at the time of publication, this is the highest average output power achieved for Q-switched Ho<sup>3+</sup>:YAG lasers operating at a single spectral line at 2122 nm [179]. It is noteworthy that both operation points for 2090 nm and 2122 nm emission were pump power limited, exhibiting no signs of thermal roll-over. The output performance aligns relatively well with the prediction from the simulation model, with the corresponding simulated power curves plotted with faint dotted lines

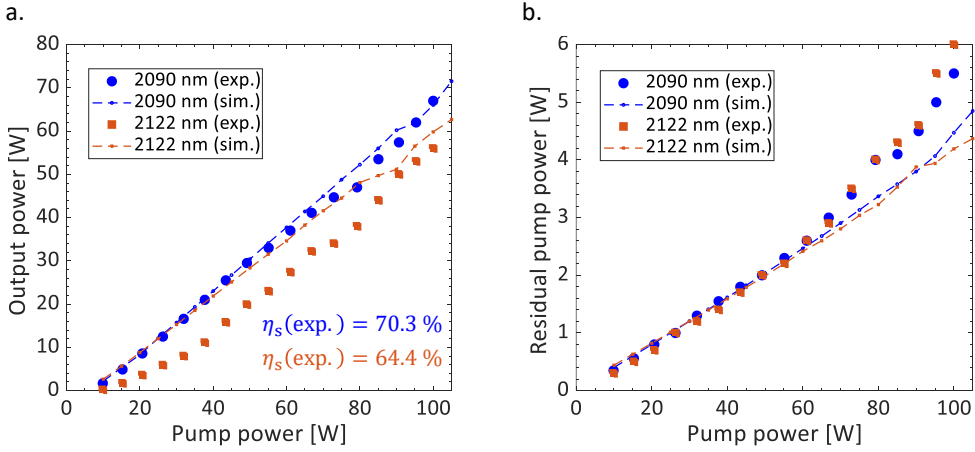


Figure 5.11: Average output power (a) and residual pump power (b) of the Ho<sup>3+</sup>:YAG resonator in Q-switched operation, relative to the incident pump power. The graphs display two operation points, 2090 nm in blue and 2122 nm in orange, where the dots correspond to the measured values while the faint dotted lines correspond to the simulation.

in the respective colors. However, the simulation underestimates the residual pump power at higher power levels. As mentioned in section 4.4.3 regarding the model implementation of thermal lensing, small deviations in mode matching and element positioning can have noticeable impacts on the laser performance. Therefore, the simulation model is not expected to show the same accuracy as demonstrated with the validation resonator in the previous chapters. Additionally, for the 2122 nm operation point, some deviations in output power performance are present, particularly at lower power levels. This behavior might be attributed to higher resonator losses in the experimental arrangement. Although a reduction in slope efficiency is expected compared to the 2090 nm line owing to the lower cross section values, the power of the reflected laser beams at the etalons seemed to be higher below the maximum power operation point. This suggests the onset of multi-line lasing along the power curve assumed to stem from a corresponding shift in spectral gain, which could contribute to the observed loss behavior.

Further characterization was conducted to examine the output properties of the Q-switched resonator operating at the 2122 nm wavelength at the maximum output power of 56 W. The beam quality measurement involved focusing the output beam using a plano-convex lens and applying the second moment method as outlined in section 5.1. To accurately determine the beam

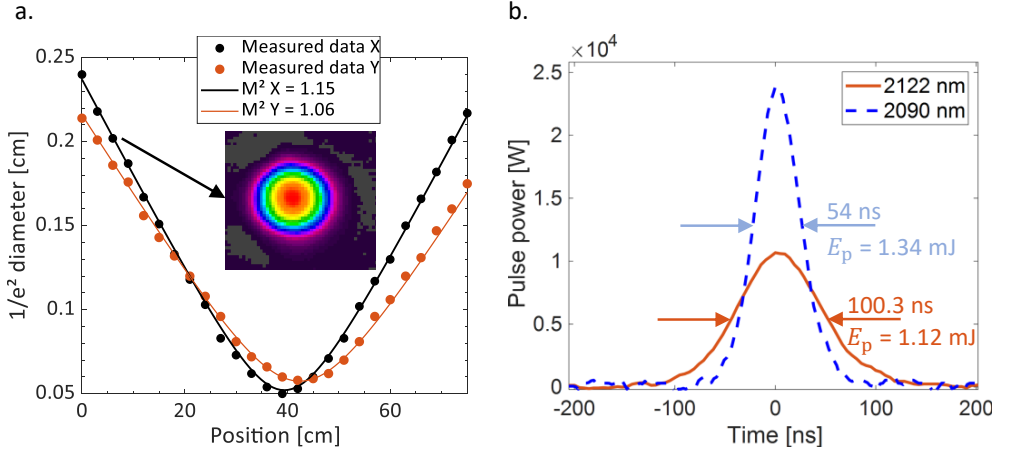


Figure 5.12: Additional resonator characterizations, where the left graph (a) presents the measurement of beam quality  $M^2$  for the 56 W operation point at 2122 nm. The inset displays the 2D beam profile measured in the far field. The right graph (b) illustrates the temporal pulse shape measured for this operation point at 2122 nm (orange curve) as well as the measured pulse for the 2090 nm operation point (dotted blue curve).

quality, the  $M^2$  values are calculated using a hyperbolic fit based on ISO Standard 11146 [83]. Figure 5.12a presents the measured beam quality results, alongside the fitted  $M^2$  values for this specific operation point. The inset shows the beam profile in the far field, captured at a distance of 25 cm behind the OC mirror without the use of a focusing lens. The beam exhibits an  $M^2$  value of 1.15 in the  $x$ -direction and 1.06 in the  $y$ -direction. These values approach diffraction-limited performance, indicating effective thermal management and efficient mode matching achieved in this resonator design, even at the red-shifted 2122 nm line. In Q-switched operation, with a fixed AOM repetition rate of 50 kHz, pulse generation was achieved at the 2122 nm emission line of the resonator. An exemplary measured pulse emitted in this configuration is depicted in Fig. 5.12b (orange curve). Corresponding to the maximum average output power of 56 W, a pulse energy of 1.12 mJ was attained. The pulse duration, with an average FWHM of 100.3 ns, results in a maximum peak power of 11.2 kW. In contrast, at the 2090 nm emission line (dotted blue curve), the pulsed output exhibits a shorter FWHM of 54 ns at the maximum average output power of 67.1 W, resulting in correspondingly higher peak powers. The deviation in the Q-switched performance regarding the FWHM between the two emission lines can be attributed to the lower achievable single pass gain at the 2122 nm emission line compared to the 2090 nm line. As the output wavelength was forced to an emission peak with a cross section

value approximately half that of the more dominant 2090 nm line, a broader pulse has to be expected.

### 5.3.3 Discussion

In conclusion, this section presents a comprehensive study on a high-power Q-switched  $\text{Ho}^{3+}$ :YAG linear laser resonator operating with single-line emission at 2122 nm. The multi-physics simulation model developed within the scope of this work was employed to design and optimize an efficient resonator. Through multiple parameter sweeps and optimization simulations, insights into the spectral behavior of the system were obtained, which would not have been possible through experiments alone, thereby demonstrating the usefulness of the model. By designing and integrating multiple etalons within the cavity, precise wavelength tuning was achieved, enabling single-line emission at the desired wavelength. The experimental results validate the effectiveness of this configuration, with a maximum output power of 56 W and a slope efficiency of 64.4 % achieved at a pump power of 100.7 W. In Q-switched operation, a maximum pulse energy of 1.12 mJ was measured at the 2122 nm operation point. The temporal pulse shape, measured with an average full-width at half-maximum (FWHM) of 100.3 ns, resulted in a maximum peak power of 11.2 kW. While previous publications with single-line emission at the 2122 nm line demonstrated high-power operation in CW [131, 180], to the author's knowledge, the results presented here achieved the highest average powers in Q-switched operation at this spectral line (refer to Fig. 5.2). Furthermore, the characterization of the output performance revealed excellent beam quality, indicating near-diffraction-limited performance. Despite the developed resonator achieving higher peak powers at the 2090 nm operation point, the pulsed output at the 2122 nm line demonstrates significant potential for various applications, particularly for pumping ZGP OPOs, where background absorption is lower for longer pump wavelengths [10]. As the power scaling of the experiment was pump power limited, even higher average output powers and pulse energies should be achievable at this operation point.

While resonator operation at the 2122 nm line is atypical compared to the standard  $\text{Ho}^{3+}$ :YAG spectra at 2090 and 2097 nm, the potential for lasing has been demonstrated before. In the subsequent section, the simulative design of a unique amplifier stage for a seed laser at a wavelength of 2048 nm is described, showcasing that  $\text{Ho}^{3+}$ :YAG can be used as an efficient gain medium even further from the typical emission lines.

## 5.4 Ho<sup>3+</sup>:YAG Amplifier for a Seed Fiber MOPA at 2048 nm

Beyond resonator systems, the simulation model can guide the design of efficient bulk solid-state amplifiers. This section explores a Ho<sup>3+</sup>:YAG power amplifier stage as the fourth stage to a fiber MOPA to bypass the energy density limitations of fibers, resulting in a hybrid fiber/bulk system. Notably, the wavelength of the fiber MOPA at 2048 nm deviates from the typical emission peaks of Ho<sup>3+</sup>:YAG, as outlined in section 5.2.2. The findings of this work suggest that the bulk gain medium can be suitable for broadband applications under specific conditions. In subsection 5.4.1, the basic arrangement of the bulk amplifier stage is discussed, and the simulation model developed within this work is utilized to design and analyze a suitable amplifier configuration. Following this, the optimized amplifier is assembled, with the experimental results shown in subsection 5.4.2 following a short discussion in subsection 5.4.3.

### 5.4.1 Description and Simulative Optimization

While all the relevant laser amplifier systems compared in section 5.2.2 are used to amplify bulk laser resonators as seed sources, the system constructed for this work is a fiber/bulk hybrid MOPA. The objective of this system is to achieve high pulse energies exceeding 1 mJ, optimized for the application of nonlinear frequency conversion in a ZGP OPO. While fiber laser systems are typically advantageous for attaining high average powers, reaching high pulse energies is more challenging. The potential for power scaling is attributed to the fundamental mode guiding capabilities of fiber lasers, which are enabled by small core diameters [187]. While the advantage is that higher order modes are actively suppressed and the fundamental mode is less dependent on thermal effects compared to bulk laser systems, the small diameters result in very high power and energy densities in the core of the fiber. Coupled with the long interaction lengths, nonlinear effects such as stimulated Raman scattering, stimulated Brillouin scattering, or self-phase modulation can affect laser performance [187, 188]. In the anomalous dispersion regime, the latter effect leads to significant broadening of the output spectrum and supercontinuum creation, which ultimately sets a limitation if the spectral quality matters to the application. These effects become particularly critical for pulsed operation, where high peak powers and energy levels are typically the goal of the laser system, and limit the scaling capabilities. To circumvent the limits of pulsed fiber laser systems, one strategy is to use fibers with larger core diameters, like

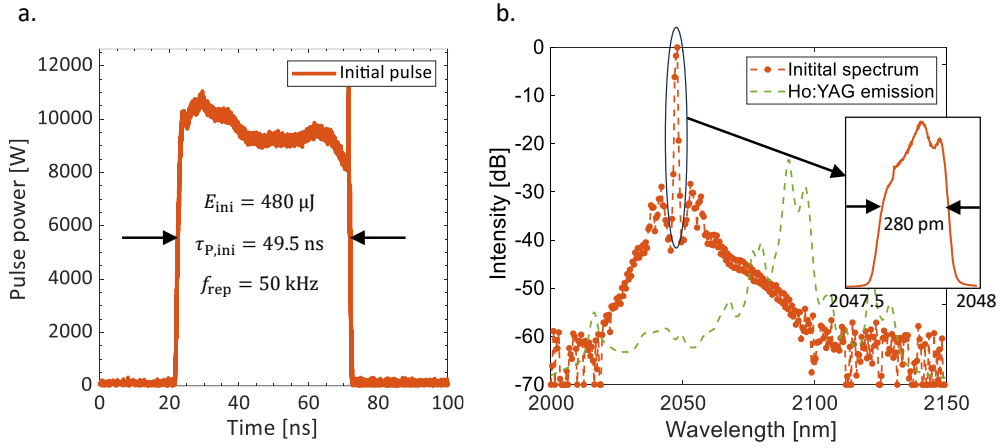


Figure 5.13: Output characteristics of the three-stage fiber MOPA, taken as input signal for the bulk amplifier stage. The left graph (a), displays the nearly rectangular pulse shape, while the graph on the right (b) presents the corresponding spectrum.

large-pitch or photonic crystal fibers [189]. However, as the guiding mechanism is necessary, the scaling of the core size is still limited.

An alternative strategy is to employ solid-state amplifier stages, as the mode diameters in free-space can be expanded without guiding requirements. However, this comes with a higher dependency on thermal effects, and resulting limitations in average power scaling. Nevertheless, this strategy is selected for this work to bypass the limitations of the fiber MOPA and achieve high pulse energies. The initial three-stage fiber system has been constructed by Lorenz et al. (refer to [190]), who also contributed to the development of the bulk amplifier stage discussed in this work. In the corresponding publication, the performance and output metrics of the fiber MOPA are detailed more extensively. For the scope of this work, the fiber system is considered only for a single operation point, where the repetition rate is 50 kHz and an average output signal power of 24 W is obtained. The resulting initial pulse energy is 0.48 mJ, with the temporal pulse behavior of the experiment depicted in Fig. 5.13a. This figure illustrates another feature of this specific fiber MOPA; the nearly rectangular shape of the pulse. The initial pulse is generated and shaped by a modulated laser diode and amplified by the subsequent three amplifier stages. The rectangular shape aims to achieve higher conversion efficiencies in the intended application of nonlinear frequency conversion [190]. The pulse has a temporal FWHM of 49.5 ns with narrow rise and fall times of less than 1.5 ns, optimized for the intended

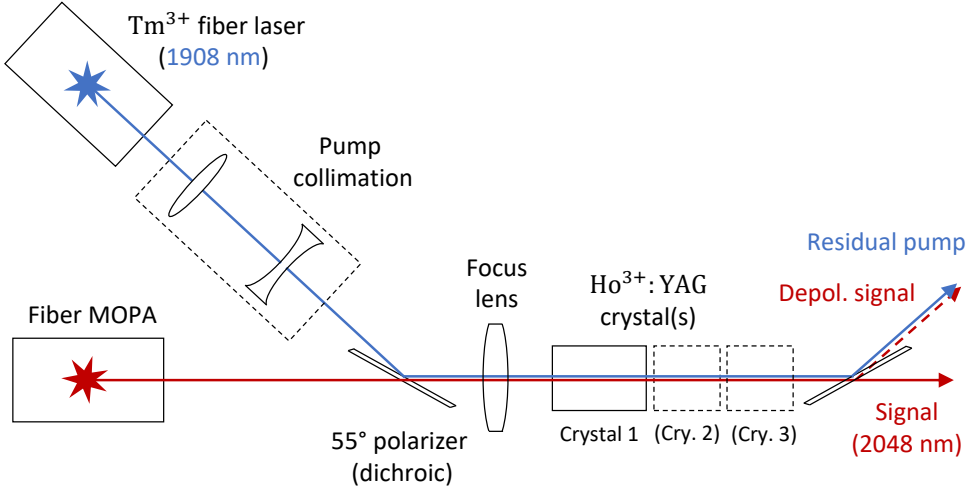


Figure 5.14: Basic schematic of the developed  $\text{Ho}^{3+}$ :YAG power amplifier stage, used to amplify the signal from the fiber MOPA.

application. Figure 5.13b, presents the output spectrum of the fiber MOPA at this operation point. Owing to the nonlinear effects of the initial fibers, the spectral power is plotted in decibels relative to the peak with a resolution of 1 nm, to highlight the broadband content. While the spectral broadening from supercontinuum generation is evident, over 98 % of the power is distributed within 1 nm of the center wavelength. This central peak, shown in the graph inset, has a spectral FWHM of 0.28 nm and is located at 2047.7 nm. The dotted green line represents the emission characteristics of  $\text{Ho}^{3+}$ :YAG, indicating that the peak wavelength is far from any cross section peak of the gain medium. However, with the insights from the simulation model, a functional and efficient bulk power amplifier can be developed, as detailed within this section.

Figure 5.14 provides a schematic representation of the basic amplifier arrangement. A commercial  $\text{Tm}^{3+}$  fiber laser, similar to the one discussed in section 5.3.1 for the laser resonator, is used as the pump source of the  $\text{Ho}^{3+}$ :YAG stage. It delivers a maximum continuous power of 102 W at a wavelength of 1908 nm, aligning with the main absorption peak of the gain medium. A two-lens telescope is employed to collimate the beam to a diameter of 0.2 cm, matching the collimated output of the fiber MOPA. Both beams are combined at a 55° dichroic polarizer, which is highly reflective at the 1908 nm wavelength and the p-polarization at 2048 nm, and

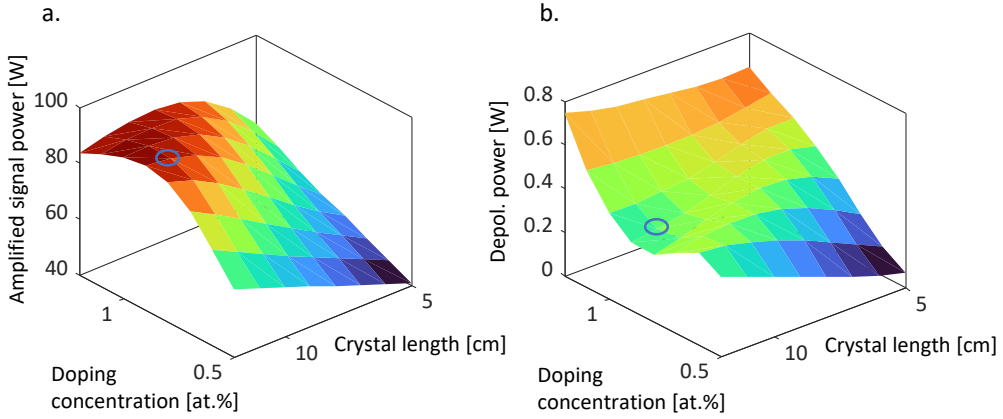


Figure 5.15: Simulative optimization of a single  $\text{Ho}^{3+}$ :YAG crystal as the amplifier gain medium. The graph on the left (a) displays the amplified signal power over the crystal length and doping concentration, while the graph on the right (b) illustrates the corresponding depolarization power.

highly transmissive for the s-polarization at 2048 nm, the primary polarization state of the signal. A subsequent convex lens focuses both beams to a similar waist position at the gain medium position; the optimized waist diameter is discussed later in this section. This co-pumping configuration is selected for its simplicity, compared to a counter- or dual-pumping scheme. After passing the bulk amplifier, the specifications of which are part of the subsequent design process, both beams are separated at a second  $55^\circ$  dichroic polarizer, where the remaining pump and depolarized signal are ejected from the main beam path.

The optimization of the bulk amplifier is initially done for a single crystal configuration. Figure 5.15 presents the outcomes of a two-dimensional parameter sweep utilizing the amplifier simulation model. The simulation is performed at a pump power of 100 W, with a signal and pump waist diameter of 0.04 cm, focused at the endface of the crystal. The first variable parameter is the crystal length, which varies from 5 to 12 cm, while the crystal doping concentration, ranging from 0.5 to 1.2 at.%, is selected as the second variable parameter. Figure 5.15a displays the amplified output signal as the dependent variable, indicating higher values at longer crystal lengths and increased doping concentrations where the crystal begins to absorb most of the pump power. The maximum is located around a length of 11 cm and a doping concentration of 0.9 at.%, as highlighted by the blue circle. The corresponding depolarization power, lost at the second dichroic polarizer, is illustrated in Fig. 5.15b. The local minima at high signal

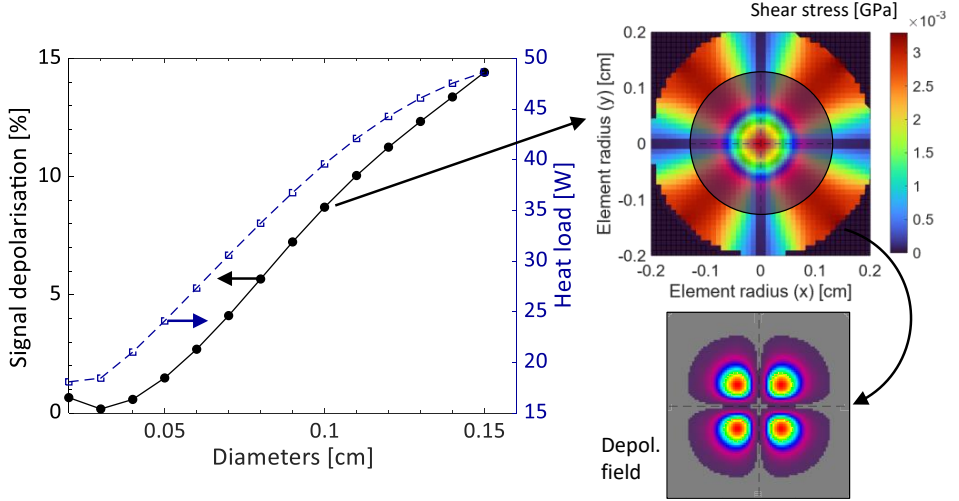


Figure 5.16: Simulated parameter sweep concerning the depolarization losses of the bulk power amplifier, relative to the signal and pump waist diameters. The black curve relates to the signal depolarization in percent while the dotted blue curve represents the power dissipated in heat. The influence of the shear stress on the cloverleaf-like depolarization field is depicted schematically on the right side of the figure.

output powers are located near the peak power crystal identified earlier (blue circle), confirming that this crystal specification is well optimized for this configuration. The depolarization power appears to increase with higher doping concentrations, likely due to the increased crystal temperature and stress response from upconversion losses.

To further optimize the amplifier configuration, the effect of the pump and signal diameters on the amplifier depolarization losses is investigated using the numerical model. The left graph in Fig. 5.16 presents the results of a parameter sweep with the optimized single crystal, where the pump and signal diameters are kept equal and are varied from 0.02 to 0.15 cm. The power lost to depolarization is plotted in black, as a percentage relative to the amplified output signal. A strong dependency on the mode diameters is found, with smaller diameters leading to less depolarization losses. As discussed in section 4.4.2, concerning the simulation of stress-induced birefringence, the depolarization in end-pumped bulk crystals arises from the phase delay induced by the shear stress contribution, which leads to the cloverleaf-like intensity pattern.

The impact of depolarization losses on high average power amplifiers has been explored by S. Mi et al. in reference [183], where the optimization of an amplifier system depending on beam diameters and crystal configurations is considered. They investigated relatively large beam diameters (0.1 to 0.15 cm) and found little influence of the diameters on polarization losses but rather a dependency on the heat load only, assuming perfect mode matching. For fixed pump diameters, they identified a strong influence of the signal diameter, where smaller diameters correspond to less depolarization. The results obtained with the parameter sweep are in agreement to the findings of their publication, as the dependency on the mode diameters can be attributed to a change in heat load as well, highlighted by the dotted blue curve in Fig. 5.16. The increased heat loads at larger beam diameters can be explained by an increase in saturation power from lower intracavity power densities, which decreases the efficiency of the stimulated emission process.

However, the increase in heat load is not the only contribution to the depolarization in the simulation, as perfect mode matching is not a given. The numerical model accounts for the effects of refraction, diffraction, and corresponding thermal lensing, leading to changes in the beam diameters over the crystal length. Thermal lensing exerts a greater influence on larger signal diameters, as the diameter corresponds to the aperture of the effective lens. Since the pump and signal beams are refracted differently at the thermal lens (owing to a difference in wavelength), strong thermal lensing can lead to a deterioration of mode matching along the length of the crystal. Worse mode matching of larger signal diameters coupled with smaller pump diameters then contributes to the depolarization content. As displayed on the right side of Fig. 5.16, a polarized signal beam with large diameter will experience phase delay over a greater area and shift more power into the perpendicular polarization component.

In the proposed  $\text{Ho}^{3+}$ :YAG amplifier, smaller mode diameters are determined to be advantageous, resulting in high gain and minimal depolarization losses. This characteristic can be used to optimize the gain medium for the 2048 nm wavelength, where the emission cross section values are significantly lower than those at the dominant emission peaks. If the mode diameters can be maintained at a small size throughout the entire crystal length, the low emission at this wavelength can be compensated, making it possible to achieve a highly efficient amplifier stage. This behavior can be achieved with a guiding effect of the thermal lens, which is a critical optimization step for this amplifier stage. However, it is important to consider that the diameters of laser beams with high pulse energies should not become too small at the coated

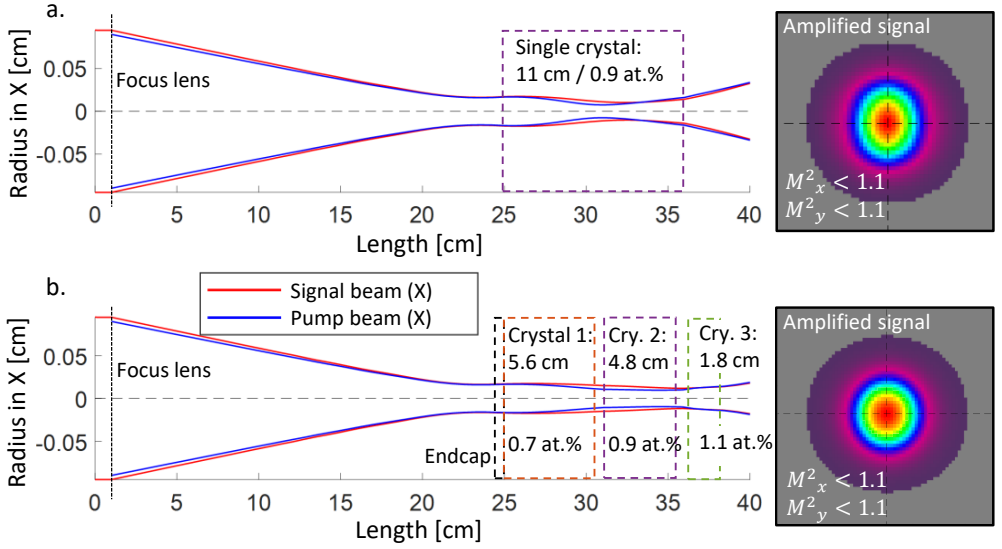


Figure 5.17: Simulated mode diameters in the power amplifier stage for the single crystal (a) as well as the cascaded design (b), with the pump mode depicted in blue and the signal mode depicted in red. The graphs on the right show the field distribution of the corresponding signal after amplification.

endfaces, as high energy densities can result in optical damage. Therefore, the objective of the designed amplifier configuration is to maintain the diameter close to 0.04 cm. This diameter is small enough for highly efficient performance and low depolarization losses, and it has been determined to not pose any risk to optical elements.

The simulated beam propagation path of the amplifier with the optimized single crystal is illustrated in Fig. 5.17a, where the beam radii for pump (blue line) and signal (red line) are propagated over the entire amplifier length. The mode matching between the two beams is well maintained within the crystal, while the diameter remains small because of the effective thermal lens, as suggested in the optimization process. The simulated signal beam profile after amplification is plotted on the right side of the graph and shows no degradation of beam quality with  $M^2_{x,y} < 1.1$  and only slight astigmatism. While this crystal configuration performs well with the simulation model, this optimized crystal was not available for the experiment. However, the simulation model can be used to identify a crystal configuration composed of multiple shorter crystals that will behave similarly to the optimized single crystal. In the

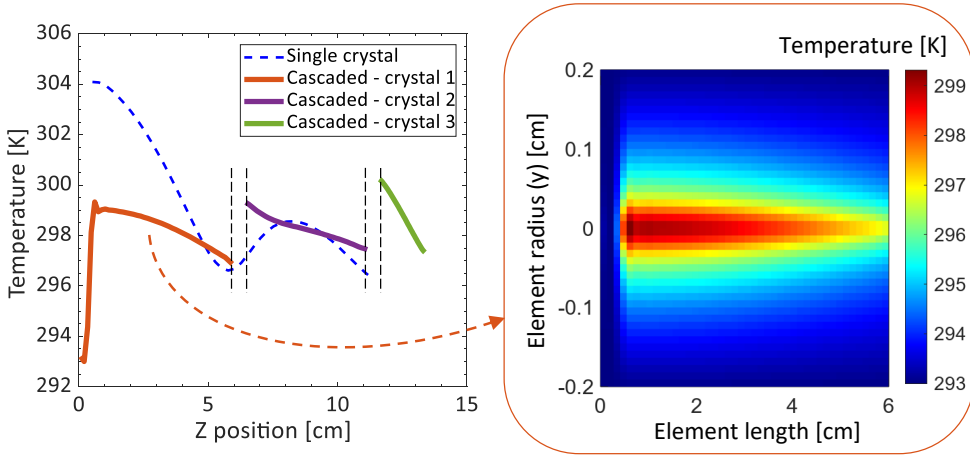


Figure 5.18: Comparison of thermal behavior between the cascaded and single crystal configurations. The left graph illustrates the simulated temperature in the crystal center along the  $z$ -axis for both configurations, with the dotted blue line representing the single crystal configuration and the orange, purple, and green lines representing the cascaded crystals. The right graph depicts the 2D temperature distribution for crystal 1 of the cascaded design, as a cut at the  $y$ - $z$ -plane.

corresponding simulation process, optimized for signal output power and residual pump power, a cascaded arrangement of three crystals with increasing doping concentrations was found. The configuration is depicted in Fig. 5.17b, where the first crystal to interact with the beams (crystal 1) has a length of 5.6 cm at a doping concentration of 0.7 %, the second crystal (crystal 2) has a length of 4.8 cm at a doping concentration of 0.9 %, and the third one (crystal 3) has a length of 1.8 cm at a doping concentration of 1.1 %. The simulated beam propagation reveals excellent mode matching between the two beams with this new design, and the beam profile after amplification exhibits even slightly less astigmatism. The cascaded design is chosen to help with thermal lens guiding, as the pump power decreases with propagation distance through the amplifier and the higher doping concentrations at the end will enhance the effective thermal lens.

Figure 5.18 presents the comparison of temperature distribution along the propagation axis within the crystals for both configurations. The dotted blue line represents the core temperature of the single crystal configuration, while the cascaded crystal configuration is represented by the orange, purple, and green lines. The cascaded design, optimized for thermal lens guiding,

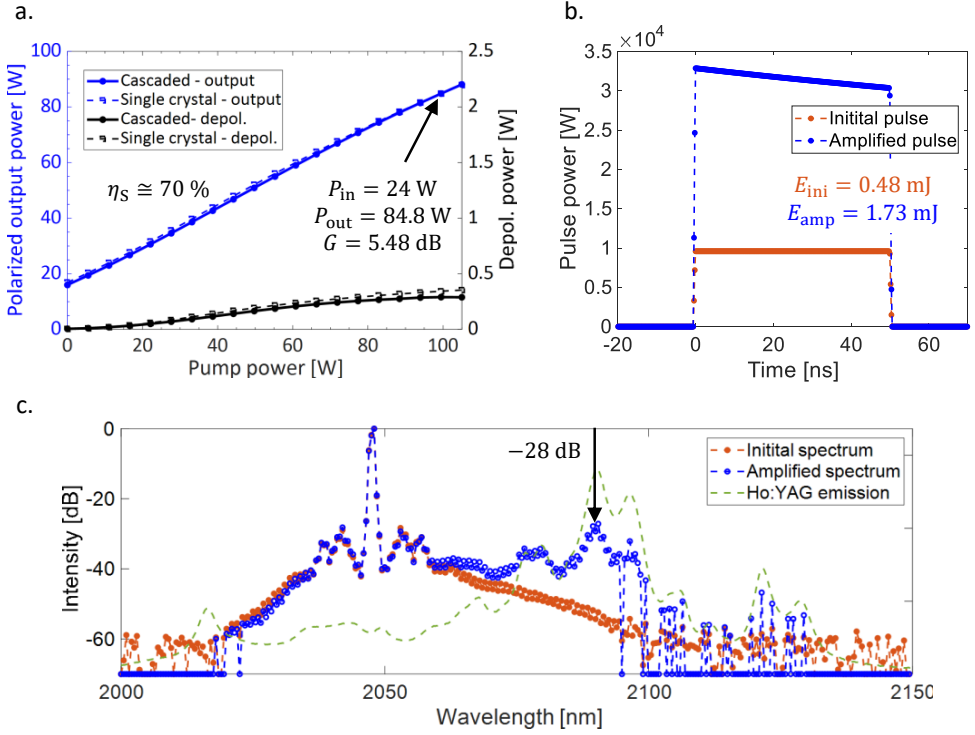


Figure 5.19: Output characteristics of the simulated Ho<sup>3+</sup>:YAG amplifier stage. The top left graph (a) displays the average polarized output (blue curves) and depolarization powers (black curves), where the dotted lines represent the single crystal and the solid lines the cascaded design. The top right graph (b) illustrates the simulated initial (orange) and amplified (blue) square pulses of the cascaded amplifier. The bottom graph represents the amplified spectrum (blue) relative to the initial spectrum (orange) across the full width of the supercontinuum.

maintains a more constant temperature over the full propagation length compared to the single crystal design. To improve this constant distribution, an undoped endcap of 0.4 cm length is bonded to the front endface of crystal 1 in the cascaded configuration, which experiences the highest temperature peak. The right graph illustrates the corresponding 2D temperature distribution as a cut at the  $y$ - $z$ -plane, where the effect of the endcap is visible. However, as the temperature increase in all crystals is small relative to the cooling temperature of 293 K, both configurations are assumed to show similar performance.

Figure 5.19 presents the simulated output characteristics of the Ho<sup>3+</sup>:YAG amplifier stage. The graph on the top left (a), illustrates the polarized output power (blue curves) and depolarization power (black curves) against the incident pump power for the fixed signal at 24 W. The dotted lines represent the single crystal and the solid lines represent the cascaded design, demonstrating that both configurations should perform similarly, as designed. At a pump power of 100 W, the simulation predicts an output signal power of 84.8 W corresponding to a gain of 5.48 dB and a slope efficiency of 70 %, indicating a highly efficient amplifier stage given the signal wavelength of 2048 nm for Ho<sup>3+</sup>:YAG. The depolarization losses are minimal for both configurations at approximately 0.3 W at the pump power of 100 W, suggesting effective thermal lens guiding. Figure 5.19b portrays the anticipated output pulse of the cascaded design at a pump power of 100 W. In the simulation, an ideal square pulse is assumed as the initial signal pulse (in orange), while the amplified pulse is shown in blue, exhibiting a pulse energy of 1.73 mJ. The depletion of the upper laser level over the pulse duration results in a decreasing pulse intensity with time. However, this effect is not substantial enough to significantly change the square pulse shape and could be mitigated by additional pre-shaping of the input pulse. Finally, the expected output spectrum is depicted in 5.19c, where the initial spectrum of the fiber MOPA is shown in orange and the amplifier spectrum is displayed in blue. All spectra are plotted with a resolution of 1 nm. Although the model does not anticipate a significant shift in the main spectral peak, it does indicate a broad amplification from 2070 to 2100 nm within the signal supercontinuum noise. This range aligns with the main spectral emission peaks of Ho<sup>3+</sup>:YAG, illustrated by the dotted green line. Despite the local spectral peak at 2090 nm being amplified by nearly 25 dB, it remains roughly 28 dB below the main peak at 2048 nm and over 98 % of the power stays concentrated there. At the edges of the initial supercontinuum the signal-to-noise ratio is too low for reliable predictions from the simulation model.

The presented results from the simulative design phase are very promising for the experimental demonstration, which will be discussed in the following section.

## 5.4.2 Experimental Results

After completing the design phase, the bulk power amplifier stage shows great promise towards achieving the objective of high pulse energies. Consequently, the optimized Ho<sup>3+</sup>:YAG cascaded configuration was experimentally constructed. Figure 5.20a illustrates the polarized signal output power of the power amplifier stage in relation to the pump power incident on the crystals.

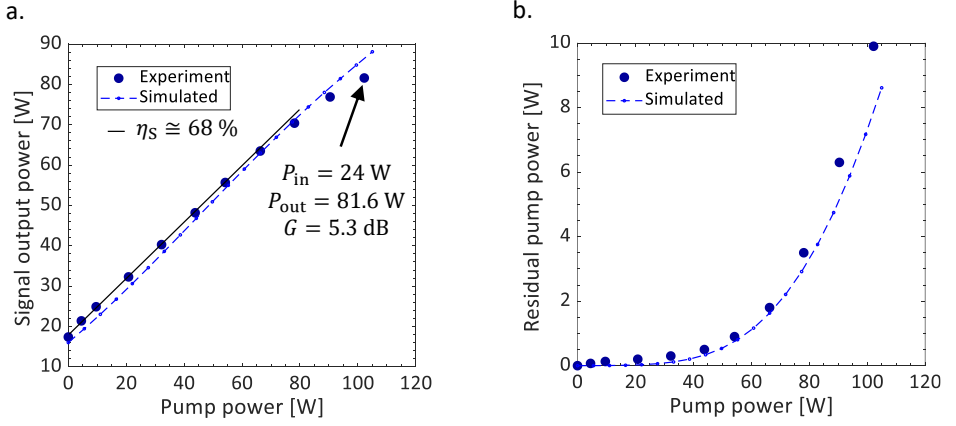


Figure 5.20: Output power performance of the experimental  $\text{Ho}^{3+}$ :YAG power amplifier stage. The graph on the left (a) depicts the signal output power against the incident pump power, while the graph on the right (b) displays the corresponding residual pump power.

The blue dots represent the values measured experimentally, while the faint dotted line portrays the power curve simulated during the design phase. The performance of the experimental amplifier is in good agreement with the simulated prediction, achieving a maximum signal power of 81.6 W at a pump power of 102 W. Given an initial signal of 24 W, this corresponds to a gain of 5.3 dB, demonstrating the efficient performance of the amplifier even at the off-peak wavelength of 2048 nm. While the slope efficiency up to a pump power of 80 W exhibits a value of 68 % (black line), close to the simulated prediction, the slope with higher pump powers falls slightly short of the expectation. This is attributed to the observed increase in residual pump power, as depicted in Fig. 5.20b. Although the model generally mirrors the experimental values, the rise in residual pump power is more pronounced in the experiment, particularly with higher pump powers. At a pump power of 102 W, a residual pump power of 9.9 W is recorded in the experiment. This earlier onset of crystal bleaching results in a reduction of pump absorption and correlates with the roll-over behavior observed with the signal output power. However, the discrepancy is small and the experimental amplifier demonstrates highly efficient performance at this operation point.

Further characterization was performed to analyze the output properties of the amplifier stage at the maximum signal output power of 81.6 W. Figure 5.21a presents the temporal pulse shape of the amplified pulse compared with the initial pulse from the fiber MOPA. At a pulse repetition

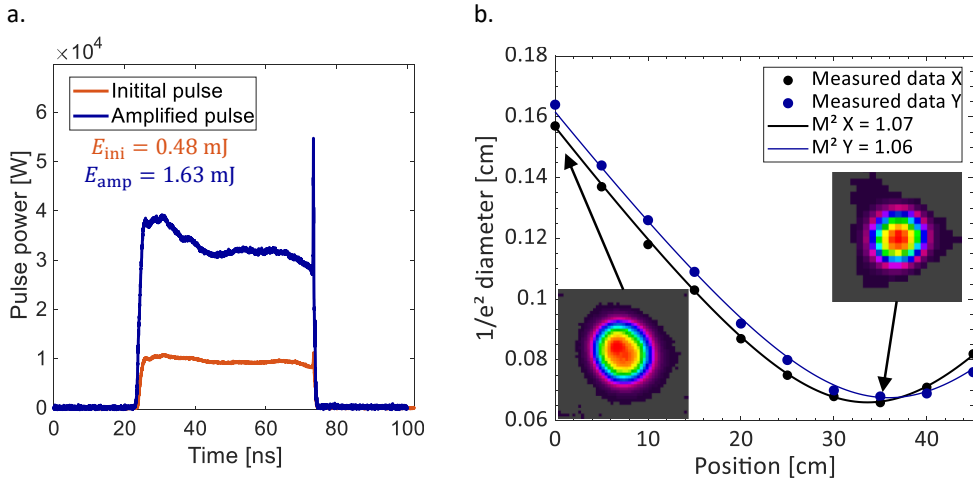


Figure 5.21: Additional output characteristics of the experimental Ho<sup>3+</sup>:YAG power amplifier. On the left (a), the initial temporal pulse (orange) is compared with the measured pulse after amplification (blue) at maximum pump power. The graph on the right (b) presents the measured beam quality  $M^2$  for the same operation point for the amplified signal. Here, the insets show the 2D beam profiles measured in the far and near field.

rate of 50 kHz, the initial pulse displays a pulse energy of 0.48 mJ, characterized by a rectangular pulse shape and a constant peak power around 10 kW. After the bulk amplifier stage, the pulse exhibits a pulse energy of 1.63 mJ at a constant peak power around 35 kW. The temporal shape of the pulse is well preserved, with a pulse FWHM of 49.3 ns and narrow rise and fall times. The pulse tail exhibits a sharp power peak, also present with the initial pulse, which is attributed to temporal effects in the modulated power diode of the fiber MOPA. These findings confirm that the initial objective of pulse energies exceeding 1 mJ was achieved, and the constraints of nonlinearities in the fiber MOPA could be overcome. Additionally, the caustic of the beam after the bulk amplifier stage was measured as shown in Fig. 5.21b, and the  $M^2$  values were calculated based on the hyperbolic fit detailed in section 5.1. The insets display the beam profile in the far and near field of the measurement distance, showcasing a nearly Gaussian distribution. In comparison to the signal beam prior to amplification, the profile now exhibits signs of slight astigmatism, which is attributed to the thermal birefringence from the bulk Ho<sup>3+</sup>:YAG crystals. Nonetheless, the beam continues to display close to diffraction-limited beam quality with  $M^2$  values below 1.1, validating that the cascaded design and corresponding thermal management were effectively optimized with the help of the simulation model.

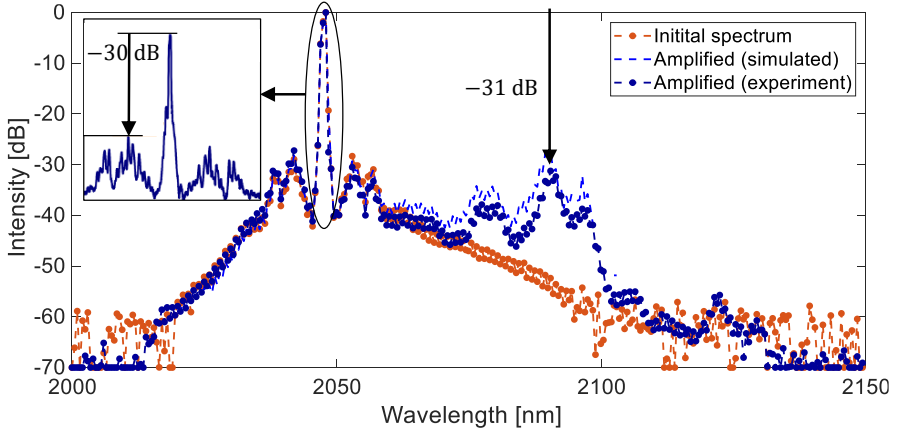


Figure 5.22: Output spectrum of the experimental  $\text{Ho}^{3+}$ :YAG power amplifier over the spectral range of interest. The orange dots represent the initial spectrum from the fiber MOPA, showcasing the broadband supercontinuum noise, while the dotted blue line and the dark blue dots depict the spectrum after amplification for the simulation and experimental measurement, respectively.

The amplified signal spectrum is provided in Fig. 5.22 over the spectral range of interest. Here, the orange dots correspond to the initial spectrum measured for the fiber MOPA, while the amplified spectrum predicted by the simulation is plotted with the dotted blue line. The spectrum measured after the amplifier stage is represented with the dark blue dots and exhibits good agreement with the simulative prediction. The supercontinuum noise at the emission peak of  $\text{Ho}^{3+}$ :YAG at 2090 nm is amplified slightly less than predicted by the model and remains below 31 dB the main spectral peak at 2048 nm. Additionally, the side peaks are plotted with higher spectral resolution in the inset and remain below 30 dB of the main peak. Consequently, over 98 % of the power lies within 1 nm at 2048 nm. For this configuration, the off-peak power content was sufficiently low to not contribute noticeably to the saturation of the amplifier gain, enabling an efficient  $\text{Ho}^{3+}$ :YAG amplifier even at a wavelength with a low emission cross section. However, the strong amplification at the emission peaks indicates that this approach is only suitable for narrow-linewidth laser signals comparable to this configuration, as larger off-peak content could result in gain saturation at undesired wavelengths.

During the experiments, the pointing stability of the beam slightly deteriorated compared to the stable output of the fiber MOPA. This observation was contributed to the thermal blooming in air. At the peak wavelength of the  $\text{Tm}^{3+}$  fiber pump source, 1908 nm, water ( $\text{H}_2\text{O}$ ) absorption

in the free space portion of the amplifier was noticeable. As the pump beam reaches high power levels and is focused down to a small diameter of approximately 0.04 cm, the high power densities cause local heating of the surrounding air. This phenomenon is similar to the thermal lensing effect for bulk media discussed in section 4.4.3, which can also occur in gases and can change the beam diameter over the propagation length. For the context of the cascaded amplifier configuration of this work, the impact of thermal blooming was investigated with an atmospheric propagation simulation based on the FFT-BPM, as detailed in reference [191]. This approach considers the heat conduction in air with a thermal model similar to the one described in chapter 4, without the contributions of displacement and stress. Strong thermal blooming could potentially deteriorate the beam quality of both pump and signal beam, as these beams are mode matched in a co-pumping configuration [191]. However, the effect on beam quality and waist diameters was determined to be minimal if the relative laboratory humidity is below 50 % at room temperature. The observed issues with pointing stability can be avoided if the free-space portion of the amplifier setup is flooded with an inert gas or dry air.

### 5.4.3 Discussion

In conclusion, the Ho<sup>3+</sup>:YAG power amplifier stage, utilized to amplify the signal of a three-stage fiber MOPA, demonstrated efficient performance and good output metrics. The energy scaling limitations of the fiber system, caused by fiber nonlinearities, were overcome by the hybrid fiber/bulk approach, achieving pulse energies of up to 1.63 mJ at a repetition rate of 50 kHz. Even at the signal wavelength of 2048 nm, which is far from the emission peaks of Ho<sup>3+</sup>:YAG and exhibits low cross section values, efficient amplification was possible. The simulation model, developed within the scope of this work, served as an essential tool as it allowed the mode evolution of the amplifier stage to be optimized for high conversion efficiencies and low depolarization losses. The main strategy was to leverage the thermal lensing effect from heat absorption to guide the signal and pump beam at small mode diameters, thereby achieving high inversion to compensate for the low cross section values. In contrast to the approach used in this work, alternative host materials such as Ho<sup>3+</sup>-doped yttrium lithium fluoride (YLF) or Ho<sup>3+</sup>-doped lithium lutetium fluoride (LLF) exhibit higher cross section values near 2048 nm, and could have been used for the intended application as well [192, 193]. However, as both these media exhibit low or even negative  $dn/dT$  parameter values, the thermal lens guiding approach is not possible and larger mode diameters are to be expected. For the goal of achieving high average powers with mJ-level pulse energies, as investigated with this amplifier system,

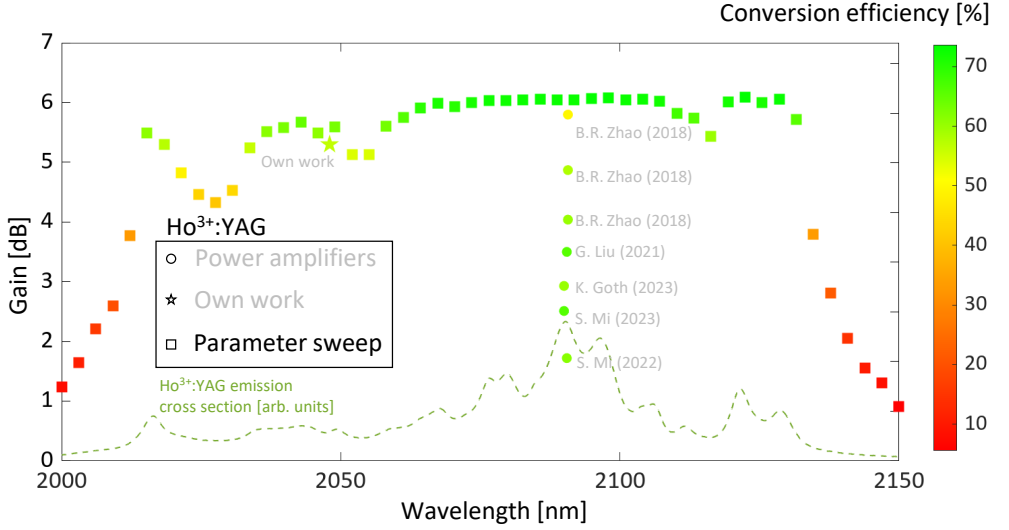


Figure 5.23: Parameter sweep regarding the cascaded  $\text{Ho}^{3+}$ :YAG amplifier gain performance over a wavelength range of 2000 to 2150 nm. Filled circles represent state-of-the-art systems, the star denotes the experimental results discussed in this section. The filled squares represent the simulated results from the sweep, colored according to their respective conversion efficiency. The dotted green line represents the  $\text{Ho}^{3+}$ :YAG emission.

$\text{Ho}^{3+}$ :YAG may be the most suitable amplifier medium available. However, to reach even higher pulse energies, and to mitigate optical damage by using large mode diameters, a transition to different host media is likely beneficial.

Finally, a simulative parameter sweep is conducted to explore the potential of  $\text{Ho}^{3+}$ :YAG as a broadband amplification medium. The results of the sweep are shown in Fig. 5.23, where the gain values are plotted over the wavelength range of interest from 2000 to 2150 nm, represented by filled squares with the color scheme corresponding to the conversion efficiency values. The  $\text{Ho}^{3+}$ :YAG emission cross section is represented by the dotted green line. For context, state-of-the-art amplifier systems are represented by filled circles, and the star denotes the experimental results discussed in this section. The sweep is conducted for the same cascaded configuration detailed in this work with the signal power of 24 W and optimized for 2048 nm. The graph suggests that efficient amplifier performance is achievable over a broad wavelength range from 2010 to 2130 nm, where the gain stays above 4 dB. Even better performance might be achievable with amplifiers optimized for their specific wavelength region. It is important

to note that this approach is only suitable for narrow-linewidth signal sources, as broadband spectral content with higher power levels can compromise the spectral properties of the laser system.

While these results are only simulative, the performance of the amplifier discussed in this section and the corresponding accuracy of the simulation model provide a strong indication that the results of the parameter sweep can be realized in experiment. With this in mind, the design approaches and results shown in this work suggest the possibility of utilizing  $\text{Ho}^{3+}$ :YAG across a broad spectral range, which could lead to new applications and use cases for this gain medium.

## 6 Conclusion and Outlook

During the course of this work, a comprehensive multi-physics simulation method for bulk solid-state laser systems was developed, validated, and utilized for the optimization of high-power  $\text{Ho}^{3+}$ :YAG lasers. The fundamental model is based on a modular approach, where the combination of various optical elements (including lenses, mirrors, gain media, etc.) allows for the simulation of complete laser configurations and systems. This modularity enables the precise modeling of laser resonators and amplifiers. The model operates iteratively, continuously updating all numerical values and arrays until a predefined end condition is reached, at which point the output characteristics of the simulated laser system are generated. For the laser field, this encompasses output power, temporal and spectral data, and a comprehensive description of the field distribution. Additionally, various distributions within the bulk optical elements, such as the temperature profile or population states in the gain medium, can be analyzed. The multi-physics model is constructed from the integration of three main submodels, designed to include the most relevant physical effects impacting laser performance:

**Beam propagation submodel:** The laser beam and additional coherent light sources, such as pump beams, are implemented using the split-step beam propagation method (BPM). This approach solves the wave equation of the electromagnetic field by propagation in a two-dimensional representation in  $x$  and  $y$ . The field is propagated incrementally along the  $z$ -direction, accounting for refraction, diffraction, and reflection, leading to a three-dimensional field representation  $\mathbb{E}(x, y, z)$  throughout the entire laser system. This method is expanded to a vectorial representation, where the field is divided into two polarization components  $\mathbb{E}_x$  and  $\mathbb{E}_y$ , taking into account polarization cross-talk and rotation at specific optical elements. Moreover, spectral resolution of laser beams is implemented into the model by propagating many monochromatic fields ( $s \rightarrow s_\lambda$ ) in parallel. Consequently, the complete field is represented in the vectorial multi-dimensional array  $\mathbb{E}_{x,y}(x, y, z, s)$ .

**Laser gain submodel:** Optical element operators can be placed between the propagation steps to achieve the modular simulation structure. For solid-state laser systems, emphasis is placed on the laser gain medium operator. Here, the laser beam is generated and amplified based on a rate equation approach, considering absorption and emission rates in the specific gain medium. The population states are calculated in a three-dimensional array  $N_i(x, y, z)$ , with a generalized approach accounting for only the upper and lower laser level, while more specific rate equation models consider multiple energy levels  $N_i$ . For this work, the specific rate equation model for  $\text{Ho}^{3+}$ -doped gain media is described in more detail, where the  ${}^5I_7 \rightarrow {}^5I_8$  laser transition is employed to generate radiation in the shortwave infrared region around  $2\text{ }\mu\text{m}$ . Advanced laser media dynamics are included to expand the model approach to a spectrally and temporally resolved model capable of simulating spectral behavior and pulse generation.

**Thermal submodel:** The validation with an experimental linear  $\text{Ho}^{3+}$ :YAG laser resonator indicates that the model aligns well when power absorption within the elements is low and a fundamental laser mode can be maintained. However, as power increases, thermal effects within the experimental resonator disrupt the laser mode and impact laser performance. Consequently, an extensive thermal model is incorporated into the multi-physical approach, aiming to account for all relevant thermal effects of high-power solid-state laser operation. This goal is achieved by numerically solving the heat equation based on the heat load  $Q(x, y, z)$  of the specific element, utilizing a finite-difference-method (FDM) algorithm. This results in the three-dimensional temperature distribution  $T(x, y, z)$ . Since thermal expansion induces a stress response within the bulk material, it can contribute to additional thermal effects that influence laser performance. The Navier-Stokes equations for elasticity can be solved using an additional FDM algorithm to compute the three-dimensional displacement distributions for the three spatial directions  $D_d(x, y, z)$ . The resulting stress tensor  $\sigma_{d,d}(x, y, z)$  can then be calculated with Hooke's law. These distributions allow for the consideration of relevant thermal effects on the laser field. This includes the temperature-dependency of material parameters, which range from thermal parameters such as heat capacity, thermal conductivity, and density to spectral parameters like emission and absorption cross sections. Thermal effects resulting from changes in the three-dimensional vectorial refractive index profile  $n_{x,y}(x, y, z)$  are also considered, including stress-induced birefringence and subsequent depolarization losses. The most significant contribution to laser performance comes from the inclusion of thermal lensing, mainly resulting from three mechanisms: the thermo-optic effect, the photoelastic effect, and endface bulging.

The specific submodels and approaches have been validated individually with comparison to analytical solutions and experimental measurements. After the implementation of all relevant physical effects into the comprehensive multi-physics model, the experimental  $\text{Ho}^{3+}$ :YAG resonator used for validation shows excellent agreement with the simulation.

The developed simulation tool was then utilized in the development of two experimental laser systems based on  $\text{Ho}^{3+}$ :YAG as the gain medium. The first system was a Q-switched linear resonator, designed for high-power generation of nanosecond pulses. Unlike typical Q-switched  $\text{Ho}^{3+}$ :YAG laser resonators, this system operates at the red-shifted wavelength of 2122 nm, where the highest average output power values (at the time of this thesis) in Q-switched operation were achieved. These results were obtained through a simulation optimization process involving various geometry and parameter sweep simulations. A particular focus was placed on suppressing the main emission peaks at 2090 and 2096 nm by utilizing high OC reflectivities and multiple intracavity etalons. The resonator demonstrated diffraction-limited beam quality at a maximum average output power of 57 W. This resonator design showed that power scaling in  $\text{Ho}^{3+}$ :YAG is feasible even at longer wavelengths, and with pulse energies exceeding 1 mJ, high pulse-energy applications benefiting from this spectral region can be addressed. The second system that was developed with the simulation tool was a  $\text{Ho}^{3+}$ :YAG power amplifier stage seeded by a fiber MOPA at a wavelength of 2048 nm. This unique hybrid fiber/bulk MOPA design is noteworthy as typical high-power  $\text{Ho}^{3+}$ :YAG amplifiers are mainly operated around the main emission peak at 2090 nm. However, a highly efficient amplifier was demonstrated even at this wavelength, where the gain medium exhibits a low emission cross section value. The design process involved various parameter sweep and crystal geometry simulation runs, with a focus on enhancing gain and minimizing astigmatism and depolarization losses by establishing mode-matching over a long amplifier crystal length. This was achieved by utilizing thermal lens guiding, where the heat development within a cascaded amplifier crystal arrangement was designed to maintain small signal and pump diameters over the full length. For a signal seed power of 24 W, an amplified output power of 81.6 W was attained at a pump power of 102 W, resulting in a gain of 5.3 dB and a conversion efficiency of 56.4 %. For both systems, exceptional performance was achieved at unique operation wavelengths far from the main emission peak, made possible only by the use of the comprehensive simulation model. Considering these experimental results, the developed model proves to be a powerful tool capable of designing, optimizing, and analyzing bulk solid-state laser systems for various applications.

The subsequent discussion briefly addresses the further development of the presented simulation model and the experimental  $\text{Ho}^{3+}$ :YAG systems:

**Outlook – Simulation model:** The demonstrated effectiveness of the multi-physics simulation approach in the design of  $\text{Ho}^{3+}$ :YAG systems suggests that its extension to various other laser gain media would be of great interest. Although the basic rate equation model is capable of simulating most in-band pumped systems, the exemplary  $\text{Ho}^{3+}$ :YAG resonator used to validate the model indicates the need for more complex multi-level rate equation models for high simulation accuracy. For instance, the pumping of  $\text{Tm}^{3+}$ -doped laser crystals with the two-to-one cross-relaxation process cannot be simulated with the generalized approach, requiring a complex model for the accurate representation of this laser system. However, it is important to note that the implementation of complex active-ions requires comprehensive material parameters as input data. For example, to account for spectral resolution, spectrally resolved cross section data is necessary. This requires either sufficient literature data or laborious material measurements, while the accuracy of the model is dependent on the accuracy of the available material parameter. Furthermore, while the modular nature of the model allows for the simulation of different geometries, highly complex laser designs will require extended simulation approaches. For instance, as the model operates on sequential beam propagation, multi-arm laser resonators with light runtime differences in respective arms pose a challenge to the model that must be addressed separately. Additionally, by substituting the gain medium element with an optical nonlinear medium element, the multi-physics model approach could even be expanded to simulate OPA, OPG, and OPO systems; although this would require an entirely new submodel and significant time investment. In conclusion, while the developed simulation model is already a powerful tool for designing basic high-power bulk laser systems, specific and complex systems will require additional model approaches and considerations.

**Outlook –  $\text{Ho}^{3+}$ :YAG design:** In addition to their specific applications, the two laser systems developed within this work aimed to provide insight into the spectral behavior of  $\text{Ho}^{3+}$ :YAG in high-power applications. While current state-of-the-art systems focus on operation near the main emission peaks for maximum efficiency, the results presented in this work demonstrate that the gain medium can be utilized far from these peaks without significant efficiency loss. Notably, the power amplifier operated at 2048 nm, and corresponding power sweep simulations suggest that  $\text{Ho}^{3+}$ :YAG can be efficiently used as an amplifier crystal from 2010 to 2130 nm, spanning a wavelength range of over 100 nm, thereby enabling broadband applications. Although the spectral tuning of resonators can be more challenging as the main emission peaks have to be

suppressed, the design of the Q-switched resonator at 2122 nm suggests that efficient operation can be achieved over a broad spectral region as well. Simulations also indicate the potential for further red-shifting to at least the 2130 nm emission peak. In conclusion, the design and development of the two resonator and amplifier systems at their unique wavelengths suggest that  $\text{Ho}^{3+}$ :YAG can serve as an efficient gain and amplification medium over a wide spectral range, where it is currently not utilized.



# References

- [1] T. H. Maiman, “Stimulated Optical Radiation in Ruby,” *Nature*, vol. 187, no. 4736, p. 493, Aug. 1960. DOI: 10.1038/187493a0.
- [2] C. Webb and J. D. Jones, Eds., *Handbook of Laser Technology and Applications*. CRC Press, Sep. 2020. DOI: 10.1201/9780429183515.
- [3] W. Koechner, *Solid-State Laser Engineering* (Springer Series in Optical Sciences). New York, NY: Springer New York, 2006, vol. 1. DOI: 10.1007/0-387-29338-8.
- [4] M. Eichhorn, “Quasi-three-level solid-state lasers in the near and mid infrared based on trivalent rare earth ions,” *Applied Physics B*, vol. 93, no. 2-3, p. 269, Nov. 2008. DOI: 10.1007/s00340-008-3214-0.
- [5] M. Schellhorn, G. Spindler, and M. Eichhorn, “Mid-infrared ZGP OPO with divergence compensation and high beam quality,” *Optics Express*, vol. 26, no. 2, p. 1402, Jan. 2018. DOI: 10.1364/OE.26.001402.
- [6] Y.-J. Shen, B.-Q. Yao, X.-M. Duan, T.-Y. Dai, Y.-L. Ju, and Y.-Z. Wang, “Performance of High Power 2  $\mu\text{m}$  Ho:YAG Laser,” in *CLEO: 2013*, Washington, D.C.: OSA, 2013, CTu3D.3. DOI: 10.1364/CLEO\_SI.2013.CTu3D.3.
- [7] G. Liu et al., “161 W middle infrared ZnGeP 2 MOPA system pumped by 300 W-class Ho:YAG MOPA system,” *Optics Letters*, vol. 46, no. 1, p. 82, Jan. 2021. DOI: 10.1364/OL.413755.
- [8] S. Mi, J. Tang, D. Wei, B. Yao, J. Li, K. Yang, T. Dai, and X. Duan, “Thermal-birefringence-induced depolarization in a 450 W Ho:YAG MOPA system,” *Optics Express*, vol. 30, no. 12, p. 21501, Jun. 2022. DOI: 10.1364/OE.462617.

- [9] X. Duan, Y. Shen, B. Yao, and Y. Wang, “146.4 W end-pumped Ho : YAG slab laser with two crystals,” *Quantum Electronics*, vol. 48, no. 8, p. 691, Sep. 2018. DOI: 10.1070/QEL16717.
- [10] P. G. Schunemann, K. T. Zawilski, L. A. Pomeranz, D. J. Creeden, and P. A. Budni, “Advances in nonlinear optical crystals for mid-infrared coherent sources,” *Journal of the Optical Society of America B*, vol. 33, no. 11, p. D36, Nov. 2016. DOI: 10.1364/JOSAB.33.000D36.
- [11] G. Verhoeven, “The reflection of two fields – Electromagnetic radiation and its role in (aerial) imaging,” *AARGnews*, vol. 55, p. 13, Oct. 2017. DOI: 10.5281/zenodo.3534245.
- [12] M. Bass, Ed., *Handbook of Optics: Volume I - Geometrical and Physical Optics, Polarized Light, Components and Instruments*, en, 3rd Editio. New York: McGraw-Hill Education, 2010, p. 1568.
- [13] H. Römer, *Theoretical Optics*. Wiley, Nov. 2004. DOI: 10.1002/3527604294.
- [14] M. Born, E. Wolf, and A. B. Bhatia, *Principles of optics : electromagnetic theory of propagation, interference, and diffraction of light*, 1st ed. Cambridge: Cambridge University Press, 1999.
- [15] C. A. Balanis, *Advanced engineering electromagnetics*, English. New York SE: Wiley, 1989. DOI: LK-<https://worldcat.org/title/18908383>.
- [16] P. Klocek, *Handbook of Infrared Optical Materials*, P. Klocek, Ed. CRC Press, Sep. 2017. DOI: 10.1201/9781315213996.
- [17] M. Eichhorn, *Laserphysik*. Berlin, Heidelberg: Springer Berlin Heidelberg, 2013. DOI: 10.1007/978-3-642-32648-6.
- [18] M. D. Feit and J. A. Fleck, “Spectral approach to optical resonator theory,” *Applied Optics*, vol. 20, no. 16, p. 2843, Aug. 1981. DOI: 10.1364/AO.20.002843.
- [19] S. Mazumder, *Numerical Methods for Partial Differential Equations: Finite Difference and Finite Volume Methods*. Elsevier Science, 2015.
- [20] D. Yevick, Jun Yu, W. Bardyszewski, and M. Glasner, “Stability issues in vector electric field propagation,” *IEEE Photonics Technology Letters*, vol. 7, no. 6, p. 658, Jun. 1995. DOI: 10.1109/68.388756.
- [21] H. Deng, W. Geng, and J. Hong, “FD-BPM analysis to design the optimum structure and size of bent waveguide with small radius,” in *Integrated Optoelectronics*, R. T. Chen, W.-T. Tsang, and B. Zhou, Eds., vol. 2891, Sep. 1996, p. 301. DOI: 10.1117/12.253202.

- 
- [22] J. Yamauchi, G. Takahashi, and H. Nakano, "Full-vectorial beam-propagation method based on the McKee-Mitchell scheme with improved finite-difference formulas," *Journal of Lightwave Technology*, vol. 16, no. 12, p. 2458, 1998. DOI: 10.1109/50.736638.
- [23] T. V. Yioultsis, G. D. Ziogos, and E. E. Kriezis, "Explicit finite-difference vector beam propagation method based on the iterated Crank-Nicolson scheme," *Journal of the Optical Society of America A*, vol. 26, no. 10, p. 2183, Oct. 2009. DOI: 10.1364/JOSAA.26.002183.
- [24] G. Hadley, "Transparent boundary condition for the beam propagation method," *IEEE Journal of Quantum Electronics*, vol. 28, no. 1, p. 363, 1992. DOI: 10.1109/3.119536.
- [25] J. Shibayama, T. Takahashi, J. Yamauchi, and H. Nakano, "A Three-Dimensional Multistep Horizontally Wide-Angle Beam-Propagation Method Based on the Generalized Douglas Scheme," *IEEE Photonics Technology Letters*, vol. 18, no. 23, p. 2535, Dec. 2006. DOI: 10.1109/LPT.2006.887201.
- [26] E. O. Brigham, *The fast Fourier transform and its applications*. USA: Prentice-Hall, Inc., 1988.
- [27] L. R. Gomaa, A. Shaaban, M. F. O. Hameed, and S. S. A. Obayya, "Competitiveness of the BPM in studying the optical beams at critical incidence on dielectric interfaces," *Optical and Quantum Electronics*, vol. 49, no. 2, p. 51, Feb. 2017. DOI: 10.1007/s11082-016-0886-2.
- [28] J. A. Fleck, J. R. Morris, and M. D. Feit, "Time-dependent propagation of high energy laser beams through the atmosphere," *Applied physics*, vol. 10, no. 2, p. 129, Jun. 1976. DOI: 10.1007/BF00896333.
- [29] N. Delen and B. Hooker, "Free-space beam propagation between arbitrarily oriented planes based on full diffraction theory: a fast Fourier transform approach," *Journal of the Optical Society of America A*, vol. 15, no. 4, p. 857, Apr. 1998. DOI: 10.1364/JOSAA.15.000857.
- [30] C. Vassallo, "Difficulty with vectorial BPM," *Electronics Letters*, vol. 33, no. 1, p. 61, 1997. DOI: 10.1049/el:19970014.
- [31] B. Cloutier, B. Muite, and P. Rigge, "Performance of FORTRAN and C GPU Extensions for a Benchmark Suite of Fourier Pseudospectral Algorithms," in *2012 Symposium on Application Accelerators in High Performance Computing*, IEEE, Jul. 2012, p. 145. DOI: 10.1109/SAAHPC.2012.24. arXiv: 1206.3215.
-

- [32] R. W. Numrich and J. Reid, "Co-array Fortran for parallel programming," *ACM SIG-PLAN Fortran Forum*, vol. 17, no. 2, p. 1, Aug. 1998. DOI: 10.1145/289918.289920.
- [33] The Mathworks Inc., *MATLAB version 9.14.0.2239454 (R2023a)*, Natick, Massachusetts, 2023.
- [34] P. E. Ciddor, "Refractive index of air: new equations for the visible and near infrared," *Applied Optics*, vol. 35, no. 9, p. 1566, Mar. 1996. DOI: 10.1364/AO.35.001566.
- [35] D. E. Zelmon, D. L. Small, and R. Page, "Refractive-index measurements of undoped yttrium aluminum garnet from 04 to 50  $\mu\text{m}$ ," *Applied Optics*, vol. 37, no. 21, p. 4933, Jul. 1998. DOI: 10.1364/AO.37.004933.
- [36] C. Huygens, *Treatise on Light*. Translated by Thompson, S. P. Project Gutenberg, 2005.
- [37] W. Koechner and D. Rice, "Effect of birefringence on the performance of linearly polarized YAG:Nd lasers," *IEEE Journal of Quantum Electronics*, vol. 6, no. 9, p. 557, Sep. 1970. DOI: 10.1109/JQE.1970.1076529.
- [38] R. W. Boyd, *Nonlinear Optics*, 3rd. USA: Academic Press, Inc., 2008.
- [39] J. A. Fleck and M. D. Feit, "Beam propagation in uniaxial anisotropic media," *Journal of the Optical Society of America*, vol. 73, no. 7, p. 920, Jul. 1983. DOI: 10.1364/JOSA.73.000920.
- [40] L. Thylen and D. Yevick, "Beam propagation method in anisotropic media," *Applied Optics*, vol. 21, no. 15, p. 2751, Aug. 1982. DOI: 10.1364/AO.21.002751.
- [41] G. Arisholm, "General numerical methods for simulating second-order nonlinear interactions in birefringent media," *Journal of the Optical Society of America B*, vol. 14, no. 10, p. 2543, Oct. 1997. DOI: 10.1364/JOSAB.14.002543.
- [42] L. Alcan, F. Teixeira, A. Cesar, and B.-H. Borges, "A new full-vectorial FD-BPM scheme: application to the analysis of magnetooptic and nonlinear saturable media," *Journal of Lightwave Technology*, vol. 23, no. 8, p. 2579, Aug. 2005. DOI: 10.1109/JLT.2005.850811.
- [43] G. Ghosh, "Dispersion-equation coefficients for the refractive index and birefringence of calcite and quartz crystals," *Optics Communications*, vol. 163, no. 1-3, p. 95, May 1999. DOI: 10.1016/S0030-4018(99)00091-7.
- [44] M. Bass, *Handbook of Optics: Volume II - Design, Fabrication, and Testing; Sources and Detectors; Radiometry and Photometry*, en, 3rd Editio, M. Bass, Ed. New York: McGraw-Hill Education, 2010.

- 
- [45] A. Smith, M. Bowers, and G. Arisholm, "Progress in modeling nanosecond optical parametric oscillators," in *1999 IEEE LEOS Annual Meeting Conference Proceedings. LEOS'99. 12th Annual Meeting. IEEE Lasers and Electro-Optics Society 1999 Annual Meeting (Cat. No.99CH37009)*, vol. 2, IEEE, 1999, p. 580. DOI: 10.1109/LEOS.1999.811860.
- [46] K. Halbach, "Matrix Representation of Gaussian Optics," *American Journal of Physics*, vol. 32, no. 2, p. 90, Feb. 1964. DOI: 10.1119/1.1970159.
- [47] A. E. Siegman, *Lasers*. University Science Books, 1986, p. 1283. DOI: 10.1007/978-3-642-18520-5\_8.
- [48] P. Tirkas, C. Balanis, M. Purchine, and G. Barber, "Finite-difference time-domain method for electromagnetic radiation, interference, and interaction with complex structures," *IEEE Transactions on Electromagnetic Compatibility*, vol. 35, no. 2, p. 192, May 1993. DOI: 10.1109/15.229421.
- [49] P. Torres and A. Guzman, "Complex finite-element method applied to the analysis of optical waveguide amplifiers," *Journal of Lightwave Technology*, vol. 15, no. 3, p. 546, Mar. 1997. DOI: 10.1109/50.557572.
- [50] LASCAD GmbH. "LASCAD 3.6 Manual," Accessed: Jun. 17, 2024. [Online]. Available: [https://www.las-cad.com/lascad\\_documentation.php](https://www.las-cad.com/lascad_documentation.php).
- [51] ASLD GmbH. "Multiphysics Laser Simulation Software," Accessed: Jun. 17, 2024. [Online]. Available: <https://www.asldweb.com/>.
- [52] LightTrans International GmbH. "Laser Systems in VirtualLab Fusion," Accessed: Jun. 17, 2024. [Online]. Available: <https://www.lighttrans.com/applications/laser-systems.html>.
- [53] COMSOL Multiphysics GmbH. "How to Use the Beam Envelope Method for Wave Optics Simulations | COMSOL Blog," Accessed: Jun. 6, 2024. [Online]. Available: <https://www.comsol.com/blogs/how-to-use-the-beam-envelopes-method-for-wave-optics-simulations>.
- [54] M. Wohlmuth, C. Pflaum, K. Altmann, M. Paster, and C. Hahn, "Dynamic multimode analysis of Q-switched solid state laser cavities," *Optics Express*, vol. 17, no. 20, p. 17303, Sep. 2009. DOI: 10.1364/OE.17.017303.

- [55] C. Pflaum, Z. Rahimi, and F. Feng, "Dynamic multi-mode analysis of passive Q-switched lasers," in *Laser Resonators, Microresonators, and Beam Control XIV*, A. V. Kudryashov, A. H. Paxton, and V. S. Ilchenko, Eds., vol. 8236, Feb. 2012, p. 823612. DOI: 10.1117/12.905201.
- [56] M. Wohlmuth and C. Pflaum, "Analysis of frequency dependent pump light absorption," in *Laser Resonators and Beam Control XIII*, A. V. Kudryashov, A. H. Paxton, and V. S. Ilchenko, Eds., vol. 7913, Feb. 2011, p. 791303. DOI: 10.1117/12.874793.
- [57] F. Wyrowski and M. Kuhn, "Introduction to field tracing," *Journal of Modern Optics*, vol. 58, no. 5-6, p. 449, Mar. 2011. DOI: 10.1080/09500340.2010.532237.
- [58] D. Asoubar, S. Zhang, M. Kuhn, and F. Wyrowski, "Laser resonator modeling by field tracing: a flexible approach for fully vectorial transversal eigenmode calculation," *Journal of the Optical Society of America B*, vol. 31, no. 11, p. 2565, Nov. 2014. DOI: 10.1364/JOSAB.31.002565.
- [59] COMSOL Multiphysics GmbH. "Waveguides and Interferometers : Simulations studies on Photonic Devices using COMSOL Multiphysics®," Accessed: Jun. 6, 2024. [Online]. Available: <https://www.comsol.de/paper/waveguides-and-interferometers-simulations-studies-on-photonic-devices-using-com-83841>.
- [60] COMSOL Multiphysics GmbH. "Multiphysics Design and Analysis of a Refractive Beam Expander and a High-Power Laser," Accessed: Jun. 6, 2024. [Online]. Available: <https://www.comsol.de/paper/multiphysics-design-and-analysis-of-a-refractive-beam-expander-and-a-high-power-121701>.
- [61] M. Eichhorn, "Numerical Modeling of Diode-End-Pumped High-Power  $\text{Er}^{3+}$ :YAG Lasers," *IEEE Journal of Quantum Electronics*, vol. 44, no. 9, p. 803, Sep. 2008. DOI: 10.1109/JQE.2008.924810.
- [62] M. Eichhorn, "Thermo-optical model for  $\text{Er}^{3+}$ :YAG gain media," M. Dubinskii and G. L. Wood, Eds., Apr. 2008, 69520P. DOI: 10.1117/12.773870.
- [63] Y. Shen, M. Gong, E. Ji, X. Fu, and L. Sun, "Spatial dynamic thermal iteration model for 888 nm end-pumped Nd:YVO<sub>4</sub> solid-state laser oscillators and amplifiers," *Optics Communications*, vol. 383, p. 430, Jan. 2017. DOI: 10.1016/j.optcom.2016.09.040.
- [64] E. Ji, Y. Shen, M. Nie, X. Fu, and Q. Liu, "Spectra- and temperature-dependent dynamics of directly end-pumped holmium lasers," *Applied Physics B*, vol. 123, no. 4, p. 129, Apr. 2017. DOI: 10.1007/s00340-017-6707-x.

- 
- [65] H. Shu and M. Bass, "Three-dimensional computer model for simulating realistic solid-state lasers," *Applied Optics*, vol. 46, no. 23, p. 5687, Aug. 2007. DOI: 10.1364/AO.46.005687.
- [66] K. Matsushima, "Formulation of the rotational transformation of wave fields and their application to digital holography," *Applied Optics*, vol. 47, no. 19, p. D110, Jul. 2008. DOI: 10.1364/AO.47.00D110.
- [67] S. A. Collins, "Lens-System Diffraction Integral Written in Terms of Matrix Optics\*," *Journal of the Optical Society of America*, vol. 60, no. 9, p. 1168, Sep. 1970. DOI: 10.1364/JOSA.60.001168.
- [68] K. T. McDonald, "Reflection of a Gaussian Optical Beam by a Flat Mirror Reflection of an Infinite Plane Waves by a Planar Mirror," *Joseph Henry Laboratories, Princeton University*, vol. 1, no. 1, p. 1, 2009.
- [69] A. G. Fox and T. Li, "Resonant Modes in a Maser Interferometer," *Bell System Technical Journal*, vol. 40, no. 2, p. 453, Mar. 1961. DOI: 10.1002/j.1538-7305.1961.tb01625.x.
- [70] P. A. Bélanger and C. Paré, "Optical resonators using graded-phase mirrors," *Optics Letters*, vol. 16, no. 14, p. 1057, Jul. 1991. DOI: 10.1364/OL.16.001057.
- [71] N. Ismail, C. C. Kores, D. Geskus, and M. Pollnau, "Fabry-Pérot resonator: spectral line shapes, generic and related Airy distributions, linewidths, finesse, and performance at low or frequency-dependent reflectivity," *Optics Express*, vol. 24, no. 15, p. 16366, Jul. 2016. DOI: 10.1364/OE.24.016366.
- [72] H. Haken and H. C. Wolf, *Atom- und Quantenphysik* (Springer-Lehrbuch). Berlin, Heidelberg: Springer Berlin Heidelberg, 2004. DOI: 10.1007/978-3-642-18519-9.
- [73] J. R. Lakowicz, "Principles of fluorescence spectroscopy," *Principles of Fluorescence Spectroscopy*, p. 1, 2006. DOI: 10.1007/978-0-387-46312-4/COVER.
- [74] Y. Song, N. Zong, K. Liu, Z. Wang, X. Wang, Y. Bo, Q. Peng, and Z. Xu, "Temperature-dependent thermal and spectroscopic properties of Yb:YAlO<sub>3</sub> perovskite crystal for a cryogenically cooled near IR laser," *Optical Materials Express*, vol. 10, no. 7, p. 1522, Jul. 2020. DOI: 10.1364/OME.392500.
- [75] 4Lasers Corporation. "Yb:YAP crystals," Accessed: Aug. 15, 2024. [Online]. Available: <https://4lasers.com/en/components/crystals/laser-crystals/yb-doped-crystals/yb-yap-crystals>.
-

- [76] D. E. McCumber, "Einstein Relations Connecting Broadband Emission and Absorption Spectra," *Physical Review*, vol. 136, no. 4A, A954, Nov. 1964. DOI: 10.1103/PhysRev.136.A954.
- [77] D. W. Goodwin, "Spectra and Energy Levels of Rare Earth Ions in Crystals," *Physics Bulletin*, vol. 20, no. 12, p. 525, Dec. 1969. DOI: 10.1088/0031-9112/20/12/010.
- [78] S. Wang, M. Tao, Q. Yang, Y. Qi, and X. Ye, "Beam quality prediction for Tm-doped fiber system based on finite-difference beam propagation method," *Physica Scripta*, vol. 99, no. 7, p. 075517, Jul. 2024. DOI: 10.1088/1402-4896/ad51b9.
- [79] R. Paschotta, "Peak Power - an encyclopedia article," in *RP Photonics Encyclopedia*, RP Photonics AG, Nov. 2005. DOI: 10.61835/eco.
- [80] R. Poprawe, K. Boucke, and D. Hoffman, *Tailored Light 1: High Power Lasers for Production*. Springer Berlin Heidelberg, 2018.
- [81] T. Graf, *Laser: Grundlagen der Laserstrahlquellen*. Vieweg+Teubner, 2009.
- [82] H. Hügel and T. Graf, *Laser in der Fertigung: Strahlquellen, Systeme, Fertigungsverfahren*. Vieweg + Teubner, 2009.
- [83] ISO Standard 11146, *Lasers and laser-related equipment – Test methods for laser beam widths, divergence angles and beam propagation ratios*, 2005.
- [84] A. E. Siegman, "How to (Maybe) Measure Laser Beam Quality," in *DPSS (Diode Pumped Solid State) Lasers: Applications and Issues*, vol. d, Washington, D.C.: OSA, 1998, MQ1. DOI: 10.1364/DLAI.1998.MQ1.
- [85] V. Magni, "Multielement stable resonators containing a variable lens," *Journal of the Optical Society of America A*, vol. 4, no. 10, p. 1962, Oct. 1987. DOI: 10.1364/JOSAA.4.001962.
- [86] V. Magni, "Resonators for solid-state lasers with large-volume fundamental mode and high alignment stability," *Applied Optics*, vol. 25, no. 13, p. 2039, Jul. 1986. DOI: 10.1364/AO.25.002039.
- [87] S. De Silvestri, P. Laporta, and V. Magni, "Rod thermal lensing effects in solid-state laser ring resonators," *Optics Communications*, vol. 65, no. 5, p. 373, Mar. 1988. DOI: 10.1016/0030-4018(88)90106-X.
- [88] M. Eichhorn, "High-power resonantly diode-pumped CW Er<sup>3+</sup>:YAG laser," *Applied Physics B*, vol. 93, no. 4, p. 773, Dec. 2008. DOI: 10.1007/s00340-008-3242-9.

- 
- [89] X. Fan, P. Kuan, K. Li, L. Zhang, D. Li, and L. Hu, "Spectroscopic properties and quenching mechanism of 2  $\mu\text{m}$  emission in  $\text{Ho}^{3+}$  doped germanate glasses and fibers," *Optical Materials Express*, vol. 5, no. 6, p. 1356, Jun. 2015. DOI: 10.1364/OME.5.001356.
- [90] B. M. Walsh, N. P. Barnes, and B. Di Bartolo, "Branching ratios, cross sections, and radiative lifetimes of rare earth ions in solids: Application to  $\text{Tm}^{3+}$  and  $\text{Ho}^{3+}$  ions in  $\text{LiYF}_4$ ," *Journal of Applied Physics*, vol. 83, no. 5, p. 2772, Mar. 1998. DOI: 10.1063/1.367037.
- [91] K. Goth, M. Rupp, M. Griesbeck, M. Eitner, M. Eichhorn, and C. Kieleck, "Limitations of homogeneous and segmented single-crystal compact TEM<sub>00</sub>-mode  $\text{Ho}^{3+}$ :YAG laser resonators," *Applied Physics B*, vol. 129, no. 6, p. 95, Jun. 2023. DOI: 10.1007/s00340-023-08033-8.
- [92] D. E. Zelmon, D. L. Small, and R. Page, "Refractive-index measurements of undoped yttrium aluminum garnet from 04 to 50  $\mu\text{m}$ ," *Applied Optics*, vol. 37, no. 21, p. 4933, Jul. 1998. DOI: 10.1364/AO.37.004933.
- [93] J. Sulc, M. Nemec, D. Vyhlidal, H. Jelinkova, K. Nejezchleb, and J. Polak, "Holmium doping concentration influence on Ho:YAG crystal spectroscopic properties," in *Solid State Lasers XXX: Technology and Devices*, W. A. Clarkson and R. K. Shori, Eds., SPIE, Mar. 2021, p. 34. DOI: 10.1117/12.2578284.
- [94] B. M. Walsh, G. W. Grew, and N. P. Barnes, "Energy levels and intensity parameters of ions in  $\text{Y}_3\text{Al}_5\text{O}_{12}$  and  $\text{Lu}_3\text{Al}_5\text{O}_{12}$ ," *Journal of Physics and Chemistry of Solids*, vol. 67, no. 7, p. 1567, Jul. 2006. DOI: 10.1016/j.jpcs.2006.01.123.
- [95] M. Falconieri, A. Lanzi, G. Salvetti, and A. Toncelli, "Fluorescence dynamics in an optically-excited Tm,Ho:YAG crystal," *Optical Materials*, vol. 7, no. 3, p. 135, Mar. 1997. DOI: 10.1016/S0925-3467(97)00004-9.
- [96] K. L. Hovhannesian, M. V. Derdzyan, I. A. Ghambaryan, A. A. Novikov, V. E. Kisel, A. S. Rudenkov, N. V. Kuleshov, and A. G. Petrosyan, "Spectral Properties of YAP:Yb Laser Crystals with Additional  $\text{Li}^+$  and  $\text{Hf}^{4+}$  Ions," *Journal of Contemporary Physics (Armenian Academy of Sciences)*, vol. 56, no. 4, p. 309, Oct. 2021. DOI: 10.3103/S1068337221040125.
-

- [97] J. Körner, M. Krüger, J. Reiter, A. Münzer, J. Hein, and M. C. Kaluza, "Temperature dependent spectroscopic study of Yb<sup>3+</sup>-doped KG(WO<sub>4</sub>)<sub>2</sub>, KY(WO<sub>4</sub>)<sub>2</sub>, YAlO<sub>3</sub> and YLiF<sub>4</sub> for laser applications," *Optical Materials Express*, vol. 10, no. 10, p. 2425, Oct. 2020. DOI: 10.1364/OME.398740.
- [98] K. W. Martin and L. G. DeShazer, "Indices of Refraction of the Biaxial Crystal YAlO<sub>3</sub>," *Applied Optics*, vol. 12, no. 5, p. 941, May 1973. DOI: 10.1364/AO.12.000941.
- [99] S. Radmard, A. Moshaii, and K. Pasandideh, "400 W average power Q-switched Yb:YAG thin-disk-laser," *Scientific Reports*, vol. 12, no. 1, p. 16918, Oct. 2022. DOI: 10.1038/s41598-022-20917-x.
- [100] N. P. Barnes, B. M. Walsh, and E. D. Filer, "Ho:Ho upconversion: applications to Ho lasers," *Journal of the Optical Society of America B*, vol. 20, no. 6, p. 1212, Jun. 2003. DOI: 10.1364/JOSAB.20.001212.
- [101] M. Malinowski, R. Piramidowicz, Z. Frukacz, G. Chadeyron, R. Mahiou, and M. Joubert, "Spectroscopy and upconversion processes in YAlO<sub>3</sub>:Ho<sup>3+</sup> crystals," *Optical Materials*, vol. 12, no. 4, p. 409, Sep. 1999. DOI: 10.1016/S0925-3467(98)00081-0.
- [102] J. Körner et al., "Spectroscopic investigations of thulium doped YAG and YAP crystals between 77 K and 300 K for short-wavelength infrared lasers," *Journal of Luminescence*, vol. 202, no. June, p. 427, Oct. 2018. DOI: 10.1016/j.jlumin.2018.05.070.
- [103] K. M A and K. Ennsner, "Model for a Thulium-Doped Silica Fiber Amplifier Pumped at 1558 nm and 793 nm," *International Journal of Engineering and Advanced Technology*, no. 54, p. 2249, 2016.
- [104] O. Buryy, D. Sugak, S. Ubizskii, I. Izhnin, M. Vakiv, and I. Solskii, "The comparative analysis and optimization of the free-running Tm<sup>3+</sup>:YAP and Tm<sup>3+</sup>:YAG microlasers," *Applied Physics B*, vol. 88, no. 3, p. 433, Aug. 2007. DOI: 10.1007/s00340-007-2718-3.
- [105] E. Honea, R. Beach, S. Sutton, J. Speth, S. Mitchell, J. Skidmore, M. Emanuel, and S. Payne, "115-W Tm:YAG diode-pumped solid-state laser," *IEEE Journal of Quantum Electronics*, vol. 33, no. 9, p. 1592, 1997. DOI: 10.1109/3.622641.
- [106] G. Rustad and K. Stenersen, "Modeling of laser-pumped Tm and Ho lasers accounting for upconversion and ground-state depletion," *IEEE Journal of Quantum Electronics*, vol. 32, no. 9, p. 1645, 1996. DOI: 10.1109/3.535370.
- [107] B. Saheya, G.-q. Chen, Y.-k. Sui, and C.-y. Wu, "A new Newton-like method for solving nonlinear equations," *SpringerPlus*, vol. 5, no. 1, p. 1269, Dec. 2016. DOI: 10.1186/s40064-016-2909-7.

- 
- [108] H. Okawa, K. Fujisawa, Y. Yamamoto, R. Hirai, N. Yasutake, H. Nagakura, and S. Yamada, "The W4 method: A new multi-dimensional root-finding scheme for nonlinear systems of equations," *Applied Numerical Mathematics*, vol. 183, no. 1, p. 157, Jan. 2023. DOI: 10.1016/j.apnum.2022.08.019. arXiv: 1809.04495.
- [109] K. M. Dinndorf and H. P. Jenssen, "Distribution of Stored Energy in the Excited Manifolds of Tm and Ho in 2 Micron Laser Materials," in *Advanced Solid State Lasers*, Washington, D.C.: OSA, 2004, HL8. DOI: 10.1364/ASSL.1994.HL8.
- [110] L. B. Shaw, R. S. Chang, and N. Djeu, "Measurement of up-conversion energy-transfer probabilities in Ho:Y<sub>3</sub>Al<sub>5</sub>O<sub>12</sub> and Tm:Y<sub>3</sub>Al<sub>5</sub>O<sub>12</sub>," *Physical Review B*, vol. 50, no. 10, p. 6609, 1994. DOI: 10.1103/PhysRevB.50.6609.
- [111] M. Malinowski, Z. Frukacz, M. Szuflińska, A. Wnuk, and M. Kaczkan, "Optical transitions of Ho<sup>3+</sup> in YAG," *Journal of Alloys and Compounds*, vol. 300-301, p. 389, Apr. 2000. DOI: 10.1016/S0925-8388(99)00770-7.
- [112] S. Bowman, M. Winings, R. Auyeung, J. Tucker, S. Searles, and B. Feldman, "Laser and spectral properties of Cr, Tm, Ho:YAG at 2.1 μm," *IEEE Journal of Quantum Electronics*, vol. 27, no. 9, p. 2142, Sep. 1991. DOI: 10.1109/3.135173.
- [113] F. Salin and J. Squier, "Gain guiding in solid-state lasers," *Optics Letters*, vol. 17, no. 19, p. 1352, Oct. 1992. DOI: 10.1364/OL.17.001352.
- [114] M. Rupp, M. Eichhorn, and C. Kieleck, "Iterative 3D modeling of thermal effects in end-pumped continuous-wave Ho<sup>3+</sup>:YAG lasers," *Applied Physics B*, vol. 129, no. 1, p. 4, Jan. 2023. DOI: 10.1007/s00340-022-07939-z.
- [115] W. Sellmeier, "Ueber die durch die Aetherschwingungen erregten Mitschwingungen der Koerpertheilchen und deren Rueckwirkung auf die ersteren, besonders zur Erklaerung der Dispersion und ihrer Anomalien," *Annalen der Physik*, vol. 223, no. 11, p. 386, Jan. 1872. DOI: 10.1002/andp.18722231105.
- [116] D. C. Brown, V. Envid, and J. Zembek, "Ho:YAG absorption cross sections from 1700 to 2200 nm at 83, 175, and 295 K," *Applied Optics*, vol. 51, no. 34, p. 8147, Dec. 2012. DOI: 10.1364/AO.51.008147.
- [117] B. R. Judd, "Optical Absorption Intensities of Rare-Earth Ions," *Physical Review*, vol. 127, no. 3, p. 750, Aug. 1962. DOI: 10.1103/PhysRev.127.750.
- [118] G. S. Ofelt, "Intensities of Crystal Spectra of Rare-Earth Ions," *The Journal of Chemical Physics*, vol. 37, no. 3, p. 511, Aug. 1962. DOI: 10.1063/1.1701366.
-

- [119] B. M. Walsh, *Advances in Spectroscopy for Lasers and Sensing*, B. Di Bartolo and O. Forte, Eds. Dordrecht: Springer Netherlands, 2006. DOI: 10.1007/1-4020-4789-4.
- [120] M. Eichhorn, "Fluorescence reabsorption and its effects on the local effective excitation lifetime," *Applied Physics B*, vol. 96, no. 2-3, p. 369, Aug. 2009. DOI: 10.1007/s00340-009-3395-1.
- [121] B. Heeg, P. A. DeBarber, and G. Rumbles, "Influence of fluorescence reabsorption and trapping on solid-state optical cooling," *Applied Optics*, vol. 44, no. 15, p. 3117, May 2005. DOI: 10.1364/AO.44.003117.
- [122] J. Degallaix, "OSCAR: A MATLAB based package to simulate realistic optical cavities," *SoftwareX*, vol. 12, p. 100587, Jul. 2020. DOI: 10.1016/j.softx.2020.100587.
- [123] R. Paschotta, "Mode Competition - an encyclopedia article," in *RP Photonics Encyclopedia*, RP Photonics AG, Nov. 2007. DOI: 10.61835/twz.
- [124] G. Stephan, A. D. May, B. Aissaoui, and R. E. Mueller, "Competition effects in the polarization of light in a quasi-isotropic laser," *Journal of the Optical Society of America B*, vol. 4, no. 8, p. 1276, Aug. 1987. DOI: 10.1364/JOSAB.4.001276.
- [125] L. Gomelsky and J. Liu, "Extension of beam propagation method to time-dependent optical waveforms," *IEEE Photonics Technology Letters*, vol. 6, no. 4, p. 546, Apr. 1994. DOI: 10.1109/68.281822.
- [126] H. M. Masoudi, "A Stable Time-Domain Beam Propagation Method for Modeling Ultrashort Optical Pulses," *IEEE Photonics Technology Letters*, vol. 19, no. 10, p. 786, May 2007. DOI: 10.1109/LPT.2007.895905.
- [127] R. Paschotta, "Q Factor - an encyclopedia article," in *RP Photonics Encyclopedia*, RP Photonics AG, Nov. 2007. DOI: 10.61835/dyf.
- [128] Xingyu Zhang, Shengzhi Zhao, Qingpu Wang, B. Ozygus, and H. Weber, "Modeling of diode-pumped actively Q-switched lasers," *IEEE Journal of Quantum Electronics*, vol. 35, no. 12, p. 1912, 1999. DOI: 10.1109/3.806608.
- [129] M. Wohlmuth, C. Pflaum, K. Altmann, M. Paster, and C. Hahn, "Dynamic multimode analysis of Q-switched solid state laser cavities," *Optics Express*, vol. 17, no. 20, p. 17303, Sep. 2009. DOI: 10.1364/OE.17.017303.
- [130] AeroDIODE Corporation. "Acousto Optic Modulator," Accessed: Jul. 27, 2024. [Online]. Available: <https://www.aerodiode.com/product/acousto-optic-modulator/>.

- 
- [131] W. C. Yao, E. H. Li, Y. J. Shen, C. Y. Ren, Y. G. Zhao, D. Y. Tang, and D. Y. Shen, "A 142 W Ho:YAG laser single-end-pumped by a Tm-doped fiber laser at 1931 nm," *Laser Physics Letters*, vol. 16, no. 11, p. 115001, Nov. 2019. DOI: 10.1088/1612-202X/ab459d.
- [132] M. Ganija, A. Hemming, K. Boyd, A. Gambell, and N. Simakov, "Progress Towards High Power Scaling of Ho:YAG Lasers," in *14th Pacific Rim Conference on Lasers and Electro-Optics (CLEO PR 2020)*, Washington, D.C.: Optica Publishing Group, 2020, C9A. DOI: 10.1364/CLEOPR.2020.C9A\_2.
- [133] D. S. Goodman, "Principles of Geometric Optics," in *Adaptive Optics for Biological Imaging*, CRC Press, Apr. 2013, p. 29. DOI: 10.1201/b14898-4.
- [134] J. H. VanSant, "Conduction heat transfer solutions," Lawrence Livermore National Laboratory (LLNL), Livermore, CA (United States), Tech. Rep., Mar. 1980. DOI: 10.2172/7035199.
- [135] H. Johnston and J.-G. Liu, "Finite Difference Schemes for Incompressible Flow Based on Local Pressure Boundary Conditions," *Journal of Computational Physics*, vol. 180, no. 1, p. 120, Jul. 2002. DOI: 10.1006/jcph.2002.7079.
- [136] B. Usievich, V. Sychugov, F. Pigeon, and A. Tishchenko, "Analytical treatment of the thermal problem in axially pumped solid-state lasers," *IEEE Journal of Quantum Electronics*, vol. 37, no. 9, p. 1210, 2001. DOI: 10.1109/3.945327.
- [137] A. Cousins, "Temperature and thermal stress scaling in finite-length end-pumped laser rods," *IEEE Journal of Quantum Electronics*, vol. 28, no. 4, p. 1057, Apr. 1992. DOI: 10.1109/3.135228.
- [138] F. Sen and M. Sayer, "Elasto-Plastic Thermal Stress Analysis in a Thermoplastic Composite Disc under Uniform Temperature Using FEM," *Mathematical and Computational Applications*, vol. 11, no. 1, p. 31, Apr. 2006. DOI: 10.3390/mca11010031.
- [139] P. Cardiff and I. Demirdžić, "Thirty Years of the Finite Volume Method for Solid Mechanics," *Archives of Computational Methods in Engineering*, vol. 28, no. 5, p. 3721, Aug. 2021. DOI: 10.1007/s11831-020-09523-0. arXiv: 1810.02105.
- [140] R. Weber, B. Neuenschwander, and H. Weber, "Thermal effects in solid-state laser materials," *Optical Materials*, vol. 11, no. 2-3, p. 245, Jan. 1999. DOI: 10.1016/S0925-3467(98)00047-0.
- [141] A. D. Polyanin and V. F. Zaitsev, *Handbook of Nonlinear Partial Differential Equations*. Chapman and Hall/CRC, Oct. 2003, p. 1. DOI: 10.1201/9780203489659.
-

- [142] M. Shallal and B. Jumaa, "Numerical Solutions Based on Finite Difference Techniques for Two Dimensional Advection-Diffusion Equation," *British Journal of Mathematics and Computer Science*, vol. 16, no. 2, p. 1, Jan. 2016. DOI: 10.9734/BJMCS/2016/25464.
- [143] F. E. Merga and H. M. Chemed, "Modified Crank–Nicolson Scheme with Richardson Extrapolation for One-Dimensional Heat Equation," *Iranian Journal of Science and Technology, Transaction A: Science*, vol. 45, no. 5, p. 1725, Oct. 2021. DOI: 10.1007/S40995-021-01141-0/FIGURES/4.
- [144] J. Douglas and J. E. Gunn, "A general formulation of alternating direction methods - Part I. Parabolic and hyperbolic problems," *Numerische Mathematik*, vol. 6, no. 1, p. 428, Dec. 1964. DOI: 10.1007/BF01386093/METRICS.
- [145] T.-Y. Wang, Y.-M. Lee, and C. C.-P. Chen, "3D thermal-ADI," in *Proceedings of the 2003 international symposium on Physical design*, New York, NY, USA: ACM, Apr. 2003, p. 10. DOI: 10.1145/640000.640007.
- [146] D. W. Peaceman and H. H. Rachford, Jr., "The Numerical Solution of Parabolic and Elliptic Differential Equations," *Journal of the Society for Industrial and Applied Mathematics*, vol. 3, no. 1, p. 28, Mar. 1955. DOI: 10.1137/0103003.
- [147] W. Ford, *Numerical Linear Algebra with Applications*. Elsevier, Sep. 2015, p. 1. DOI: 10.1016/C2011-0-07533-6.
- [148] M. J. Weber, *Handbook of Optical Materials*. CRC Press, Oct. 2018, vol. 20, p. 499. DOI: 10.1201/9781315219615.
- [149] Crytur Corporation. "YAG (undoped)," Accessed: Aug. 6, 2024. [Online]. Available: <https://www.crytur.com/materials/yag-undoped/>.
- [150] Crytur Corporation. "YAP (undoped)," Accessed: Aug. 6, 2024. [Online]. Available: <https://www.crytur.com/materials/yap-undoped/>.
- [151] L. Cini and J. I. Mackenzie, "Analytical thermal model for end-pumped solid-state lasers," *Applied Physics B*, vol. 123, no. 12, p. 273, Dec. 2017. DOI: 10.1007/s00340-017-6848-y.
- [152] J. A. Trangenstein, "Introduction to Finite Element Methods," in *Numerical Solution of Elliptic and Parabolic Partial Differential Equations*, Cambridge University Press, Apr. 2013, p. 179. DOI: 10.1017/CBO9781139025508.005.

- 
- [153] J. Hattel and P. Hansen, "A control volume-based finite difference method for solving the equilibrium equations in terms of displacements," *Applied Mathematical Modelling*, vol. 19, no. 4, p. 210, Apr. 1995. DOI: 10.1016/0307-904X(94)00015-X.
- [154] F. H. Harlow and J. E. Welch, "Numerical Calculation of Time-Dependent Viscous Incompressible Flow of Fluid with Free Surface," *The Physics of Fluids*, vol. 8, no. 12, p. 2182, Dec. 1965. DOI: 10.1063/1.1761178.
- [155] S. V. Patankar, *Numerical Heat Transfer and Fluid Flow*. CRC Press, Oct. 2018. DOI: 10.1201/9781482234213.
- [156] K. Harangus and A. Kakucs, "Finite-difference Solution Using Displacement Potential Function for Plane Stresses and Displacements," *Procedia Technology*, vol. 12, p. 394, 2014. DOI: 10.1016/j.protcy.2013.12.505.
- [157] X. Xue, J. Tian, and G. Xiu, "Numerical Simulation of Thermal Stress in Castings Using FDM/FEM Integrated Method," *Materials Science Forum*, vol. 490-491, no. 5, p. 85, Jul. 2005. DOI: 10.4028/www.scientific.net/MSF.490-491.85.
- [158] K. Shibib, M. Minshid, and N. Alattar, "Thermal and stress analysis in Nd: YAG laser rod with different double end pumping methods," *Thermal Science*, vol. 15, no. suppl. 2, p. 399, 2011. DOI: 10.2298/TSCI101201004S.
- [159] C. Kittel, *Introduction to solid state physics*. Wiley, 2005, p. 680.
- [160] D. Brown, "Ultrahigh-average-power diode-pumped Nd:YAG and Yb:YAG lasers," *IEEE Journal of Quantum Electronics*, vol. 33, no. 5, p. 861, May 1997. DOI: 10.1109/3.572162.
- [161] M. Eichhorn, S. Fredrich-Thornton, E. Heumann, and G. Huber, "Spectroscopic properties of  $\text{Er}^{3+}$ :YAG at 300–550 K and their effects on the 1.6  $\mu\text{m}$  laser transitions," *Applied Physics B*, vol. 91, no. 2, p. 249, May 2008. DOI: 10.1007/s00340-008-2981-y.
- [162] M. Rupp, M. Eichhorn, and C. Kieleck, "Improved 3D modeling of end-pumped continuous-wave  $\text{Ho}^{3+}$ :YAG lasers by inclusion of temperature-dependent material parameters," in *Optica Advanced Photonics Congress 2022*, Washington, D.C.: Optica Publishing Group, 2022, JW3A.4. DOI: 10.1364/ASSL.2022.JW3A.4.
- [163] Q. Lü, U. Wittrock, and S. Dong, "Photoelastic effects in Nd:YAG rod and slab lasers," *Optics and Laser Technology*, vol. 27, no. 2, p. 95, Apr. 1995. DOI: 10.1016/0030-3992(95)93621-W.
-

- [164] M. Schmid, R. Weber, T. Graf, M. Roos, and H. Weber, "Numerical simulation and analytical description of thermally induced birefringence in laser rods," *IEEE Journal of Quantum Electronics*, vol. 36, no. 5, p. 620, May 2000. DOI: 10.1109/3.842105.
- [165] M. Ostermeyer, D. Mudge, P. J. Veitch, and J. Munch, "Thermally induced birefringence in Nd:YAG slab lasers," *Applied Optics*, vol. 45, no. 21, p. 5368, 2006. DOI: 10.1364/AO.45.005368.
- [166] S. Mi, J. Tang, D. Wei, B. Yao, J. Li, K. Yang, T. Dai, and X. Duan, "Thermal-birefringence-induced depolarization in a 450 W Ho:YAG MOPA system," *Optics Express*, vol. 30, no. 12, p. 21501, Jun. 2022. DOI: 10.1364/OE.462617.
- [167] N. Kugler, S. Dong, Q. Lü, and H. Weber, "Investigation of the misalignment sensitivity of a birefringence-compensated two-rod Nd:YAG laser system," *Applied Optics*, vol. 36, no. 36, p. 9359, Dec. 1997. DOI: 10.1364/AO.36.009359.
- [168] Y. Wang, K. Inoue, H. Kan, T. Ogawa, and S. Wada, "Birefringence compensation of two tandem-set Nd:YAG rods with different thermally induced features," *Journal of Optics A: Pure and Applied Optics*, vol. 11, no. 12, p. 125501, Dec. 2009. DOI: 10.1088/1464-4258/11/12/125501.
- [169] W. Koehnner, "Thermal Lensing in a Nd:YAG Laser Rod," *Applied Optics*, vol. 9, no. 11, p. 2548, Nov. 1970. DOI: 10.1364/AO.9.002548.
- [170] R. Paschotta, "Thermal Lensing - an encyclopedia article," in *RP Photonics Encyclopedia*, RP Photonics AG, Nov. 2008. DOI: 10.61835/v71.
- [171] A. S. Dement'ev, A. Jovaiša, E. Stupak, and R. Kačianauskas, "Thermal Stresses and End-Bulging in Cylindrical Laser Rods Under Longitudinal Diode Laser Pumping," *Journal of Thermal Stresses*, vol. 37, no. 1, p. 73, Jan. 2014. DOI: 10.1080/01495739.2013.839462.
- [172] R. Paschotta, "Optical Power Meters - an encyclopedia article," *RP Photonics Encyclopedia*, Nov. 2023. DOI: 10.61835/SSH.
- [173] R. Paschotta, "Photoelectric Effect - an encyclopedia article," *RP Photonics Encyclopedia*, Nov. 2023. DOI: 10.61835/MES.
- [174] W. van Roosbroeck, "Theory of the Photomagnetolectric Effect in Semiconductors," *Physical Review*, vol. 101, no. 6, p. 1713, Mar. 1956. DOI: 10.1103/PhysRev.101.1713.
- [175] M. Czerny and A. F. Turner, "Ueber den Astigmatismus bei Spiegelspektrometern," *Zeitschrift fuer Physik*, vol. 61, no. 11-12, p. 792, Nov. 1930. DOI: 10.1007/BF01340206.

- 
- [176] V. S. Serebryakov, É. V. Bořko, A. G. Kalintsev, A. F. Kornev, A. S. Narivonchik, and A. L. Pavlova, "Mid-IR laser for high-precision surgery," *Journal of Optical Technology*, vol. 82, no. 12, p. 781, Dec. 2015. DOI: 10.1364/JOT.82.000781.
- [177] A. Sijan, "Development of military lasers for optical countermeasures in the mid-IR," *Technologies for Optical Countermeasures VI, SPIE*, vol. 7483, M. A. Richardson, Ed., p. 748304, Sep. 2009. DOI: 10.1117/12.835439.
- [178] Y.-J. Shen, B.-Q. Yao, X.-M. Duan, G.-L. Zhu, W. Wang, Y.-L. Ju, and Y.-Z. Wang, "103 W in-band dual-end-pumped Ho:YAG laser," *Optics Letters*, vol. 37, no. 17, p. 3558, Sep. 2012. DOI: 10.1364/OL.37.003558.
- [179] M. Rupp, K. Goth, M. Eichhorn, and C. Kieleck, "High average power Q-switched Ho<sup>3+</sup>:YAG laser with a single-line emission at 2122 nm," *Optics Letters*, vol. 48, no. 21, p. 5619, Nov. 2023. DOI: 10.1364/OL.501824.
- [180] S. Lamrini, P. Koopmann, M. Schäfer, K. Scholle, and P. Fuhrberg, "Efficient high-power Ho:YAG laser directly in-band pumped by a GaSb-based laser diode stack at 1.9  $\mu\text{m}$ ," *Applied Physics B*, vol. 106, no. 2, p. 315, Feb. 2012. DOI: 10.1007/s00340-011-4670-5.
- [181] A. Berrou, T. Ibach, and M. Eichhorn, "High-energy resonantly diode-pumped Q-switched Ho<sup>3+</sup>:YAG laser," *Applied Physics B*, vol. 120, no. 1, p. 105, Jul. 2015. DOI: 10.1007/s00340-015-6108-y.
- [182] B.-R. Zhao, B.-Q. Yao, C.-P. Qian, G.-Y. Liu, Y. Chen, R.-X. Wang, T.-Y. Dai, and X.-M. Duan, "231 W dual-end-pumped Ho:YAG MOPA system and its application to a mid-infrared ZGP OPO," *Optics Letters*, vol. 43, no. 24, p. 5989, Dec. 2018. DOI: 10.1364/OL.43.005989.
- [183] S. Mi, D. Wei, B. Yao, Z. Lei, J. Li, J. Tang, T. Dai, and X. Duan, "Power improvement of a Ho:YAG power amplifier and its application to a 150 W ZGP-OPO," *Applied Physics B*, vol. 129, no. 11, p. 166, Nov. 2023. DOI: 10.1007/s00340-023-08112-w.
- [184] K. Goth, I. Vergara, M. Griesbeck, M. Eitner, M. Rupp, M. Eichhorn, and C. Kieleck, "High-Beam Quality Highly-Efficient High-Average-Power Pulse Amplification in Ho<sup>3+</sup>:YAG," in *Laser Congress 2023 (ASSL, LAC)*, vol. 2023, Washington, D.C.: Optica Publishing Group, 2023, JM4A.23. DOI: 10.1364/ASSL.2023.JM4A.23.
- [185] N. Kugler, S. Dong, Q. Lü, and H. Weber, "Investigation of the misalignment sensitivity of a birefringence-compensated two-rod Nd:YAG laser system," *Applied Optics*, vol. 36, no. 36, p. 9359, Dec. 1997. DOI: 10.1364/AO.36.009359.
-

- [186] J. Kwiatkowski and J. Sotor, “Laser wavelength shift and dual-wavelength generation in continuous-wave operation of Ho:YAG laser pumped by thulium-doped fiber laser,” *Optics and Laser Technology*, vol. 146, p. 107544, Feb. 2022. DOI: 10.1016/j.optlastec.2021.107544.
- [187] J. Meyer, J. Sompo, and S. von Solms, *Fiber Lasers*. Boca Raton: CRC Press, Dec. 2021. DOI: 10.1201/9781003256380.
- [188] R. Paschotta, “Nonlinearities - an encyclopedia article,” *RP Photonics Encyclopedia*, Nov. 2023. DOI: 10.61835/08E.
- [189] J. Schneider et al., “High-energy nanosecond pulse extraction from a Tm<sup>3+</sup>-doped photonic crystal fiber laser emitting at 2050 nm with narrow linewidth,” *Optics Express*, vol. 32, no. 18, p. 32309, Aug. 2024. DOI: 10.1364/OE.531146.
- [190] D. Lorenz, C. Romano, D. Panitzek, P. Forster, J. Schneider, H. Büker, M. Eichhorn, and C. Kieleck, “Nanosecond pulsed narrow-linewidth all-fiber source for ZGP-OPO pumping,” *Optics Continuum*, vol. 2, no. 3, p. 660, Mar. 2023. DOI: 10.1364/OPTCON.486081.
- [191] D. Lorenz, M. Rupp, D. Panitzek, C. Romano, P. Forster, J. Schneider, M. Eichhorn, and C. Kieleck, “Simulation and investigation of conduction-driven thermal blooming at 2055 nm,” in *Free-Space Laser Communications XXXVI*, H. Hemmati and B. S. Robinson, Eds., SPIE, Mar. 2024, p. 68. DOI: 10.1117/12.3003038.
- [192] J. Lahyani, M. Thiers, F. Gibert, D. Edouart, J. L. Gouët, and N. Cézard, “Hybrid fiber/bulk laser source designed for CO<sub>2</sub> and wind measurements at 2.05 μm,” *Optics Letters*, vol. 49, no. 4, p. 969, Feb. 2024. DOI: 10.1364/OL.510598.
- [193] M. Schellhorn, “A comparison of resonantly pumped Ho:YLF and Ho:LLF lasers in CW and Q-switched operation under identical pump conditions,” *Applied Physics B*, vol. 103, no. 4, p. 777, Jun. 2011. DOI: 10.1007/s00340-011-4467-6.

# Publications and Conference Contributions

## Peer-Reviewed Publications (First Author)

**M. Rupp**, M. Eichhorn, and C. Kieleck, “Iterative 3D modeling of thermal effects in end-pumped continuous-wave  $\text{Ho}^{3+}$ :YAG lasers,” *Applied Physics B*, vol. 129, no. 1, p. 4, 2023. DOI: 10.1007/s00340-022-07939-z.

**M. Rupp**, K. Goth, M. Eichhorn, and C. Kieleck, “High average power Q-switched  $\text{Ho}^{3+}$ :YAG laser with a single-line emission at 2122 nm,” *Optics Letters*, vol. 48, no. 21, p. 5619, 2023. DOI: 10.1364/OL.501824.

## Peer-Reviewed Publications (Co-Author)

**K. Goth**, **M. Rupp**, M. Griesbeck, M. Eitner, M. Eichhorn, and C. Kieleck, “Limitations of homogeneous and segmented single-crystal compact  $\text{TEM}_{00}$ -mode  $\text{Ho}^{3+}$ :YAG laser resonators,” *Applied Physics B*, vol. 129, no. 6, p. 95, 2023. DOI: 10.1007/s00340-023-08033-8.

**K. Goth**, M. Eitner, M. Griesbeck, **M. Rupp**, D. Lorenz, J. Deutsch, M. Eichhorn, and C. Kieleck, “Beam quality improvement in a linear ZPG OPO pumped by a Q-switched compact high-power  $\text{Ho}^{3+}$ :YAG laser,” *Optics Continuum*, vol. 3, no. 2, p. 112, 2024. DOI: 10.1364/OPTCON.505473.

## Conference Contributions

**M. Rupp**, K. Goth, M. Eichhorn, and C. Kieleck, “Iterative 3D modeling of thermal effects in end-pumped continuous-wave  $\text{Ho}^{3+}$ :YAG lasers,” in *EPJ Web of Conferences*, Talk, vol. 267, Hannover, Germany, Aug. 2022, p. 01003. DOI: 10.1051/epjconf/202226701003.

**M. Rupp**, M. Eichhorn, and C. Kieleck, “Improved 3D modeling of end-pumped continuous-wave  $\text{Ho}^{3+}$ :YAG lasers by inclusion of temperature-dependent material parameters,” in *Optica Advanced Photonics Congress 2022*, Poster, Barcelona, Spain, Dec. 2022, JW3A.4. DOI: 10.1364/ASSL.2022.JW3A.4.

**M. Rupp**, K. Goth, M. Eichhorn, and C. Kieleck, “Iterative 3D Modeling of Pulse Generation in End-Pumped  $\text{Ho}^{3+}$ :YAG Laser Resonators Utilizing Active Q-switching,” in *2023 Conference on Lasers and Electro-Optics Europe & European Quantum Electronics Conference (CLEO/Europe-EQEC)*, Poster, Munich, Germany, Jun. 2023, p. 1. DOI: 10.1109/CLEO/Europe-EQEC57999.2023.10232536.

**M. Rupp**, M. Eichhorn, and C. Kieleck, “Advanced numerical simulation model for end-pumped  $\text{Ho}^{3+}$ :YAG laser resonators,” in *SPIE Photonics West (Solid State Lasers XXXIII: Technology and Devices)*, Talk, vol. 12864, San Francisco, USA, Jan. 2024, p. 26. DOI: 10.1117/12.2690256.

**M. Rupp**, D. Lorenz, K. Goth, M. Eichhorn, and C. Kieleck, “Advancing solid-state laser capabilities with a multi-physics modeling approach,” in *High-Power Lasers and Technologies for Optical Countermeasures II*, Talk, vol. PC13201, Edinburgh, UK, Sep. 2024, PC132010C. DOI: 10.1117/12.3031652.

## Awards

**IPG Student Poster Award** for “Improved 3D Modeling of end-Pumped Continuous-Wave  $\text{Ho}^{3+}$ :YAG Lasers by Inclusion of Temperature-Dependent Material Parameters” at *Optica Laser Congress 2022 (ASSL, LAC)*, Barcelona, Spain, Dec. 2022

# List of Acronyms

<b>LASER</b>	light amplification by stimulated emission of radiation
<b>CW</b>	continuous wave
<b>OC</b>	output coupler
<b>HR</b>	high reflectance
<b>IC</b>	incoupling mirror
<b>MOPA</b>	master oscillator power amplifier
<b>YAG</b>	yttrium aluminium garnet
<b>YALO</b>	yttrium orthoaluminate
<b>YLF</b>	yttrium lithium fluoride
<b>LLF</b>	lithium lutetium fluoride
<b>Ho<sup>3+</sup></b>	holmium(III) oxide
<b>Tm<sup>3+</sup></b>	thulium(III) oxide
<b>Nd<sup>3+</sup></b>	neodymium(III) oxide
<b>Yb<sup>3+</sup></b>	ytterbium(III) oxide
<b>Er<sup>3+</sup></b>	erbium(III) oxide
<b>ZGP</b>	zinc germanium phosphide
<b>BPM</b>	beam propagation method
<b>TEM</b>	transverse electromagnetic
<b>FDTD</b>	finite difference time domain
<b>FEM</b>	finite element method

<b>SVEA</b>	slowly varying envelope approximation
<b>DMA</b>	dynamic mode analysis
<b>FFT</b>	fast Fourier transform
<b>FDM</b>	finite difference method
<b>PDE</b>	partial differential equation
<b>ADI</b>	alternating-direction implicit method
<b>CFL</b>	Courant–Friedrichs–Lewy condition
<b>ETU</b>	energy transfer upconversion
<b>FWHM</b>	full width at half maximum
<b>EOM</b>	electro-optic modulator
<b>AOM</b>	acousto-optic modulator
<b>RF</b>	radio frequency
<b>SWIR</b>	short wave infrared
<b>PEM</b>	photoelectromagnetic
<b>OPO</b>	optical parametric oscillator
<b>OPA</b>	optical parametric amplification
<b>OPG</b>	optical parametric generation
<b>LIDT</b>	laser-induced damage threshold
<b>LIDAR</b>	light detection and ranging
<b>2D</b>	two-dimensional
<b>3D</b>	three-dimensional

# Acknowledgements

At the end of my doctoral studies, I would like to thank all the people who have contributed to this work over the last (almost) five years. I regret not being able to name each person individually, as there are many who have supported me during this time.

First and foremost, I would like to thank my doctoral supervisor at the KIT, Prof. Dr. Marc Eichhorn. It was only through the scientific freedom and guidance he provided, that this work could take the shape it did. Additionally, I would like to thank my department head and supervisor at Fraunhofer IOSB, Dr. Christelle Kieleck, who gave me the opportunity to conduct my scientific work at IOSB and has supported me there.

Next, it is important for me to acknowledge those who have directly contributed to this work by providing feedback on my thesis and taking the time for helpful discussions – my colleagues Dominik Lorenz, Katharina Goth, Patrick Forster, Michael Griebbeck and Julian Schneider. In this context, I would like to thank all my colleagues from the LAS working group, as working with them has been a lot of fun. Additionally, I would like to thank Patrick (again) and Johannes Eckhardt for being great office mates, and Nicolas Wannenmacher, who provided the infrastructure for my simulations.

Besides my colleagues at the IOSB, I would also like to thank everyone at the KIT IRS, where I have always experienced a friendly and open atmosphere. I would particularly like to thank Dr. Armin Teltschik and Andrea Bindschädel for their support.

Lastly, I would like to express my gratitude to my family and friends. Without their support, I would have never been able to start and complete this journey. Special thanks goes to my parents, Solveig and Andreas Rupp, my brother Adrian Rupp, and my late grandmother Christa Palmowski, who have supported me long before this work as well. I am also very thankful to my

girlfriend, Rebecca Keilhauer, who has managed to keep me motivated with her encouragement during this time.





INSTITUTE OF CONTROL SYSTEMS

LASERS AND OPTRONICS: MATERIALS,  
TECHNOLOGIES AND APPLICATIONS

05

This series contains scientific reports on laser technology and optronics performed at or in cooperation with the IRS. The topics range from laser-related materials like crystals and glasses and their elaboration over laser physics and technologies up to laser and optronic applications.

Lasers are indispensable today in many fields such as communication, environmental sensing, metrology, and defense. This work deals with the simulation-based investigation of solid-state lasers. As laser systems can be very complex, simulations help to optimize them efficiently. They provide insights into processes that are difficult to access, such as temperature, stress, and population dynamics. In this work, a novel multi-physics model is developed that combines laser beam propagation, laser dynamics, and thermal effects to simulate high-power solid-state lasers. The numerical model is highly precise and is used in the course of this work for the design and optimization of  $\text{Ho}^{3+}$ :YAG lasers, which are important sources for direct and pumping applications in SWIR and MWIR wavelength ranges. The developed model demonstrates its effectiveness as a tool for the development of high-power lasers and amplifiers.